

THE ROLE OF SHP2 IN METASTATIC BREAST CANCER

by

Hao Chen

A Dissertation

Submitted to the Faculty of Purdue University

In Partial Fulfillment of the Requirements for the degree of

Doctor of Philosophy



Department of Medicinal Chemistry and Molecular Pharmacology

West Lafayette, Indiana

May 2022

THE PURDUE UNIVERSITY GRADUATE SCHOOL
STATEMENT OF COMMITTEE APPROVAL

Dr. Michael K. Wendt, Chair

Department of Medicinal Chemistry and Molecular Pharmacology

Dr. Zhong-Yin Zhang

Department of Medicinal Chemistry and Molecular Pharmacology

Dr. Seung-Oe Lim

Department of Medicinal Chemistry and Molecular Pharmacology

Dr. Daniel P. Flaherty

Department of Medicinal Chemistry and Molecular Pharmacology

Approved by:

Dr. Jason R. Cannon

Dr. Andy Hudmon

Dedicated to my parents and grandparents, for their love and support

ACKNOWLEDGMENTS

First, I would like to thank my advisor, Dr. Michael K. Wendt for his guidance and support in this 6-year journey towards the degree. Dr. Wendt is always open to discussion with me about the projects and gives all the experience he has to me. I have learned a lot from him in these years. Without his guidance, it is not possible for me to accomplish the research in this thesis efficiently and smoothly. He also cares about the career of the students, and supports my choices. Besides the academic guidance, Dr. Wendt is one of my best friends in daily life. I am very happy to share everyday life with him and ask his opinion. I am very glad that I have the best luck to meet such a perfect advisor.

Meanwhile, I want to thank the members of my thesis committee, Dr. Zhong-Yin Zhang, Dr. Seung-Oe Lim and Dr. Daniel P. Flaherty for their helpful comments during these years. I also want to thank Dr. Alice Chang, who served previously on my thesis committee.

The accomplishment of my thesis research will not be possible without the help of my labmates and collaborators. Thus, I acknowledge the current members at Wendt lab, Dr. Eylem Kulkoyluoglu Cotul, Sebastian Paez, Mitchell Ayers, Hassan Safdar, Aneesha Kulkarni, Marvis Monteiro and Brenna Vaughn. The alumni of Wendt lab, Dr. Hang Lin, Dr. Ammara Abdullah, Sherry Liang, Dr. Saeed Salehin Akhand, Dr. Remah Ali, Dr. Aparna Shinde and Dr. Wells S. Brown, also helped me a lot, and I want to give my thankfulness to them. The collaborators, Dr. Zhong-Yin Zhang, Dr. Luis Solorio, Dr. Timothy L. Ratliff, Dr. Daniel P. Flaherty and their lab members also provided resources and helped with my research, and I want to thank them as well. I also want to thank Dr. Jill E. Hutchcroft, Dr. Wen-Hung Wang, and Flow Cytometry and Cell Separation Core Facility at Bindley Bioscience Center, Purdue University for cell sorting.

I also want to thank the funding resource that provided support to me in these years, including the Purdue Interdisciplinary Life Science (PULSe) Program, the SIRG Graduate Research Assistantships Award from the Purdue University Center for Cancer Research, a grant from the Lilly Endowment, Inc., to the College of Pharmacy at Purdue University and Bilsland Dissertation Fellowships offered by College of Pharmacy at Purdue University.

Finally, I must give my thankfulness to my parents, grandparents, family members and friends for their love and support.

TABLE OF CONTENTS

LIST OF TABLES	10
LIST OF FIGURES	11
ABSTRACT	22
CHAPTER 1. INTRODUCTION.....	24
1.1 Metastatic Breast Cancer	24
1.1.1 Mapping the categories of breast cancer	24
1.1.2 Metastatic breast cancer is the most advanced stage of breast cancer.....	28
1.1.3 Challenges in treating metastatic breast cancer	29
1.1.4 Metastatic breast cancer is complicated and flexible	30
1.2 Multiple signaling drivers in metastatic breast cancer cells	32
1.2.1 Metastatic breast cancer is complicated and flexible	33
1.2.2 Extracellular matrix signaling.....	34
1.2.3 Regulators of anti-tumor immunity	36
1.3 Heterogeneous tumor microenvironment in metastatic breast cancer	37
1.4 SHP2 is an oncogenic phosphatase in both tumor cells and immune cells	38
1.4.1 SHP2 is a non-receptor protein tyrosine phosphatase	38
1.4.2 Oncogenic functions of SHP2 in tumor cells and immune cells	40
1.5 SHP2 is a druggable promising therapeutic target.....	41
1.6 Hypotheses and aims.....	42
CHAPTER 2. TARGETING SHP2 TO INHIBIT METASTATIC BREAST CANCER	44
2.1 Disclaimer	44
2.2 Introduction.....	44
2.3 Materials and Methods.....	46
2.3.1 Cell lines, culture conditions, drug and reagents	46
2.3.2 Cell viability assays and colony formation assays on tissue culture treated polystyrene (2D culture)	47
2.3.3 Cell viability assays on ECM matrix (3D culture)	48
2.3.4 Immunoblotting and signaling wash-off assays	49
2.3.5 Depletion of SHP2 with doxycycline inducible shRNA	50

2.3.6	Studies with in vivo metastatic models and animal care	51
2.3.7	Statistical analysis.....	52
2.4	Results.....	53
2.4.1	SHP2 inhibitors block the grow of MBC cells in vitro	53
2.4.2	Three dimensional culture environment enhances growth inhibitory effects of SHP2 blockade.....	54
2.4.3	Drug resistant breast cancer cells can be targeted by SHP2 inhibitors.....	59
2.4.4	Depletion of SHP2 inhibits the growth of metastatic breast cancer cells.....	62
2.4.5	SHP2 inhibitor delays the pulmonary metastasis <i>in vivo</i>	67
2.4.6	SHP2 inhibitor reduces the pulmonary growth of metastatic breast cancer in vivo..	70
2.5	Conclusions.....	71
CHAPTER 3. DIVERSE SIGNALING INPUTS OF SHP2 IN METASTATIC BREAST CANCER CELLS		73
3.1	Disclaimer.....	73
3.2	Introduction.....	73
3.3	Materials and Methods.....	74
3.3.1	Cell lines, culture conditions, drug and reagents.....	74
3.3.2	Clinical dataset analysis.....	74
3.3.3	Immunoblotting for samples under different culture conditions	75
3.3.4	Cell viability assays with growth factors.....	76
3.3.5	Tumor sphere assays under 3D culture conditions	77
3.3.6	Statistical analysis.....	77
3.4	Results.....	77
3.4.1	Phosphorylation of SHP2 at Y542 is a key signaling readout with clinical significance	77
3.4.2	Phosphorylation of SHP2 at Y542 is induced by multiple growth factors.....	79
3.4.3	Growth factor induced growth of MBC cells depends on SHP2.....	81
3.4.4	Phosphorylation of SHP2 at Y542 is induced by three dimensional culture environments.....	85
3.4.5	The induction of phosphorylation of SHP2 at Y542 depends on differential mechanisms.....	87

3.5	Conclusions.....	90
CHAPTER 4.	TUMOR-CELL AUTONOMOUS SHP2 SUPPORTING IMMUNOSUPPRESSIVE TUMOR MICROENVIRONMENT.....	92
4.1	Disclaimer.....	92
4.2	Introduction.....	92
4.3	Materials and Methods.....	93
4.3.1	Cell line, culture condition, drugs and reagents	93
4.3.2	Clinical dataset analysis and code availability	94
4.3.3	Animal care and SHP2 depletion experiments <i>in vivo</i>	95
4.3.4	Pulmonary tumor and spleen isolation/digestion and flow cytometry	95
4.3.5	Incucyte-based T cell killing assays	96
4.3.6	Statistical analysis.....	96
4.4	Results.....	97
4.4.1	Phosphorylation of SHP2 at Y542 is a promising marker to predict immune profiles	97
4.4.2	Depletion of tumor-cell autonomous SHP2 reduces pulmonary metastasis <i>in vivo</i>	100
4.4.3	Depletion of tumor-cell autonomous SHP2 adjusted T-cell composition and relieved T-cell exhaustion	103
4.4.4	Depletion of tumor-cell autonomous SHP2 adjusted TAMs composition	105
4.4.5	Tumor-cell autonomous SHP2 facilitates growth factors to reduce T cell cytotoxicity	107
4.5	Conclusions.....	110
CHAPTER 5.	SIGNALING OUTPUTS OF SHP2 REGULATING TUMOR GROWTH AND IMMUNOSUPPRESSION.....	111
5.1	Disclaimer.....	111
5.2	Introduction.....	111
5.3	Materials and Methods.....	111
5.3.1	Cell lines, culture conditions, drugs and reagents	111
5.3.2	Immunoblotting assays	112
5.3.3	Flow cytometry for MBC cells <i>in vitro</i>	113

5.3.4	RNA isolation and Quantitative real-time PCR analysis.....	113
5.3.5	Statistical analysis.....	114
5.4	Results.....	114
5.4.1	Phosphorylation of ERK1/2 and ATK are the signaling output of SHP2 in MBC cells	114
5.4.2	SHP2 regulates PD-L1 as a signaling output under multiple RTKs signaling	116
5.4.3	SHP2 regulates PD-L1 as a signaling output under 3D culture environments.....	119
5.4.4	Expression of MHC class I depends on the balance between MAPK and STAT1 signaling regulated by SHP2 in MBC cells	121
5.5	Conclusions.....	123
CHAPTER 6. COMBINATION STRATEGIES WITH SHP2 INHIBITION TO TREAT METASTATIC BREAST CANCER.....		124
6.1	Disclaimer	124
6.2	Introduction.....	124
6.3	Materials and Methods.....	124
6.3.1	Cell lines, culture conditions, drugs and reagents	124
6.3.2	Cell viability assays and drug combination study	125
6.3.3	Animal care and combination experiments in vivo	125
6.3.4	Pulmonary tumor and spleen isolation/digestion and flow cytometry	125
6.3.5	Statistical analysis.....	126
6.4	Results.....	126
6.4.1	Combination of SHP2 inhibitors with FIIN4 blocks the growth of MBC cells under 2D culture conditions.....	126
6.4.2	SHP2 inhibitors synergize with FIIN4 in vitro.....	128
6.4.3	Combination of SHP2 inhibitors with FIIN4 blocks the growth of MBC cells under 3D culture conditions.....	129
6.4.4	Pharmacological SHP2 inhibition synergizes with FIIN4 in vivo.....	131
6.4.5	Pharmacological SHP2 inhibition sensitizes MBC cells in lungs to α -PD-L1 <i>in vivo</i>	133
6.4.6	Pharmacological SHP2 inhibition relieves T-cell exhaustion induced by α -PD-L1	136

6.4.7	Combination of SHP099 and α -PD-L1 adjusted TAMs composition	138
6.5	Conclusions.....	140
CHAPTER 7. DISCUSSION AND FUTURE DIRECTIONS		141
7.1	Disclaimer	141
7.2	SHP2 is dynamic in response to varies signaling inputs.....	141
7.3	SHP2 contributes immunosuppression and multiple signaling outputs.....	143
7.4	Optimization for combination strategies with SHP2 inhibition.....	144
APPENDIX A. SUPPLEMENTARY TABLES		148
APPENDIX B. SUPPLEMENTARY INFORMATION		153
REFERENCES		157
VITA		173
PUBLICATIONS.....		174

LIST OF TABLES

Table 1.1. The detailed information for two types of SHP2 inhibitors used in this study. The Name, development method, mechanism of action, IC₅₀ value to SHP2, selectivity, key interactions to ensure selectivity, solubility, bioavailability and corresponding references for 11a-1, SHP099 and TNO155 are listed in the table below..... 41

LIST OF FIGURES

- Figure 1.1. Categories of breast cancer by intrinsic subtypes and stages. Breast cancer can be categorized into ER positive, HER2 positive and triple negative by intrinsic molecular markers (top). Breast cancer can also be categorized into localized (stage 0), invasive (stage I-III) and metastatic (stage IV) by stages (bottom). The predicted prognosis and therapeutic options for each category are listed, in which metastatic breast cancer has the worst prognosis and fewer treatment options compared to the other stages (middle). Parts of the figure are created with BioRender. 25
- Figure 1.2. Steps for the progression of metastatic breast cancer. Metastatic breast cancer is a disease in which the cancer cells move from the primary site to the distant organs via the blood circulation. The metastatic breast cancer cells have to go through major steps, including coming out of the primary site (left), moving into the circulation (middle), and disseminating in the distant organs (right). There are more sequential and complicated small steps in each major step. Parts of the figure are created with BioRender. 31
- Figure 1.3. Receptor tyrosine kinases signaling pathways induced by multiple growth factors play an important role in resistance to HER2-targeted therapies in MBC cells. The growth and survival signaling pathways (PI3K and MAPK) are blocked by HER2-targeted therapies, lapatinib, and neratinib. The MBC cells resistant to HER2-targeted therapies are capable of activating multiple receptor tyrosine kinases signaling pathways induced by multiple growth factors to reactivate original growth and survival pathways or introduce novel by-pass pathways. 33
- Figure 1.4. Extracellular matrix-mediated integrin signaling has crosstalk with receptor tyrosine kinases signaling in MBC cells. Extracellular matrix components, including fibronectin, can regulate Src and FAK to activate growth and survival signaling pathways. ECM signaling can also interact with receptor tyrosine kinases and activate receptor tyrosine kinases signaling without ligand binding, which enhances the growth of MBC cells. Parts of the figure are created with BioRender. 35
- Figure 1.5. Immune checkpoints and major histocompatibility complexes control the anti-tumor immunity via T-cell cytotoxic events. The major histocompatibility complex class I molecules presents the antigen and activate T-cell receptor signaling. The interaction by MHC I and T-cell receptor triggers an immune response and kills the cells, which is interrupted by the interaction of immune checkpoint PD-1 and its partner PD-L1 (top). When the interaction of PD-1 and PD-L1 is blocked by immune checkpoint blockade, the T-cell activity is relieved to induce T-cell mediated tumor killing events (bottom). Parts of the figure are created with BioRender. 37
- Figure 1.6. Activation of SHP2 requires a conformational change from an auto-inhibitory basal state to an activation state. In the basal state, the SH2 domain at N-terminal (N-SH2 domain) interacts with the PTP domain, which inhibits the substrate binding and activity of SHP2 (left). Upon interacting with specific phosphorylated tyrosine motifs, the interaction between the N-SH2 domain and PTP domain is weakened, and the SHP2 is in the activation state (right). SHP2 can be phosphorylated at Y542, which is essential to the activation of downstream MAPK signaling. 39

Figure 1.7. Hypotheses and aims of the study. We hypothesize that SHP2 is a key shared node in MBC cells to promote tumor cell survival and immune evasion. The aim of the study is to identify which signaling inputs regulate corresponding signaling outputs through SHP2 in MBC cells. The successful accomplishment of this study will support the SHP2 inhibitors as novel therapeutics in the management of MBC..... 43

Figure 2.1. SHP2 inhibitors block the growth of MBC cells. A, Viability curves of 4T1 cells in response to SHP2 inhibitors, 11a-1 (red), SHP099 (blue) and TNO155 (green), at different concentrations. B, Viability curves of D2.A1 cells in response to SHP2 inhibitors, 11a-1 (red), SHP099 (blue) and TNO155 (green), at different concentrations. C, Viability curves of different human MBC cell lines, ZR-75-1 cells (black), SK-BR-3 cells (red) and MDA-MB-435 cells (blue), in response to 11a-1 at different concentrations. D, Viability curves of different human MBC cell lines, ZR-75-1 cells (black), SK-BR-3 cells (red) and MDA-MB-435 cells (blue), in response to SHP099 at different concentrations. In all panels, the percentage of viability is normalized to corresponding media controls..... 54

Figure 2.2. The effects of SHP2 inhibitors to block cell growth are enhanced under 3D culture conditions compared to 2D in 4T1 cells. A, Schematic representation of 2D and 3D culture conditions. The MBC cells are cultured directly on tissue-cultured plastic in 2D culture, while the MBC cells are supported by a layer of Cultrex matrix in 3D culture. B, Cell viability of 4T1 cells cultured in 2D for 6 days in the absence or presence of 11a-1 at 5 μ M and SHP099 at 2 μ M. C, Representative photomicrographs and quantification of 4T1 cell viability after 16 days in 3D culture in the absence or presence of 11a-1 at 5 μ M and SHP099 at 2 μ M. D, Crystal violet visualization of the viable cells of 4T1 cells cultured in 2D for 6 days in the absence or presence of the indicated different concentrations of TNO155. E, Representative photomicrographs and quantification of 4T1 cell viability in 3D culture in the absence or presence of TNO155 at 0.625 μ M. In all panels, data are normalized to vehicle controls and are the mean \pm s.e.m. of three experiments where NS as no significance, * p <0.05, ** p < 0.01 and *** p < 0.001..... 55

Figure 2.3. MBC cell lines are more sensitive to SHP2 inhibition under 3D culture conditions compared to 2D. A-N, Differential cell viability of D2.A1 (A, B), HME2 (C, D), SK-BR-3 (E, F), BT474 (G, H), UACC812 (I, J), ZR-75-1 (K, L) and MDA-MB-435 (M, N) upon treatment with SHP099 or 11a-1 at the indicated concentrations under 2D or 3D culture conditions. O, Q, Crystal violet visualization of the viable cells of D2.A1 cells (O) and 4TO7 cells (Q) cultured in 2D for 6 days in the absence or presence of the indicated different concentrations of TNO155. P, R, Representative photomicrographs and quantification of D2.A1 cells (P) and 4TO7 cells (R) viabilities in 3D culture in the absence or presence of TNO155 at 0.625 μ M. In all cases data are the mean \pm s.e.m of cell viability normalized to vehicle controls, resulting in * p <0.05, ** p <0.01, *** p <0.001 as determined via a student's t-test..... 57

Figure 2.4. Drug resistant breast cancer cells can be targeted by SHP2 inhibitors via blocking signaling rebound. A, Representative dose response of HME2 parental (HME2-Par) and lapatinib resistant (HME2-LAPR) cells treated with neratinib for 6 days (left). The IC₅₀ values for each independent experiment were calculated (n=4) and analyzed using a two-tail student's t-test where * p <0.05. B, Representative dose response upon 6 days treatment with 11a-1 (left). Cell viability upon treatment with 10 μ M 11a-1 for each independent experiment was calculated (n=4) and analyzed using a two-tail student's t-test where ** p <0.01. C, Representative dose response curves of HME2 parental (HME2-Par) and HME2-LAPR cells treated with SHP099 for 6 days

(left). The IC50 values for each independent experiment were calculated (n = 3) and analyzed using two-tail student's t-test where $**p < 0.01$. D, Growth inhibitory effects of neratinib are enhanced when combined with SHP2 inhibitors in HME2 parental cells. HME2 parental cells were seeded in 96-well plates, and treated with the indicated concentrations of neratinib, SHP2 inhibitors, or both compounds for 2 days. Cell growth was quantified by relative luminescence ratio compared to untreated cells. (n = 4, resulting in $*p < 0.05$, or no significance (NS) using a two-tail Student's t-test). E, Immunoblotting showing phosphorylation of AKT, ERK1/2, and HER2 in HME2-Par and HME2-LAPR cells upon the indicated time-course neratinib treatments. F, Schematic representation of the signaling recovery assays (top). HME2-LAPR cells were treated with neratinib for 1 h, the drug was removed, and the cells were allowed to recover in serum free media in the presence or absence of SHP2 or FGFR inhibitors for 12 hours. DMSO was used as a vehicle control. Recovery of AKT, ERK1/2, and HER2 phosphorylation was analyzed by immunoblotting (bottom)..... 60

Figure 2.5. Isolation of GFP⁺ cells upon doxycycline induction to construct 4T1 and D2.A1 with inducible SHP2 depletion. A, B, Representative photomicrographs showing doxycycline induction of GFP⁺ 4T1 cells (A) and D2.A1 cells (B) stably expressing shScramble control and PTPN11-targeting shRNAs (shPTPN11 146, 369 and 404) from the SMARTvector. C, D, FACS sorting plots of 4T1 cells (C) and D2.A1 cells (D) transiently induced with doxycycline. GFP⁻ cells were highlighted as red dots, while GFP⁺ cells were highlighted as green ones. The corresponding percentage of GFP⁻ and GFP⁺ are listed on the plots. E, F, Comparison of the GFP induction with doxycycline at 10µg/ml in the 4T1 cells (E) and D2.A1 cells (F) before and after FACS for GFP⁺ cells..... 63

Figure 2.6. Validation of SHP2 depletion efficiencies in 4T1 and D2.A1 after sorting. A-F, Three independent repeats of immunoblot analyses with quantification for SHP2 in 4T1 cells (A, C, E) and D2.A1 cells (B, D, F) stably expressing three independent doxycycline-inducible shRNA sequences targeting PTPN11 with and without doxycycline induction, compared with scrambled (scram) shRNA controls. G, Quantification of SHP2 depletion for each shRNA construct in 4T1 and D2.A1 cells (n = 3). Depletion efficiency was defined as the percentage of SHP2 protein decrease normalized to scramble controls upon doxycycline induction..... 65

Figure 2.7. Depletion of SHP2 inhibits the growth of metastatic breast cancer cells. A, Cell viability assays under 2D culture conditions showing differential cell viability of 4T1 and D2.A1 cells upon doxycycline-induced depletion of SHP2. Data are the mean ± s.e.m. of two biological replicates completed in triplicate. B, Representative photos showing 3D morphologies of 4T1 cells upon depletion of SHP2. C, Quantification of differential cell viability of 4T1 cells upon depletion of SHP2. Data are shown as mean ± s.e.m. n = 3, $*p < 0.05$. D, Representative photos showing 3D morphologies of D2.A1 cells upon depletion of SHP2. E, Quantification of differential cell viability of D2.A1 cells upon depletion of SHP2. Data are shown as mean ± s.e.m. n = 4 for D2.A1, $**p < 0.01$ 67

Figure 2.8. SHP099 q.o.d. at 50mg/kg fails to inhibit the 4T1 metastasis *in vivo*. A, Schematic representation of the 4T1 post-surgical model of metastasis and treatment plan of SHP099 q.o.d. at 50mg/kg. B, Representative bioluminescent images were taken on Day 0 and Day 14 of SHP099 q.o.d. treatments at 50mg/kg. C, Bioluminescence values for pulmonary regions of interest (ROI) from mice bearing 4T1 metastases normalized to values at the initiation of treatment (Day 0). Data are the mean ± s.e.m. of 5 mice per treatment group. D, Bioluminescent

values of pulmonary regions of interest (ROI) which were quantified as a measure of metastasis. Data are the ratio of luminescence values on Day 14 of treatment compared to Day 0. NS: no significance for n=5 mice per group as determined by a Mann-Whitney test. E, F, Plots comparing lung weights (E) and spleen weights (F) from control and SHP099 treated mice. NS: no significance for n=5 mice per group as determined by a Mann-Whitney test. 68

Figure 2.9. SHP099 q.d. at 50mg/kg inhibits the 4T1 metastasis *in vivo*. A, Schematic representation of the 4T1 post-surgical model of metastasis and treatment plan of SHP099 q.d. at 50mg/kg. B, Representative bioluminescent images taken at Day 0 and Day 11 of SHP099 q.d. treatments at 50mg/kg. C, Bioluminescent values of pulmonary regions of interest (ROI) which were quantified as a measure of 4T1 metastasis. Data are the ratio of luminescence values at Day 11 of treatment compared to Day 0. *p<0.05 for n=5 mice per group as determined by a Mann-Whitney test. D, Representative photos of pulmonary metastases (White arrow heads to show the nodules) and H&E staining of pulmonary histological sections in control and SHP099 treated mice. E, F, Plots comparing pulmonary nodules (E) and spleen weights (F) from control and SHP099 treated mice. *p<0.05, **p<0.01 for n=5 mice per group as determined by a Mann-Whitney test..... 69

Figure 2.10. SHP099 q.d. at 100mg/kg inhibits the pulmonary growth of D2.A1 cells *in vivo*. A, Schematic of the D2.A1 model of pulmonary tumor growth and treatment plan of SHP099 q.d. at 100mg/kg. B, Representative images of pulmonary growth monitored by bioluminescence at Day 7 and Day 21 post injection. C, Bioluminescent values from pulmonary ROI quantified as the ratio of day 21 to day 7 following tumor cell injection (*p<0.05 as determined by a Mann-Whitney test, n=5 mice per group). D, Kaplan–Meier analyses of control and SHP099 treated mice, bearing D2.A1 pulmonary tumors, resulting in the indicated p-value (n=5 mice per group)..... 71

Figure 3.1. Phosphorylation of SHP2 at Y542 is elevated in drug resistant breast cancer cells and has clinical significance. A, Immunoblotting showing differential expression of FGFR1 and phosphorylation of SHP2 at Y542 in HME2-LAPR cells compared to HME2-Par cells. B, Kaplan–Meier analyses of patients from The Cancer Genome Atlas Program (TCGA) breast cancer cohort separated into two groups based on the median mRNA expression value of SHP2 (left) or median phosphorylation level of SHP2 at Y542 (right). Overall survival between the two groups was compared by a log-rank test resulting in the indicated p-values..... 78

Figure 3.2. Phosphorylation of SHP2 at Y542 is elevated with multiple growth factors induction in MBC cells. A, Immunoblotting showing the expression levels of FGFR1, PDGFR α , PDGFR β , C-MET, and EGFR in the 4T1, D2.A1, BT549, HME2-Par and HME2-LAPR cells. B, Immunoblotting showing the phosphorylation of SHP2 at Y542 and ERK1/2 (ERK) induced by the indicated growth factors (FGF2, PDGF, hGF, VEGF and EGF) for 5 minutes in D2.A1 cells. C-E, Immunoblotting showing differential phosphorylation of SHP2 at Y542 and ERK1/2 (ERK) in D2.A1 cells induced by addition of exogenous FGF2 (C), PDGF (D) and hGF (E) in 2D culture conditions for the indicated amounts of time. F, Immunoblotting showing the phosphorylation of SHP2 at Y542 and ERK1/2 (ERK) induced by the indicated growth factors (FGF2, PDGF, hGF, VEGF and EGF) for 5 minutes in BT549 cells. G, H, Immunoblotting showing differential phosphorylation of SHP2 at Y542 and ERK1/2 (ERK) in BT549 cells induced by addition of exogenous FGF2 (G) and EGF (H) in 2D culture conditions for the indicated amounts of time. 80

Figure 3.3. SHP2 inhibition and depletion block the growth of D2.A1 cells under 2D culture conditions. A, Cell viability assays under 2D culture conditions in which D2.A1 cells were induced by addition of exogenous FGF2, PDGF, and hGF for 6 days. B, C, Cell viability assays under 2D culture conditions in which D2.A1 cells were stimulated with FGF2 (B) or hGF (C) in the presence or absence of SHP2 inhibitors. D, Cell viability assays under 2D culture conditions in which D2.A1 cells expressing doxycycline inducible shRNAs targeting PTPN11 and Scramble control were treated with doxycycline in the presence of FGF2 and hGF as indicated. In all panels, data are the mean \pm s.e.m. for at least three independent assays resulting in NS as no significance, * $p < 0.05$, *** $p < 0.001$, determined by a student's t-test. 82

Figure 3.4. SHP2 inhibition and depletion block the growth of D2.A1 cells under 3D culture conditions. A, Cell viability assays under 3D culture conditions in which D2.A1 cells were induced by addition of exogenous FGF2, PDGF, and hGF. B, C, Cell viability assays under 3D culture conditions in which D2.A1 cells were stimulated with FGF2 (B) or PDGF (C) in the presence or absence of SHP2 inhibitors. D, Cell viability assays under 3D culture conditions in which D2.A1 cells expressing doxycycline inducible shRNAs targeting PTPN11 and Scramble control were treated with doxycycline in the presence of FGF2 and PDGF as indicated. In all panels, data are the mean \pm s.e.m. for at least three independent assays resulting in NS as no significance, * $p < 0.05$, ** $p < 0.01$, *** $p < 0.001$, determined by a student's t test. 83

Figure 3.5. SHP2 inhibition and depletion block the growth of tumor spheres induced by FGF2. A-D, HME2-LAPR (A, B) and D2.A1 (C, D) spheres were formed in a round bottom plate and then plated onto a bed of gel matrix in the presence of the indicated concentrations of SHP2 or FGFR inhibitors. The growth of spheres was further induced by the addition of exogenous FGF2 at 20ng/ml. The area of the sphere 9 days after placement on the ECM was measured from the photos (A, C), and these values were normalized to the initial sphere size on Day 0 (B, D). E, F, D2.A1 spheres expressing doxycycline inducible shRNAs targeting PTPN11 and Scramble control were treated with doxycycline in the presence of FGF2. The area of the sphere 9 days after placement on the ECM was measured from the photos (E), and these values were normalized to the initial sphere size on Day 0 (F). In all panels, data are the mean \pm s.e.m. (n = 3), NS as no significance, * $p < 0.05$, ** $p < 0.01$, *** $p < 0.001$ 84

Figure 3.6. Phosphorylation of SHP2 at Y542 is elevated in the MBC cells under 3D culture conditions compared to 2D. A, Immunoblotting showing differential phosphorylation of SHP2 at Y542 in 4T1 cells following 3D culture conditions (post 3D) compared to 2D. B, Immunoblotting showing differential phosphorylation of SHP2 at Y542 in 4T1 cells (left) and D2.A1 cells (right) lysed directly from gel-based 3D culture compared to 2D. C, Representative photomicrographs showing 4T1 cells (left) and D2.A1 cells (right) cultured on fibronectin-coated tessellated scaffolds. D, Immunoblotting showing differential phosphorylation of SHP2 at Y542 in 4T1 cells (left) and D2.A1 cells (right) cultured on fibronectin-coated scaffolds as compared to 2D..... 86

Figure 3.7. The extracellular matrix promotes the phosphorylation of SHP2. A, Immunoblotting showing differential phosphorylation of Src at Y416 and Y527 in 4T1 cells following culture under gel-based 3D conditions as compared to 2D. B, RPPA data from the TCGA breast cancer dataset were analyzed for correlation of total expression levels and post-translational modifications of the indicated proteins in relation to SHP2-Y542 phosphorylation. The heat map indicates the Pearson correlation coefficient and the size of the circle is representative of the

value. C, Immunoblotting showing differential phosphorylation of FAK at Y925 in 4T1 cells isolated directly from gel-based 3D cultures as compared to 2D. D, Immunoblotting showing differential phosphorylation of Src at Y416 and FAK at Y925 in 4T1 cells (left) and D2.A1 cells (right) cultured on fibronectin-coated scaffolds as compared to 2D. E, Immunoblotting showing phosphorylation of SHP2 at Y542 in 4T1 cells cultured on fibronectin-coated scaffolds for 16 days and treated with the indicated concentrations of a Src inhibitor (PP2) or a FAK inhibitor (PF271) for the last 24 hours. F, Immunoblotting showing phosphorylation of SHP2 at Y542 in D2.A1 cells cultured on fibronectin-coated scaffolds for 16 days and treated with the indicated concentrations of PP2, PF271 or a FGFR inhibitor (FIIN4) for the last 24 hours. G, H, Immunoblotting showing phosphorylation of SHP2 at Y542 and FAK at Y925 in 4T1 cells (G) and D2.A1 cells (H) cultured on fibronectin-coated scaffolds for 16 days and treated with the indicated concentrations of PF271 for the last 24 hours. I, D2.A1 cells were pre-treated with PP2 or PF271 for 24 h in serum-free media, and cells were then induced for 5 min with FGF2, PDGF, or hGF. Immunoblot analyses were used to detect phosphorylation of SHP2 at Y542..... 88

Figure 3.8. SHP2 is a shared node for ECM and RTK signaling as the signaling inputs. Growth factor receptor signaling additionally contributes to phosphorylation of SHP2 via Src and FAK. SHP2 activity contributes to various downstream signaling pathways that facilitate metastatic tumor growth in the presence of currently used targeted therapies. Targeted inhibition of SHP2 (SHP2i) blocks the growth of MBC cells. The figure was created using BioRender..... 91

Figure 4.1. Phosphorylation of SHP2 at Y542 predicts immune profiles in MBC patients. A, B, Violin and box plots comparing the differential immune scores and stroma scores in patients grouped by phosphorylation levels of SHP2 at Y542 (A) or expression levels of SHP2 (B). C, Violin and box plots comparing the differential phosphorylation levels of SHP2 at Y542 and expression levels of SHP2 in patients grouped by CD4⁺ T-cell infiltration levels. D, E, Heat maps comparing the differential gene expression in patients grouped by phosphorylation levels of SHP2 at Y542 (D) or expression levels of SHP2 (E). *p<0.05, **p<0.01, ***p<0.001. F, Volcano plots demonstrating pathways of differential ssGSEA scores in patients grouped by phosphorylation levels of SHP2 at Y542 with statistical significance. Specific pathways of interest are annotated. G, H, GSEA plots, Enrichment scores and p-values of the key pathways from GO (G) and KEGG (H) enriched in patients with lower phosphorylation levels of SHP2 at Y542..... 98

Figure 4.2. Depletion of SHP2 in tumor cells reduces pulmonary metastasis *in vivo*. A, Schematic of the study by doxycycline inducible depletion of SHP2 in tumor cells in 4T1 model. BALB/c mice (n = 7 mice per group for shScramble and shPTPN11 146, n=6 mice per group for shPTPN11 369) were engrafted with 4T1 cells (5 × 10⁴) via intraductal injection into mammary fat pads. Primary tumors were surgically removed 2 weeks following the injection. Doxycycline was administrated in drinking water at 2mg/ml 3 days following the removal of primary tumors. B, Plots comparing the primary tumor volume at Day 14 post injection. (NS: no significance) C, Representative bioluminescent images of 4T1 pulmonary metastasis at Day 17 and Day 31 post injection. D, Bioluminescent values from pulmonary ROI quantified as the ratio of day 31 to day 17 post injection (*p<0.05, **p<0.01). E, Bioluminescence values for pulmonary regions of interest (ROI) from mice with 4T1 metastatic growth in lungs normalized to Day 0 of doxycycline treatments. Data are the mean ± s.e.m. of n = 7 mice per group for shScramble and shPTPN11 146, n=6 mice per group for shPTPN11 369. F, The body weight of mice was monitored every 2 days, and the percentage of weight gain/loss was normalized to Day 0 of the

treatments. G, Representative Green Fluorescence (eGFP) images (left) of the lungs at Day 17 of doxycycline treatments and quantified eGFP values (right) of the lungs. 101

Figure 4.3. The gating ancestry for the populations in the study of 4T1 model. A, Spleens and tumors from lung tissues were isolated and digested into single cell suspensions, and stained with lymphoid antibody panel as described in the materials and methods. These cells were sequentially gated as shown to identify a population of cells, single cells, CD45⁺ and CD4⁺/CD8⁺ cells prior to analysis of TIM3⁺, LAG3⁺, LAG3⁺TIM3⁺ and PD-1⁺. The LAG3⁺TIM3⁺ cells were also gated under PD-1⁺ population. B, Tumors from lung tissues were isolated and digested into single cell suspensions, and stained with myeloid antibody panel as described in the materials and methods. These cells were sequentially gated as shown to identify a population of cells, single cells, CD45⁺, CD11b⁺ and F4/80⁺ cells prior to analysis of CD86⁺ and CD206⁺..... 104

Figure 4.4. Depletion of tumor-cell autonomous SHP2 adjusts T-cell composition and relieves the T-cell exhaustion. A, D, Representative dot plots and quantification of CD4⁺ and CD8⁺ population as a frequency of CD45⁺ cells in isolated spleens (A) and lung tissues (D) of each group. B, C Representative dot plots and quantification of LAG3⁺ and TIM3⁺ population as a frequency of CD45⁺CD4⁺ cells (B) or CD45⁺CD8⁺ cells (C) in isolated spleens of each group. E, Representative dot plots and quantification of LAG3⁺TIM3⁺ population as a frequency of CD45⁺CD4⁺PD1⁺ cells and CD45⁺CD8⁺ PD-1⁺ cells in isolated lung tissues of each group. In all panels, *p<0.05, **p<0.01, ***p<0.001, n = 4 for shScramble and shPTPN11 146, n = 5 for shPTPN11 369 for cells isolated from lung tissues; while n=4 for cells isolated from spleens. 106

Figure 4.5. Depletion of tumor-cell autonomous SHP2 adjusts tumor associated macrophages composition. A, B, Representative dot plots and quantification of CD11b⁺ population as a frequency of CD45⁺ cells (A) and F4/80⁺ population as a frequency of CD45⁺CD11b⁺ cells (B) in isolated lung tissues of each group. C, Representative dot plots and quantification of CD86⁺ and CD206⁺ population as a frequency of CD45⁺CD11b⁺F4/80⁺ cells in isolated lung tissues of each group. D, Plots comparing the ratio of the frequency of CD86⁺ and CD206⁺. In all panels, *p<0.05, n = 4 for shScramble and shPTPN11 146, n = 5 for shPTPN11 369. 107

Figure 4.6. SHP2 blockade in MBC cells rescues T-cell cytotoxicity reduced by growth factors. A, Schematic of the Incucyte-based T cell cytotoxicity assays. CD8⁺ T cells are isolated from the spleens of 4TO7 tumor-bearing mice. The MBC cells are treated with growth factors and inhibitors, and co-cultured with CD8⁺ T cells. The dead cells are monitored with Incucyte. B, Representative images of the D2.A1 cells at 1 hour following co-culturing with T cells and treated with SHP099 or TNO155. The D2.A1 cells without T cells served as background. C, Bar graph comparing the dead cell counts per image with different treatments, ***p<0.001, n=9. D, Representative images of the MBC cells treated with FGF2 and PDGF at 1 hour following co-culturing with T cells. The MBC cells without T cells served as the background. E, Bar graph comparing the percentage of dead cell counts of FGF2 and PDGF groups to No Stem (NS) group. *p<0.05, n=4 individual repeats. F, Representative images of the MBC cells treated with FGF2 / PDGF and TNO155 at 1 hour following co-culturing with T cells. G, Bar graph comparing the dead cell counts per image with different treatments. *p<0.05, **p<0.01, n=9. H, Representative images of the D2.A1 cells treated with FGF2 / PDGF and IgG / α -PD-L1 at 1 hour following co-culturing with T cells. I, Bar graph comparing the percentage of dead cell counts with different treatments normalized to the control group. NS: not significant, *p<0.05, ***p<0.001, n=4 individual repeats..... 108

Figure 5.1. Phosphorylation of AKT and ERK1/2 are the signaling outputs of SHP2. A, B, D2.A1 cells were pre-treated with SHP099 or FIIN4 for 24 h in serum-free media and cells were subsequently induced for 5 min with FGF2 (A), PDGF (B, top), or hGF (B, bottom) as indicated. Immunoblotting was used to detect phosphorylation of FGFR, FRS2, ERK1/2, AKT, and SHP2. C, Immunoblotting showing phosphorylation of ERK1/2, AKT and SHP2 in D2.A1 cells induced with FGF2, PDGF and hGF for 5 minutes in the presence of TNO155 at 5 μ M. D, Immunoblotting showing phosphorylation of ERK1/2 and AKT in 4T1 and D2.A1 cells cultured on fibronectin-coated scaffolds for 8 days and treated with TNO155 at 5 μ M for the last 24 hours. 115

Figure 5.2. SHP2 blockade reduces PD-L1 induced by growth factors in MBC cells. A, Cell surface analysis of PD-L1 in D2.A1 cells induced by different growth factors at desired concentrations for 24 hours using flow cytometer. B, Bar graph comparing fold change of PD-L1 Mean Fluorescence Intensity (MFI) induced by different growth factors relative to no stem (NS). * p <0.05, ** p <0.01, n =3 as determined by a student's t-test. C, Bar graph comparing fold change of PD-L1 mRNA relative to GAPDH induced by different growth factors compared to no stem (NS). D, E, Cell surface analysis of PD-L1 using flow cytometer and bar graph comparing fold change of PD-L1 Mean MFI in D2.A1 cells induced by PDGF and treated with 11a-1, SHP099, TNO155, PP2 and PF271. * p <0.05, ** p <0.01, *** p <0.001, n =3 as determined by a student's t-test. F, G, Cell surface analysis of PD-L1 using flow cytometer and bar graph comparing fold change of PD-L1 Mean MFI in D2.A1 cells induced by FGF2 or PDGF and treated with Trametinib. NS: not significant, * p <0.05, n =3 as determined by a student's t-test. H, I, Cell surface analysis of PD-L1 using flow cytometer and bar graph comparing fold change of PD-L1 Mean MFI in BT549 cells induced by FGF2 or EGF and treated with TNO155. NS: not significant, ** p <0.01, *** p <0.001, n =3 as determined by a student's t-test. 117

Figure 5.3. SHP2 blockade reduces PD-L1 induced by 3D culture environments in MBC cells. A, B, Cell surface analysis of PD-L1 using flow cytometer and bar graph comparing fold change of PD-L1 Mean MFI in 4T1 and D2.A1 cells cultured on fibronectin-coated or laminin-coated scaffolds compared to 2D. C, D, Cell surface analysis of PD-L1 using flow cytometer and bar graph comparing fold change of PD-L1 Mean MFI in D2.A1 cells induced by FN-scaffold 3D culture environment and treated with TNO155 and PF271. E, Bar graph comparing fold change of PD-L1 mRNA relative to GAPDH compared to 2D. ** p <0.01, n =3 as determined by a student's t-test. F, Cell surface analysis of eGFP and PD-L1 using flow cytometer showing the influence of cell surface PD-L1 by doxycycline inducible depletion of SHP2 in D2.A1 cells. G, Cell surface analysis of PD-L1 using flow cytometer comparing D2.A1 cells cultured on fibronectin-coated scaffolds treated with Trametinib and interferon- γ to 2D culture. 120

Figure 5.4. SHP2 regulates MHC class I expression via the balance between MAPK and STAT1 signaling. A, Cell surface analysis of H-2 in D2.A1 cells treated with different growth factors, interferon- γ and TNO155 using flow cytometer. B, Bar graph comparing fold change of H-2 MFI induced by different growth factors, interferon- γ and TNO155 compared to DMSO+ interferon- γ . NS: not significant, ** p <0.01, *** p <0.001, n =3 as determined by a student's t-test. C, Cell surface analysis of HLA-A, B, C in BT549 cells treated with different growth factors, interferon- γ and TNO155 using flow cytometer. D, Bar graph comparing fold change of HLA-A, B, C MFI induced by different growth factors, interferon- γ and TNO155 compared to DMSO + no stem group. NS: not significant, * p <0.05, n =3 as determined by a student's t-test. E, Immunoblotting showing differential p-STAT1 and p-ERK in D2.A1 cells treated with different

growth factors, interferon- γ and TNO155. F, Bar graph comparing fold change of H-2 MFI induced by different growth factors, interferon- γ and inhibitors compared to ns+ interferon- γ . NS: not significant, ** $p < 0.01$, *** $p < 0.001$, $n = 3$ as determined by a student's t-test. 122

Figure 5.5. Tumor-cell autonomous SHP2 is a key signaling node in response to dynamic TME to induce immune suppression. SHP2 contributes to various downstream signaling pathways including PD-L1 and MHC class I to facilitate immune suppression in response to a varieties of additional signaling inputs in TME, such as growth factor receptor signaling. Figure was created using BioRender..... 123

Figure 6.1. SHP2 inhibitors synergize with FIIN4 to inhibit the growth of 4T1 cells under 2D culture conditions. A, crystal violet visualization of the viable 4T1 cells treated with SHP099 and FIIN4 at indicated concentrations. B, C, 4T1 cells were seeded in 2D culture, and treated with the indicated concentrations of SHP099 (B) or 11a-1 (C), FIIN4 alone, or both compounds for 6 days. Data are the mean \pm s.e.m. ** $p < 0.01$ as determined by a two-tail Student's t-test. D, Combination Index (CI) plots and charts of 4T1 cells treated with SHP2 inhibitors and FIIN4 generated by Compusyn 1.0. E, HME2-LAPR cells were seeded in 2D culture, and treated with SHP099, FIIN4 or a combination of the two compounds for 6 days. Data are the mean \pm s.e.m. NS: no Significance or *** $p < 0.001$ as determined by a two-tail Student's t-test. F, CI plots and charts of SHP2 inhibitors and FIIN4 generated by Compusyn 1.0 in HME2-LAPR cells according to the 2D growth data. 127

Figure 6.2. Inhibition of SHP2 synergizes with FGFR inhibition in other MBC cells under 2D culture conditions. CI plots and charts of SHP2 inhibitors and FIIN4 generated by Compusyn 1.0 in BT474 (A), SK-BR-3 (B) and UACC812 (C) cells according to the corresponding 2D growth data in these cells. 129

Figure 6.3. SHP2 inhibitors enhance the effects of FIIN4 to inhibit the growth of MBC cells under 3D culture conditions. Single-cell suspensions of 4T1 cells (A-D) and D2.A1 cells (E-H) were plated under 3D culture conditions and treated with the indicated compounds alone or in combination. Media containing DMSO was used as a vehicle control. Data are the mean \pm s.e.m. of at least three independent experiments where NS: no significance, * $p < 0.05$, ** $p < 0.01$, *** $p < 0.001$ as determined by a two-tail Student's t-test. 130

Figure 6.4. SHP2 inhibitors enhance the effects of FIIN4 to inhibit the tumor spheres growth of MBC cells. D2.A1 spheres were treated with FIIN4 or 11a-1 at indicated concentrations alone, or combination. The area of the sphere 9 days after placement on the ECM was measured from the photos (A), and these values were normalized to the initial sphere size at Day 0 (B). In all panels, data are the mean \pm s.e.m. ($n = 3$), NS as no significance, * $p < 0.05$ as determined by a student's t-test..... 131

Figure 6.5. Inhibition of SHP2 synergizes with FIIN4 *in vivo*. A, Bioluminescence values for regions of interest (ROI) in the lungs from mice bearing 4T1 metastases relative to values at the initiation of treatment. Data are the mean \pm s.e.m. of 5 mice per treatment group. B, Representative bioluminescent images of metastasis (bottom) and quantified pulmonary ROI values from mice bearing 4T1 metastases 14 days after treatment initiation (top). Data are the mean \pm s.e.m. of 5 mice per group resulting in * $p < 0.05$ as determined by a two-tailed Mann Whitney test. C, Differential survival analyses of tumor bearing mice in each treatment group, resulting in the indicated p-values as determined by a log-rank test. D, Mice bearing 4T1

metastases were treated with SHP099 and FIIN4 alone or in combination as indicated. Data are the mean \pm s.d., body weights (n=5) normalized to day 1 of treatment..... 132

Figure 6.6. Systemic inhibition of SHP2 sensitizes D2.A1 cells to α -PD-L1 antibody *in vivo* A, Schematic of the study combining SHP099 with α -PD-L1 antibody to inhibit pulmonary tumor growth in D2.A1 model. BALB/c mice (n = 5 / group) were injected with 1 million/mouse D2.A1 cells via tail veins. Cells were allowed to seed for 1 week, and the mice were treated with the doses and frequency described on the schematic. B, Representative bioluminescent images of pulmonary D2.A1 growth on Day 8 and Day 20 post injection. C, Bioluminescent values from pulmonary ROI quantified as the ratio of day 20 to day 8 post injection ****p < 0.01**, n = 5 mice per group as determined by a Mann Whitney test. D, Plots comparing the wet lung weights of the mice on day 22 post injection, ****p < 0.01**, n = 5 mice per group as determined by a Mann Whitney test. E, Bioluminescence values for pulmonary ROI from mice with D2.A1 cell growth in lungs normalized to Day 8 post injection. Data are the mean \pm s.e.m. of 5 mice per treatment group. F, Representative bioluminescent images of the lungs at Day 22 post injection (top) and quantified ROI values of the lungs relative to the average ROI values of Day 8 post injection (bottom). Data are the individual plots and mean \pm s.e.m. of 5 mice per group, NS: not significant, ****p < 0.01** determined by a Mann Whitney test. G, Dot plot showing the spleen weights of the mice at Day 22 post injection. Data are the individual plots and mean \pm s.e.m. of 5 mice per group, NS: not significant determined by a Mann Whitney test..... 134

Figure 6.7. The gating ancestry for the populations in the study of D2.A1 model. A, Spleens and tumors from lung tissues were isolated and digested into single cell suspensions, and stained with lymphoid antibody panel as described in the materials and methods. These cells were sequentially gated as shown to identify a population of cells, live cells, CD45⁺ and CD4⁺/CD8⁺ cells prior to analysis of TIM3⁺, LAG3⁺, LAG3⁺TIM3⁺ and PD-1⁺. The LAG3⁺TIM3⁺ cells were also gated under PD-1⁺ population. B, Tumors from lung tissues were isolated and digested into single cell suspensions, and stained with myeloid antibody panel as described in the materials and methods. These cells were sequentially gated as shown to identify a population of single cells, live cells, CD45⁺/CD45⁻, CD11b⁺ and F4/80⁺ cells prior to analysis of CD86⁺ and CD206⁺. The PD-L1⁺ cells were also gated under CD45⁻ population. 136

Figure 6.8. Combination of SHP099 and α -PD-L1 relieves T-cell exhaustion. A, C Representative dot plots and quantification of CD4⁺ and CD8⁺ population as a frequency of CD45⁺ cells in isolated spleens (A) and lung tissues (C) of each group. B, Representative dot plots and quantification of LAG3⁺ and TIM3⁺ population as a frequency of CD45⁺CD4⁺ cells in isolated spleens of each group. D, E, Representative dot plots and quantification of LAG3⁺, TIM3⁺ and LAG3⁺TIM3⁺ population as a frequency of CD45⁺CD4⁺ cells (D) and CD45⁺CD8⁺ cells (E) in isolated lung tissues of each group. F, Representative dot plots and quantification of PD-L1⁺ population as a frequency of CD45⁻ cells in isolated lung tissues of each group. In all panels, *p < 0.05, **p < 0.01, ***p < 0.001, n = 3 as determined by a student's t-test..... 138

Figure 6.9. Combination of SHP099 and α -PD-L1 adjusts the composition of tumor associated macrophages. A, Representative dot plots and quantification of CD11b⁺ population as a frequency of CD45⁺ cells in isolated lung tissues of each group. B, Representative dot plots and quantification of F4/80⁺ population as a frequency of CD45⁺CD11b⁺ cells in isolated lung tissues of each group. C, Representative dot plots and quantification of CD86⁺ and CD206⁺ population as a frequency of CD45⁺CD11b⁺F4/80⁺ cells in isolated lung tissues of each group. D, Plots

comparing the ratio of CD86⁺ and CD206⁺. In all panels, *p<0.05, **p<0.01, ***p<0.001, n=3 as determined by a student's t-test. 139

ABSTRACT

Metastatic breast cancer (MBC) is an extremely recalcitrant disease capable of overcoming targeted therapies and evading immune surveillance via the engagement of complicated signaling networks. Resistance to targeted therapies and therapeutic failure of immune checkpoint blockade (ICB) are two major challenges in treating MBC. To survive in the dynamic tumor microenvironment (TME) during metastatic progression, shared signaling nodes are required for MBC cells to regulate the signaling networks efficiently, which are potential multifunctional therapeutic targets. SH2 containing protein tyrosine phosphatase-2 (SHP2) is a druggable oncogenic phosphatase that is a key shared node in both tumor cells and immune cells. How tumor-cell autonomous SHP2 manages its signaling inputs and outputs to facilitate the growth of tumor cells, drug resistance, immunosuppression, and the limited response of ICB in MBC is not fully understood. Herein, we used inducible genetic depletion and two distinct types of pharmacological inhibitors to investigate anti-tumor effects with immune reprogramming during SHP2 targeting.

We first focus on the signaling inputs and outputs of SHP2. We find that phosphorylation of SHP2 at Y542 predicts the survival rates of breast cancer patients and their immune profiles. Phosphorylation of SHP2 at Y542 is elevated with differential activation mechanisms under a growth-factor-induced and extracellular matrix (ECM)-rich culture environment. Phosphorylation of SHP2 at Y542 is also elevated in HER2 positive MBC cells upon acquired resistance to the HER2 kinase inhibitor, neratinib. The resistant cells can be targeted by SHP2 inhibitors. SHP2 inhibitors block ERK1/2 and AKT signaling and readily prevented MBC cell growth induced by multiple growth factors. Inhibition of SHP2 also blocks these signaling events generated from the ECM signaling. In fact, the inhibitory effects of SHP2 blockade are actually enhanced in the ECM-rich culture environment. We utilize the *in vitro* T-cell killing assays and demonstrate that pretreatment of tumor cells with FGF2 and PDGF reduces the cytotoxicity of CD8⁺ T cells in a SHP2-dependent manner. Both growth factors and ECM-rich culture environment transcriptionally induce PD-L1 via SHP2. SHP2 inhibition balances MAPK signaling and STAT1 signaling, which prevents growth factor-mediated suppression of INF- γ -induced expression of MHC class I.

Next, we evaluate the efficacy of SHP2 inhibitors. Blockade of SHP2 in the adjuvant setting decreased pulmonary metastasis *in vivo* and extended the survival of systemic tumor-bearing mice. Tumor-cell autonomous depletion of SHP2 reduces pulmonary metastasis and relieves exhaustion markers on CD8⁺ and CD4⁺ cells. Meanwhile, both systemic SHP2 inhibition and tumor-cell autonomous SHP2 depletion reduce tumor-infiltrated CD4⁺ T cells and M2-polarized tumor associated macrophages.

Finally, we investigate potential combination therapies with SHP2 inhibitors. The combination of SHP2 inhibitors and FGFR-targeted kinase inhibitors synergistically blocks the growth of MBC cells. Pharmacological inhibition SHP2 sensitizes MBC cells growing in the lung to α -PD-L1 antibody treatment via relieving T cell exhaustion induced by ICB.

Overall, our findings support the conclusion that MBC cells are capable of simultaneously engaging several survival pathways and immune-suppressive mechanisms via SHP2 in response to multiple growth factors and ECM signaling. Inhibition of SHP2, potentially in combination with other targeted agents and ICB, holds promise for the therapeutic management of MBC.

CHAPTER 1. INTRODUCTION

1.1 Metastatic Breast Cancer

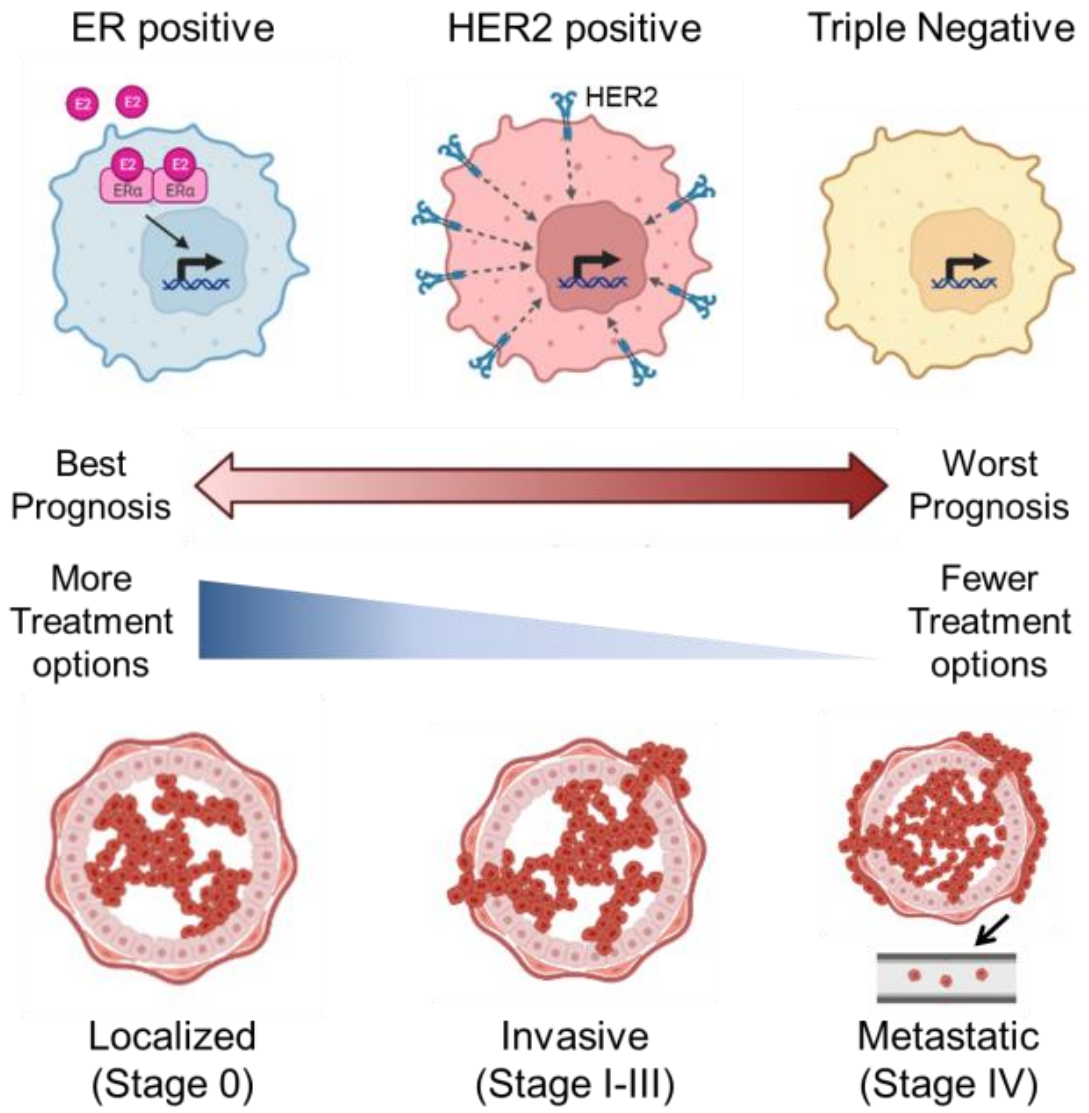
1.1.1 Mapping the categories of breast cancer

Breast cancer is estimated as the most common cancer diagnosed in women in the United States, in 2022, which accounts for almost one-third of all new diagnoses [1]. Although breast cancer mortality rates have been decreasing in most high-income countries, the worldwide breast cancer mortality rates are still going up, together with the incidence rates [2, 3]. The diverse mortality of breast cancer also occurs among different age groups, races, and disease categories [4-6]. Because of the difference in mortality among different disease categories, we need to find the key categories influencing the mortality, which should be focused on in the research and development of future therapeutics targeting breast cancer.

With the blooming research and ongoing clinical practice to understand and treat breast cancer in these decades, there are multiple ways to identify the categories of breast cancer to estimate the potential prognosis and treatment options (Figure 1.1).

One of the popular ways to categorize breast cancer is by the intrinsic subtypes. The basic idea of this method is to utilize the levels of primary breast cancer markers, such as estrogen receptor (ER) status, progesterone receptor (PR) status, and human epidermal growth factor receptor 2 (HER2), as determined by immunohistochemistry (IHC) or fluorescence in situ hybridization (FISH) in clinical practice [7-10]. Therefore, breast cancer can be briefly categorized as ER positive (ER +, PR +, HER2+/-), HER2 positive (ER-, PR-, HER2+) and triple negative (ER-, PR-, HER2-) in the top panel of Figure 1.1. Recently, advanced technologies have refined these categories into more elegant subgroups based on molecular markers. For example, breast cancer can also be grouped as Luminal A, Luminal B, HER2-enriched, Basal-like and Normal-like according to the genomic assay called Prediction Analysis of Microarray 50 (PAM50) [11-13]

Breast Cancer by Intrinsic Subtypes



Breast Cancer by Stages

Figure 1.1. Categories of breast cancer by intrinsic subtypes and stages. Breast cancer can be categorized into ER positive, HER2 positive and triple negative by intrinsic molecular markers (top). Breast cancer can also be categorized into localized (stage 0), invasive (stage I-III) and metastatic (stage IV) by stages (bottom). The predicted prognosis and therapeutic options for each category are listed, in which metastatic breast cancer has the worst prognosis and fewer treatment options compared to the other stages (middle). Parts of the figure are created with BioRender.

In the clinics, the pathologists have not only implemented these criteria and technologies to categorize breast cancer but also summarized the patient's survival according to the subtypes. Clinical observation has revealed that triple negative (ER-, PR-, HER2-) has the worst overall survival compared to the other subtypes [14]. The PAM50 method also highlighted the larger recurrence rates and lower survival rates in the patients with HER2-enriched and basal-like subtypes [15]. Besides the prediction of prognosis, the primary breast cancer markers which are enriched in certain types of breast cancer also provide opportunities for the development of targeted therapies. For example, selective estrogen receptor modulators (SERMs), selective estrogen receptor degrader (SERD) and aromatase inhibitors, such as tamoxifen, fulvestrant and letrozole, are effective targeted therapies for ER positive breast cancer [16]. The therapeutic antibody targeting HER2, antibody-drug conjugates and tyrosine kinase inhibitors (TKIs) targeting HER2, such as trastuzumab, trastuzumab emtansine (T-DM1) and neratinib, are useful targeted therapies for HER2 positive breast cancer [17, 18]. In contrast, triple negative breast cancer has limited targeted therapies available because this subtype lacks the intrinsic molecular markers for the drugs to target compared to the other subtypes. Non-targeted therapies are still used in clinics, such as chemotherapies and cyclin-dependent kinases 4/6 (CDK4/6) inhibitors, but the response is still limited. Interestingly, the patients' response to chemotherapies can be improved by further molecular profiling, which emerges the importance of finding novel therapeutic targets and benefits of targeted therapies [19, 20]. Hence, we can summarize here that ER positive breast cancer has the best prognosis and more therapeutic options, while triple negative breast cancer has the worst prognosis and fewer therapeutic options (Figure 1.1, middle). Validating novel therapeutic targets and the development of targeted therapeutics for HER2 positive and triple negative breast cancer is one of the unmet needs in clinics.

Although the intrinsic subtypes of breast cancer can accurately predict the patients' survival and guide the therapeutic options available, there is still a limitation to this categorization method. Recent reports show that the intrinsic molecular profiles of breast cancer are dynamic and unstable throughout the progression of the disease, especially during metastasis [21, 22]. Thus, besides these intrinsic subtypes of breast cancer only considering the molecular markers, another important way to categorize breast cancer is by the stages of disease progression. The stages of breast cancer progression are determined based on the TNM classification system, which is used not only in breast cancer categorization but also in a wide

range of cancers [23]. In this system, the stage is determined by scoring the cancer progression in 3 dimensions, including tumor size (T), lymph nodes involvement (N), and metastasis (M) [24]. With the help of this system, the progression of breast cancer can be divided into five stages, from stage 0 to IV. To further simplify the classification, we decide to categorize the breast cancer into three major stages (Figure 1.1 bottom) with significant differences, which are Localized (stage 0), Invasive (stage I-III) and Metastatic (stage IV). As figure 1.1 shows here, breast cancer comes from the abnormal growth of luminal mammary epithelial cells into neoplasms inside the lumen, which is surrounded by a layer of myoepithelial cells and basement membrane [25]. In the early stage of the disease, the neoplasms are limited inside the lumen with no invasiveness. Hence, this stage is named localized breast cancer, in which the N and M scores are both zero. Next, if the cancer cells invade through the layer of myoepithelial cells and basement membrane, the stage is called invasive breast cancer. This stage is composed of stages I to III, in which stage III has a non-zero N score, while the others have zero N and M scores. Finally, if the cancer cells come into the circulation system and grow in distant organs, such as lungs, bone and brain, this stage is called metastatic breast cancer (stage IV). The metastatic breast cancer, also called stage IV breast cancer, usually features a non-zero M score, regardless of the scores of T and N. Because the stages of breast cancer cover the progression of the disease, it is apparent that the stage IV breast cancer has the worst prognosis compared to the other stages. As the metastatic breast cancer is very heterogenous and complicated, the treatment options are also limited to local (surgery and radiotherapy) and chemotherapy options [26]. As a result, finding targeted therapeutics for metastatic breast cancer is also one of the unmet clinical needs to improve the survival rates of breast cancer patients.

To sum up, we have summarized two major ways to categorize breast cancer, by intrinsic molecular subtypes and stages of disease progression. With the comparison of prognosis and therapeutic options among these categories, we identified that the HER2 positive and triple negative breast cancer and metastatic breast cancer have overlapping lower survival rates and unmet therapeutic needs in the clinics. To address the problems, our solution here is to find a novel therapeutic target for metastatic breast cancer in HER2 positive or triple negative background and promote the development of targeted therapies.

1.1.2 Metastatic breast cancer is the most advanced stage of breast cancer

In the last section, we have introduced metastatic breast cancer (MBC), also called stage IV breast cancer, which has lower patients' survival rates and fewer therapeutic options (Figure 1.1). In fact, MBC is the most advanced stage of breast cancer and a hot topic, which has already raised attention both in the academia and pharmaceutical industry. The ability of tissue invasion and metastasis has been listed as one of the major hallmarks of cancer in 2000 [27]. With further understanding of the mechanisms in MBC progression, some therapeutic options have been introduced and improved the survival of patients with MBC. Chemotherapies and corresponding neoadjuvant therapies have been used as one of the first-line therapies to treat MBC effectively; for example, clinical observation has revealed that anthracycline-based chemotherapy improves the survival of MBC patients with a 1% risk reduction per year [28, 29]. For advanced HER2 positive breast cancer, there are more targeted options including monoclonal therapeutic antibodies, antibody drug conjugates and tyrosine kinase inhibitors (TKIs), which prolong the patients' survival [30]. Besides these therapies used in clinics, there are agents in open clinical trials, such as immune checkpoint blockade (ICB). Taking these therapeutic options together, we can conclude that MBC has treatments, but most of them are not targeted therapies.

With these efforts made in recent decades, the survival rates of patients with MBC are increasing, especially when the patients are diagnosed at younger ages [31, 32]. However, the 5-year survival rates are still lower for patients with MBC compared to the ones with the localized disease despite the benefits achieved by current therapies. Currently, the 5-year survival rates for MBC are less than 30%; while the ones for non-metastatic breast cancer are more than 80% [33, 34]. Clinical observation shows that the median survival of patients with MBC who undergo treatment with chemotherapies is only 24 months [35]. Besides the lower survival rate, the incidence of MBC is increasing; for example, the estimated prevalent cases of MBC will increase by 54.8% by the end of this decade compared to 2015 [36]. Finally, MBC also has higher treatment costs than localized ones, which can be a huge economic burden for the patients [37]. The lower survival rate, increasing cases and higher cost of treatments are still the problems to be solved before we consider MBC as a curable disease.

In conclusion, MBC, the most advanced stage of breast cancer (stage IV), remains a knotty clinical challenge with lower patient survival rates and limited targeted therapies. Besides these

problems, there are more challenges in treating MBC in the clinical practice we will discuss in the next section.

1.1.3 Challenges in treating metastatic breast cancer

The fact that limited targeted therapies are available to treat MBC is one of the major barriers to curing this disease. We also noticed that there are still some targeted therapies available for HER2 positive MBC. However, even with these targeted treatment options, the challenge remains as the patients acquire resistance to these therapies, and the resistance reduces the therapeutic benefits.

Because HER2 amplification is the major driver for HER2 positive breast cancer, monoclonal antibodies (trastuzumab and pertuzumab) are effective targeted therapies, which bind to the HER2 to prevent its dimerization and shut down the downstream signaling cascade initiated by HER2 [38, 39]. These antibodies plus chemotherapies are considered the standard first-line treatment. Based on monoclonal antibodies targeting HER2, antibody drug conjugates (ADC), such as trastuzumab emtansine (T-DM1), were developed by linking trastuzumab with a microtubule-inhibitory agent. T-DM1 is also considered the first-line treatment for HER2 positive MBC in some situations [40]. However, not all the patients respond to these therapies. Our recent report also shows the abilities of MBC cells to acquire resistance to T-DM1 by downregulating the levels of HER2 [41]. To overcome the resistance and treat the patients with progression following anti-HER2 treatments, tyrosine kinase inhibitors targeting HER2 (lapatinib and neratinib) have been utilized in clinics [42-44]. Although the therapeutic benefits of neratinib are promising, inevitably, the inherent and acquired drug resistance still occurs in the metastatic setting [45]. As lapatinib and neratinib are considered the current goalkeeper in treating HER2 positive MBC, it is important to understand how breakthrough resistance happens and find solutions to manage resistance with novel targeted therapies.

Besides the HER2-targeted therapies, the family of immune checkpoint blockade (ICB) is a rising star in treating MBC. Immune checkpoints, the gatekeepers of the immune response, are the proteins on the surface of immune cells to interact with the partner proteins on the surface of target cells and shut down cytotoxic events upon interaction [46]. As immune evasion is one of the important hallmarks of cancer, the cancer cells take the advantage of immune checkpoint system to protect themselves from being killed by the immune system [47]. Blocking the

interaction between the immune checkpoints and their partner proteins is an effective way to induce anti-tumor immunity. Programmed cell death protein 1 (PD-1) on the surface of immune cells, and its partner programmed death-ligand 1 (PD-L1) on the surface of tumor cells are one of the most successful targets for ICB, with approved antibody-based therapies targeting blood, skin, lung, liver, bladder and kidney cancers [48]. Moreover, ICB has more than two hundred active clinical trials, among which the PD-1/PD-L1 axis is mostly focused [49, 50]. However, monotherapies of ICB, such as an α -PD-L1 antibody pembrolizumab, have shown limited responses when treating patients with MBC in clinical trials [51, 52]. The lower response rates of MBC patients to ICB limit the therapeutic benefits to treat MBC, regardless of the success in other cancer types. The mechanisms behind this therapeutic failure remain not fully understood. It is important to identify targets and find novel agents to sensitize the MBC cells to ICB.

In summary, we discuss the two major challenges in treating MBC in this section, including resistance to HER2-targeted therapies and limited response to ICB. To find solutions to these challenges, the first step is to understand the life cycle of MBC and detailed mechanisms.

1.1.4 Metastatic breast cancer is complicated and flexible

Breast cancer is estimated as the most common cancer diagnosed in women in the United States. In the previous sections, we conclude the fact that MBC is the most advanced stage of breast cancer and two major challenges remain in treating MBC. However, how MBC is capable of progressing into a life-threatening disease and becoming drug resistant or insensitive is still not fully understood. To identify the detailed mechanisms by which MBC takes advantage, we should analyze the life cycle of MBC step-by-step to find the answers and solutions.

MBC is defined as breast cancer cells spreading from the primary site (breast) to the distant organs (other parts of the body) via the blood circulation (or lymph nodes), which is proved by observation in clinics and animal models [53-55]. Thus, MBC cells are required to go through at least three major steps before they become life-threatening, including coming out of the primary site, moving in the circulation and disseminating in the distant organs (Figure 1.2). Inside these major steps, there are more complicated small processes for the MBC to go through. First, the MBC cells should invade through the layer of myoepithelial cells and basement membrane, and migrate towards the blood vessels. The next step is called intravasation, in which the MBC cells penetrate through the wall of blood vessels into the blood circulation [56]. Upon

the MBC cells come into the bloodstream, most cells may not survive; while only a small proportion of cells can then grow into low abundant but detectable clusters of circulating tumor cells (CTCs) [57]. Finally, after the survived MBC cells reach distant organs, such as lungs, bone, brain and liver, they will start extravasation and form pre-metastatic niche, which facilitates further metastatic growth [58]. In summary, the road for MBC cells is not smooth and there are multiple barriers to overcome.

Metastatic Breast Cancer Progression in dynamic tumor microenvironments

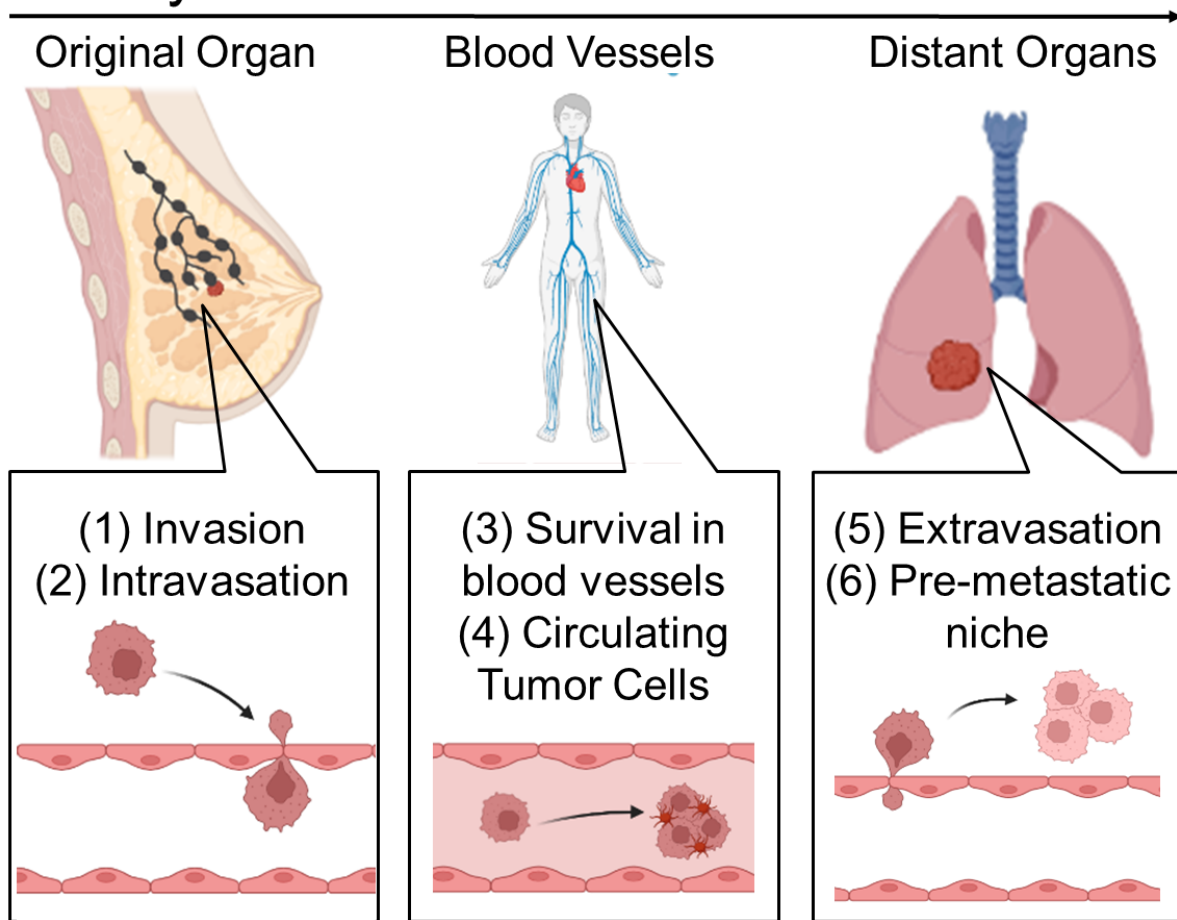


Figure 1.2. Steps for the progression of metastatic breast cancer. Metastatic breast cancer is a disease in which the cancer cells move from the primary site to the distant organs via the blood circulation. The metastatic breast cancer cells have to go through major steps, including coming out of the primary site (left), moving into the circulation (middle), and disseminating in the distant organs (right). There are more sequential and complicated small steps in each major step. Parts of the figure are created with BioRender.

There are a lot of detailed mechanisms involved in these steps of breast cancer metastasis, but here we focus on the shift of dynamic tumor microenvironments (TME) during the process. From the primary site to the blood vessel and distant organs, the MBC cells have two strategies for them to progress in the dynamic TME. Apparently, the MBC cells should always reprogram themselves to fit different TME. For example, our previous finding suggests that MBC cells regulate pyruvate carboxylase to survive in the oxygen-abundant lung tissues [59]. MBC cells are also capable of adjusting themselves to ensure the critical steps happen. For instance, MBC cells change the expression of lamin A/C to regulate the integrity of the nuclear envelope and ensure the successfulness of intravasation [60, 61]. The epithelial-mesenchymal transition (EMT) is also important for the invasiveness of MBC cells, which provides the plasticity of phenotype for the MBC cells in different TME [62]. On the other hand, MBC cells can also change the TME to make the soil suitable for their seeding. There are a lot of tools for MBC cells to reprogram TME, including paracrine growth factors, extracellular vesicles and even microRNA [63-65]. Other cells in the TME, such as T-cell and macrophages, may also be involved in this process.

Hence, the lifecycle of MBC is complicated and flexibility is the lifestyle of MBC in response to the dynamic TME. No matter which way the MBC cells choose, they should always be able to alter their characterization efficiently. In fact, dozens of changes in mutation and signature frequencies have been observed within the genomic landscape of MBC [66]. To regulate these genomic changes in an efficient way, MBC cells must have key signaling nodes linking multiple signaling drivers together, which are important to maintain the flexibility of MBC. These key signaling nodes are ideal candidates for multifunctional therapeutic targets to treat MBC.

1.2 Multiple signaling drivers in metastatic breast cancer cells

In the last section, we discuss the MBC cells must fit themselves to the TME efficiently to maintain flexibility in this dynamic environment. There are multiple signaling drivers in MBC cells to support this function, which are the key to metastatic progression and drug resistance of MBC cells. Targeting these drivers together will apparently reduce the growth, drug resistance, and immune evasion of MBC cells.

1.2.1 Metastatic breast cancer is complicated and flexible

The HER2-targeted TKIs, such as lapatinib and neratinib, can block the downstream signaling cascade from HER2 through phosphoinositide 3-kinases (PI3K) and mitogen-activated protein kinase (MAPK) pathways and reduce the growth of MBC cells. However, the MBC cells are able to activate other receptor tyrosine kinases (RTKs) on the cell surface via induction of corresponding growth factors and acquire resistance to HER2-targeted TKIs, either by reactivation of original pathways originally induced by HER2, or activation of bypass pathways (Figure 1.3).

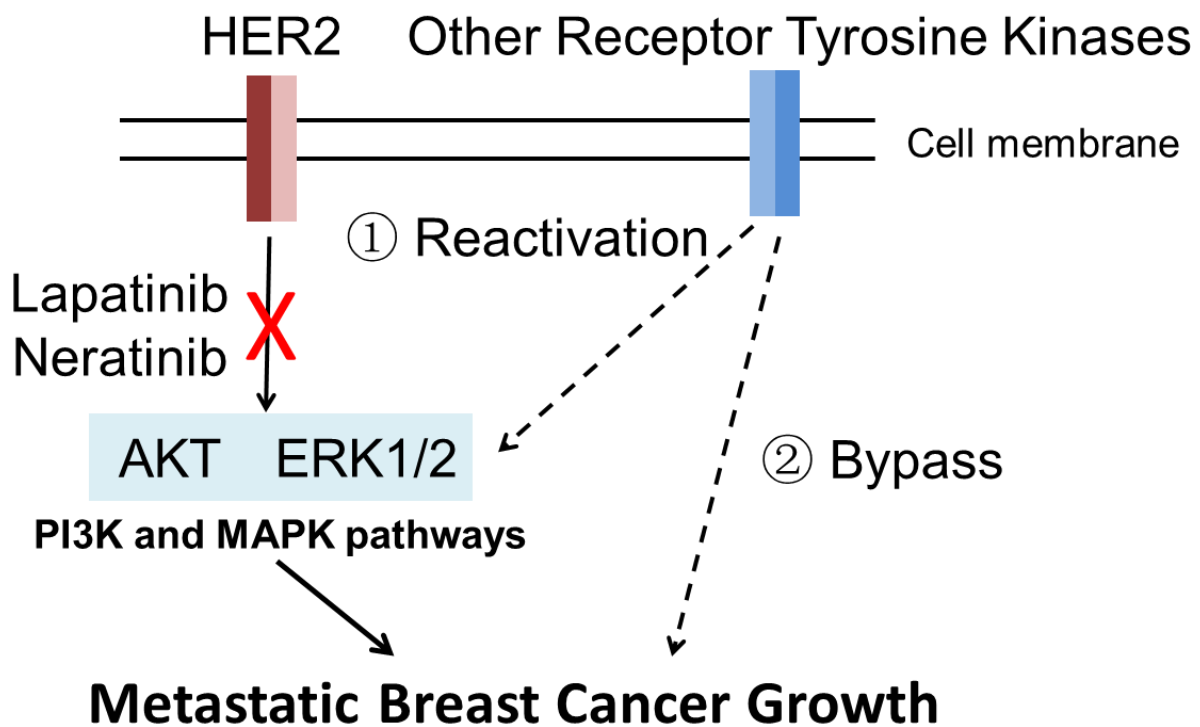


Figure 1.3. Receptor tyrosine kinases signaling pathways induced by multiple growth factors play an important role in resistance to HER2-targeted therapies in MBC cells. The growth and survival signaling pathways (PI3K and MAPK) are blocked by HER2-targeted therapies, lapatinib, and neratinib. The MBC cells resistant to HER2-targeted therapies are capable of activating multiple receptor tyrosine kinases signaling pathways induced by multiple growth factors to reactivate original growth and survival pathways or introduce novel by-pass pathways.

These RTKs bind to the corresponding growth factors, which induce dimerization to activate their tyrosine kinase activity. The intercellular signaling complex is recruited upon the activation of RTKs, and the downstream growth and survival signaling pathways are turned on. There are 58 RTKs discovered in human, which share similar structures (extracellular ligand-binding domain, transmembrane domain, intracellular region and tyrosine kinase domain), intercellular signaling complex and downstream pathways of activation (PI3K and MAPK pathways) [67, 68]. Because of the shared structure and signaling events among these RTKs, understanding which RTKs are involved in drug resistance is critical.

Multiple experimental studies, including findings from our lab, have described that one of the RTKs named fibroblast growth factor receptor 1 (FGFR1) promotes the acquired and inherent resistance to lapatinib in HER2 positive breast cancer cells [69-72]. The locus encoding FGFR1 is amplified in 14% of breast cancer patients, and the expression of FGFR1 can be upregulated through EMT, which is a key driver of both drug resistance and metastasis [73, 74]. In addition to FGFR1, multiple other RTKs have been linked to drug resistance and metastasis, including Platelet-derived growth factor receptor (PDGFR), cMET, vascular endothelial growth factor receptor (VEGFR) and epidermal growth factor receptor (EGFR) [75-77]. As these RTKs also overlap downstream signaling pathways of activation, they should have shared signaling nodes to regulate the phenotype of the cells efficiently. The shared signaling nodes should play an important role in the recruitment of the intercellular signaling complex. But which signaling nodes are responsible and which RTKs are involved are not fully understood.

1.2.2 Extracellular matrix signaling

Besides the RTKs signaling, extracellular matrix (ECM) signaling also plays an important role in drug resistance and metastasis. ECM is a dynamic network with an array of multi-domain macromolecules, which include collagen, proteoglycans, laminin, fibronectin, and elastin [78]. The ECM is dynamic as it can be organized in a specific manner according to the microenvironment. For example, ECM remodeling and active deposition are critical for the formation of pre-metastatic niche and tumor metastasis [79]. Among the components of ECM, fibronectin is secreted as a dimer and serves as biological glue among cells, which is critical for cell migration and attachment. Fibronectin in the ECM can initiate the integrin-mediated

signaling cascades and have crosstalk with RTKs signaling, which promotes MBC growth and survival (Figure 1.4).

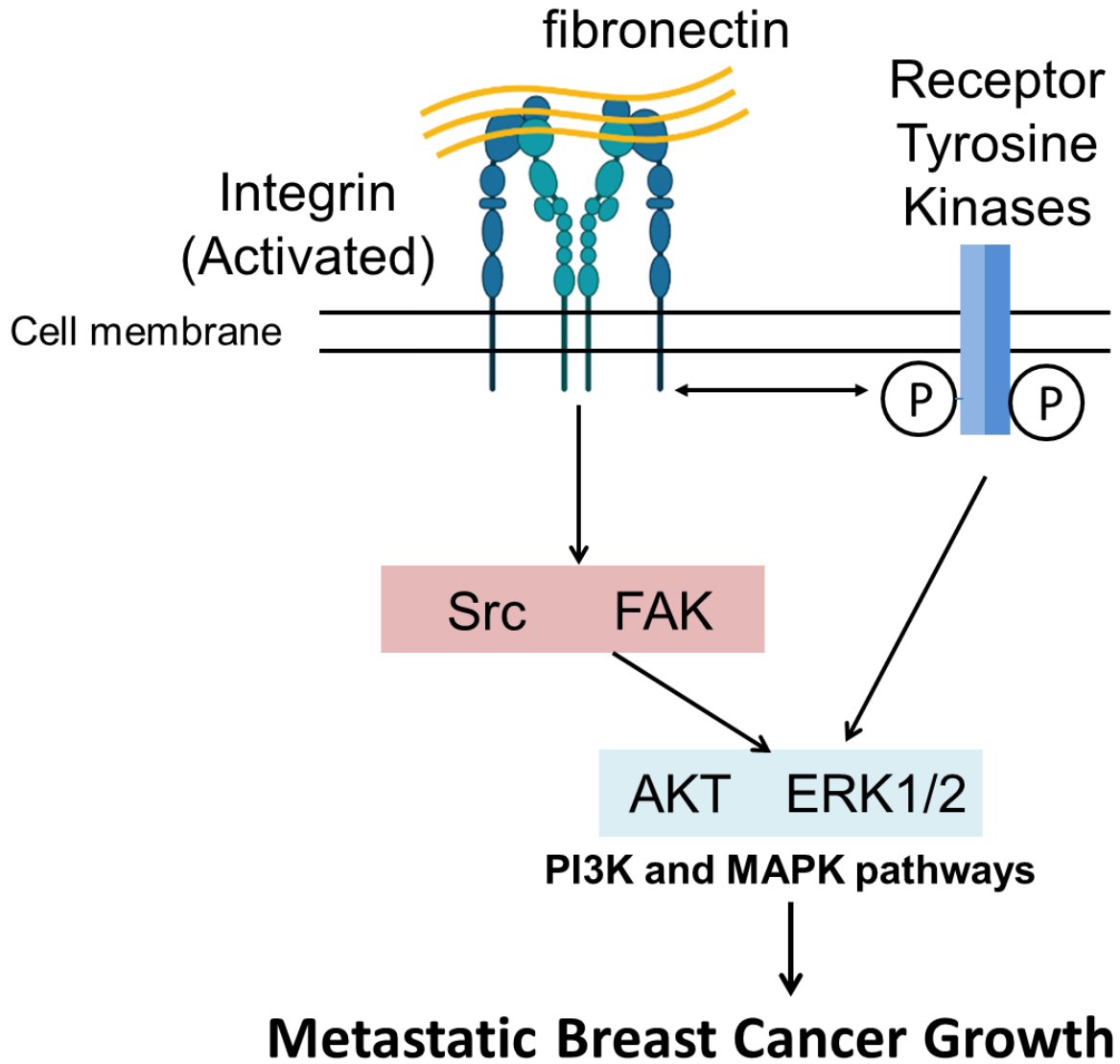


Figure 1.4. Extracellular matrix-mediated integrin signaling has crosstalk with receptor tyrosine kinases signaling in MBC cells. Extracellular matrix components, including fibronectin, can regulate Src and FAK to activate growth and survival signaling pathways. ECM signaling can also interact with receptor tyrosine kinases and activate receptor tyrosine kinases signaling without ligand binding, which enhances the growth of MBC cells. Parts of the figure are created with BioRender.

In detail, fibronectin is the ligand for a cell surface receptor, integrin, to form clusters and activate them. Activated integrin can activate downstream signaling via phosphorylation of Src and focal adhesion kinase (FAK) to promote growth and survival signaling. Besides the signaling role by itself, the activated integrin by fibronectin can also initiate ligand-independent activation of RTKs signaling, such as c-Met [80]. The integrin-fibronectin complex can even bind with RTKs to synergistically facilitate the signaling cascades [81]. In fact, multiple reports have demonstrated that active signaling events generated through integrin-mediated sensing of the ECM can function independently and in conjunction with RTKs to support the growth and survival of MBC cells in the presence of targeted and chemotherapies [82, 83]. Considering the close relationship between RTKs and ECM signaling, uncovering shared nodes in the network is a good strategy to identify new targets for MBC therapies.

1.2.3 Regulators of anti-tumor immunity

The MBC cells utilize the network of RTKs and ECM signaling to maintain their growth and survival, and they are also required to have regulators to evade immune surveillance. The ICB targets these regulators, such as PD-L1, to induce the recognition of tumor cells and the tumor-killing events (Figure 1.5). In the physiological condition, the major histocompatibility complex class I (MHC I) molecules on the surface of cells present the antigen to the cytotoxic T cells and activate T cell receptor (TCR) signaling. The interaction by MHC I will trigger an immune response and kill the cells. However, the MBC cells are capable of expressing the partner of immune checkpoints, such as PD-L1 on the surface, and it can interact with PD-1 on the surface of T cells. The immune response is interrupted by the interaction of PD-L1 and PD-1 (Figure 1.5, top). Besides overexpression of PD-L1, the MBC cells can also reduce the expression of MHC I to block the antigen presentation and T-cell cytotoxic events [84]. When the interaction of PD-1 and PD-L1 is blocked by ICB, the T-cell activity is relieved and the MBC cells are killed by T cells (Figure 1.5, bottom).

With the important role of MHC I and PD-L1 on the surface of MBC cells in regulating anti-tumor immunity, the mechanisms of how these intrinsic regulators are controlled by the dynamic TME are the key to understanding and solving the problem of the limited response to ICB in treating MBC patients.

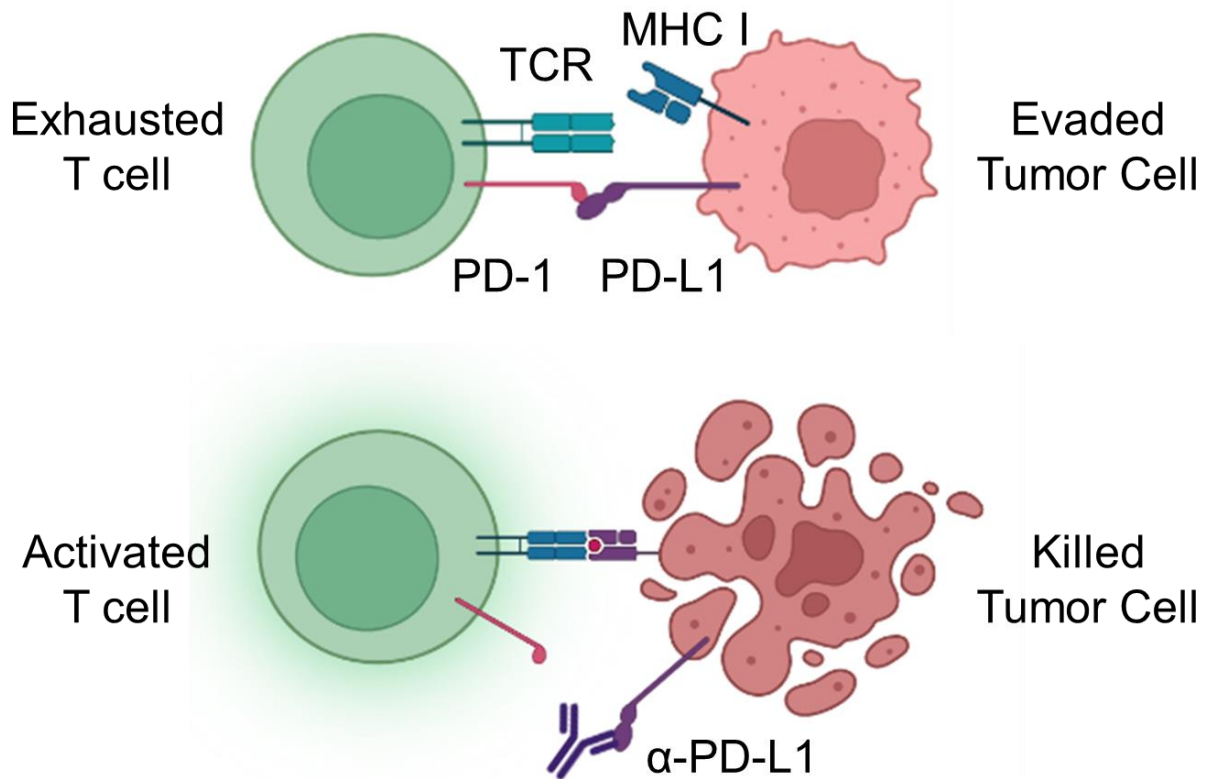


Figure 1.5. Immune checkpoints and major histocompatibility complexes control the anti-tumor immunity via T-cell cytotoxic events. The major histocompatibility complex class I molecules presents the antigen and activate T-cell receptor signaling. The interaction by MHC I and T-cell receptor triggers an immune response and kills the cells, which is interrupted by the interaction of immune checkpoint PD-1 and its partner PD-L1 (top). When the interaction of PD-1 and PD-L1 is blocked by immune checkpoint blockade, the T-cell activity is relieved to induce T-cell mediated tumor killing events (bottom). Parts of the figure are created with BioRender.

1.3 Heterogeneous tumor microenvironment in metastatic breast cancer

In the previous section, we discuss multiple signaling drivers in MBC cells, which regulate the growth and survival of MBC cells. The intrinsic regulators in the MBC cells also control the anti-tumor immunity. These signaling drivers may share nodes, which can be candidates for multifunctional therapeutic targets to treat MBC.

In addition to regulating internal pathways to fit the dynamic TME, the MBC cells must communicate efficiently with the other cells in the TME, including fibroblasts, epithelium and immune cells. Among these cells, the functions of the immune cells are the most variable, especially when the immune cells are influenced by different signaling inputs such as growth factors and ECM components. Some immune cells are immunogenic in most situations, such as CD8⁺ cytotoxic T cells; while a lot of immune cells can be either immunogenic or immunosuppressive to the tumor cells. For example, the tumor associated macrophages (TAMs) have two subtypes, M1-polarized macrophages are tumor-promoting, while M2-polarized ones are tumor-suppressing [85]. Chemotherapies have drawbacks in treating MBC not only because they are not targeted, but also because they only make blocking the growth of tumor cells into consideration and neglect the importance of immune cells in the TME. The diversity of the immune cells also limits the therapeutic potential of targeted therapies designed for one certain population. Thus, validation of multifunctional therapeutic targets covering the heterogeneous cell populations in TME is a good solution.

1.4 SHP2 is an oncogenic phosphatase in both tumor cells and immune cells

We previously concluded that we need to find multifunctional therapeutic targets to treat MBC, due to the complexity of MBC in the dynamic TME. The ideal candidates for multifunctional therapeutic targets should be shared nodes in the signaling networks driving the growth and survival of MBC, and/or the key components to regulate anti-tumor immunity in MBC cells. Here, we would like to introduce SH2 containing protein tyrosine phosphatase-2 (SHP2) as a promising target due to its oncogenic roles in both tumor cells and immune cells.

1.4.1 SHP2 is a non-receptor protein tyrosine phosphatase

A kinase is an enzyme that adds a phosphate group to the target protein, while a phosphatase is an enzyme that reverses this process; and the kinase-phosphatase balance controls a lot of physiological and pathological processes, such as metabolism and cancer [86, 87]. According to the substrate preference and catalytic mechanism, the family of phosphatases can be classified into four subgroups, including phosphotyrosine phosphatases, phosphoprotein phosphatases, Mg²⁺/Mn²⁺-dependent protein phosphatases and aspartate-based protein

phosphatases [88]. Besides this classification method, the phosphatases can be also categorized into two subfamilies according to their cellular localization, including receptor-like phosphatases and non-receptor phosphatases [89]. The receptor-like phosphatase locates on the surface of the membrane, while the non-receptor one locates inside the membrane with no transmembrane structures.

SHP2 is a non-receptor protein tyrosine phosphatase (PTP), which is coded by PTPN11 located on human chromosome 12. SHP2 is composed of three major domains, two SH2 domains (N-SH2 closer to N-terminal and C-SH2 closer to C-terminal) and one PTP domain, which is responsible for phosphatase activity. The activation of SHP2 catalytic activity is controlled by conformational change (Figure 1.6).

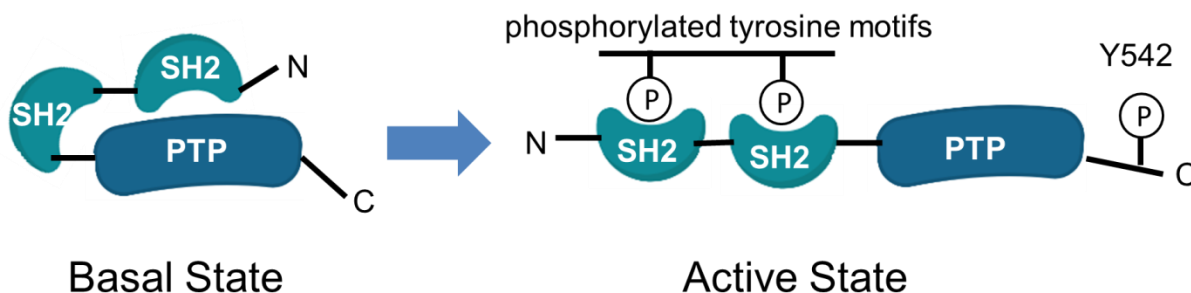


Figure 1.6. Activation of SHP2 requires a conformational change from an auto-inhibitory basal state to an activation state. In the basal state, the SH2 domain at N-terminal (N-SH2 domain) interacts with the PTP domain, which inhibits the substrate binding and activity of SHP2 (left). Upon interacting with specific phosphorylated tyrosine motifs, the interaction between the N-SH2 domain and PTP domain is weakened, and the SHP2 is in the activation state (right). SHP2 can be phosphorylated at Y542, which is essential to the activation of downstream MAPK signaling.

In detail, SHP2 is auto-inhibitory in its basal state by the interaction between the N-SH2 domain and PTP domain, which blocks the catalytic site from binding to the substrate [90]. The N-SH2 and C-SH2 domains can bind to specific phosphorylated tyrosine motifs, which weakens the interaction between the N-SH2 domain and PTP domain and activate the catalytic activity of SHP2 [91, 92]. After being released from auto-inhibitory conformation, SHP2 is phosphorylated at Y542, which is required for downstream signaling activation including MAPK pathways [93].

Hence, because SHP2 is activated upon binding to phosphorylated tyrosine motifs and SHP2 can activate downstream signaling pathways, SHP2 is located in the middle layer of the signaling network with multiple signaling inputs and outputs. This characterization ensures that SHP2 can regulate dynamic and complicated signaling events, which is critical for developmental biology and cancer progression.

1.4.2 Oncogenic functions of SHP2 in tumor cells and immune cells

With the involvement of the signaling networks in growth and survival, SHP2 is considered an oncogenic protein tyrosine phosphatase in tumor cells. SHP2 promotes the growth and survival of tumor cells via regulating multiple signaling pathways, including MAPK, PI3K, and JNK/STAT pathways [94-96]. These pathways are downstream of multiple RTKs, as the activated RTKs have the specific phosphotyrosine motifs to interact with SH2 domains of SHP2 and activate SHP2. For example, one of the major drivers of MBC, FGFR1, binds to its ligand to activate its kinase activity. The phosphorylated FGFR1 reveals the catalytic site of SHP2 and localizes it to its intracellular substrates. Upon activation of SHP2, required signaling components of FGFR1, such as Fibroblast Growth Factor Receptor Substrate 2 (FRS2) and GRB2-associated binding protein 1 (Gab1), are recruited to form a signaling complex with SHP2 to activate downstream pathways [97, 98]. Besides the RTKs signaling, SHP2 can regulate the activities of Src and FAK kinase, which are downstream of ECM signaling [99, 100].

SHP2 promotes cancer progression, not only through facilitating its growth and survival signaling pathways in tumor cells but also by suppressing the anti-tumor immunity in immune cells. In T cells, SHP2 interacts with immune checkpoints including PD-1 and inhibits CD28 signaling to induce T-cell suppression and tumor immune invasion [101-105]. Myeloid-specific deletion of SHP2 also suppresses tumor growth *in vivo*, which suggests that SHP2 in the T cells is not the only reason for immune suppression [106]. In KRAS mutant-driven non-small cell lung cancer, SHP2 is responsible for remodeling the TME and the efficacy of PD-1/PD-L1 blockades [107, 108].

In summary, SHP2 is a key component of the signaling complex downstream of multiple RTKs signaling in tumor cells. It also regulates ECM signaling. SHP2 in the immune cells also promotes immune suppression. It is clear that SHP2 is required for critical cancer-associated signaling pathways and immune evasion, but the biochemical mechanisms of how SHP2

supports oncogenic events with a variety of downstream signaling outputs in response to diverse signaling inputs in the TME are not fully understood.

1.5 SHP2 is a druggable promising therapeutic target

In the previous section, we have summarized that SHP2 is an oncogenic phosphatase in both tumor cells and immune cells, which is a potential drug target. While phosphatases have traditionally been thought of as undruggable, two types of small molecule inhibitors targeting SHP2 have recently been developed. The detailed information for these inhibitors is listed in Table 1.1.

Table 1.1. The detailed information for two types of SHP2 inhibitors used in this study. The Name, development method, mechanism of action, IC₅₀ value to SHP2, selectivity, key interactions to ensure selectivity, solubility, bioavailability and corresponding references for 11a-1, SHP099 and TNO155 are listed in the table below.

Type	Phosphatase Activity Inhibitor	Allosteric Inhibitors	
Name	11a-1	SHP099	TNO155
Development method	Structure-guided and fragment-based library approach	High-throughput Screening	Optimization by Structure-activity relationship (SAR) based on SHP099
Mechanism of action	Occupation of SHP2 active site and prevention of phosphatase activity	Serving as ‘molecular glue’ by stabilizing SHP2 at its basal form.	
IC ₅₀ value to SHP2	200nM	71nM	11nM
Selectivity	> 5-fold selectivity against 20 mammalian phosphotyrosine phosphatases	no detectable activity against a panel of 21 phosphatases and 66 kinases	Completely selective over commercial panels of phosphatases/kinases
Key interactions to ensure selectivity	phenylthiophene tail of 11a-1 interacting with SHP2 in the β5–β6 loop (residues 362–365)	with R111, the central tunnel of SHP2 in which SHP099 binds is unique in shape/size	new direct interactions between TNO155 and SHP2 in S109, E110, and F113
Solubility	Soluble at 10mM in DMSO	Soluble at 10mM in water	Soluble at 10mM in water
Bioavailability	N/A	46% (oral in mouse)	78% (oral in mouse)
Corresponding references	[112]	[110]	[111]

One type of inhibitors is allosteric inhibitors, which serves as molecular glue to stabilize SHP2 at the basal state. These inhibitors strengthen the interaction between the N-SH2 domain and PTP domain via binding to a tunnel-like pocket formed by the confluence of three domains of SHP2 and prevent the required conformational change for SHP2 activation [109]. The tunnel-like pocket is unique for SHP2, which ensures the high selectivity of allosteric inhibitors targeting SHP2. Currently, two generations of allosteric inhibitors have been developed by Novartis, which are SHP099 and TNO155 [110, 111]. The similarity between these two generations is that these molecules are water-soluble, orally available and highly potent. Compared to SHP099, TNO155 has some new direct interactions with the SH2 domain, improved cellular penetration and balanced lipophilicity. Another type of inhibitors is catalytic activity inhibitors, which targets the PTP domain directly to inhibit the phosphatase activity of SHP2 directly. We have recently developed 11a-1, which is an active-site inhibitor of SHP2 [112]. This active-site inhibitor can also achieve anti-tumor effects [113]. In fact, systemic administration of these two types of SHP2 inhibitors showed promising anti-tumor effects, and some active clinical trials with SHP2 inhibitors have recently emerged [113-116]. TNO155 is currently in phase 1 clinical trials (NCT03114319). Besides TNO155, there are other allosteric inhibitors in pre-clinical studies and clinical trials, including RMC-4630 (NCT05054725) and JAB-3068 (NCT04721223).

In summary, SHP2 is a druggable target. We will use both types of SHP2 inhibitors in our study; however, the aim is not to compare which type of inhibitors is better but to identify the biochemical mechanisms for SHP2 to promote MBC.

1.6 Hypotheses and aims

Based on the information above, we hypothesize that SHP2 in the tumor cells may promote the growth and immune evasion of MBC cells in response to different signaling inputs in the dynamic TME. The study aims to identify which signaling inputs regulate corresponding signaling outputs through SHP2 in MBC cells (Figure 1.7). Achievement of the aim will validate SHP2 as a multifunctional therapeutic target to treat MBC. SHP2 inhibitors and combination strategies with SHP2 inhibition will provide new solutions to the management of advanced metastatic and drug resistant breast cancer in clinics.

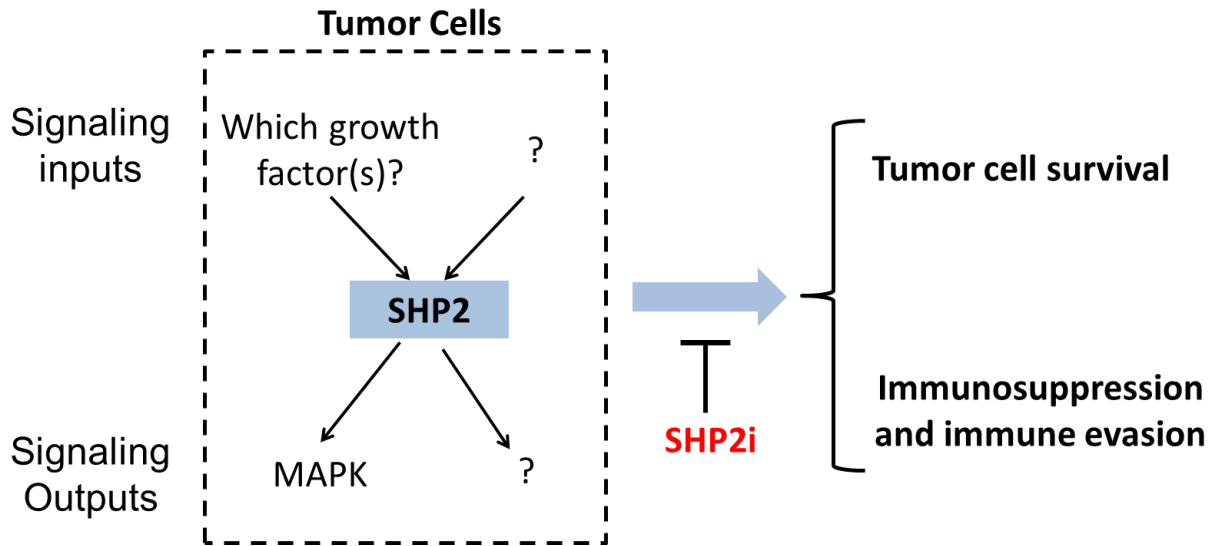


Figure 1.7. Hypotheses and aims of the study. We hypothesize that SHP2 is a key shared node in MBC cells to promote tumor cell survival and immune evasion. The aim of the study is to identify which signaling inputs regulate corresponding signaling outputs through SHP2 in MBC cells. The successful accomplishment of this study will support the SHP2 inhibitors as novel therapeutics in the management of MBC.

CHAPTER 2. TARGETING SHP2 TO INHIBIT METASTATIC BREAST CANCER

2.1 Disclaimer

The material in this chapter was published in a peer-reviewed journal *Oncogene* in 2020. The citation information for the article is listed below. The article is open access and licensed under a Creative Commons Attribution 4.0 International License.

Chen, H., Libring, S., Ruddraraju, K.V. et al. SHP2 is a multifunctional therapeutic target in drug resistant metastatic breast cancer. *Oncogene* 39, 7166–7180 (2020).

2.2 Introduction

Metastatic breast cancer (MBC) remains a knotty challenge in clinics. In the last chapter, we discussed the complexity of MBC. MBC cells must go through multiple steps for them to fit and survive before they can form pre-metastatic niche in the distant organs. The distant organs for MBC are lungs, liver, brain and bone. The detailed mechanisms by which the MBC cells select these distant organs as their new homes are not fully understood. There are multiple hypotheses, including the seed and soil hypothesis and the mechanical mechanisms hypothesis [117, 118]. In the seed and soil hypothesis, the local TME determines where the MBC cells go, just as a seed can only grow on its favorable soil. It is also possible that the growth of MBC in certain distant organ has unique mechanisms, which result in the difference in prognosis. A recent report has demonstrated different overall survival and breast cancer-specific survival among the MBC patients with lung, liver, bone and brain metastasis [119]. The MBC patients with lung metastasis have the second-lowest breast cancer-specific survival compared to the others. Although MBC brain metastasis has the worst prognosis, the blood brain barrier is difficult for the therapeutics to penetrate, which limits the possible benefits achieved by novel therapeutics. In contrast, the MBC lung metastasis has the second-lowest patient survival, but the organ is very accessible for therapeutics. Hence, we will focus on the MBC lung metastasis considering its clinical significance and potential for improvement with novel therapeutics.

We have introduced that SHP2 is an oncogenic phosphatase with type types of inhibitors, which have achieved anti-tumor effects in pre-clinical models. To evaluate the efficacy of these

SHP2 inhibitors to block the growth of MBC cells in the lung, it is required for us to implement reasonable *in vitro* and *in vivo* models. In the previous chapter, we have also summarized that the dynamic TME is very important to support the growth of MBC cells. Hence, we would like to highlight here that the activation of ECM signaling and the involvement of immune cell populations should be considered in the evaluation of the SHP2 inhibitors.

We have previously demonstrated that ECM signaling and components play an important role in supporting the growth of MBC and drug resistance [120, 121]. Moreover, the MBC cells are in favor of the anchorage-independent growth environment and cell-cell junction, especially when they are forming clusters of CTCs in the blood vessels [122]. On the other hand, the anchorage-independent growth environment can also activate signaling pathways, which results in the unique signaling response for the MBC cells to fit the dynamic TME [123]. In the *in vitro* assays, we will take the ECM components and anchorage-independent growth environment into consideration.

The immune cell populations are key components of TME; however, a lot of the animal models lost that feature, such as patient derived xenograft models. To evaluate the efficacy of SHP2 inhibitors under the full consideration of TME, we will use immunocompetent mice. In this study, we will use the murine breast cancer cell line, 4T1, to produce systemic metastases following orthotopic engraftment of mammary fat pad tumors [124]. We will also utilize another murine breast cancer cell line, D2.A1, to form the metastatic growth in the lung following tail vein injection, and the metastatic potential of D2.A1 can maintain stably [125]. We are considering these two *in vivo* models because we have proved that the metastatic phenotypes in these cells are driven by a variety of RTK and ECM signaling events [74, 126].

Herein, we implement these *in vitro* assays and *in vivo* models to evaluate the efficacy of SHP2 inhibitors to block the growth of MBC cells. We also confirm the effects of SHP2 inhibitors are on-target with doxycycline inducible genetic depletion of SHP2. We also identify whether the MBC cells resistant to HER2-targeted therapies are sensitive to SHP2 inhibitors. The detailed mechanisms by which SHP2 inhibitors block the growth of drug resistant MBC cells are also further investigated. Achievement of the results will strongly support SHP2 inhibitors as a potential therapeutics to treat MBC.

2.3 Materials and Methods

2.3.1 Cell lines, culture conditions, drug and reagents

The 4TO7 and D2.A1 cells were obtained from Fred Miller lab at Wayne State University, Detroit, MI. The other cell lines were purchased from ATCC. Luciferase expressing, 4T1, HMLE cells transformed by HER2 overexpression (HME2-PAR), their lapatinib resistant counterparts (HME2-LAPR), 4TO7 and D2.A1 cells were constructed as we previously described [72, 74, 127]. Briefly, these cells were transfected with a pNifty-CMV-luciferase to stably express luciferase.

The HME2-PAR and HME2-LAPR cells were cultured with DMEM media (GE Healthcare) with 10% Fetal Bovine Serum (FBS) (Gibco) and 0.1% Human Insulin solution (ThermoFisher). The ZR-75-1 cells were cultured with RPMI-1640 media (ATCC) with 10% Fetal Bovine Serum (FBS). The BT549 cells were cultured with RPMI-1640 media with 10% Fetal Bovine Serum (FBS) and 0.1% Human Insulin solution. The UACC812 cells were cultured with DMEM media with 10% Fetal Bovine Serum (FBS) and 32ng/ml EGF (GoldBio). The other cell lines were cultured with DMEM media with 10% Fetal Bovine Serum (FBS). All the media for cell culturing was supplemented with 1% Penicillin-Streptomycin (Gibco). The cells were maintained in the tissue culture incubator (ThermoFisher) at 37 °C in a 5% CO₂ incubator with 80% humidity. All cell lines were authenticated via the IDEXX IMPACT III CellCheck. All cell lines were regularly tested for mycoplasma contamination via PCR. The detailed information for cell lines and culture conditions can also be found in APPENDIX A Table A.1.

11a-1 was synthesized as previously described [112]. 11a-1 was reconstituted in DMSO (Fisher) to 10mM stock. SHP099 dihydrochloride for *in vitro* studies was purchased from Selleck, while SHP099 dihydrochloride for *in vivo* studies was purchased from Chemietek. For *in vitro* assays, SHP099 was reconstituted in sterilized double distilled water to 10mM stock. TNO155 was also purchased from Chemietek. TNO155 was reconstituted in DMSO to 5mM stock. The FGFR inhibitor, FIIN4 was purchased from Achemtek, and its development and synthesis were described previously [74, 128]. Neratinib was purchased from Selleck. FIIN4 and Neratinib were reconstituted in DMSO to 1mM stock. All these constituted drugs were aliquoted and stored at -80 °C. The ECM matrix, growth-factor-reduced Cultrex for 3D culture, was purchased from Sigma. Cultrex was diluted to 80% with serum-free DMEM and stored at 4 °C.

The D-Luciferin Potassium Salt for bioluminescence live imaging *in vivo* was purchased from GoldBio. One gram of D-Luciferin was reconstituted in 66ml sterilized Phosphate Buffered Saline (PBS) in dark, aliquoted to 850 μ L/tube, and stored at -20 °C. The detailed information for these drugs and reagents can also be found in APPENDIX A Table A.3.

2.3.2 Cell viability assays and colony formation assays on tissue culture treated polystyrene (2D culture)

In cell viability assays under 2D culture conditions, the drugs were first prepared at the 2X highest concentration as designed in full growth media. Vehicle at the same volume was added to another parallel tube as a media control. For example, if the designed highest concentration for 11a-1 in the assay was 10 μ M, we prepared a 20 μ M stock. We then performed a series of gradient dilutions with full growth media at a 1:1 ratio until 9 tubes of drugs at different concentrations were made. The media control and 9 tubes of drugs were added to a 96-well flat-bottom white plate (Corning) at 100 μ L/well, and three biological repeats were designed for each concentration. To avoid the disruption of vaporization to the results, the wells at the edges of the 96-well plate were not be used, and filled with 200 μ L/well PBS. After adding the drugs, the MBC cells were seeded at 1,000 cells/well in the plate at 100 μ L/well. The total volume in the wells was 200 μ L, and the cells and drugs were at a 1:1 ratio to make the final concentrations of the drugs 1X as designed.

Then, the plate was incubated in the tissue culture incubator for 30 minutes to help the cells settle down. Luciferin was added to each well at a ratio of 1:100 (2 μ L/well), and the plate was incubated in the tissue culture incubator for 15 minutes. Luminescence reading at an interval of 1 second as baseline reading was obtained with a plate reader (Promega). This step to achieve baseline reading was optional if the MBC cells were not constructed with luciferase.

Finally, the plate was incubated in the tissue culture incubator for 6 days. The plate was washed with 200 μ L/well PBS to remove residue media and drugs. Promega CellTiter-Glo solution was diluted with PBS at a ratio of 1:3 and added 30 μ L/well to the plate. The plate was incubated in the tissue culture incubator for 30 minutes before acquiring a luminescence reading with plate reader.

To analyze and quantify the viability, the luminescence reading in each well on day 6 was first normalized to the baseline reading on day 0. If the MBC cells were not constructed with

luciferase, raw luminescence reading on day 6 was used directly. The average luminescence reading of vehicle controls was calculated. Hence, the viability of the cells in each well was calculated as the percentage of luminescence reading relative to the average of vehicle controls. The dose-response curves and IC₅₀ values were achieved using the nonlinear regression (curve fit) function in GraphPad Prism 5.0.

In the colony formation assays, the drugs and vehicle controls were prepared at different concentrations with the same method described in the cell viability assays described above. The drugs were added to a 12-well flat-bottom clear tissue culture plate at 500µL/well. The cells were seeded in the 12-well plate at 5,000 cells/well in the volume of 500µL/well. The plate was incubated in the tissue culture incubator for 6 days. The plate was washed with 1ml/well PBS twice, and the viable cells were visualized with crystal violet staining. The results were achieved by scanning the plates with a document scanner under the white background.

2.3.3 Cell viability assays on ECM matrix (3D culture)

In cell viability assays under 3D culture conditions, the 96-well flat bottom white plate was coated with 50µL/well 80% Cultrex (Sigma), which is a growth-factor-reduced 3D culture hydrogel matrix. The plate was incubated in the cell culture incubator for at least 30 minutes to allow the gel to solidify. Similar to the 2D culture, to avoid the disruption of vaporization to the results, the wells at the edges of the 96-well plate were not be used, and filled with 200µL/well PBS. The drugs were prepared at the 2.5X concentration as designed in full growth media. If multiple concentrations of drug were needed, a gradient dilution like the one in 2D culture will be performed. Vehicle at the same volume was added to another parallel tube as a media control. The single-cell suspension of MBC cells was adjusted to the 30K cell/ml with full growth media. 10% Cultrex was also added to the cell suspension. Next, the cells and drugs were added to the plate coated with 80% Cultrex at 75µL/well, respectively. The drugs were diluted to 1X. The final seeding density was 2,250 cells/well, and the final concentration of the top layer hydrogel matrices was 5% Cultrex. The day of seeding was marked as day 0.

Then, the plate was incubated in the tissue culture incubator for 30 minutes to help the cells settle down. Luciferin was added to each well at a ratio of 1:100 (2µL/well), and the plate was incubated in the tissue culture incubator for 15 minutes. Luminescence reading at an interval

of 1 second as baseline reading at day 0 was obtained with a plate reader (Promega). This step was optional if the MBC cells were not constructed with luciferase.

The growth of the MBC cells and viabilities were monitored on day 4, day 8, day 12, day 16, and day 20 following the day of seeding. The cells were observed with a microscope (Nikon), and representative photos were taken under 40X and 100X. The drugs were refreshed after taking photos. If the cells were constructed with luciferase, to monitor the viabilities, luminescence reading at this date was achieved as described above at day 0. If the cells were not constructed with luciferase, at the desired date at the end of the study (usually day 16 or 20), the plate was washed with 200 μ L/well PBS to remove residue media and drugs. Promega CellTiter-Glo solution was diluted with PBS at a ratio of 1:1 and added 30 μ L/well to the plate. The plate was incubated in the tissue culture incubator for 30 minutes before acquiring a luminescence reading with a plate reader.

The analyses and quantification of the viabilities were the same as described in the viability assays under 2D culture conditions. The visualization and statistical analyses were performed with GraphPad Prism 5.0.

2.3.4 Immunoblotting and signaling wash-off assays

The cells were cultured in 12-well flat-bottom plates with treatments. The cells were then lysed using a modified RIPA lysis buffer with three detergents (50 mM Tris, 150 mM NaCl, 0.25% sodium deoxycholate, 1.0% NP40, 0.1% SDS, protease inhibitor cocktail, 10 mM activated sodium orthovanadate, 40 mM β -glycerolphosphate, and 20 mM sodium fluoride) at 80 μ L/well. The lysed cells were stored at -20 °C overnight and shaken on ice for 30 minutes before being harvested into tubes. The tubes were centrifuged at maximum speed at 4 °C for 3.5 minutes, and the suspension was transferred to a new set of tubes. The protein concentrations of the suspension were determined by Pierce BCA Protein Assay Kit (ThermoFisher) according to the manufacturer's instructions. The protein concentrations of the suspension were adjusted to the same with RIPA lysis buffer. Bromophenol blue dye was added to the samples before boiling at 95 °C for 5 minutes. The samples were stored at -20 °C.

Next, these samples were separated by 10% SDS-PAGE and transferred to Polyvinylidene difluoride (PVDF) membrane (Millipore) at 100V for 1.5 hours. The membrane was washed with methanol and dried on bench for at least 30 minutes (blocking), and probed with primary

antibodies at 4 °C overnight for p-ERK, t-ERK, p-AKT, t-AKT, p-HER2, t-HER2, Tubulin and SHP2. SHP2 antibody was purchased from Santa Cruz Biotechnology, and Tubulin antibody was purchased from Developmental Studies Hybridoma Bank (DHSB) in Iowa City, IA. The other antibodies here were bought from Cell Signaling Technology (CST). The detailed information for these antibodies can also be found in APPENDIX A Table A.6.

After probing the secondary antibodies (APPENDIX A Table A.7) at room temperature for 1 hour, the results were collected and recorded using X-ray films, ChemiDoc Gel Imaging System (Bio-Rad) and LI-COR imaging (LI-COR Biosciences). Quantification of the blots was performed with ImageJ 1.52a (NIH).

In the signaling wash-off assays, the HME2-LAPR cells at a single layer were seeded in 35mm tissue culture plates overnight. The cells were treated with neratinib at 500nM for 1 hour. Cells without neratinib treatments were set as no stem (NS) control. The neratinib-treated cells were washed twice with 1ml/plate DMEM without serum to remove any residue drug. The cells were next treated with 11a-1 at 10 μ M, SHP099 at 10 μ M, FIIN4 at 200nM or DMSO as vehicle control in serum-free DMEM media, respectively. The cells were cultured in a cell culture incubator for 12 hours and moved to immunoblotting analysis as described above.

2.3.5 Depletion of SHP2 with doxycycline inducible shRNA

Doxycycline inducible shRNA constructs (shPTPN11 146, 369 and 404) with eGFP expression and puromycin resistance gene were purchased from Dharmacon. The targeting sequences of these shRNA constructs are listed in APPENDIX A Table A.2. The same vector with a scrambled non-targeting control shRNA (shScramble) was also purchased from Dharmacon. Plasmids with these shRNA constructs were prepared with E.Z.N.A. Endo-Free Plasmid DNA Maxi Kit (Omega Bio-tek) according to the manufacturer's instructions. The concentrations of the plasmids were determined by NanoDrop 2000 Spectrophotometers (ThermoFisher).

These plasmids were co-transfected with psPAX2 and pMD2.G into HEK-293 cells respectively using polyethylenimine [58] at a ratio of 1:3 to obtain lentiviral particles 48 hours following the transfection. The supernatant containing lentiviral particles was harvested and filtered through a 45 μ m filter (Millipore) to remove cell debris. The lentiviral particles were aliquoted and stored at -80 °C. Next, the lentiviral particles were used to transduce 4T1 and

D2.A1 cells with 5 µg/ml polybrene (Sigma). Stable integration was selected with 5 µg/ml puromycin (Fisher). The stable cell lines were induced with 10 µg/ml doxycycline (Fisher) for 3 days, and sorted for GFP positivity. Photos were taken with a fluorescence microscope (ThermoFisher) to ensure the expression of eGFP with doxycycline induction before cell sorting. The cell sorting was performed by Dr. Jill E. Hutchcroft from Flow Cytometry and Cell Separation Core Facility at Bindley Bioscience Center, Purdue University.

To confirm the efficiency of cell sorting, the cells before and after cell sorting were induced by doxycycline under the same condition. Flow cytometry was performed by Guava EasyCyte (Millipore) to analyze the GFP positivity. The percentage of GFP-positive cells was determined by applying a flat gate to the viable cells with FlowJo 7.3.1.

To determine the depletion efficiency of SHP2 in the sorted cells, we induced the sorted cells with 10 µg/ml doxycycline and performed immunoblotting as described above to identify the protein levels of SHP2. At least three independent biological repeats were performed. The results of immunoblotting were quantified with ImageJ 1.52a (NIH). The efficiency was defined as the percentage of SHP2 reduction normalized to the shScramble construct with doxycycline induction.

2.3.6 Studies with in vivo metastatic models and animal care

All *in vivo* studies here were conducted in 4–6 week old, female BALB/cJ mice purchased from Jackson Laboratories.

In the 4T1 spontaneous metastasis model, 5×10^4 /mouse 4T1 cells were engrafted onto the mammary fat pad via an intraductal injection with 27 gauge needles and 1ml syringes [129]. The cells were triple washed with sterilized PBS to remove any residual serum and media, and stored on ice before injection. The primary tumors were measured twice per week by a Vernier caliper. Two weeks following the fat pad injection, the primary tumors were expected to exceed 200mm³. The primary tumors were surgically removed, and the wound was clipped and supplied with antibiotic pastes. The drugs for the treatments were prepared after the surgery. SHP099 was reconstituted with sterilized double distilled water, and formulated with 0.5% Hydroxypropyl Methylcellulose. Water at the same volume was also formulated as the vehicle controls. The drugs were administered via oral gavage at the indicated concentrations and frequencies. In the 4T1 model, the SHP099 was administrated at 50mg/kg q.o.d. or q.d. with oral gavage.

Monitoring of the metastasis was initiated at the date when the treatments started and continued every 3 days until the study ended. Metastasis was monitored using bioluminescent imaging after intraperitoneal injection with 30 gauge needles and 1ml syringes [129] of luciferin solution (150 μ L/mouse) using an AMI HT (Spectral Instruments). At the endpoint of the study, the mice were sacrificed, and the lungs were pulled out and weighed to get wet weights. The lungs were fixed overnight with 10% formaldehyde (Fisher) immediately after sacrificing the mice and stored in 75% ethanol (Fisher). Photos of each lung were taken, and the nodules on the lungs were counted manually with photos. Paraffin sectioning at 5 μ m thickness and H&E staining were performed by AML Laboratories, Inc. (Jacksonville, FL). The photos of lung sections were acquired by Cytation 5 cell imaging multi-mode reader with Gen5 software (BioTek Instruments, Inc.).

In the D2.A1 model, 1×10^6 /mouse D2.A1 cells were injected via the lateral tail vein with 30 gauge needles and 1ml syringes [129]. The cells were triple washed with sterilized PBS to remove any residual serum and media, and stored on ice before injection. One week following the injection, the mice were treated with drugs by oral gavage. The drugs for the treatments were prepared just before the treatments. SHP099 was reconstituted with sterilized double distilled water, and formulated with 0.5% Hydroxypropyl Methylcellulose. Water at the same volume was also formulated as the vehicle controls. In the D2.A1 model, the SHP099 was administered at 100mg/kg q.d. with oral gavage. Monitoring of metastasis initiated at the date when the treatments started. The process was the same as the one in the 4T1 model. The survival of the mice was monitored until all the mice were dead.

All *in vivo* assays were conducted under IACUC approval from Purdue University. No randomization or blinding was done.

2.3.7 Statistical analysis

No exclusion criteria were used in these studies. A student's t-test was used for comparing differences between two groups of measurements in *in vitro* assays with GraphPad Prism 5.0 software. Error bars show the standard error of the mean. The results of immunoblotting were quantified with ImageJ 1.52a (NIH). Group measurements of the *in vivo* assays were compared with a Mann-Whitney non-parametric test with GraphPad Prism 5.0 software. Survival analysis

was performed with GraphPad Prism 5.0 software, and the distributions of survival were compared by a log-rank test.

2.4 Results

2.4.1 SHP2 inhibitors block the grow of MBC cells in vitro

As SHP2 has been reported as an oncogenic phosphatase in tumor cells by multiple studies, it is reasonable for us to form the hypothesis that SHP2 is sufficient to promote the growth of MBC [130, 131]. To test the hypothesis, we treated the MBC cells cultured on tissue culture treated polystyrene with different types of SHP2 inhibitors, and observed the viabilities of the MBC cells following the treatments.

As we planned to engraft two mouse MBC cell lines, 4T1 and D2.A1, in immunocompetent mice to evaluate the efficacy of SHP2 inhibition *in vivo*, we started *in vitro* tests with these two cell lines. As the dose-response curves show the viabilities of the MBC cells with SHP2 inhibitors at different concentrations, the growth of 4T1 and D2.A1 cells was blocked by 11a-1, SHP099 and TNO155 at 10 μ M (Figure 2.1A, 2.1B). However, the viabilities of MBC cells were not reduced with 11a-1, SHP099 or TNO155 at concentrations lower than 1 μ M. Meanwhile, the 4T1 cells were more sensitive to SHP2 inhibition compared to the D2.A1 cells, and TNO155 performed better than 11a-1 and SHP099, especially in the 4T1 cells. To further identify the growth inhibitory effects of SHP2 inhibitors in human MBC cell lines, we treated ZR-75-1, SK-BR-3, and MDA-MB-435 cells with 11a-1 and SHP099. The dose-response curves indicated that the growth of these three cell lines was blocked by 11a-1 and SHP099 at 10 μ M, but the viabilities were not less than 50% (Figure 2.1C, 2.1D). The viabilities of these cell lines were also not reduced with 11a-1 or SHP099 at concentrations lower than 1 μ M.

In summary, the data in this section suggested that pharmacological inhibition of SHP2 was capable of partially blocking the growth of MBC cells *in vitro* at desired concentrations. But the inhibitory effects attenuated with lower concentrations. More optimizations about dosing and culturing systems were necessary for the following sections to predict the efficacy of SHP2 inhibitors with *in vitro* assays.

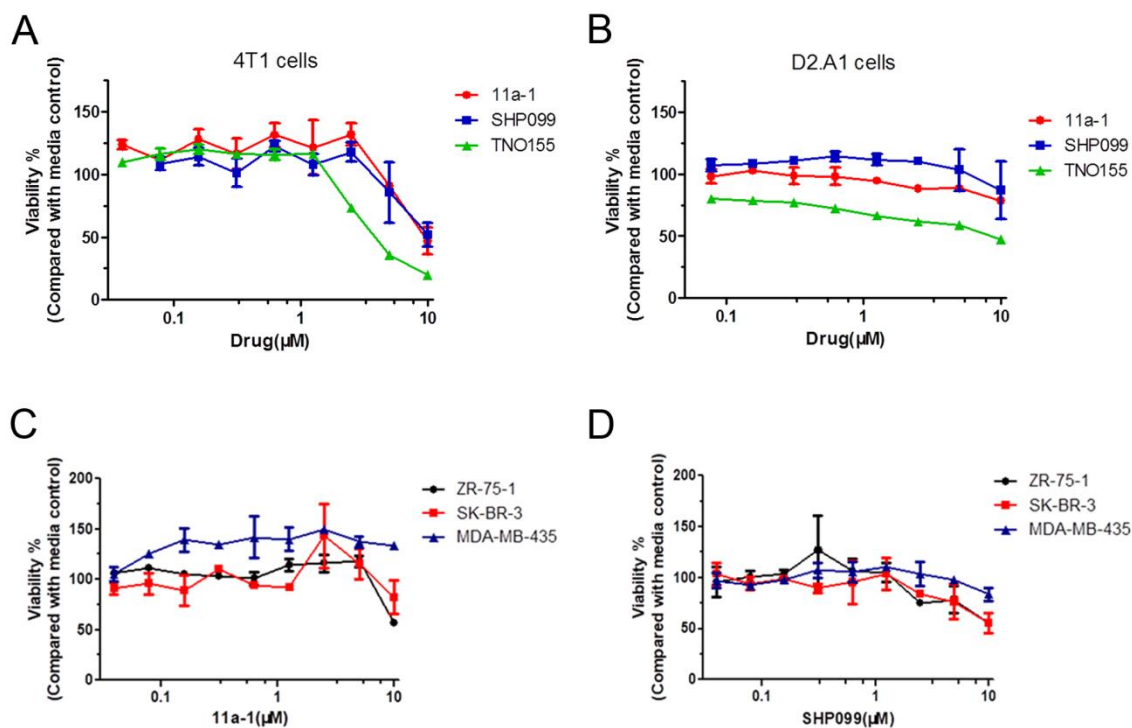


Figure 2.1. SHP2 inhibitors block the growth of MBC cells. A, Viability curves of 4T1 cells in response to SHP2 inhibitors, 11a-1 (red), SHP099 (blue) and TNO155 (green), at different concentrations. B, Viability curves of D2.A1 cells in response to SHP2 inhibitors, 11a-1 (red), SHP099 (blue) and TNO155 (green), at different concentrations. C, Viability curves of different human MBC cell lines, ZR-75-1 cells (black), SK-BR-3 cells (red) and MDA-MB-435 cells (blue), in response to 11a-1 at different concentrations. D, Viability curves of different human MBC cell lines, ZR-75-1 cells (black), SK-BR-3 cells (red) and MDA-MB-435 cells (blue), in response to SHP099 at different concentrations. In all panels, the percentage of viability is normalized to corresponding media controls.

2.4.2 Three dimensional culture environment enhances growth inhibitory effects of SHP2 blockade

In the previous section, we found that SHP2 inhibitors partially blocked the growth of MBC cells on the tissue culture treated polystyrene at desired concentrations. However, the culture condition here for the MBC cell lines could not fully mimic the real-world TME during breast cancer metastasis. There are several reasons to optimize the culture condition for us to

better evaluate the effects of SHP2 inhibitors in MBC cells. First, there is ECM matrix in TME, such as fibronectin and laminin, to support the growth of MBC cells, which is not provided by a plain polystyrene surface. Meanwhile, as the MBC cells attach to the polystyrene surface during the process, they lose the anchorage-independent growth properties, which is important for tumorigenicity *in vivo*. Finally, survival in the non-adhesive culture environment such as blood vessels is essential to MBC cells before their dissemination in the distance organs.

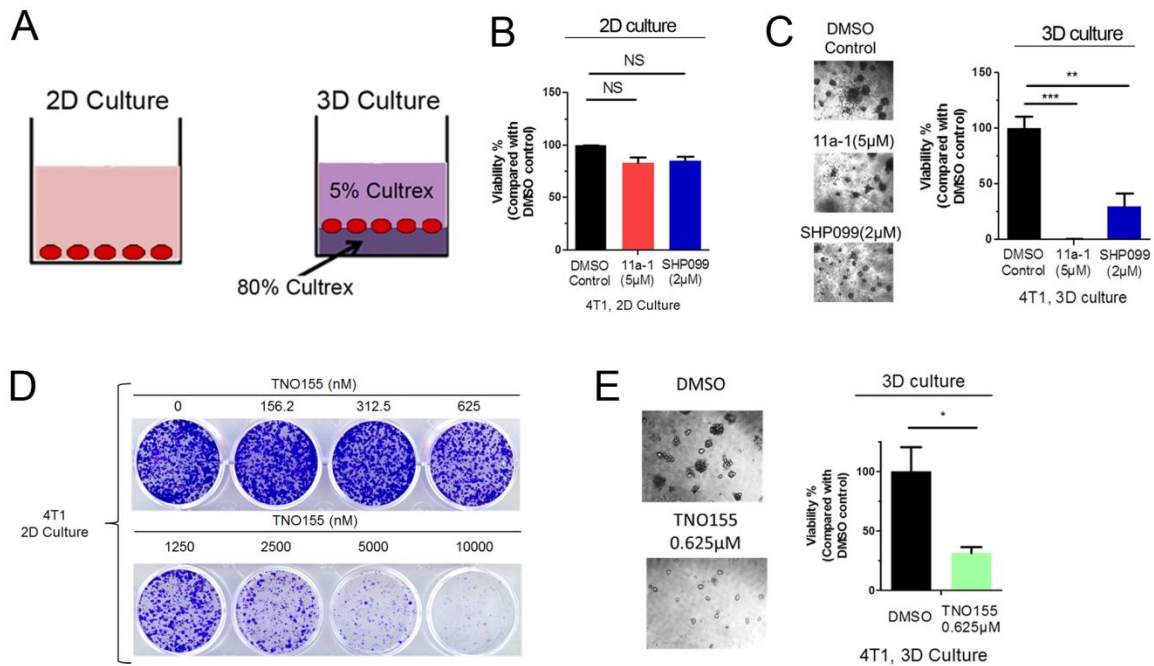


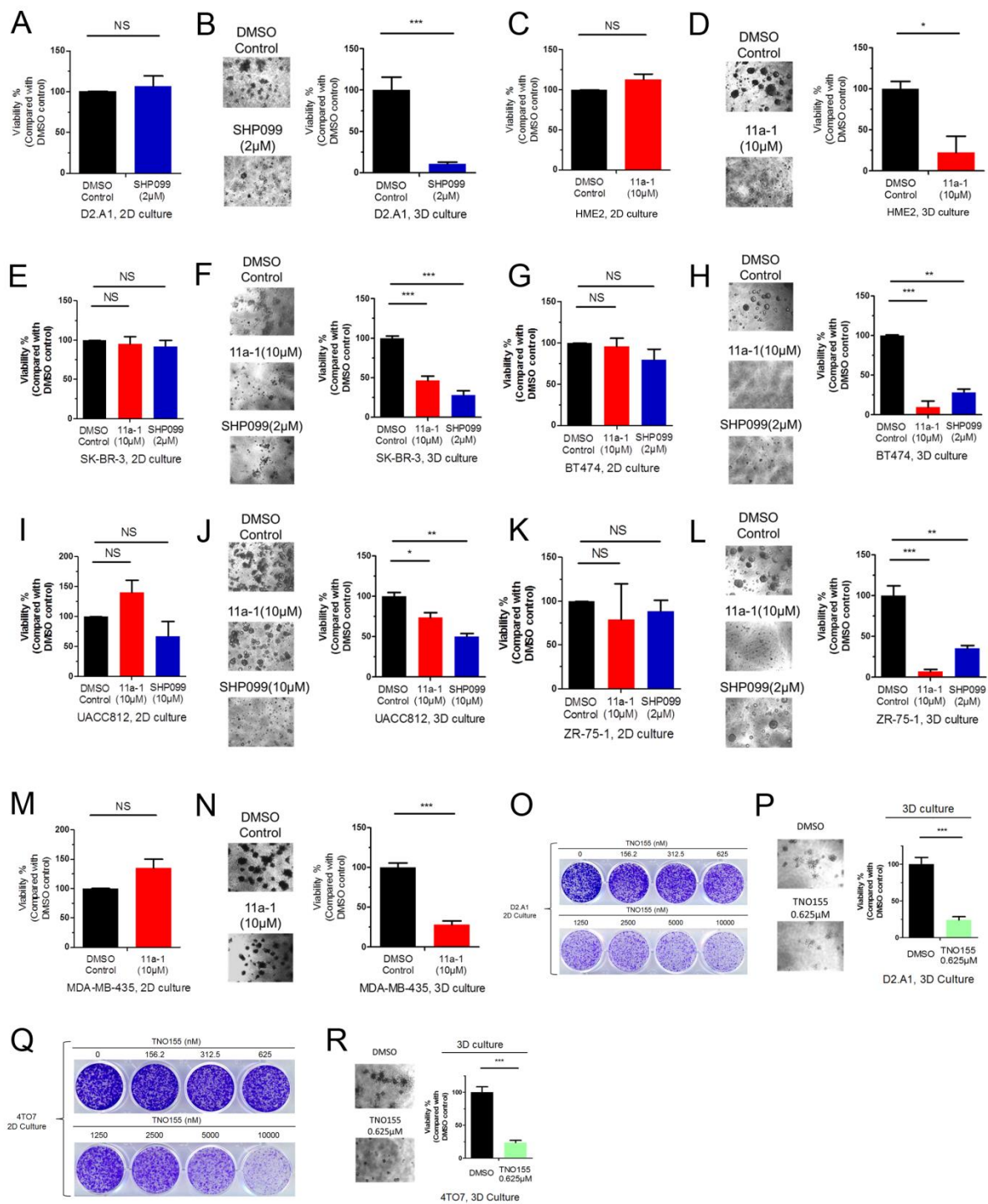
Figure 2.2. The effects of SHP2 inhibitors to block cell growth are enhanced under 3D culture conditions compared to 2D in 4T1 cells. A, Schematic representation of 2D and 3D culture conditions. The MBC cells are cultured directly on tissue-cultured plastic in 2D culture, while the MBC cells are supported by a layer of Cultrex matrix in 3D culture. B, Cell viability of 4T1 cells cultured in 2D for 6 days in the absence or presence of 11a-1 at 5µM and SHP099 at 2µM. C, Representative photomicrographs and quantification of 4T1 cell viability after 16 days in 3D culture in the absence or presence of 11a-1 at 5µM and SHP099 at 2µM. D, Crystal violet visualization of the viable cells of 4T1 cells cultured in 2D for 6 days in the absence or presence of the indicated different concentrations of TNO155. E, Representative photomicrographs and quantification of 4T1 cell viability in 3D culture in the absence or presence of TNO155 at 0.625µM. In all panels, data are normalized to vehicle controls and are the mean ± s.e.m. of three experiments where NS as no significance, *p<0.05, **p < 0.01 and ***p < 0.001.

Hence, we decided to develop a non-adhesive and matrix-supported culture environment to better simulate the TME and predict the efficacy of SHP2 inhibitors *in vivo* in the next step. Instead of the 2D culture indicating directly culturing cells on tissue culture treated polystyrene, we implemented the 3D culture by placing the cells at the interface of two semi-solid layers of ECM matrix (Cultrex), 80% at the bottom and 5% on the top (Figure 2.2A). We compared the differential responses of MBC cells to SHP2 inhibitors between 2D and 3D culture. Under the 2D culture, 11a-1 at 5 μ M or SHP099 at 2 μ M in serum-containing conditions did not significantly inhibit the growth of 4T1 cells, which was consistent with the results observed in Figure 2.1A (Figure 2.2B). While treatments of 11a-1 and SHP099 at the same concentrations significantly reduced the viabilities of 4T1 cells under the 3D culture (Figure 2.2C). The clone formation assays under the 2D culture also revealed that TNO155 at 0.625 μ M failed to significantly block the growth of 4T1 cells (Figure 2.2D). In contrast, treatments of TNO155 at the same concentration significantly restrained the growth of 4T1 cells under 3D culture (Figure 2.2E).

We then confirmed these results observed in 4T1 cells with other MBC cell lines. Both SHP099 at 2 μ M and TNO155 at 0.625 μ M significantly blocked the growth of D2.A1 cells under 3D culture, but not 2D culture (Figure 2.3A, 2.3B, 2.3O, 2.3P). Similar results were also confirmed with one of SHP2 inhibitors (11a-1, SHP099 and TNO155) in HER2-transformed mammary epithelial cells (HME2) cells (Figure 2.3C, 2.3D), SK-BR-3 cells (Figure 2.3E, 2.3F), BT474 cells (Figure 2.3G, 2.3H), UACC812 cells (Figure 2.3I, 2.3J), ZR-75-1 cells (Figure 2.3K, 2.3L), MDA-MB-435 cells (Figure 2.3M, 2.3N) and 4TO7 cells (Figure 2.3Q, 2.3R).

Taken together, these data in this section indicated that the growth inhibitory effects of SHP2 inhibitors were enhanced in 3D culture condition compared to 2D culture condition. As the enhancement of sensitivity was not occasionally observed with small molecular inhibitors, it was worthwhile for us to understand the detailed mechanisms as the next step.

Figure 2.3. MBC cell lines are more sensitive to SHP2 inhibition under 3D culture conditions compared to 2D. A-N, Differential cell viability of D2.A1 (A, B), HME2 (C, D), SK-BR-3 (E, F), BT474 (G, H), UACC812 (I, J), ZR-75-1 (K, L) and MDA-MB-435 (M, N) upon treatment with SHP099 or 11a-1 at the indicated concentrations under 2D or 3D culture conditions. O, Q, Crystal violet visualization of the viable cells of D2.A1 cells (O) and 4TO7 cells (Q) cultured in 2D for 6 days in the absence or presence of the indicated different concentrations of TNO155. P, R, Representative photomicrographs and quantification of D2.A1 cells (P) and 4TO7 cells (R) viabilities in 3D culture in the absence or presence of TNO155 at 0.625 μ M. In all cases data are the mean \pm s.e.m of cell viability normalized to vehicle controls, resulting in *p<0.05, **p<0.01, ***p<0.001 as determined via a student's t-test.

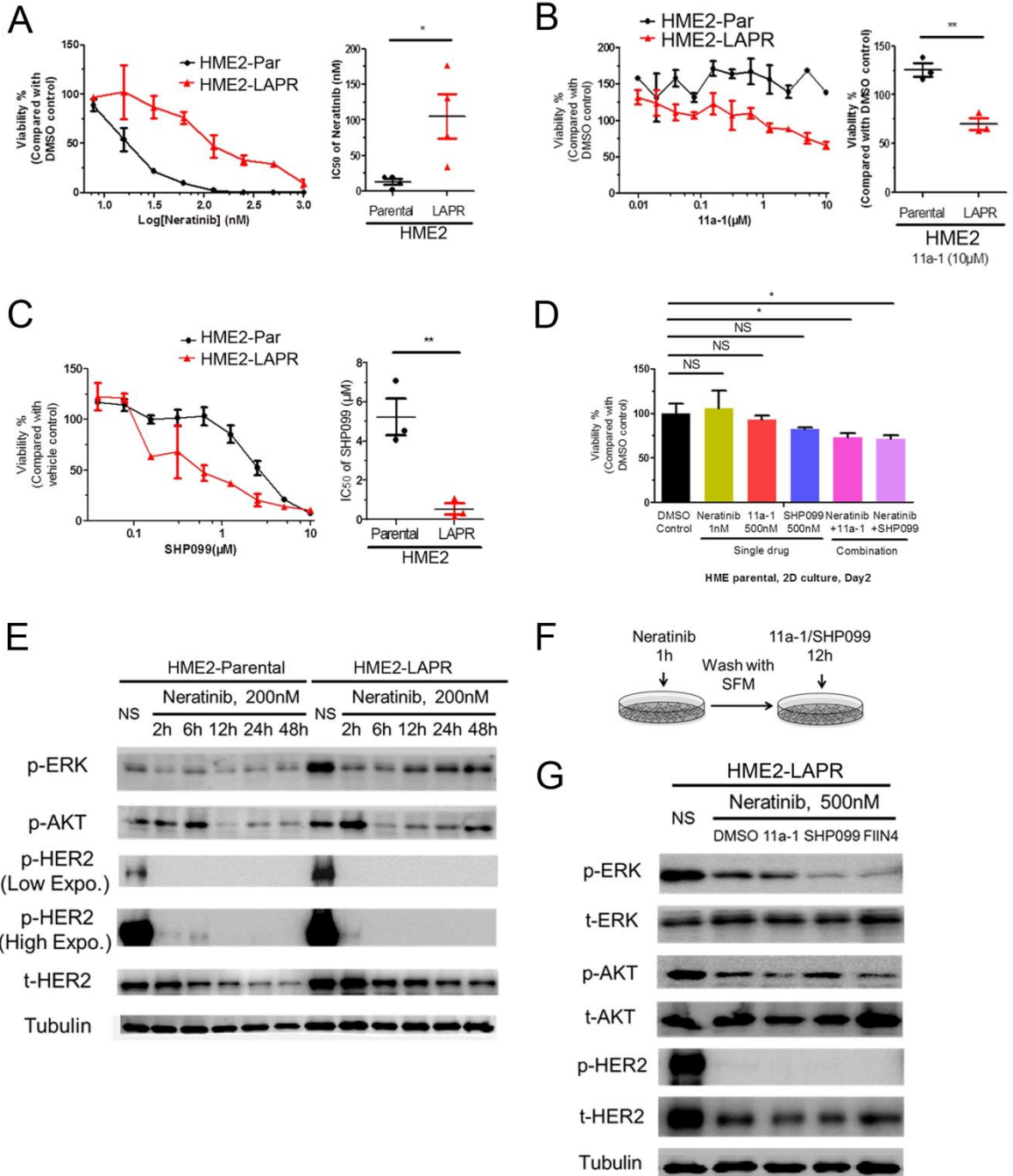


2.4.3 Drug resistant breast cancer cells can be targeted by SHP2 inhibitors

As we proved that HME2 cells were more sensitive to 11a-1 in 3D culture compared to 2D culture (Figure 2.3C, 2.3D), we thought that ECM matrix proteins and corresponding signaling pathways might be important for the oncogenic functions of SHP2 in MBC cells. Meanwhile, we previously reported that HME2 cells with acquired resistance to lapatinib (HME2-LAPR) resulted in a mesenchymal phenotype with upregulations of several ECM matrix proteins compared to parental cells (HME2-Par), including fibronectin [72, 129]. We hypothesized that SHP2 might facilitate MBC cells acquiring resistance to ErbB-targeted inhibitors, which could be targeted by SHP2 inhibitors. First, we demonstrated that HME2-LAPR cells were similarly resistant to a pan-ErbB inhibitor, neratinib, with a significantly higher IC_{50} compared to HME2-Par cells (Figure 2.4A). This fact indicated that the growth of HME2-LAPR cells was independent of all ErbB signaling pathways, which was driven by some alternative pathways instead. To prove the involvement of SHP2 in these alternative pathways, we treated the HME2-Par and HME2-LAPR cells with SHP2 inhibitors under 2D culture in serum-containing condition. The results showed that both 11a-1 and SHP099 preferentially inhibited the growth of the HME2-LAPR cells compared to HME2-Par cells, with a significantly lower IC_{50} respectively (Figure 2.4B and 2.4C). We further identified that the addition of 11a-1 or SHP099 at 500nM to a low dose of neratinib could significantly reduce the growth of HME2-Par cells (Figure 2.4D). The enhancement of growth inhibitory effects to neratinib by SHP2 inhibitors also supported the involvement of SHP2 in the alternative pathways independent of ErbB signaling.

To dig out which alternative pathways SHP2 contributes to in HME2-LAPR cells, we next focus on the signaling recovery events following ErbB blockade by neratinib. Neratinib apparently prevented phosphorylation of HER2 in both HME2-Par and HME2-LAPR cells from 2 hours to 48 hours following neratinib treatment, while the downstream phosphorylation of AKT and ERK1/2 recovered quicker in HME2-LAPR cells compared to HME2-Par cells from 12 hours to 48 hours following neratinib treatment (Figure 2.4E). The result here indicated that MAPK and PI3K pathways were listed as alternative pathways driving resistance. Moreover, we also noted that neratinib decreased the level of total HER2 in HME2-Par cells from 24 hours to 48 hours following neratinib treatment, but not in HME2-LAPR cells (Figure 2.4E). This result suggested that HME2-LAPR cells might have alternative pathways, such as disrupting protein degradation, to retain the levels of HER2 to drive resistance.

Figure 2.4. Drug resistant breast cancer cells can be targeted by SHP2 inhibitors via blocking signaling rebound. A, Representative dose response of HME2 parental (HME2-Par) and lapatinib resistant (HME2-LAPR) cells treated with neratinib for 6 days (left). The IC₅₀ values for each independent experiment were calculated (n = 4) and analyzed using a two-tail student's t-test where *p < 0.05. B, Representative dose response upon 6 days treatment with 11a-1 (left). Cell viability upon treatment with 10µM 11a-1 for each independent experiment was calculated (n = 4) and analyzed using a two-tail student's t-test where **p < 0.01. C, Representative dose response curves of HME2 parental (HME2-Par) and HME2-LAPR cells treated with SHP099 for 6 days (left). The IC₅₀ values for each independent experiment were calculated (n = 3) and analyzed using two-tail student's t-test where **p < 0.01. D, Growth inhibitory effects of neratinib are enhanced when combined with SHP2 inhibitors in HME2 parental cells. HME2 parental cells were seeded in 96-well plates, and treated with the indicated concentrations of neratinib, SHP2 inhibitors, or both compounds for 2 days. Cell growth was quantified by relative luminescence ratio compared to untreated cells. (n = 4, resulting in *p < 0.05, or no significance (NS) using a two-tail Student's t-test). E, Immunoblotting showing phosphorylation of AKT, ERK1/2, and HER2 in HME2-Par and HME2-LAPR cells upon the indicated time-course neratinib treatments. F, Schematic representation of the signaling recovery assays (top). HME2-LAPR cells were treated with neratinib for 1 h, the drug was removed, and the cells were allowed to recover in serum free media in the presence or absence of SHP2 or FGFR inhibitors for 12 hours. DMSO was used as a vehicle control. Recovery of AKT, ERK1/2, and HER2 phosphorylation was analyzed by immunoblotting (bottom).



To elucidate whether SHP2 was one of the mediators of ErbB bypass signaling indicated above, we implemented the signaling wash-off assays with HME2-LAPR cells. As the scheme shown here, we treated HME2-LAPR cells with neratinib for 1 hour before washing off the drug, and the cells were subsequently recovered in the presence or absence of SHP2 or FGFR inhibitors for an additional 12 hours (Figure 2.4F). We found that recovery of AKT and ERK1/2 phosphorylation were delayed by SHP2 or FGFR inhibitors compared to vehicle control of DMSO following the short-term neratinib treatment (Figure 2.4G). However, the total levels of HER2 did not change significantly, indicating SHP2 and FGFR might not be involved in this process.

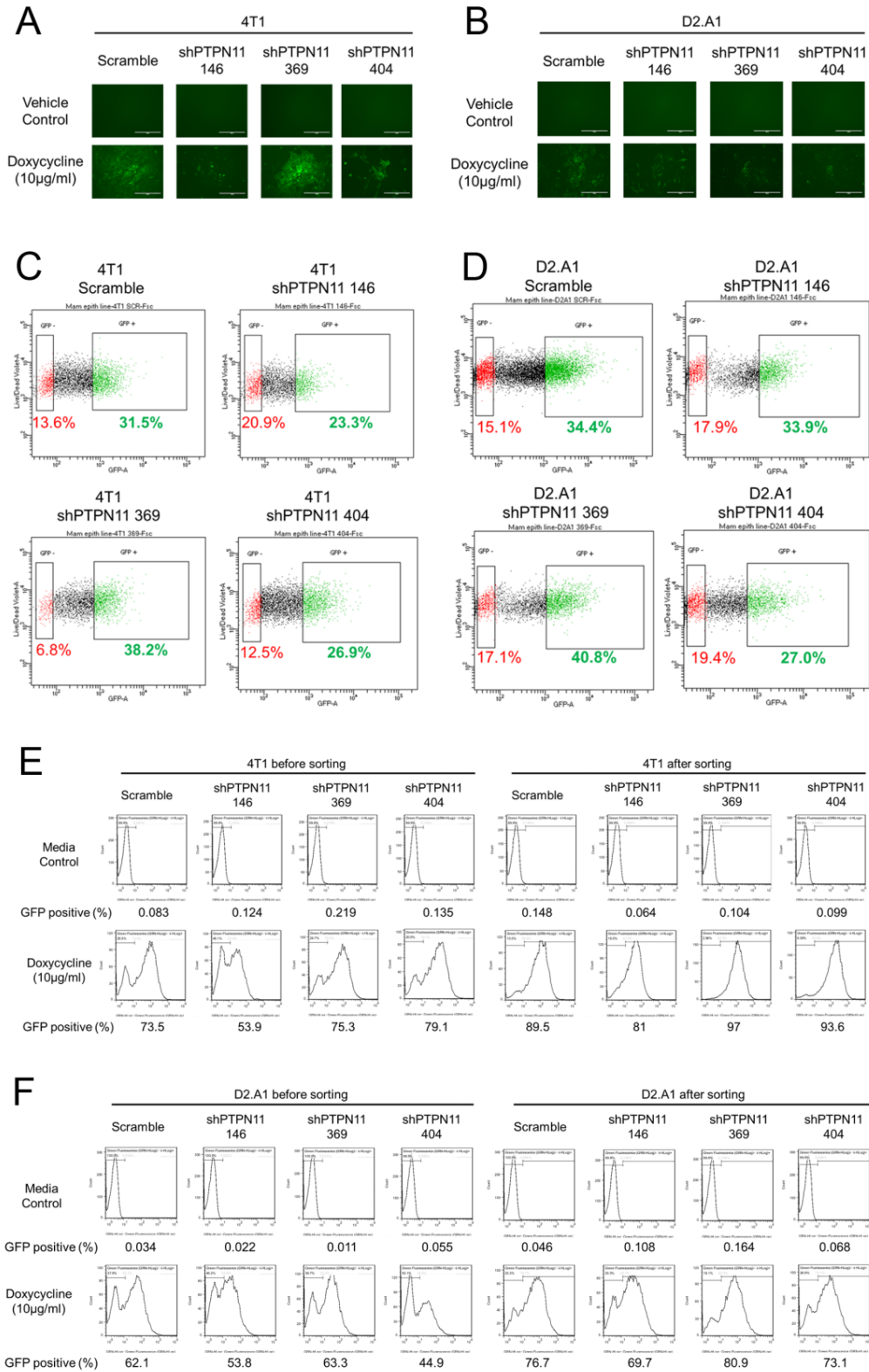
Summarized from the data in this section, SHP2 facilitated the phosphorylation of AKT and ERK1/2 as alternative pathways during ErbB inhibition to drive resistance to ErbB-targeted therapies, which could be targeted by SHP2 inhibitors. How the resistant cells retained the total level of HER2 during ErbB inhibition might be another interesting topic to investigate in the future.

2.4.4 Depletion of SHP2 inhibits the growth of metastatic breast cancer cells

In the first three sections, we used two types of inhibitors targeting SHP2 pharmacologically to explore its oncogenic functions in MBC. We first found that SHP2 inhibitors blocked the growth of MBC cells, and the effects were enhanced under 3D culture environment compared to 2D. Moreover, SHP2 inhibitors also targeted the MBC cells resistant to ErbB-targeted therapies by delaying the signaling recovery events. However, it was necessary for us to confirm the results achieved by SHP2 inhibitors were on target before moving to the *in vivo* studies.

Hence, we used three independent doxycycline-inducible shRNAs targeting PTPN11 to genetically manipulate SHP2 expression in 4T1 and D2.A1 cells. Upon stable transduction with doxycycline-inducible shRNA expression constructs, the cells were transiently treated with doxycycline at 10 μ g/ml for 2 days, and green fluorescence could be observed under fluorescence microscope (Figure 2.5A, 2.5B). The GFP⁺ cells here were responsive to doxycycline and more likely to be genetically manipulated. Next, these GFP⁺ cells (marked as green dots in the GFP⁺ gates) were isolated by Fluorescence-activated Cell Sorting (FACS) (Figure 2.5C, 2.5D).

Figure 2.5. Isolation of GFP⁺ cells upon doxycycline induction to construct 4T1 and D2.A1 with inducible SHP2 depletion. A, B, Representative photomicrographs showing doxycycline induction of GFP⁺ 4T1 cells (A) and D2.A1 cells (B) stably expressing shScramble control and PTPN11-targeting shRNAs (shPTPN11 146, 369 and 404) from the SMARTvector. C, D, FACS sorting plots of 4T1 cells (C) and D2.A1 cells (D) transiently induced with doxycycline. GFP⁻ cells were highlighted as red dots, while GFP⁺ cells were highlighted as green ones. The corresponding percentage of GFP⁻ and GFP⁺ are listed on the plots. E, F, Comparison of the GFP induction with doxycycline at 10µg/ml in the 4T1 cells (E) and D2.A1 cells (F) before and after FACS for GFP⁺ cells.



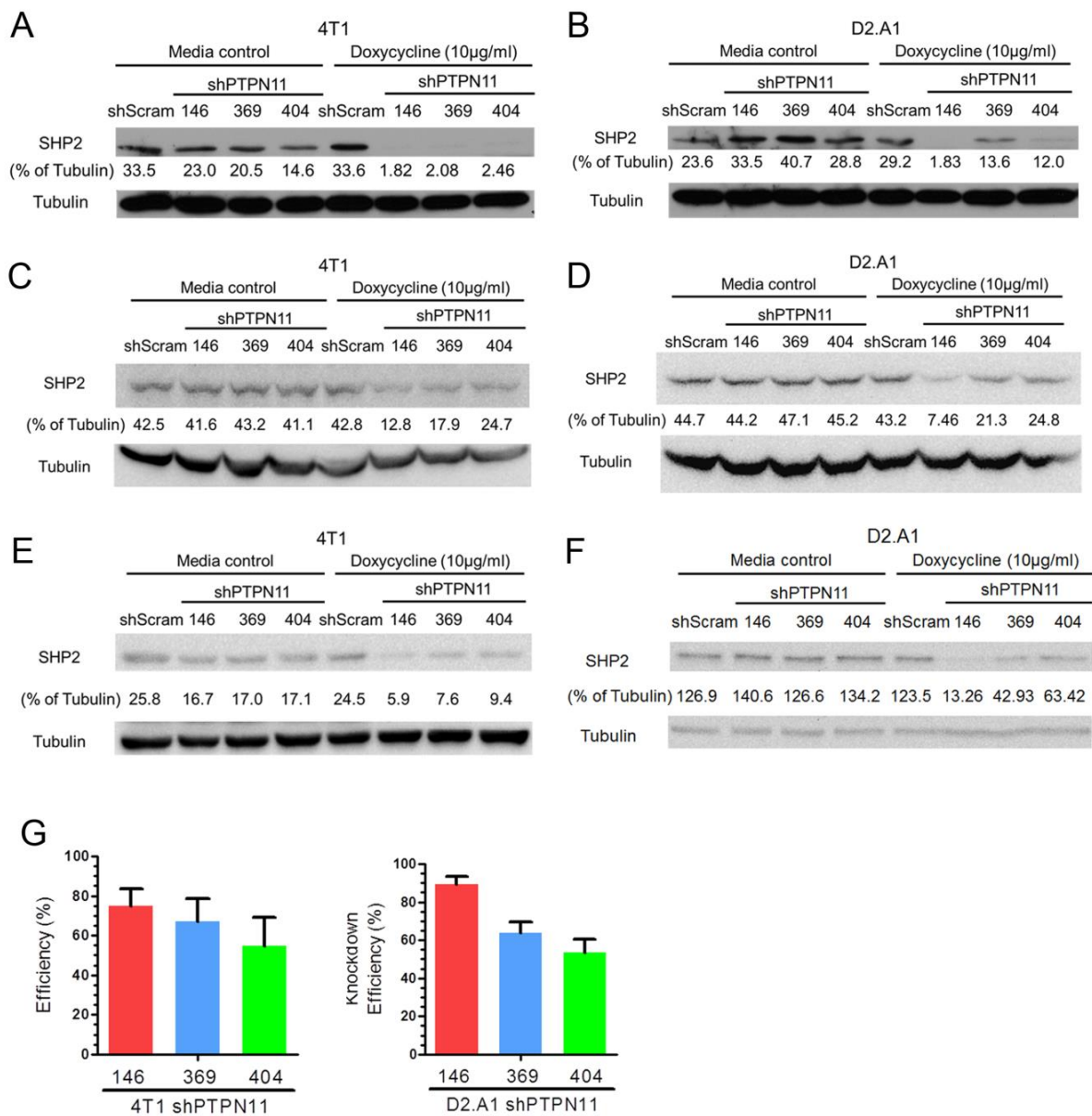


Figure 2.6. Validation of SHP2 depletion efficiencies in 4T1 and D2.A1 after sorting. A-F, Three independent repeats of immunoblot analyses with quantification for SHP2 in 4T1 cells (A, C, E) and D2.A1 cells (B, D, F) stably expressing three independent doxycycline-inducible shRNA sequences targeting PTPN11 with and without doxycycline induction, compared with scrambled (scram) shRNA controls. G, Quantification of SHP2 depletion for each shRNA construct in 4T1 and D2.A1 cells (n = 3). Depletion efficiency was defined as the percentage of SHP2 protein decrease normalized to scramble controls upon doxycycline induction.

To confirm the success of sorting, we compared the green fluorescence rates with doxycycline induction between the cells before and after sorting by flow cytometry. The percentage of GFP positive all increased in the cells after sorting compared to the ones before sorting with doxycycline induction (Figure 2.5E, 2.5F). But the induction of green fluorescence with doxycycline efficiently did not represent that SHP2 was depleted in protein levels in these cells.

To identify the successful depletion of SHP2 in protein levels and the depletion efficiency, we implemented immunoblotting of SHP2 in sorted cells in the presence or absence of doxycycline. With three individual biological repeats in 4T1 cells (Figure 2.6A, 2.6C, 2.6E) and D2.A1 cells (Figure 2.6B, 2.6D, 2.6F) and corresponding quantification normalized to Tubulin, we were able to deplete the protein levels in SHP2 by up to 79.8% in the 4T1 cells and 89.5% in the D2.A1 cells upon addition of doxycycline (Figure 2.6G). Considering the depletion efficiency shown in Figure 2.6G, we decided to continue with shPTPN11 146 and 369 in our future studies.

Next, we implemented the depletion systems to perform *in vitro* growth assays under 2D and 3D culture environments. Depletion of SHP2 significantly inhibited the growth of the 4T1 cells under both 2D and 3D culture conditions (Figure 2.7A left panel, 2.7B, 2.7C). However, the growth inhibitory effects of SHP2 depletion in D2.A1 cells were only observed under 3D culture condition, but not 2D culture condition (Figure 2.7A right panel, 2.7D, 2.7E).

These results were consistent with our findings that the 4T1 cells were more sensitive to SHP2 inhibition than D2.A1 cells under 2D culture condition (Figure 2.1A, 2.1B), and the effects of SHP2 inhibitors were enhanced under 3D culture condition compared to 2D (Figure 2.2B, 2.2C).

In summary, we confirmed the growth inhibitory effects of SHP2 inhibitors were on-target with genetic depletion of SHP2 in MBC cells. The establishment of doxycycline inducible genetic depletion system also paved the way for investigating the contributions of tumor-cell autonomous SHP2 to breast cancer metastasis.

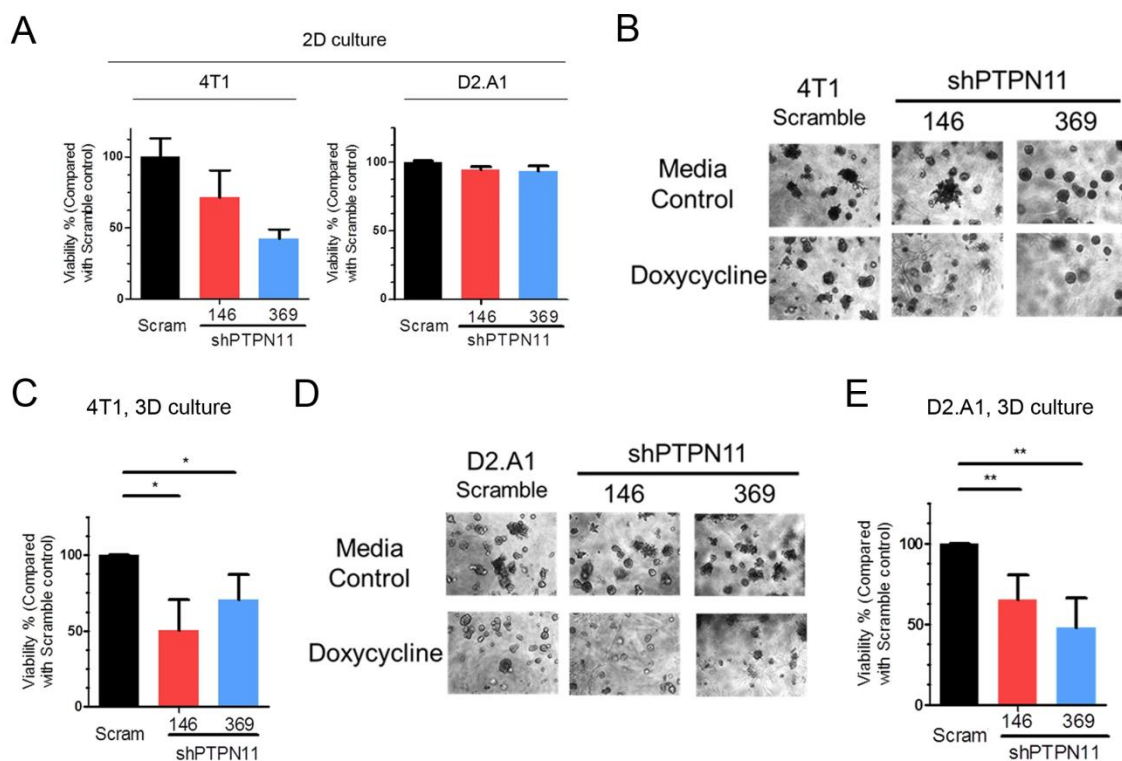


Figure 2.7. Depletion of SHP2 inhibits the growth of metastatic breast cancer cells.

A, Cell viability assays under 2D culture conditions showing differential cell viability of 4T1 and D2.A1 cells upon doxycycline-induced depletion of SHP2. Data are the mean \pm s.e.m. of two biological replicates completed in triplicate. B, Representative photos showing 3D morphologies of 4T1 cells upon depletion of SHP2. C, Quantification of differential cell viability of 4T1 cells upon depletion of SHP2. Data are shown as mean \pm s.e.m. $n = 3$, $*p < 0.05$. D, Representative photos showing 3D morphologies of D2.A1 cells upon depletion of SHP2. E, Quantification of differential cell viability of D2.A1 cells upon depletion of SHP2. Data are shown as mean \pm s.e.m. $n = 4$ for D2.A1, $**p < 0.01$.

2.4.5 SHP2 inhibitor delays the pulmonary metastasis *in vivo*

In the previous sections, we identified that inhibition of SHP2 blocked the growth of MBC cells *in vitro*. To further identify whether targeting SHP2 can inhibit metastatic tumor growth *in vivo*, we started a treatment plan of SHP099 in conjunction with the 4T1 orthotopic model of

metastasis in immunocompetent mice. We chose SHP099 as it was water-soluble, and its bioavailability had been previously reported.

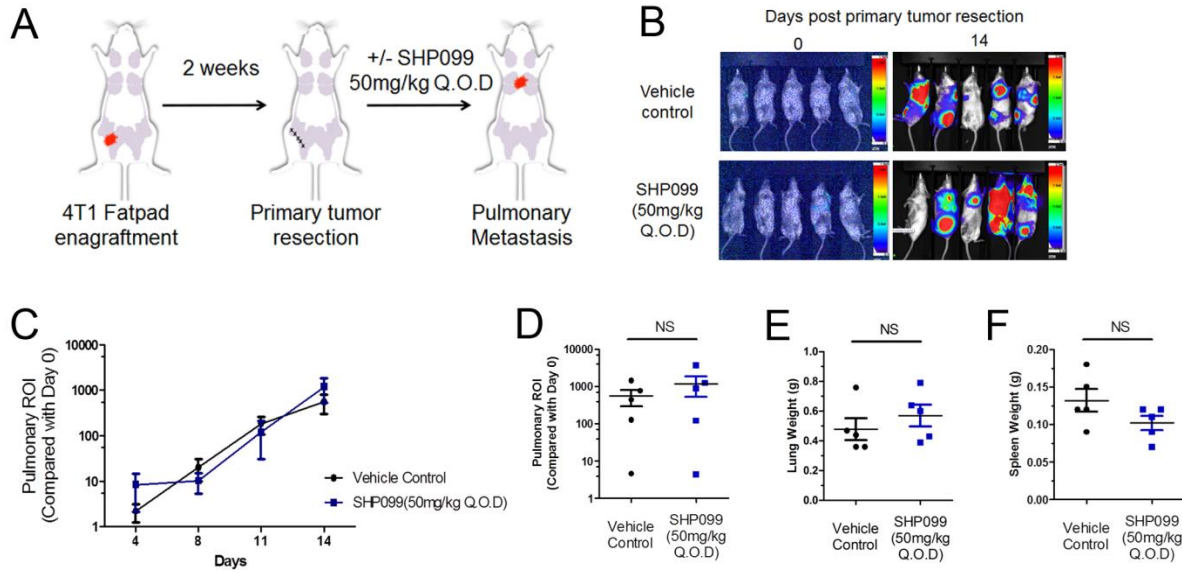


Figure 2.8. SHP099 q.o.d. at 50mg/kg fails to inhibit the 4T1 metastasis *in vivo*. A, Schematic representation of the 4T1 post-surgical model of metastasis and treatment plan of SHP099 q.o.d. at 50mg/kg. B, Representative bioluminescent images were taken on Day 0 and Day 14 of SHP099 q.o.d. treatments at 50mg/kg. C, Bioluminescence values for pulmonary regions of interest (ROI) from mice bearing 4T1 metastases normalized to values at the initiation of treatment (Day 0). Data are the mean \pm s.e.m. of 5 mice per treatment group. D, Bioluminescent values of pulmonary regions of interest (ROI) which were quantified as a measure of metastasis. Data are the ratio of luminescence values on Day 14 of treatment compared to Day 0. NS: no significance for $n = 5$ mice per group as determined by a Mann-Whitney test. E, F, Plots comparing lung weights (E) and spleen weights (F) from control and SHP099 treated mice. NS: no significance for $n = 5$ mice per group as determined by a Mann-Whitney test.

We decided to start with the dose of SHP099 at 50mg/kg once every other day (Q.O.D). As the scheme is shown, following surgical resection of the 4T1 primary tumors at mammary fat pads, systemic tumor-bearing animals were treated with SHP099 at 50mg/kg Q.O.D or vehicle via oral gavage for 2 weeks (Figure 2.8A). Bioluminescent live imaging and quantification of pulmonary regions of interest (ROI) showed that this treatment plan failed to delay the metastatic progression (Figure 2.8B, 2.8C). There was no significant difference in pulmonary ROI, lung

weights and spleen weights at the end of this study between the SHP099 group and the vehicle group (Figure 2.8D, 2.8E, 2.8F). These results indicated that SHP099 at 50mg/kg Q.O.D failed to block 4T1 metastatic progression in this model.

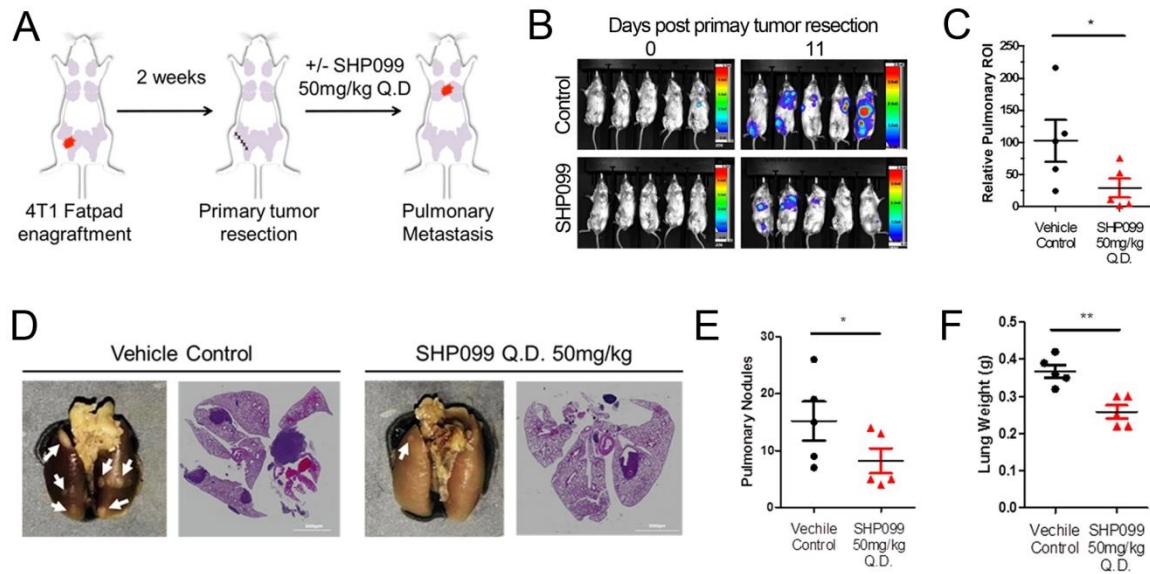


Figure 2.9. SHP099 q.d. at 50mg/kg inhibits the 4T1 metastasis *in vivo*. A, Schematic representation of the 4T1 post-surgical model of metastasis and treatment plan of SHP099 q.d. at 50mg/kg. B, Representative bioluminescent images taken at Day 0 and Day 11 of SHP099 q.d. treatments at 50mg/kg. C, Bioluminescent values of pulmonary regions of interest (ROI) which were quantified as a measure of 4T1 metastasis. Data are the ratio of luminescence values at Day 11 of treatment compared to Day 0. *p<0.05 for n = 5 mice per group as determined by a Mann-Whitney test. D, Representative photos of pulmonary metastases (White arrow heads to show the nodules) and H&E staining of pulmonary histological sections in control and SHP099 treated mice. E, F, Plots comparing pulmonary nodules (E) and spleen weights (F) from control and SHP099 treated mice. *p<0.05, **p<0.01 for n = 5 mice per group as determined by a Mann-Whitney test.

The negative data here inspired us to optimize the dose of SHP099 in the future study, and we simply increased the dose of SHP099 to 50mg/kg once every day (Q.D.) in the second trial. As the scheme is shown here, we changed the treatment plan of SHP099 to 50mg/kg Q.D. following the primary tumor resection (Figure 2.9A). Treatment at this dose led to a significant

reduction of 4T1 pulmonary metastases as determined by bioluminescent live imaging and quantification of pulmonary ROI (Figure 2.9B, 2.9C). We also observed less tumor tissue staining in the SHP099 group than the vehicle group by H&E staining of histological lung sections (Figure 2.9D). There was a significant reduction in the SHP099 group compared to the vehicle group in *ex vivo* quantification of pulmonary metastatic nodules and lung weights (Figure 2.9E, 2.9F).

In summary, systemic treatments of an allosteric SHP2 inhibitor, SHP099 could significantly reduce the MBC pulmonary metastasis *in vivo* at a certain dose. These data also indicated that optimization of the treatment plan was important for future clinical application of SHP2 inhibitors to achieve the best patient response rate.

2.4.6 SHP2 inhibitor reduces the pulmonary growth of metastatic breast cancer in vivo

The 4T1 orthotropic model was perfect to mimic the whole process of MBC metastasis, which could be delayed by SHP099. However, we were still curious about which steps of the MBC metastatic process SHP2 was involved. Hence, we chose the D2.A1 tail vein model, as this model imposed MBC cells into blood vessels and focused on the survival of circulating tumor cells (CTCs), extravasation, dissemination and pulmonary growth of MBC cells.

To further determine the efficacy of SHP2 inhibitors in the pulmonary microenvironment, we injected immunocompetent mice with D2.A1 cells via tail veins as the scheme shown. One week after tail vein engraftment, mice were again treated with SHP099 (Figure 2.10A). Consistent with the results observed in the 4T1 model, 14 days of SHP099 treatments resulted in a significant reduction in pulmonary tumor burden (Figure 2.10B, 2.10C). What's more, the 14-day SHP099 treatment period also extended the subsequent survival of mice compared to the vehicle group (Figure 2.10D).

These results confirmed the efficacy of SHP099 in blocking MBC metastasis to the lungs *in vivo*. The results also suggested that SHP2 might contribute to CTCs survival, extravasation, dissemination and growth of MBC cells in the lungs. Further studies may be necessary to determine the detailed steps could be blocked by SHP2 inhibitors.

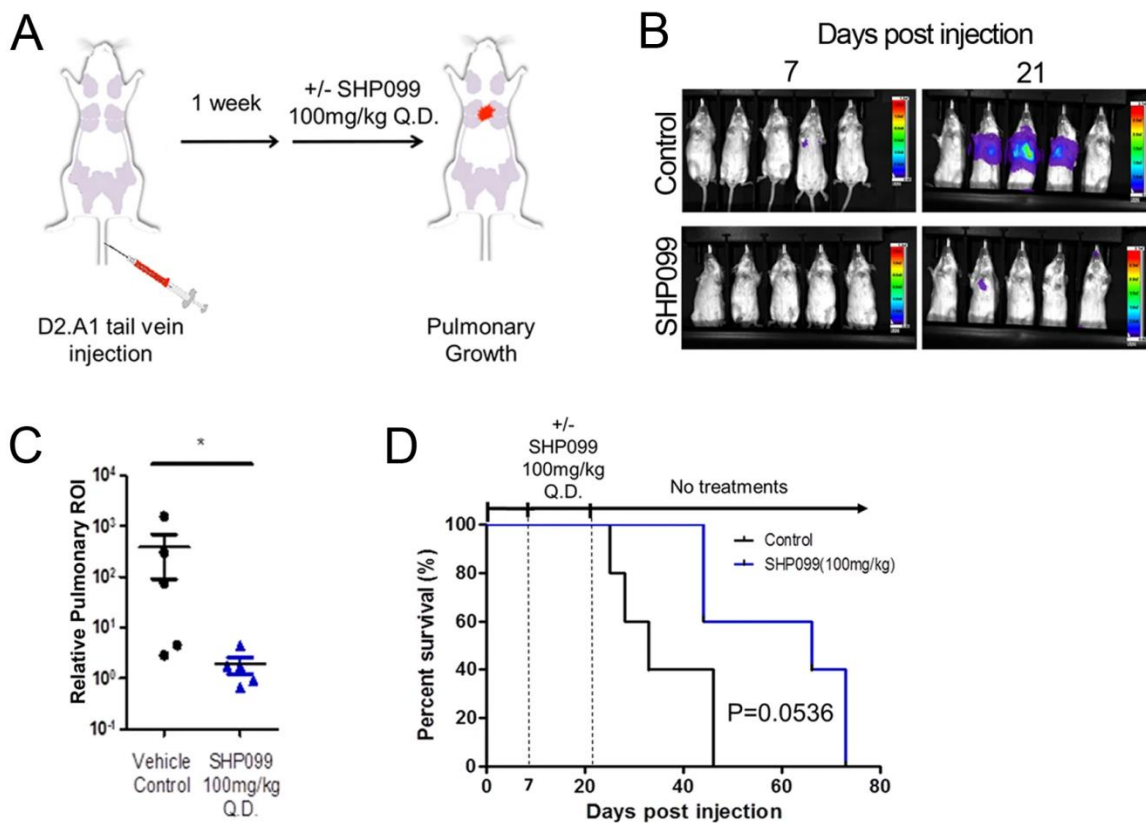


Figure 2.10. SHP099 q.d. at 100mg/kg inhibits the pulmonary growth of D2.A1 cells *in vivo*. A, Schematic of the D2.A1 model of pulmonary tumor growth and treatment plan of SHP099 q.d. at 100mg/kg. B, Representative images of pulmonary growth monitored by bioluminescence at Day 7 and Day 21 post injection. C, Bioluminescent values from pulmonary ROI quantified as the ratio of day 21 to day 7 following tumor cell injection (* $p < 0.05$ as determined by a Mann-Whitney test, $n = 5$ mice per group). D, Kaplan–Meier analyses of control and SHP099 treated mice, bearing D2.A1 pulmonary tumors, resulting in the indicated p-value ($n = 5$ mice per group).

2.5 Conclusions

In this section, we found that SHP2 inhibitors block the growth of MBC cells under 2D and 3D culture conditions. The effects of SHP2 pharmacological inhibition were confirmed with doxycycline inducible genetic depletion of SHP2. The growth inhibitory effects were enhanced

under matrix-supported 3D culture conditions with ECM signaling compared to 2D. MBC cells resistant to HER2-targeted therapies could be targeted by SHP2 inhibitors. The mechanisms were due to the blockades of signaling recovery by SHP2 inhibitors in the resistant cell lines. SHP2 inhibitors delayed the metastatic progression in the lungs *in vivo* and extended the survival of mice. These results indicate that MBC cells can be targeted by SHP2 inhibitors.

CHAPTER 3. DIVERSE SIGNALING INPUTS OF SHP2 IN METASTATIC BREAST CANCER CELLS

3.1 Disclaimer

The material in this chapter was published in a peer-reviewed journal *Oncogene* in 2020. The citation information for the article is listed below. The article is open access and licensed under a Creative Commons Attribution 4.0 International License.

Chen, H., Libring, S., Ruddraraju, K.V. et al. SHP2 is a multifunctional therapeutic target in drug resistant metastatic breast cancer. *Oncogene* 39, 7166–7180 (2020).

3.2 Introduction

RTKs and ECM signaling pathways are the major drivers of MBC. To regulate the signaling network efficiently, the MBC cells should have signaling nodes, which are shared by these two signaling pathways. SHP2 is involved in the regulation of multiple RTKs signaling and the key component in the signaling complex downstream of RTKs, but the biochemical details are not fully understood. As we observed the effects of SHP2 inhibitors to block the growth of MBC cells were enhanced in 3D culture conditions compared to 2D, the enhancement suggests the involvement of ECM signaling in SHP2-mediated signaling pathways of growth and survival. Phosphorylation of SHP2 at Y542 has been reported as a key phosphorylation site required for full MAPK signaling activation upon induction by several growth factors [93]. However, the clinical significance of phosphorylation of SHP2 at Y542 and how it is regulated under ECM signaling under a 3D culture environment are not determined. The signaling inputs of SHP2 remain one of the knowledge gaps in understanding the role of SHP2 in MBC.

Herein, we demonstrate the correlation between phosphorylation of SHP2 at Y542 and survival rates of breast cancer patients. We show the induction of SHP2 phosphorylation under multiple growth factors in a time-dependent transient manner. We also identify that SHP2 becomes phosphorylated through ECM signaling, correlating with enhanced efficacy of SHP2 inhibitors in 3D growth environments as compared to traditional 2D culture. Finally, with Src and FAK inhibitors, we show differential activation mechanisms of SHP2 phosphorylation under RTKs and ECM signaling.

3.3 Materials and Methods

3.3.1 Cell lines, culture conditions, drug and reagents

The sources and culture conditions for 4T1, D2.A1, BT549, HME2-PAR, and HME2-LAPR cells were previously described in chapter 2. The detailed information for cell lines and culture conditions can also be found in APPENDIX A Table A.1.

The sources and preparation methods for 11a-1, SHP099, FIIN4, Cultrex and luciferin were previously described in chapter 2. A Src inhibitor, PP2 was purchased from Selleck and reconstituted in DMSO to 10mM stock. A FAK inhibitor, PF-562,271 (PF271) was purchased under agreement from Pfizer Inc. and reconstituted in DMSO to 10mM stock. All these constituted drugs were aliquoted and stored at -80 °C. Human basic fibroblast growth factor (FGF2) and epidermal growth factor (EGF) were purchased from GoldBio and reconstituted according to manufacturer's instruction. Human platelet-derived growth factor (PDGF), mouse hepatocyte growth factor (hGF) and vascular endothelial growth factor (VEGF) were purchased from R&D systems and reconstituted according to the manufacturer's instructions. The master stock concentration for FGF2 and EGF was 200µg/ml. The master stock concentration for PDGF, hGF and VEGF was 100µg/ml. The master stocks were diluted to working stocks at 2µg/ml, aliquoted and stored at -20 °C. The working stocks were considered single-use to avoid any freeze-thaw cycle that reducing the efficacy of growth factors. The detailed information for these drugs and reagents can also be found in APPENDIX A Table A.3.

3.3.2 Clinical dataset analysis

The mRNA, Reverse Phase Protein Array (RPPA) and clinical outcomes raw data from Breast Invasive Carcinoma (BRCA) cohort of the Cancer Genome Atlas (TCGA) were downloaded from FireBrowse (www.firebrowse.org, Broad Institute of MIT and Harvard, MA). The RPPA data were first input into R, and the correlation plot of different genes was generated using the “corrplot” R package. To analyze patient survival, we set 1500 days as the threshold of survival and then selected data from non-living patients. The patients were separated into two groups based on median values of SHP2 phosphorylation levels at Y542 and SHP2 expression levels. Finally, the survival curves were created by GraphPad Prism 5.0, and analyzed via a

log-rank test. The detailed step-by-step methods and the R scripts for the correlation plot and data cleaning are included in APPENDIX B.

3.3.3 Immunoblotting for samples under different culture conditions

To identify the phosphorylation of SHP2 and expression levels of growth factor receptors in different MBC cells, the HME2-PAR, HME2-LAPR, 4T1, D2.A1 and BT549 cells were seeded in 12-well flat-bottom plate before harvesting for lysis. The immunoblotting to detect the expression levels of FGFR1, p-SHP2, SHP2, PDGFR α , PDGFR β , C-Met, EGFR, Tubulin and GAPDH was performed according to the protocol described in chapter 2. SHP2 and GAPDH antibodies were purchased from Santa Cruz Biotechnology, and Tubulin antibody was purchased from Developmental Studies Hybridoma Bank (DHSB) in Iowa City, IA. The other antibodies here were bought from Cell Signaling Technology (CST). The detailed information for these antibodies can also be found in APPENDIX A Table A.6.

In the growth factor-induced signaling assays, the D2.A1 and BT549 cells were seeded as single layers in 12-well flat-bottom plates overnight. The cells were washed twice with 1ml/well serum-free media to remove any residual serum. The cells were cultured in serum-free media for 24 hours to synchronize. If there were pretreatments, the drugs were prepared with serum-free media (PP2 at 10 μ M and PF271 at 2.5 μ M) and added to the cell in this synchronization step. Vehicle at the same volume was used as a control in the pretreatment step. After 24 hours of synchronization and pretreatments, the cells were then stimulated with FGF2 (20 ng/ml), PDGF (100 ng/ml), hGF (50 ng/ml), VEGF (100 ng/ml), and EGF (50 ng/ml) for 5 minutes or different periods in the time course stimulation. The cells were harvested for lysis immediately after stimulation. The immunoblotting to detect the expression levels of p-ERK, ERK, p-SHP2, SHP2, Tubulin and GAPDH was performed according to the protocol described in chapter 2. The information of these antibodies was described above and APPENDIX A Table A.3.

To identify the protein expression levels in the cells under 3D culture conditions, the 24-well flat bottom plate was coated with 120 μ L 80% Cultrex. The plate was incubated in the tissue culture incubator for at least 30 minutes to allow the gel to solidify. The 4T1 and D2.A1 cells were seeded in the plate with 5% Cultrex. The media was refreshed every 4 days, and the cells were harvested at the end of the study. To get rid of the gel in harvesting the cells, the plate was first stored at 4 $^{\circ}$ C for 30min, and the gel became liquids in low temperature. The pallets

were next centrifuged and the supernatants containing the gel were removed. The pallets were washed twice with iced PBS to remove any residue gel, serum and media. Finally, RIPA lysis buffer was added to the pallets, and the samples were moved to the standard immunoblotting protocol described in chapter 2. The levels of p-FAK, FAK, p-SHP2 and SHP2 were probed in the immunoblotting. The FAK antibody was bought from Invitrogen, and the other antibodies here were bought from Cell Signaling Technology (CST). The information on these antibodies was described above and APPENDIX A Table A.6.

In the immunoblotting with a tessellated scaffold culture system, the fibronectin-coated scaffolds were prepared as previously described [129]. The cells were grown on scaffolds for 16 days, and treated with inhibitors for 24 hours before harvesting. To harvest the cells from the scaffolds, the cells were dissociated with Trypsin solution (Gibco) in cell culture incubator. The dissociation was terminated with full growth media, and the cell suspension was transferred to tubes. The pallets were collected by centrifuge, and washed twice with ice-cold PBS before adding RIPA lysis buffer. The samples were then moved to the standard immunoblotting protocol described in chapter 2. The levels of p-FAK, FAK, p-Src (Y416), p-Src (Y527), Src p-SHP2 and SHP2 were probed in the immunoblotting. The FAK antibody was bought from Invitrogen, and the other antibodies here were bought from Cell Signaling Technology (CST). The information on these antibodies was described above and APPENDIX A Table A.6.

3.3.4 Cell viability assays with growth factors

The standard protocols for cell viability assays under 2D and 3D culture conditions were described in chapter 2. Specifically, in the cell viability assays with growth factors, the D2.A1 cell growth was induced by the addition of exogenous FGF2, PDGF, and hGF for 6 days under 2D and 3D culture conditions as described in chapter 2. The treatments were added together with the growth factors at the beginning of the assays as day 0. With the D2.A1 cells expressing doxycycline inducible shRNAs targeting PTPN11, the cells, together as the shScramble control, were treated with doxycycline in the presence of FGF2, hGF, or PDGF as indicated under 2D and 3D culture conditions. The cell viability was determined by luminescence reading relative to day 0 as described. The bar graphs and statistical analysis were created and performed with GraphPad Prism 5.0.

3.3.5 Tumor sphere assays under 3D culture conditions

The 3D tumor sphere assay was performed as we introduced previously [132]. The D2.A1 cells and HME2-LAPR cells were seeded in ultra-low attachment round bottom plate (Corning). These cells formed large multicellular spheres after a few days. Then, the cells were transferred to a 96-well flat-bottom plate coated with 80% Cultrex as previously described in cell viability assays under 3D culture conditions. Growth factors and drug treatments were added the next day following the transfer of spheres. The photos of the spheres were taken immediately under the microscope at the beginning of treatments as day 0. The spheres were monitored and recorded with photos every 3 days, and the media was refreshed. The area that tumor spheres occupied was quantified by ImageJ 1.52a (NIH). The tumor sphere growth and invasion rate were defined as the area of spheres on day 9 relative to the one on day 0.

3.3.6 Statistical analysis

A student's t-test was used for comparing differences between two groups of measurements with GraphPad Prism 5.0 software. Error bars show the standard error of the mean. The area of spheres was quantified with ImageJ 1.52a (NIH).

3.4 Results

3.4.1 Phosphorylation of SHP2 at Y542 is a key signaling readout with clinical significance

In the previous chapter, we found that HME2-LAPR cells were more sensitive to SHP2 inhibitors than HME2-Par cells due to the delayed signaling recovery events. HME2-LAPR cells had a mesenchymal phenotype with overexpression of several ECM proteins [72]. However, the detailed mechanisms by which SHP2 inhibitors targeted HME2-LAPR cells were not fully understood. As we had discussed that phosphorylation of SHP2 at Y542 was important for its activation and signaling cascades, we hypothesized that elevated phosphorylation of SHP2 at Y542 might also drive resistance to ErbB-targeted therapies and promote MBC progression.

To test our hypothesis here, we checked the levels of phosphorylation of SHP2 at Y542 in both HME2-Par cells and HME2-LAPR cells by immunoblotting. We found that HME2-LAPR displayed an elevated level of phosphorylation of SHP2 at Y542, and an equal level of total

SHP2 compared to HME2-Par (Figure 3.1A). Furthermore, we observed overexpression of FGFR1 in HME2-LAPR cells compared to HME2-Par cells (Figure 3.1A). These results indicated that elevated phosphorylation of SHP2 at Y542 was acquired together with resistance to ErbB-targeted therapies. In contrast, expression levels of SHP2 were not closely related to the acquired resistance. Growth factor receptor signaling, such as FGFR1, might be responsible for the elevation of SHP2 phosphorylation. To further explore the clinical significance of phosphorylation of SHP2 at Y542, we analyzed the TCGA datasets. The analysis showed that differential expression levels of SHP2 failed to predict breast cancer patient survival, but elevated phosphorylation of SHP2 at Y542 was associated with decreased breast cancer patient survival with statistical significance (Figure 3.1B).

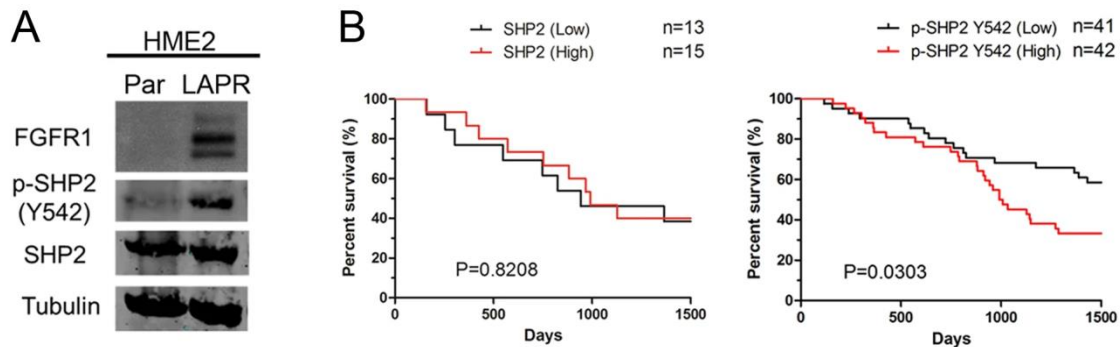


Figure 3.1. Phosphorylation of SHP2 at Y542 is elevated in drug resistant breast cancer cells and has clinical significance. A, Immunoblotting showing differential expression of FGFR1 and phosphorylation of SHP2 at Y542 in HME2-LAPR cells compared to HME2-Par cells. B, Kaplan–Meier analyses of patients from The Cancer Genome Atlas Program (TCGA) breast cancer cohort separated into two groups based on the median mRNA expression value of SHP2 (left) or median phosphorylation level of SHP2 at Y542 (right). Overall survival between the two groups was compared by a log-rank test resulting in the indicated p-values.

To sum up, in this section, we identified phosphorylation of SHP2 at Y542, but not the expression level of SHP2, was elevated in drug resistant MBC cells. Differential levels of phosphorylation of SHP2 at Y542 also predicted breast cancer patient survival. Because FGFR1 and ECM proteins were also overexpressed at the same time, we decided to implement phosphorylation of SHP2 at Y542 as a key signaling readout of these signaling inputs with

clinical significance. The next step was to investigate the detailed signaling inputs and the mechanisms of SHP2 phosphorylation.

3.4.2 Phosphorylation of SHP2 at Y542 is induced by multiple growth factors

As the levels of phosphorylation of SHP2 and FGFR1 were both increased in the HME2-LAPR, we thought that there might be a correlation between SHP2 and growth factor receptor signaling. In chapter 1, we discussed that growth factors and corresponding RTKs signaling pathways were involved in resistance and metastasis. Hence, we started to investigate whether SHP2 facilitates proliferative signaling from multiple RTKs as signaling inputs in MBC cells. To determine the abilities of multiple growth factors to induce phosphorylation of SHP2, we first detected the expression levels of their cognate RTKs in several MBC cell lines by immunoblotting. We found that FGFR1 was detected in D2.A1, BT549 and HME2-LAPR cells, PDGFR β was detected in D2.A1 cells; while c-Met and EGFR were detected in BT549, HME2-Par and HME2-LAPR cells (Figure 3.2A). Although these MBC cells had diverse expressions level of multiple RTKs, the expression of most RTKs was detectable in D2.A1 and BT549. Thus, we decided to implement D2.A1 and BT549 in the growth factor induction studies.

To investigate the SHP2-dependent signaling events downstream of RTKs, we next treated D2.A1 cells with multiple growth factors in serum-free condition for 5 minutes. We found that transient addition of FGF2, PDGF and hGF, but not VEGF or EGF, induced phosphorylation of SHP2 at Y542 and downstream phosphorylation of ERK1/2 in D2.A1 cells (Figure 3.2B). As we considered that fact that detecting dynamic phosphorylation events could be difficult to interpret and translate into differences observed in patient samples, we also emphasized the dynamics of SHP2 phosphorylation upon growth factor stimulation. We implemented time courses growth factor treatments in D2.A1 cells that demonstrated the transient nature of growth-factor-induced SHP2 phosphorylation. The D2.A1 cells were treated with FGF2, PDGF and hGF for 5, 10, 30, 60 and 120 minutes, respectively. With FGF2 induction, the phosphorylation of SHP2 remained to be elevated for 120 minutes, but the phosphorylation of ERK1/2 attenuated 30 minutes after induction in D2.A1 cells (Figure 3.2C). While, with PDGF induction, both phosphorylation of SHP2 and ERK1/2 sharply decreased 10 minutes after induction in D2.A1 cells (Figure 3.2D). With hGF induction in D2.A1 cells, both phosphorylation of SHP2 and ERK1/2 reached the peak at 30 minutes after induction, and decreased later (Figure 3.2E).

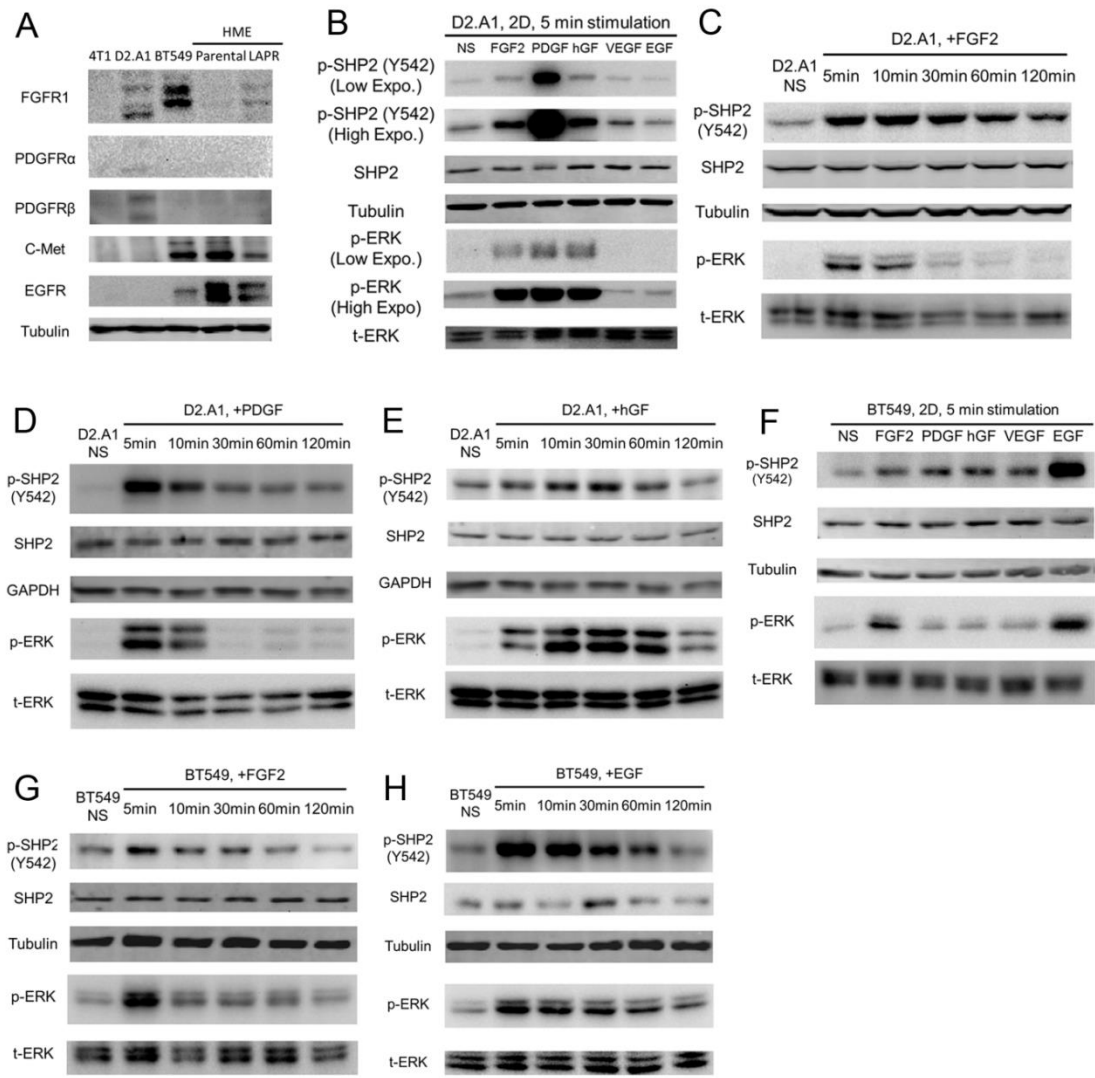


Figure 3.2. Phosphorylation of SHP2 at Y542 is elevated with multiple growth factors induction in MBC cells. A, Immunoblotting showing the expression levels of FGFR1, PDGFR α , PDGFR β , C-MET, and EGFR in the 4T1, D2.A1, BT549, HME2-Par and HME2-LAPR cells. B, Immunoblotting showing the phosphorylation of SHP2 at Y542 and ERK1/2 (ERK) induced by the indicated growth factors (FGF2, PDGF, hGF, VEGF and EGF) for 5 minutes in D2.A1 cells. C-E, Immunoblotting showing differential phosphorylation of SHP2 at Y542 and ERK1/2 (ERK) in D2.A1 cells induced by addition of exogenous FGF2 (C), PDGF (D) and hGF (E) in 2D culture conditions for the indicated amounts of time. F, Immunoblotting showing the phosphorylation of SHP2 at Y542 and ERK1/2 (ERK) induced by the indicated growth factors (FGF2, PDGF, hGF, VEGF and EGF) for 5 minutes in BT549 cells. G, H, Immunoblotting showing differential phosphorylation of SHP2 at Y542 and ERK1/2 (ERK) in BT549 cells induced by addition of exogenous FGF2 (G) and EGF (H) in 2D culture conditions for the indicated amounts of time.

Then, we made the same treatments in BT549 cells. Five-minute stimulation of FGF2 and EGF, but not the other growth factors, induced the phosphorylation of SHP2 at Y542 and ERK1/2 in BT549 cells (Figure 3.2F). With the time courses growth factor treatments, we found that phosphorylation of SHP2 and ERK1/2 maxed out at 5 minutes after the induction and sharply reduced in BT549 cells (Figure 3.2G). Meanwhile, the phosphorylation of SHP2 and ERK1/2 remained to be elevated for 60 minutes with EGF induction in BT549 cells (Figure 3.2H).

In summary, the data in this section indicated that phosphorylation of SHP2 at Y542 could be induced by multiple growth factors in several MBC cells. Thus, RTKs signaling induced by multiple growth factors was one of the signaling inputs of SHP2. Phosphorylation of ERK1/2 was also elevated together with phosphorylation of SHP2, as one of the downstream signaling outputs. It was also important to pinpoint that the induction of SHP2 and ERK1/2 phosphorylation was not necessarily correlated with the expression of RTKs in these MBC cells. Moreover, the induction of SHP2 and ERK1/2 was transient and dynamic upon induction, and the elevated phosphorylation could go back to the baseline within 2 hours. The time for the phosphorylation to reach peak upon induction varied among different growth factors. Phosphorylation of ERK1/2 could remain elevated even when phosphorylation of SHP2 was reduced to the baseline. Finally, not all the growth factors could induce phosphorylation of SHP2 and ERK1/2, and which growth factors could do so varied among different MBC cells.

3.4.3 Growth factor induced growth of MBC cells depends on SHP2

In the previous section, we determined that RTKs signaling was one of the signaling inputs of SHP2. However, whether the signaling cascades from RTKs signaling through SHP2 contributed to the growth of MBC remained to be determined.

We first started the 2D culture in D2.A1 cells with different growth factors. We found that FGF2 and hGF significantly induced the growth of D2.A1 cells under 2D culture condition, but not PDGF (Figure 3.3A).

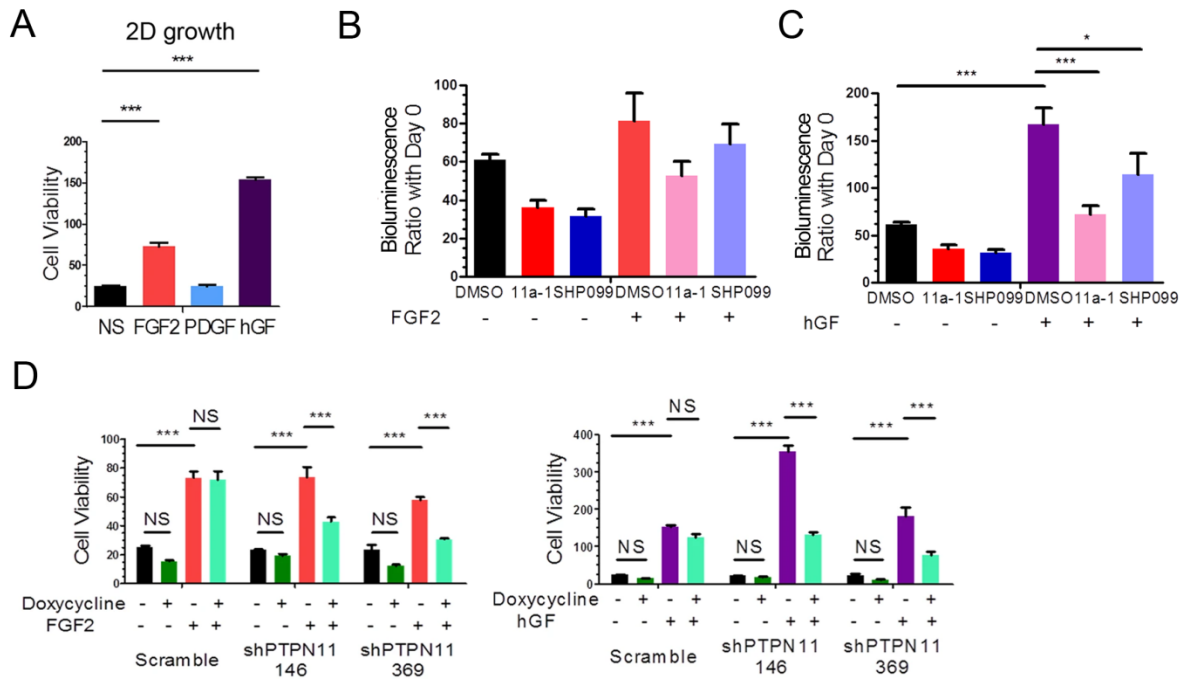


Figure 3.3. SHP2 inhibition and depletion block the growth of D2.A1 cells under 2D culture conditions. A, Cell viability assays under 2D culture conditions in which D2.A1 cells were induced by addition of exogenous FGF2, PDGF, and hGF for 6 days. B, C, Cell viability assays under 2D culture conditions in which D2.A1 cells were stimulated with FGF2 (B) or hGF (C) in the presence or absence of SHP2 inhibitors. D, Cell viability assays under 2D culture conditions in which D2.A1 cells expressing doxycycline inducible shRNAs targeting PTPN11 and Scramble control were treated with doxycycline in the presence of FGF2 and hGF as indicated. In all panels, data are the mean \pm s.e.m. for at least three independent assays resulting in NS as no significance, * $p < 0.05$, *** $p < 0.001$, determined by a student's t-test.

We next treated the D2.A1 with SHP2 inhibitors in the presence of FGF2 and hGF. The growth of D2.A1 cells induced by FGF2 was reduced by both 11a-1 and SHP099 (Figure 3.3B). Meanwhile, the growth of D2.A1 cells induced by hGF was significantly blocked by 11a-1 and SHP099 (Figure 3.3C). The growth inhibitory effects under 2D culture conditions were confirmed on-target by D2. A1 cells with doxycycline-inducible depletion of SHP2, as doxycycline treatments significantly reduced the growth in the cells with SHP2 depletion but not scramble control (Figure 3.3D).

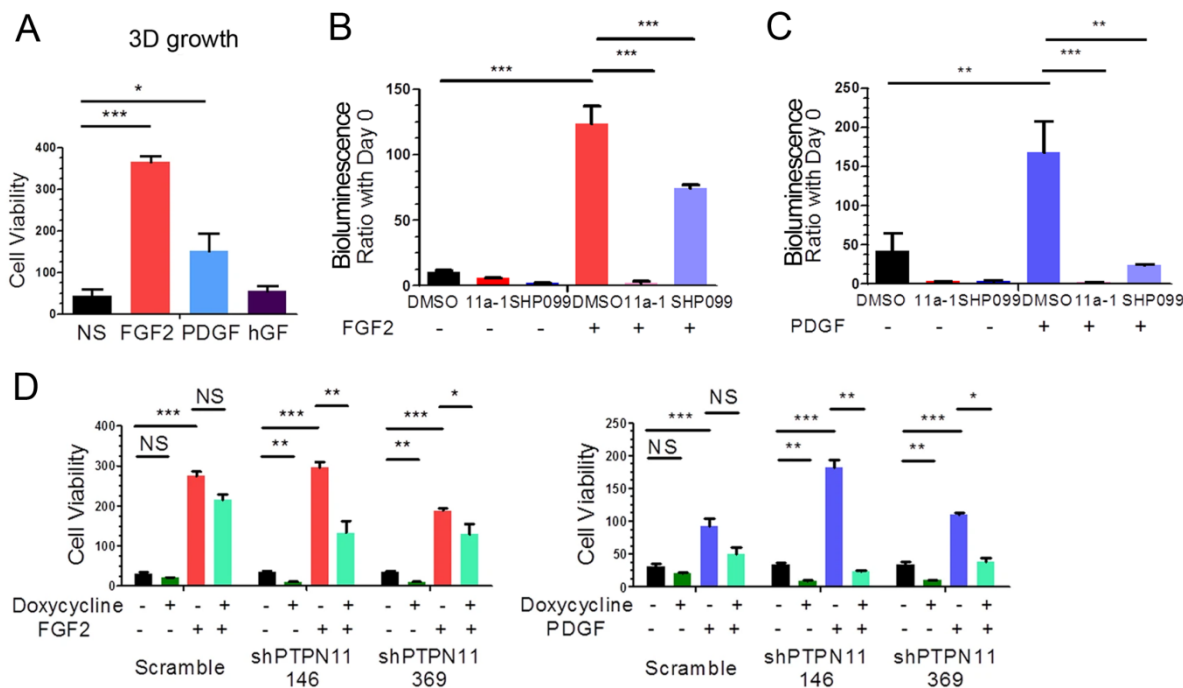


Figure 3.4. SHP2 inhibition and depletion block the growth of D2.A1 cells under 3D culture conditions. A, Cell viability assays under 3D culture conditions in which D2.A1 cells were induced by addition of exogenous FGF2, PDGF, and hGF. B, C, Cell viability assays under 3D culture conditions in which D2.A1 cells were stimulated with FGF2 (B) or PDGF (C) in the presence or absence of SHP2 inhibitors. D, Cell viability assays under 3D culture conditions in which D2.A1 cells expressing doxycycline inducible shRNAs targeting PTPN11 and Scramble control were treated with doxycycline in the presence of FGF2 and PDGF as indicated. In all panels, data are the mean \pm s.e.m. for at least three independent assays resulting in NS as no significance, * $p < 0.05$, ** $p < 0.01$, *** $p < 0.001$, determined by a student's t test.

As we had already introduced 3D culture condition to our studies in chapter 2, we copied the similar treatment plans above to the D2.A1 cells under 3D culture condition. Strikingly, not as we expected, FGF2 and PDGF significantly induced the growth of D2.A1 cells under 3D culture condition, but not hGF (Figure 3.4A). The growth of D2.A1 cells induced by FGF2 and PDGF under 3D culture was significantly blocked by 11a-1 and SHP099 (Figure 3.4B, 3.4C). Consistent with the results in Chapter 2, the growth inhibitory effects were also enhanced under 3D culture conditions compared to 2D. The growth inhibitory effects under the 3D culture conditions were also confirmed on-target by D2. A1 cells with doxycycline-inducible depletion of SHP2 (Figure 3.4D).

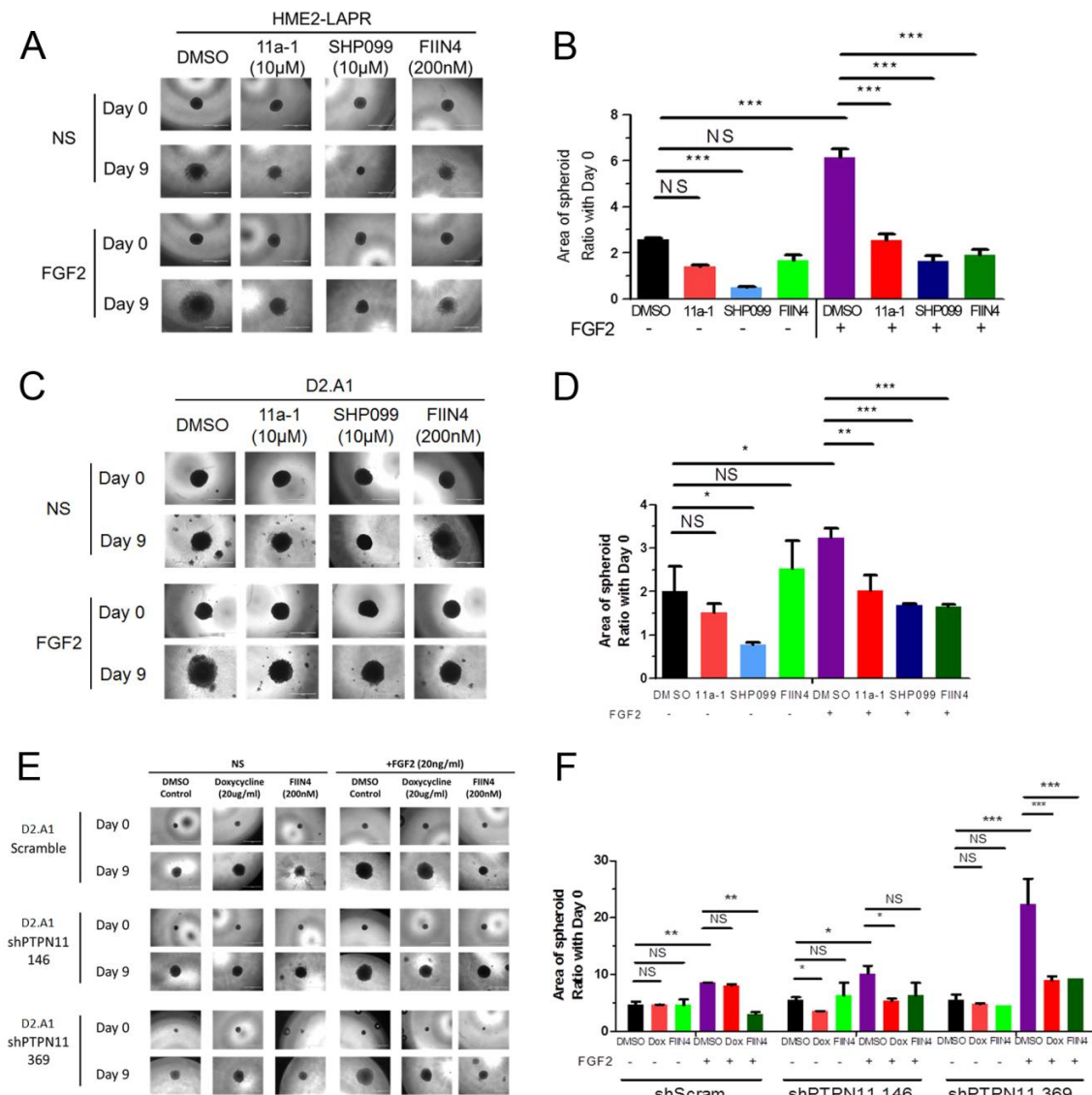


Figure 3.5. SHP2 inhibition and depletion block the growth of tumor spheres induced by FGF2. A-D, HME2-LAPR (A, B) and D2.A1 (C, D) spheres were formed in a round bottom plate and then plated onto a bed of gel matrix in the presence of the indicated concentrations of SHP2 or FGFR inhibitors. The growth of spheres was further induced by the addition of exogenous FGF2 at 20ng/ml. The area of the sphere 9 days after placement on the ECM was measured from the photos (A, C), and these values were normalized to the initial sphere size on Day 0 (B, D). E, F, D2.A1 spheres expressing doxycycline inducible shRNAs targeting PTPN11 and Scramble control were treated with doxycycline in the presence of FGF2. The area of the sphere 9 days after placement on the ECM was measured from the photos (E), and these values were normalized to the initial sphere size on Day 0 (F). In all panels, data are the mean \pm s.e.m. (n = 3), NS as no significance, *p < 0.05, **p < 0.01, ***p < 0.001.

With the results above, we found that among all the growth factors which could induce the phosphorylation of SHP2 at Y542, only FGF2 significantly induced the growth of D2.A1 under both 2D and 3D culture conditions. Hence, we then focused on HME2-LAPR cells as FGFR1 was overexpressed compared to HME2-Par cells. We hypothesized that SHP2 might contribute to FGFR signaling cascades in HME2-LAPR to induce its growth and signaling recovery events with FGF2 stimulation. Unfortunately, HME2-LAPR cells were much more mesenchymal compared to 4T1 and D2.A1 cells, and they grew poorly under 3D culture conditions. To still test our hypothesis under 3D culture environment, we used a 3D tumor sphere assay as we recently described [132]. This two-step assay started with forming a large multicellular sphere of tumor cells using an ultra-low attachment round bottom plate, and followed by transferring the sphere to ECM to allow tumor growth and invasion. The growth of HME2-LAPR spheres was significantly increased FGF2, which was abolished by SHP2 inhibitors, or direct targeting of FGFR kinase activity with FIIN4 as a control (Figure 3.5A, 3.5B). We also observed similar results in D2.A1 cells (Figure 3.5C, 3.5D), which was consistent with the results in 2D and 3D culture conditions. The growth inhibitory effects in 3D tumor sphere assays were also confirmed on-target by D2. A1 cells with doxycycline-inducible depletion of SHP2 (Figure 3.5E, 3.5F).

In this section, the take-home message was that SHP2 contributed to the growth-factor-induced growth of MBC cells under both 2D and 3D culture conditions. One of the signaling inputs of SHP2, RTKs signaling, had oncogenic outcomes via promoting the growth of MBC cells, which could be targeted by SHP2 inhibitors and genetic depletion of SHP2.

3.4.4 Phosphorylation of SHP2 at Y542 is induced by three dimensional culture environments

When analyzing the results in the previous section, we noticed that doxycycline induced depletion of SHP2 significantly reduced the growth of D2.A1 cells even without growth factor induction under 3D culture conditions, but not 2D (Figure 3.3D, 3.4D). The results also matched with our conclusion in Chapter 2 that the growth inhibitory effects of SHP2 inhibitors were enhanced under 3D culture conditions. Thus, we thought that 3D culture environments with ECM matrix might also be one of the signaling inputs of SHP2 and induce the phosphorylation of SHP2 at Y542.

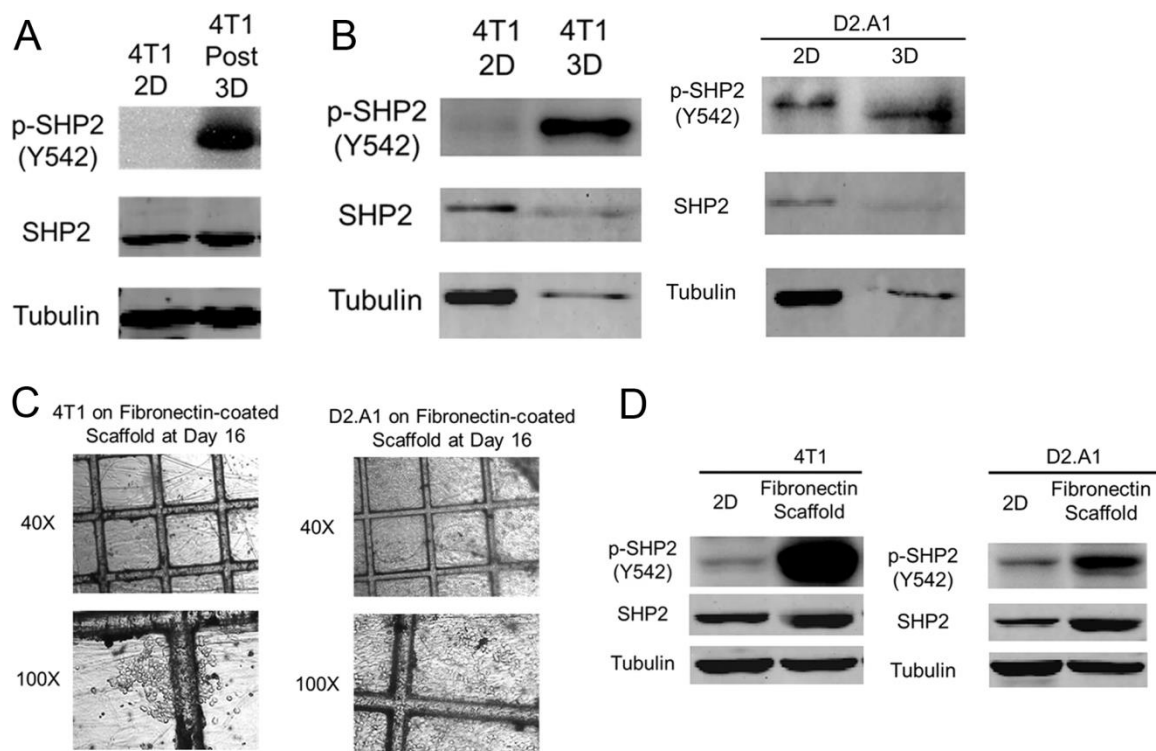


Figure 3.6. Phosphorylation of SHP2 at Y542 is elevated in the MBC cells under 3D culture conditions compared to 2D. A, Immunoblotting showing differential phosphorylation of SHP2 at Y542 in 4T1 cells following 3D culture conditions (post 3D) compared to 2D. B, Immunoblotting showing differential phosphorylation of SHP2 at Y542 in 4T1 cells (left) and D2.A1 cells (right) lysed directly from gel-based 3D culture compared to 2D. C, Representative photomicrographs showing 4T1 cells (left) and D2.A1 cells (right) cultured on fibronectin-coated tessellated scaffolds. D, Immunoblotting showing differential phosphorylation of SHP2 at Y542 in 4T1 cells (left) and D2.A1 cells (right) cultured on fibronectin-coated scaffolds as compared to 2D.

To test our hypothesis, we first shifted the 4T1 cells under 3D culture conditions back to 2D conditions, and established a ‘post 3D’ cell line. We found that phosphorylation of SHP2 at Y542 was elevated in the 4T1 post 3D cell line compared to 2D (Figure 3.6A). Next, we tried to lysate the cells directly from the 3D culture, regardless of the disruption of gel in the system. Although the protein concentrations of the lysates from 3D culture were significantly lower than 2D, it was clear that phosphorylation of SHP2 at Y542 was induced under 3D culture conditions in both 4T1 and D2.A1 cells (Figure 3.6B). To get rid of the disruption from the gel during immunoblotting, we utilized our recently developed tessellated scaffold system, in which the

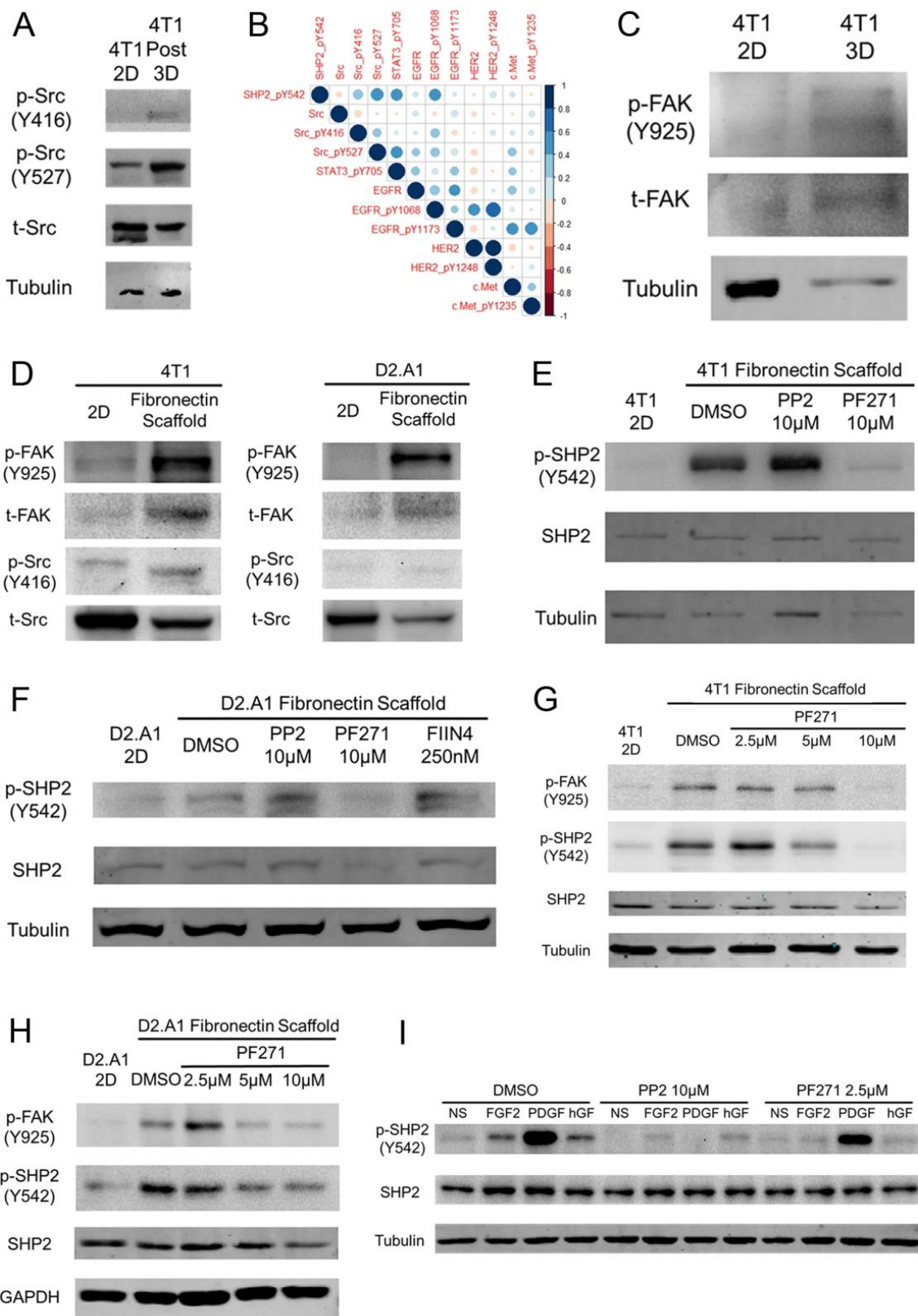
ECM matrix was created as fibular networks, instead of the globular forms in gel-based 3D culture system to better mimic *in vivo* conditions [129]. We found that the system was more suitable for signaling analyses, as the 4T1 and D2.A1 cells could grow on the fibronectin-coated scaffolds for up to 16 days in the absence of gel, which allowed for more efficient cell recovery (Figure 3.6C). Phosphorylation of SHP2 at Y542 in 4T1 and D2.A1 cells was elevated when cultured on the fibronectin-coated scaffolds (Figure 3.6D).

These results in this section suggested that 3D culture environments with ECM matrix induced the phosphorylation of SHP2 at Y542. The activation of ECM signaling with 3D culture environments was one of the signaling inputs besides multiple RTKs. The detailed mechanisms by which SHP2 was phosphorylated under these two signaling inputs remained to be uncovered.

3.4.5 The induction of phosphorylation of SHP2 at Y542 depends on differential mechanisms

To figure out the detailed mechanisms of SHP2 phosphorylation, we focused on the comparison of signaling molecules between 2D and 3D culture conditions. We found that phosphorylation of Src at Y416 (activation of Src) was elevated in the 4T1 post 3D cell line compared to 2D (Figure 3.7A). Although the phosphorylation of Src at Y527 (inhibitory of Src) was also elevated, we thought the reduction of this phosphorylation site might be dynamic, which was not observed in post 3D condition. Further analysis of the TCGA dataset also demonstrated a positive correlation between phosphorylation of SHP2 at Y542 and phosphorylation of EGFR, STAT3, and Src (Figure 3.7B). Next, we also identified phosphorylation of FAK at Y925 was induced in 4T1 cells under 3D culture conditions compared to 2D (Figure 3.7C). Similar results were confirmed with 4T1 and D2.A1 cultured on fibronectin-coated scaffolds (Figure 3.7D). Next, we utilized a Src inhibitor, PP2 and a FAK inhibitor, PF-562271 (PF271) to identify the roles of these kinases in SHP2 phosphorylation under these two signaling inputs. In the 4T1 cells cultured on fibronectin-coated scaffolds, the phosphorylation of SHP2 at Y542 could be abolished by the addition of PF271, but not by PP2 (Figure 3.7E). Similar results were also observed in the D2.A1 cells cultured on fibronectin scaffolds (Figure 3.7F). It was also worthwhile to pinpoint that the FGFR inhibitor, FIIN4 failed to block the phosphorylation of SHP2 at Y542 induced under fibronectin-coated scaffolds, indicating that FGFR signaling was not engaged in the process (Figure 3.7F).

Figure 3.7. The extracellular matrix promotes the phosphorylation of SHP2. A, Immunoblotting showing differential phosphorylation of Src at Y416 and Y527 in 4T1 cells following culture under gel-based 3D conditions as compared to 2D. B, RPPA data from the TCGA breast cancer dataset were analyzed for correlation of total expression levels and post-translational modifications of the indicated proteins in relation to SHP2-Y542 phosphorylation. The heat map indicates the Pearson correlation coefficient and the size of the circle is representative of the value. C, Immunoblotting showing differential phosphorylation of FAK at Y925 in 4T1 cells isolated directly from gel-based 3D cultures as compared to 2D. D, Immunoblotting showing differential phosphorylation of Src at Y416 and FAK at Y925 in 4T1 cells (left) and D2.A1 cells (right) cultured on fibronectin-coated scaffolds as compared to 2D. E, Immunoblotting showing phosphorylation of SHP2 at Y542 in 4T1 cells cultured on fibronectin-coated scaffolds for 16 days and treated with the indicated concentrations of a Src inhibitor (PP2) or a FAK inhibitor (PF271) for the last 24 hours. F, Immunoblotting showing phosphorylation of SHP2 at Y542 in D2.A1 cells cultured on fibronectin-coated scaffolds for 16 days and treated with the indicated concentrations of PP2, PF271 or a FGFR inhibitor (FIIN4) for the last 24 hours. G, H, Immunoblotting showing phosphorylation of SHP2 at Y542 and FAK at Y925 in 4T1 cells (G) and D2.A1 cells (H) cultured on fibronectin-coated scaffolds for 16 days and treated with the indicated concentrations of PF271 for the last 24 hours. I, D2.A1 cells were pre-treated with PP2 or PF271 for 24 h in serum-free media, and cells were then induced for 5 min with FGF2, PDGF, or hGF. Immunoblot analyses were used to detect phosphorylation of SHP2 at Y542.



To confirm the engagement of FAK in the induction of SHP2 phosphorylation under 3D culture environments, we treated the cells with PF271 at different concentrations from 2.5 μ M to 10 μ M, and detected the phosphorylation of FAK and SHP2 by immunoblotting. The results demonstrated that the required concentrations of these compounds to inhibit FAK nicely matched the impact on SHP2 phosphorylation (Figure 3.7G, 3.7H). To identify the contribution of Src and FAK under growth factor induction, we treated the cells with PF271 and PP2 with the induction of FGF2, PDGF and hGF, respectively in D2.A1 cells. Unlike what we observed upon ECM-mediated signaling under 3D culture environments, growth factor-mediated phosphorylation of SHP2 was readily blocked by the addition of PP2 (Figure 3.7I).

In summary, the results in this section indicated that phosphorylation of SHP2 at Y542 induced by two distinct signaling inputs, RTKs signaling from growth factors and ECM signaling from 3D culture environments, depended on both FAK and Src. Either FAK or Src might be favorable with different signaling inputs. The differential mechanisms of SHP2 phosphorylation enhanced its role as a key node in the oncogenic signaling network, and emerged the development of combination therapies with SHP2 inhibitors.

3.5 Conclusions

In this section, we show that both ECM components and growth factors are the signaling inputs to induce phosphorylation of SHP2 at Y542 via Src and FAK, and activated SHP2 facilitates multiple RTKs signaling to regulate PI3K and MAPK signaling cascades in metastatic and drug resistant breast cancer (Figure 3.8). We also highlight the importance of SHP2 activity to clinical prognosis in breast cancer patients.

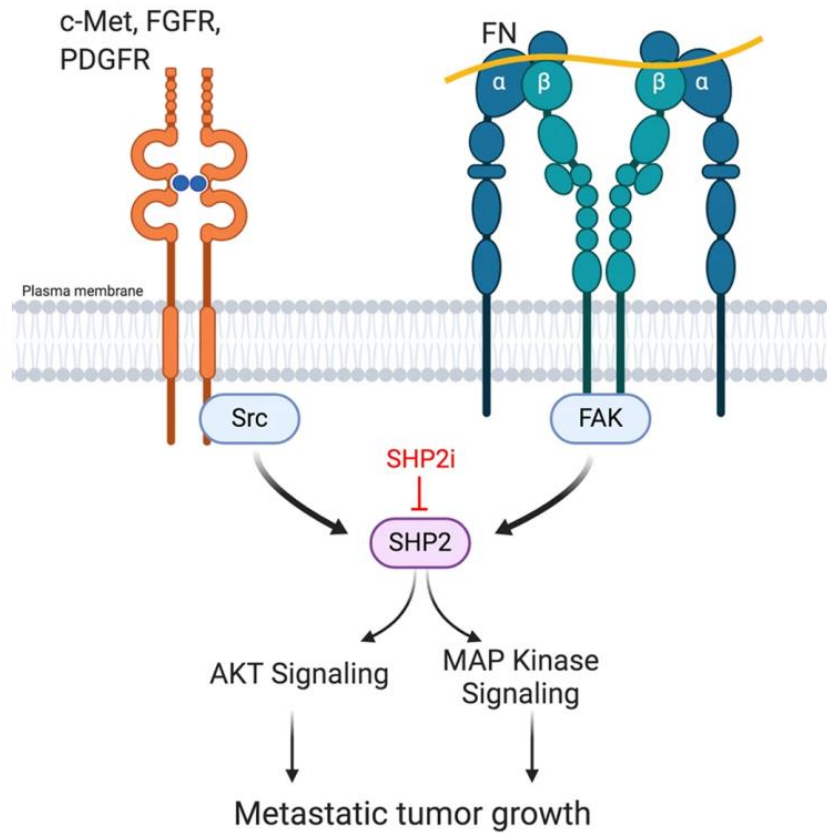


Figure 3.8. SHP2 is a shared node for ECM and RTK signaling as the signaling inputs. Growth factor receptor signaling additionally contributes to phosphorylation of SHP2 via Src and FAK. SHP2 activity contributes to various downstream signaling pathways that facilitate metastatic tumor growth in the presence of currently used targeted therapies. Targeted inhibition of SHP2 (SHP2i) blocks the growth of MBC cells. The figure was created using BioRender.

CHAPTER 4. TUMOR-CELL AUTONOMOUS SHP2 SUPPORTING IMMUNOSUPPRESSIVE TUMOR MICROENVIRONMENT

4.1 Disclaimer

The material in this chapter has been prepared as a manuscript for submission to a peer-reviewed scientific journal for publication.

4.2 Introduction

The level of SHP2 phosphorylation at Y542 correlates with the survival rate of breast cancer patients; however, there is no analysis of clinical datasets to illustrate the mechanisms. The immune cell populations are very important for TME, and immune profiles in MBC patients are closely related to patient prognosis [133]. The contribution of SHP2 to predicting the immune profiles of MBC patients is not determined.

The T cells are important immune cells for immune surveillance but are suppressed in the TME. The cytotoxic events of T cells are controlled by a balance between T-cell activation and T-cell exhaustion. There are multiple markers on the surface of T cells to induce T-cell exhaustion, such as PD-1, lymphocyte activating protein 3 (LAG3) and T-cell immunoglobulin domain and mucin domain 3 (TIM3), which can be induced by ICB [134]. When the TIM3 and LAG3 are overexpressed on the surface of T cells, the T cells will be suppressed, which facilitates the immune evasion of MBC cells. These T-cell exhaustion markers are also critical to predicting the patient's response to ICB [135]. Unfortunately, the detailed mechanisms, by which TIM3 and LAG3 are overexpressed especially upon the treatment of ICB, are not fully understood. Uncovering how TIM3 and LAG3 are regulated will also provide a solution to enhance the therapeutic effects of ICB in MBC patients. Besides the T-cell exhaustion markers, T cell infiltration in the tumor tissue is also important for the tumor-killing effects of ICB. The T-cell composition can be divided into two subgroups, helper T cells with CD4⁺ and cytotoxic T cells with CD8⁺. A recent report shows that the ratio of CD4⁺ and CD8⁺ T cells has a correlation with the survival rates of breast cancer patients [136]. Increasing the tumor-infiltrating CD8⁺ T cells can suppress the tumor growth and correlate with a better prognosis for breast cancer patients [137]. While the CD4⁺ T cells may have an opposing role compared to the CD8⁺ T cells

to predict the prognosis of breast cancer patients [138]. The proportion of T-cell composition and expression of T-cell exhaustion markers can be determined by a multi-color flow cytometry analysis. Although SHP2 in T cells has been reported to suppress the T cell functions, the contributions of tumor-cell autonomous SHP2 in the regulation are not fully understood. Hence, we are interested in understanding how T cells are modulated with SHP2 genetic depletion in the doxycycline inducible model.

Besides the T cells, TAMs are also critical components of TME. Macrophages in TME can be divided into two groups, which are M1-polarized and M2-polarized [139]. The M2-polarized macrophages and a small proportion of M1-polarized macrophages are considered immune suppressive. Thus, the composition of TAMs (ratio of M1 and M2) is critical for the patient's response to ICB [140]. Systemic inhibition of SHP2 has been reported to stimulate anti-tumor immunity via adjusting M2-polarized macrophages [141]. We are interested in whether tumor-cell autonomous SHP2 can also support immunosuppressive TME via adjusting TAMs composition.

Herein, we demonstrate that MBC-cell-specific depletion of SHP2 in a syngeneic mice model reduces the pulmonary metastasis by relieving exhaustion markers on T cells, increasing peripheral and tumor-infiltrating CD8⁺ T cells and reducing M2-polarized TAMs. Clinically, phosphorylation of SHP2 is a promising marker to predict immune-cell infiltration, T-cell activation and antigen presentation. Blocking tumor-cell autonomous SHP2 rescues T-cell cytotoxicity suppressed by growth factors.

4.3 Materials and Methods

4.3.1 Cell line, culture condition, drugs and reagents

The sources and culture conditions for 4T1, D2.A1 and 4TO7 cells were previously described in chapter 2. The detailed information for cell lines and culture conditions can also be found in APPENDIX A Table A.1.

The sources and preparation methods for 11a-1, SHP099, TNO155 and luciferin were previously described in chapter 2. The sources and preparation methods for FGF2 and PDGF were previously described in chapter 3. The α -PD-L1 antibody and IgG isotype control were bought from Bio X Cell. The Incucyte Cytotox Dye for counting dead cells was bought from

Essen BioScience. The detailed information for these drugs and reagents can also be found in APPENDIX A Table A.3.

4.3.2 Clinical dataset analysis and code availability

RPPA, mRNA and clinical outcomes raw data of breast cancer patients in TCGA were achieved from Firebrowse (<http://firebrowse.org/>) hosted by Broad Institute. The raw data were accessed on this website by selecting cohort as ‘Breast Invasive Carcinoma (BRCA)’ on the left panel, and clicking ‘Reverse Phase Protein Array’, ‘mRNA’ and ‘Clinical’ bars on the right panel. The primary files ‘RPPA_AnnotateWithGene (MD5)’ for RPPA data, ‘mRNA_Preprocess_Median (MD5)’ for mRNA data and ‘Merge_Clinical (MD5)’ for clinical outcomes were downloaded as txt file, and stored locally as raw files named ‘RPPA_raw.csv’, ‘mRNA_raw.csv’ and ‘Clinical_raw.csv’.

Immune scores and stromal scores were achieved from an online tool provided by MD Anderson Cancer Center (<https://bioinformatics.mdanderson.org/estimate/disease.html>). The raw data were achieved by selecting ‘Disease Type’ as ‘Breast Cancer’ and ‘Platform Type’ as ‘RNA-Seq-v2’. The immune scores and stroma scores here were calculated by ESTIMATE (Estimation of Stromal and Immune cells in Malignant Tumor tissues using Expression data) at the backend of the tool [142]. The file was downloaded as txt file, and stored locally as a raw file named ‘immune_score_raw.csv’.

These four locally stored files were the inputs of the downstream analyses listed below. We first compared the differential immune scores and stroma scores in patients grouped by phosphorylation levels of SHP2 at Y542 or expression levels of SHP2. We also compared differential phosphorylation levels of SHP2 at Y542 and expression levels of SHP2 in patients grouped by CD4⁺ T-cell infiltration levels. Next, we compared differential gene expression in patients grouped by phosphorylation levels of SHP2 at Y542 or expression levels of SHP2. We finally performed ssGSEA and GSEA analyses to find enriched pathways in patients with different levels of SHP2 phosphorylation. The pathway files were downloaded from GSEA websites (<http://www.gsea-msigdb.org/gsea/index.jsp>). The GSEA (Gene Set Enrichment Analysis) and result-visualization were performed with GSEA 4.1.0 developed by UC San Diego and Broad Institute [143, 144]. The other analyses and result-visualization were performed with the original codes executed with Python 3.8.5 on Anaconda 3 and R 4.0.2 on R studio. The

Python and R scripts to execute the analyses and visualize the results are included in APPENDIX B and https://github.com/benchlover/SHP2_immunology.

4.3.3 Animal care and SHP2 depletion experiments in vivo

All *in vivo* studies in this section were performed in 4-6-week old, female BALB/cJ mice purchased from Jackson Laboratories. All *in vivo* studies were performed under IACUC approval from Purdue University. No randomization or blinding was done. The 4T1 cells bearing doxycycline inducible depletion of SHP2 were constructed, sorted and verified as previously described in chapter 2. Then, 5×10^4 cells were engrafted onto the mammary fat pads via an intraductal injection. The primary tumor was measured by Vernier caliper once a week. Doxycycline was administrated in drinking water at 2 mg/ml and refreshed every fourth day following the surgical removal of primary tumors. Metastasis was monitored using bioluminescent imaging after intraperitoneal injection of luciferin (GoldBio) using an AMI HT (Spectral Instruments). Tumor-bearing lungs were harvested, imaged, weighed and processed into single-cell dissociation for flow cytometry at the end of the studies.

4.3.4 Pulmonary tumor and spleen isolation/digestion and flow cytometry

Tumor bearing lungs were dissociated with mouse tumor dissociation kit (Miltenyi Biotec) and gentleMACS Dissociator (Miltenyi Biotec) immediately after sacrificing the mice. The samples were incubated for further digestion at 40 °C for 30 minutes. The spleens were harvested, weighted and mechanically disrupted by grinding. The cell suspension was filtered through 70 µm sterile cell strainers and treated with ACK buffer to lyse red blood cells. The single-cell suspension was incubated with TruStain FcX (BioLegend) at 1:50 and Zombie violet (BioLegend) at 1:100. The single-cell suspension from pulmonary tumors was separated into two tubes and subsequently stained with panels of lymphoid antibodies and panels of myeloid antibodies at 1:200 per antibody, respectively. The single-cell suspension from the spleens was subsequently stained with panels of lymphoid antibodies only. Considering the influence of GFP induction with doxycycline induction, the FITC-labeled primary antibody was not included in the antibody panels. The primary antibodies were all purchased from BioLegend. The panels of lymphoid antibodies included PerCP anti-mouse CD45 Antibody, Pacific Blue™ anti-mouse CD8a

Antibody, Brilliant Violet 711™ anti-mouse CD4 Antibody, APC anti-mouse CD366 (TIM-3) Antibody, PE/Dazzle™ 594 anti-mouse CD279 (PD-1) Antibody and PE/Cyanine7 anti-mouse CD223 (LAG-3) Antibody. The panels of myeloid antibodies included PerCP anti-mouse CD45 Antibody, PE/Cyanine7 anti-mouse/human CD11b Antibody, Brilliant Violet 605™ anti-mouse F4/80 Antibody, PE anti-mouse CD274 (B7-H1, PD-L1) Antibody, Brilliant Violet 711™ anti-mouse CD206 (MMR) Antibody, PE/Dazzle™ 594 anti-mouse CD86 Antibody, APC/Cyanine7 anti-mouse Ly-6G Antibody and APC anti-mouse Ly-6C Antibody. The detailed information for these antibodies can also be found at APPENDIX A Table A.5. The stained cells were fixed with 10% formaldehyde.

Within 1 week of staining, flow cytometry was performed using Fortessa LSR flow cytometry cell analyzer [129] by Dr. Gregory M. Cresswell. The results were analyzed in a closed-label manner with Flowjo (10.0.7) software.

4.3.5 Incucyte-based T cell killing assays

To induce anti-tumor immunity, 1×10^6 4T07 cells were engrafted onto the mammary fat pads of BALB/cJ mice via an intraductal injection. The enlarged spleens of tumor-bearing mice were harvested 3 weeks following the injection, and mechanically disrupted by grinding. CD8⁺ cells were isolated from the splenocytes using EasySep™ Mouse CD8⁺ T Cell Isolation Kit (STEMCELL Technologies Inc.) following the manufacturer's instructions. The tumor cells were pretreated with growth factors (FGF2 at 20ng/ml and PDGF at 100ng/ml) and inhibitors (SHP099 and TNO155 at 10μM, IgG isotype control and α-PD-L1 antibody at 10μg/ml) for 24 hours. The growth factors and inhibitors were washed-off with full growth media before adding CD8⁺ cells. The ratio of tumor cells and T cells was 1:10. The co-culture system was stained with Incucyte Cytotox Dye for Counting Dead Cells (Essen BioScience), and monitored using Incucyte S3 (Essen BioScience). The dead cells were counted automatically with the software included within Incucyte S3 with a 35μm size filter.

4.3.6 Statistical analysis

A Mann-Whitney U-test was used for comparing differences between two patient groups with differential CD4⁺ T-cell infiltration; while a student's t-test was used for the comparison in

analyses of other clinical datasets. No exclusion criteria were used in the *in vivo* studies. A student's t test was used for comparing differences between two groups of measurements in *in vitro* assays and flow cytometry results with GraphPad Prism 5.0 software. Error bars show the standard error of the mean. Group measurements of the *in vivo* assays were compared with a Mann-Whitney non-parametric test with GraphPad Prism 5.0 software.

4.4 Results

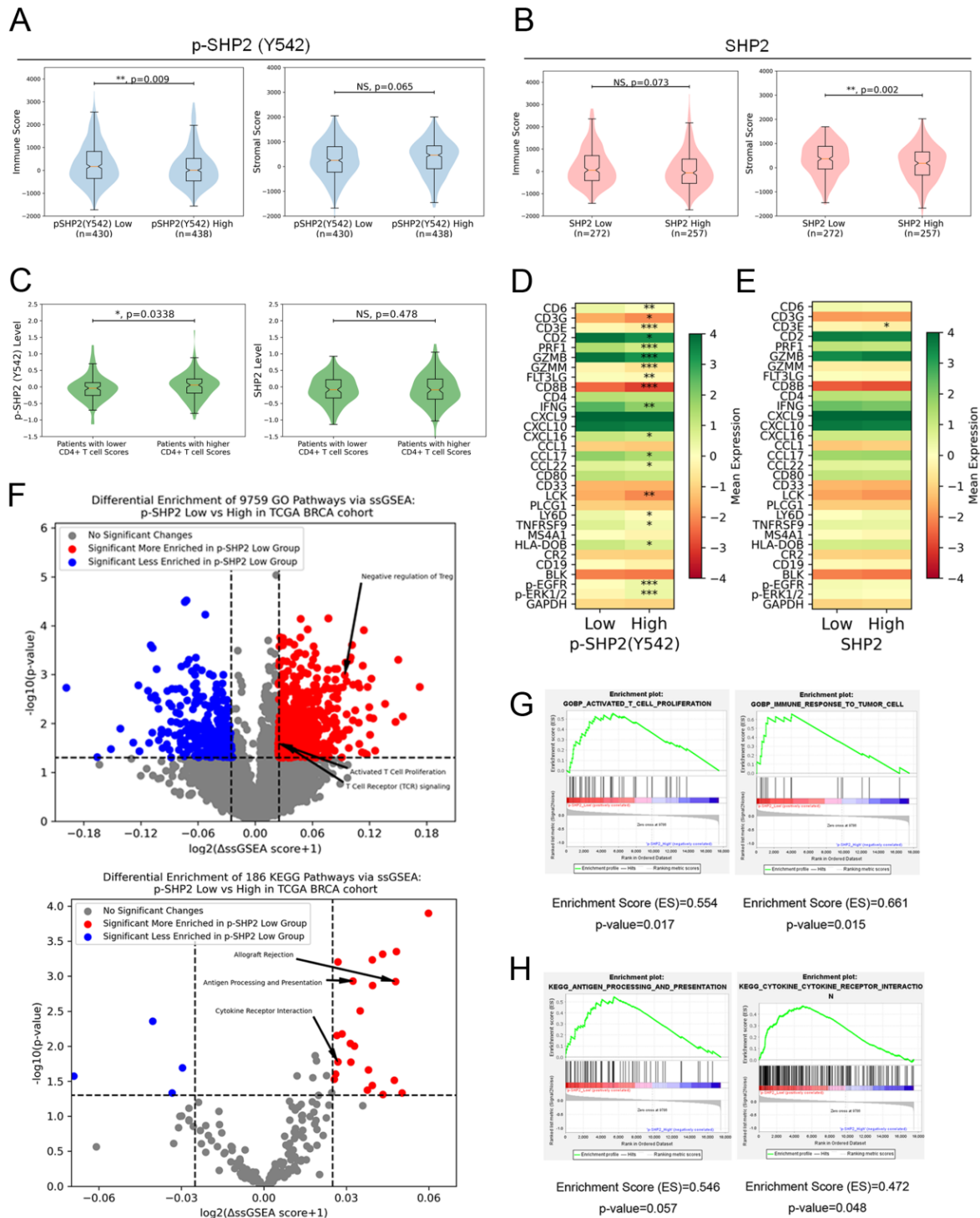
4.4.1 Phosphorylation of SHP2 at Y542 is a promising marker to predict immune profiles

In the previous chapter, we demonstrated that phosphorylation of SHP2 at Y542 was a key signaling readout with clinical significance. In detail, the phosphorylation of SHP2 in tumor cells had two distinct signaling inputs with differential activation mechanisms. As we discussed in chapter 1 that SHP2 in T cells played an important role in regulating anti-tumor immunity, we hypothesized that the phosphorylation of SHP2 at Y542 was a key signaling readout in tumor cells that might also predict the immune profiles in breast cancer patients.

To test our hypothesis, we analyzed the TCGA clinical datasets. We first divided the breast cancer patients into two groups according to their SHP2 phosphorylation levels and expression levels, respectively. We found that patients with lower phosphorylation of SHP2 at Y542 had significantly higher immune scores indicating immune-cell infiltration in tumors; while no significant difference was observed in stroma scores indicating stroma-cell infiltration (Figure 4.1A). In contrast, differential expression levels of SHP2 were not predictive of the immune scores, but stroma scores in breast cancer patients (Figure 4.1B). To further identify which immune population was predicted by differential phosphorylation of SHP2, we grouped the patients by CD4⁺ T-cell infiltration levels via Tumor Immune Estimation Resource (TIMER) prediction. The results demonstrated that patients with higher CD4⁺ T-cell infiltration levels had significantly higher phosphorylation levels of SHP2, but not expression levels (Figure 4.1C).

Next, we tried to find out immune-related differentially expressed genes (DEGs) associated with phosphorylation levels of SHP2. We found that the key genes in T-cell activation and antigen presentation, including PRF1, CD8B, GZMB, LCK, IFNG and HLA-DOB, were significantly correlated with the phosphorylation levels of SHP2, but not expression levels of SHP2 (Figure 4.1D, 4.1E).

Figure 4.1. Phosphorylation of SHP2 at Y542 predicts immune profiles in MBC patients. A, B, Violin and box plots comparing the differential immune scores and stroma scores in patients grouped by phosphorylation levels of SHP2 at Y542 (A) or expression levels of SHP2 (B). C, Violin and box plots comparing the differential phosphorylation levels of SHP2 at Y542 and expression levels of SHP2 in patients grouped by CD4⁺ T-cell infiltration levels. D, E, Heat maps comparing the differential gene expression in patients grouped by phosphorylation levels of SHP2 at Y542 (D) or expression levels of SHP2 (E). *p<0.05, **p<0.01, ***p<0.001. F, Volcano plots demonstrating pathways of differential ssGSEA scores in patients grouped by phosphorylation levels of SHP2 at Y542 with statistical significance. Specific pathways of interest are annotated. G, H, GSEA plots, Enrichment scores and p-values of the key pathways from GO (G) and KEGG (H) enriched in patients with lower phosphorylation levels of SHP2 at Y542.



With the single-sample gene set enrichment analysis (ssGSEA), we listed the significantly enriched KEGG and GO pathways in patients grouped by differential SHP2 phosphorylation levels. The results demonstrated that the pathways of Activated T cell Proliferation and Antigen Processing & Presentation were significantly more enriched in patients with lower phosphorylation of SHP2 (Figure 4.1F). The enrichment of these two pathways was further confirmed with gene set enrichment analysis (Figure 4.1G, 4.1H).

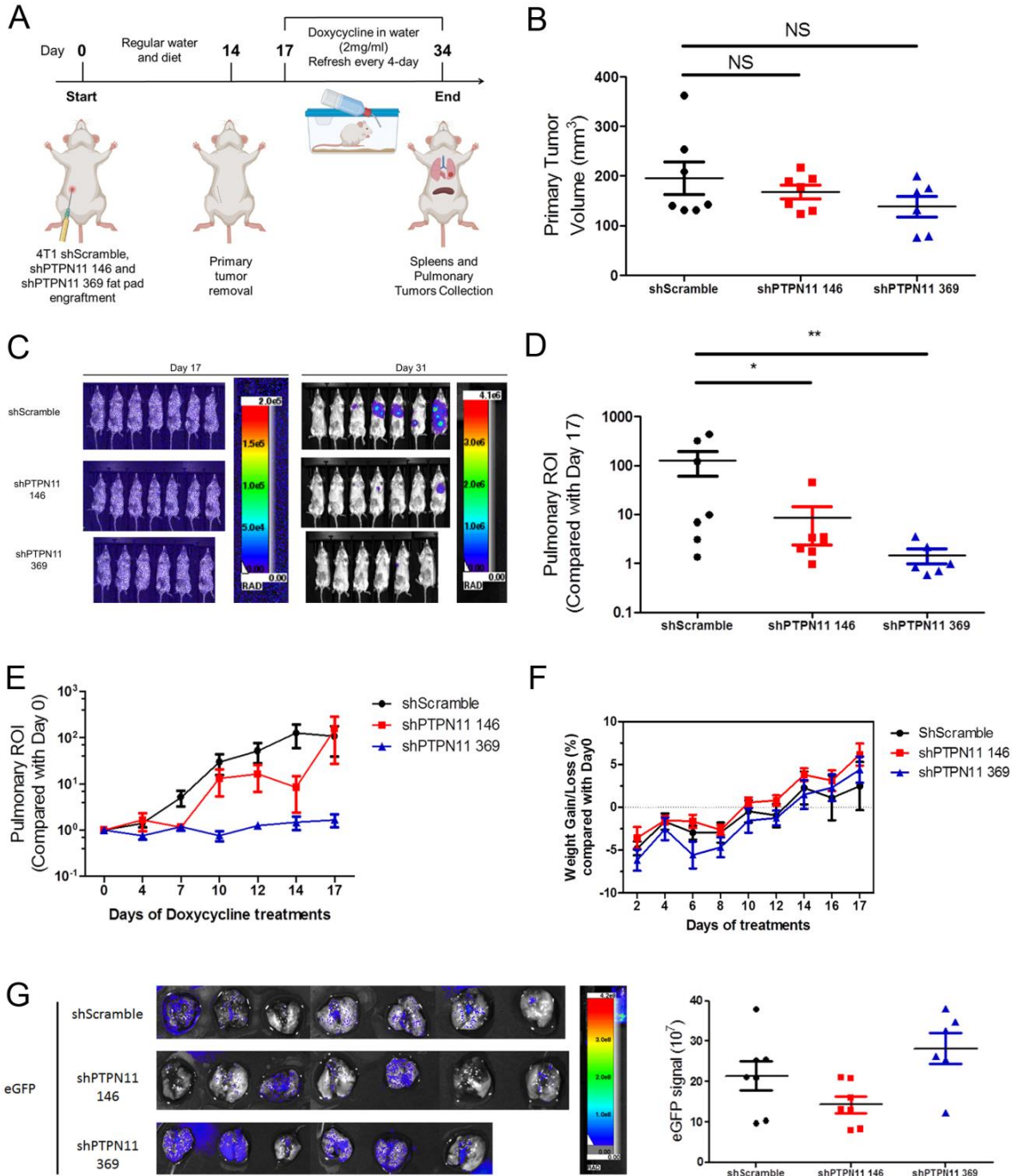
In summary, the results in this section indicated that phosphorylation levels of SHP2 at Y542, but not expression levels of SHP2, predicted the immune profiles in breast cancer patients, including the immune cell infiltration, key genes and enriched pathways related to immune functions. The results enhanced the clinical significance of phosphorylation of SHP2, which emerges the need to identify the signaling outputs of SHP2 in driving these changes in immune profiles. Moreover, the results inspired us to analyze the regulation of anti-tumor immunity by manipulating tumor-cell autonomous SHP2.

4.4.2 Depletion of tumor-cell autonomous SHP2 reduces pulmonary metastasis *in vivo*

In the previous section, we found that phosphorylation of SHP2 at Y542 predicts the immune profiles in breast cancer patients. Hence, the results suggested the correlation between SHP2 and immune evasion of MBC. As the regulation of anti-tumor immunity by the SHP2 in T cells had been widely reported, we focused on tumor-cell autonomous SHP2 because we had already proved that it promoted the growth of MBC via facilitating signaling from multiple inputs in Chapter 2 and Chapter 3. We then thought that tumor-cell autonomous SHP2 might be sufficient to support an immunosuppressive TME and contribute to MBC pulmonary metastasis *in vivo*.

To test our hypothesis here, we applied the 4T1 cell lines with doxycycline inducible genetic depletion of SHP2 in Chapter 2 on syngeneic mice to establish an orthotopic *in vivo* model of metastasis. We planned to use this model as we considered the fact that SHP2 had been reported to be sufficient to promote primary tumor growth. With the benefits of doxycycline inducible depletion, we could specifically deplete SHP2 in tumor cells only during the progression of residual systemic disease following primary tumor removal via surgical intervention, which better imitated MBC progression in clinical settings.

Figure 4.2. Depletion of SHP2 in tumor cells reduces pulmonary metastasis *in vivo*. A, Schematic of the study by doxycycline inducible depletion of SHP2 in tumor cells in 4T1 model. BALB/c mice (n = 7 mice per group for shScramble and shPTPN11 146, n=6 mice per group for shPTPN11 369) were engrafted with 4T1 cells (5×10^4) via intraductal injection into mammary fat pads. Primary tumors were surgically removed 2 weeks following the injection. Doxycycline was administered in drinking water at 2mg/ml 3 days following the removal of primary tumors. B, Plots comparing the primary tumor volume at Day 14 post injection. (NS: no significance) C, Representative bioluminescent images of 4T1 pulmonary metastasis at Day 17 and Day 31 post injection. D, Bioluminescent values from pulmonary ROI quantified as the ratio of day 31 to day 17 post injection (* $p < 0.05$, ** $p < 0.01$). E, Bioluminescence values for pulmonary regions of interest (ROI) from mice with 4T1 metastatic growth in lungs normalized to Day 0 of doxycycline treatments. Data are the mean \pm s.e.m. of n = 7 mice per group for shScramble and shPTPN11 146, n=6 mice per group for shPTPN11 369. F, The body weight of mice was monitored every 2 days, and the percentage of weight gain/loss was normalized to Day 0 of the treatments. G, Representative Green Fluorescence (eGFP) images (left) of the lungs at Day 17 of doxycycline treatments and quantified eGFP values (right) of the lungs.



As we planned, sorted 4T1 cells with doxycycline inducible shRNA constructs, together with the scramble control, were injected to the mammary fat pad of mice to grow primary tumors. To induce depletion of SHP2 specifically in tumor cells, doxycycline was administered to the mice in drinking water 3 days after the surgical primary tumor removal (Figure 4.2A).

To ensure that the residual systemic metastasis was not influenced by the sizes of primary tumors, we measure the primary tumors 2 weeks after the injection. We observed no significant change in primary tumor growth (Figure 4.2B).

As determined by the bioluminescence live imaging, we found that 14-day administration of doxycycline induced SHP2 depletion led to a significant reduction in pulmonary metastases (Figure 4.2C, 4.2D). The time-course monitoring by bioluminescence live imaging also demonstrated a delayed progression of residual metastatic disease following doxycycline administration (Figure 4.2E).

These results were consistent with the reduction of pulmonary metastasis in the 4T1 model by pharmacological inhibition of SHP2 in Chapter 2. The weights of the mice increased by approximately 10% following doxycycline administration, which indicated no significant toxicity was observed in the study (Figure 4.2F).

Finally, to confirm the effects of doxycycline to induce SHP2 depletion, we measured the eGFP signals in the lungs (Figure 4.2G).

In summary, the results in this section suggested that depletion of tumor-cell autonomous SHP2 significantly reduced the MBC pulmonary metastasis *in vivo*. The results were consistent with our previous finding that depletion of SHP2 in tumor cells reduced the growth of MBC cells *in vitro* in chapter 2.

4.4.3 Depletion of tumor-cell autonomous SHP2 adjusted T-cell composition and relieved T-cell exhaustion

To further analyze the immune profiles of the TME possibly reprogrammed by depletion of SHP2 in tumor cells, we collected the pulmonary tumors and spleens from the mice 17 days following the doxycycline administration to dissociate single cells. The single cells were stained with different panels of antibodies, and analyzed by flow cytometry with desired gating strategies to identify desired immune populations (Figure 4.3A, 4.3B).

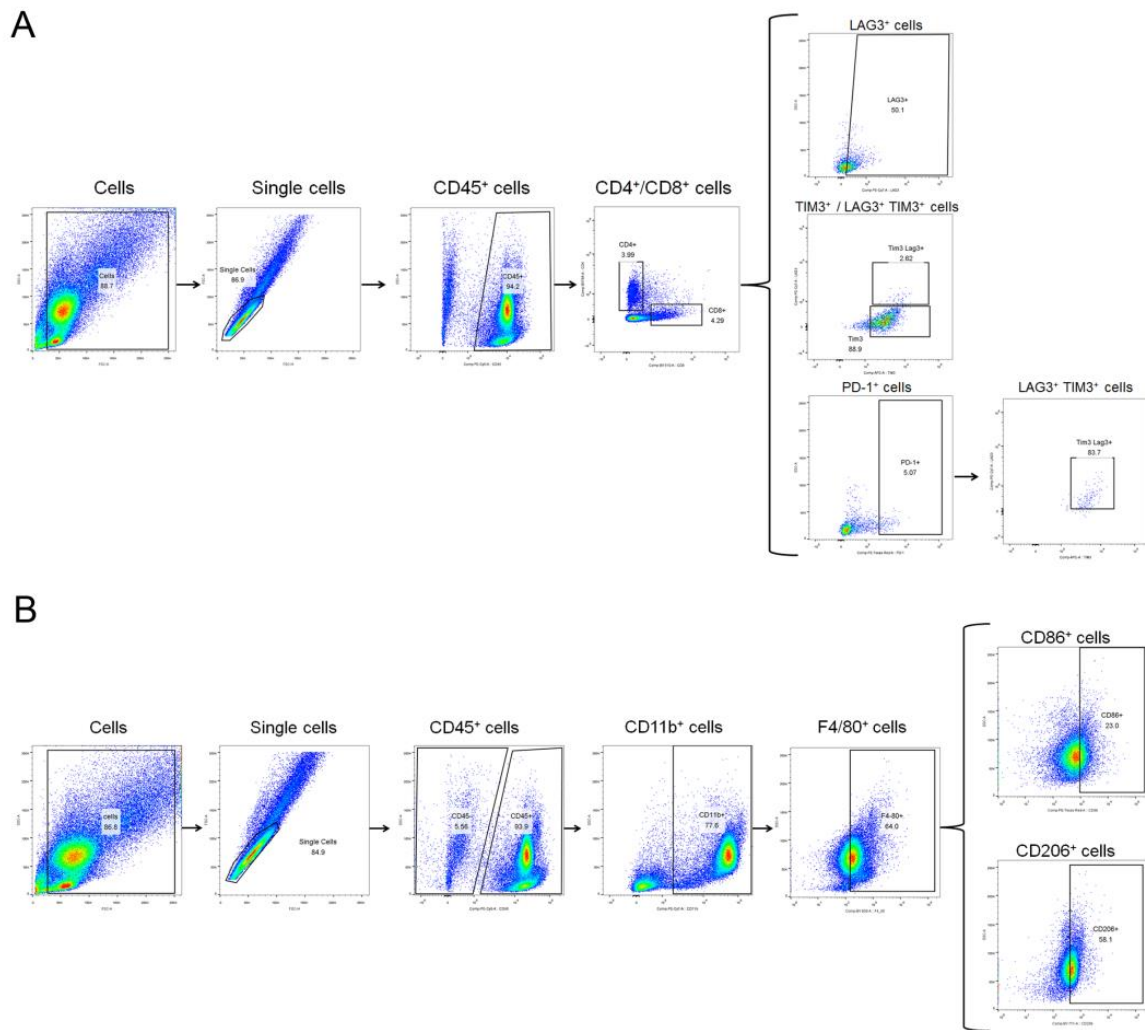


Figure 4.3. The gating ancestry for the populations in the study of 4T1 model. A, Splens and tumors from lung tissues were isolated and digested into single cell suspensions, and stained with lymphoid antibody panel as described in the materials and methods. These cells were sequentially gated as shown to identify a population of cells, single cells, CD45⁺ and CD4⁺/CD8⁺ cells prior to analysis of TIM3⁺, LAG3⁺, LAG3⁺TIM3⁺ and PD-1⁺. The LAG3⁺TIM3⁺ cells were also gated under PD-1⁺ population. B, Tumors from lung tissues were isolated and digested into single cell suspensions, and stained with myeloid antibody panel as described in the materials and methods. These cells were sequentially gated as shown to identify a population of cells, single cells, CD45⁺, CD11b⁺ and F4/80⁺ cells prior to analysis of CD86⁺ and CD206⁺.

Inspired by the enriched pathways of Activated T cell Proliferation in patients with lower levels of SHP2 phosphorylation (Figure 4.1G), we first focused on T cells composition and T cell

exhaustion markers. Here, we focused on two exhaustion markers on T cells, lymphocyte activating protein 3 (LAG3) and T-cell immunoglobulin domain and mucin domain 3 (TIM3).

With the depletion of tumor-cell autonomous SHP2, the percentage of CD4⁺ in CD45⁺ cells in spleens significantly decreased; while the percentage of CD8⁺ in CD45⁺ cells in spleens significantly increased (Figure 4.4A). Meanwhile, the percentage of LAG3⁺ and TIM3⁺ in both CD4⁺ and CD8⁺ cells in spleens significantly decreased (Figure 4.4B, 4.4C). The reduction of CD4⁺ and induction of CD8⁺ were also observed in CD45⁺ cells from pulmonary tumors, which was correlated with the outcomes of pulmonary metastasis (Figure 4.4D). SHP2 depletion in tumor cells also reduced the percentage of LAG3⁺TIM3⁺ in PD1⁺CD4⁺ and PD1⁺CD8⁺ cells from pulmonary tumors (Figure 4.4E).

These results indicated that tumor-cell autonomous SHP2 could reprogram the T cell composition and induce T-cell exhaustion to support an immunosuppressive TME.

4.4.4 Depletion of tumor-cell autonomous SHP2 adjusted TAMs composition

We next focused on TAMs composition with these samples.

There was a reduction of CD11b⁺ monocytes in CD45⁺ cells with depletion of SHP2 in tumor cells (Figure 4.5A). But no significant change was observed in the percentage of F4/80⁺ TAMs with tumor-cell autonomous SHP2 depletion (Figure 4.5B).

In the F4/80⁺ TAMs population, the percentage of M1 macrophages (CD86⁺) increased, and the percentage of M2 macrophages (CD206⁺) decreased with tumor-cell autonomous SHP2 depletion (Figure 4.5C). Hence, the changes led to a significant elevation of the M1/M2 ratio in TAMs (Figure 4.5D).

These results suggested that tumor-cell autonomous SHP2 did not induce the number or infiltration of TAMs in pulmonary tumors.

In contrast, tumor-cell autonomous SHP2 led to a lower M1/M2 ratio in TAMs, which supported the immunosuppressive TME.

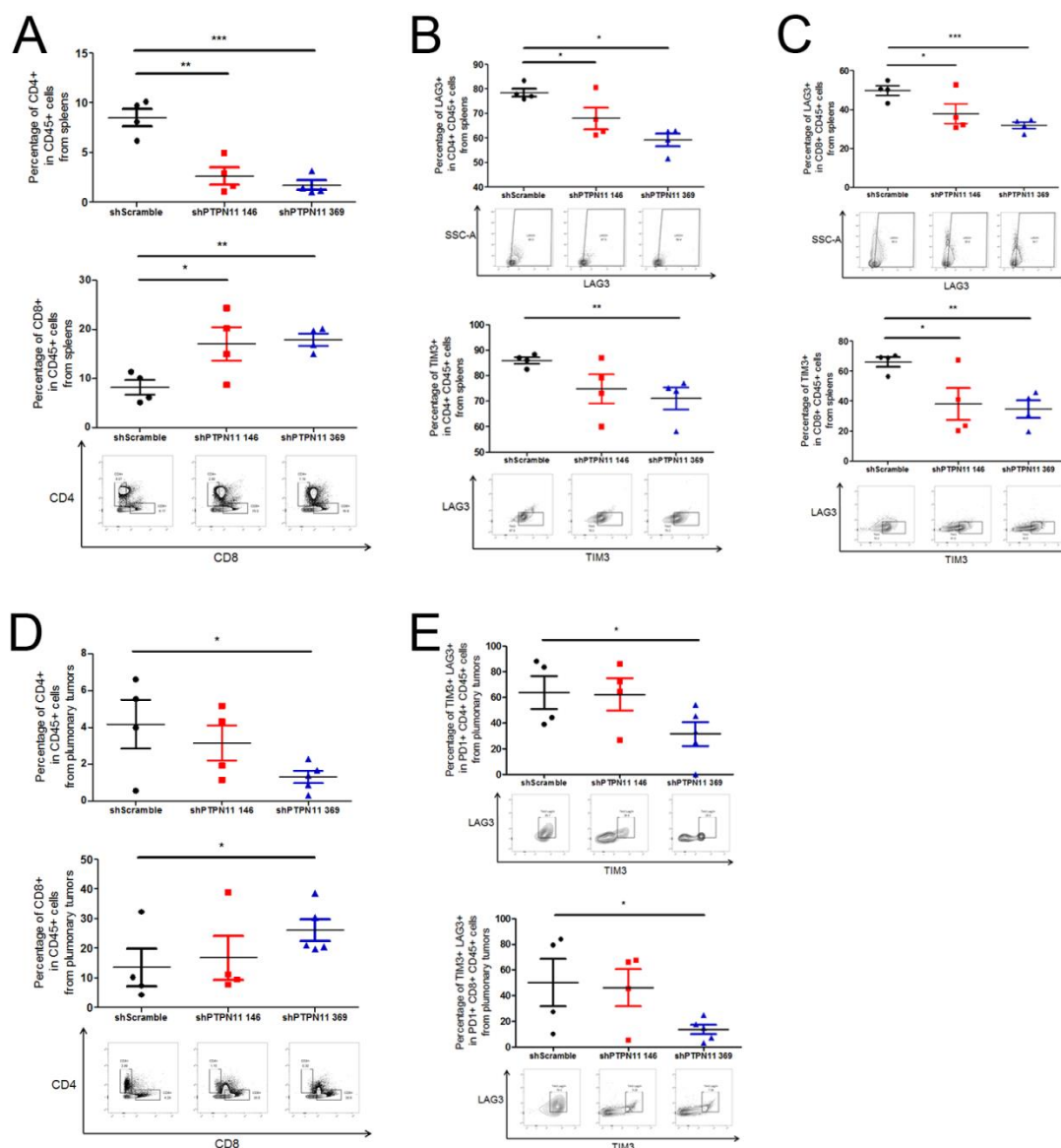


Figure 4.4. Depletion of tumor-cell autonomous SHP2 adjusts T-cell composition and relieves the T-cell exhaustion. A, D, Representative dot plots and quantification of CD4⁺ and CD8⁺ population as a frequency of CD45⁺ cells in isolated spleens (A) and lung tissues (D) of each group. B, C Representative dot plots and quantification of LAG3⁺ and TIM3⁺ population as a frequency of CD45⁺CD4⁺ cells (B) or CD45⁺CD8⁺ cells (C) in isolated spleens of each group. E, Representative dot plots and quantification of LAG3⁺TIM3⁺ population as a frequency of CD45⁺CD4⁺PD1⁺ cells and CD45⁺CD8⁺ PD-1⁺ cells in isolated lung tissues of each group. In all panels, *p<0.05, **p<0.01, ***p<0.001, n = 4 for shScramble and shPTPN11 146, n = 5 for shPTPN11 369 for cells isolated from lung tissues; while n=4 for cells isolated from spleens.

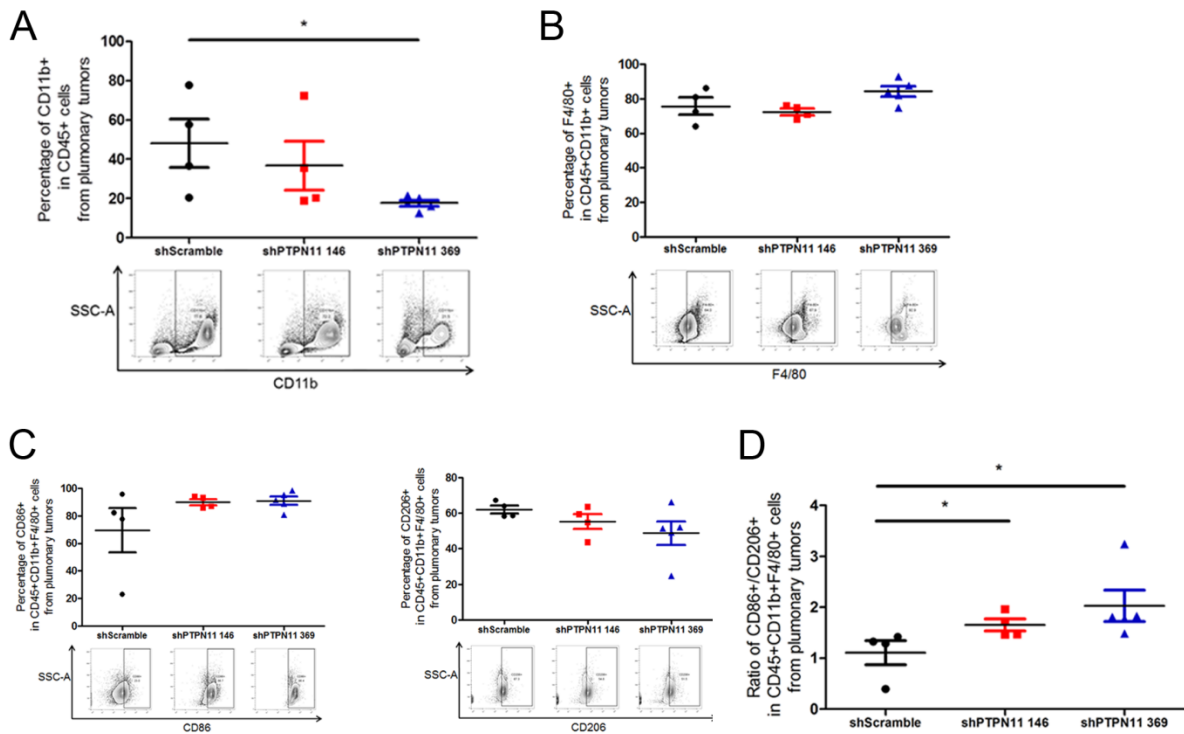
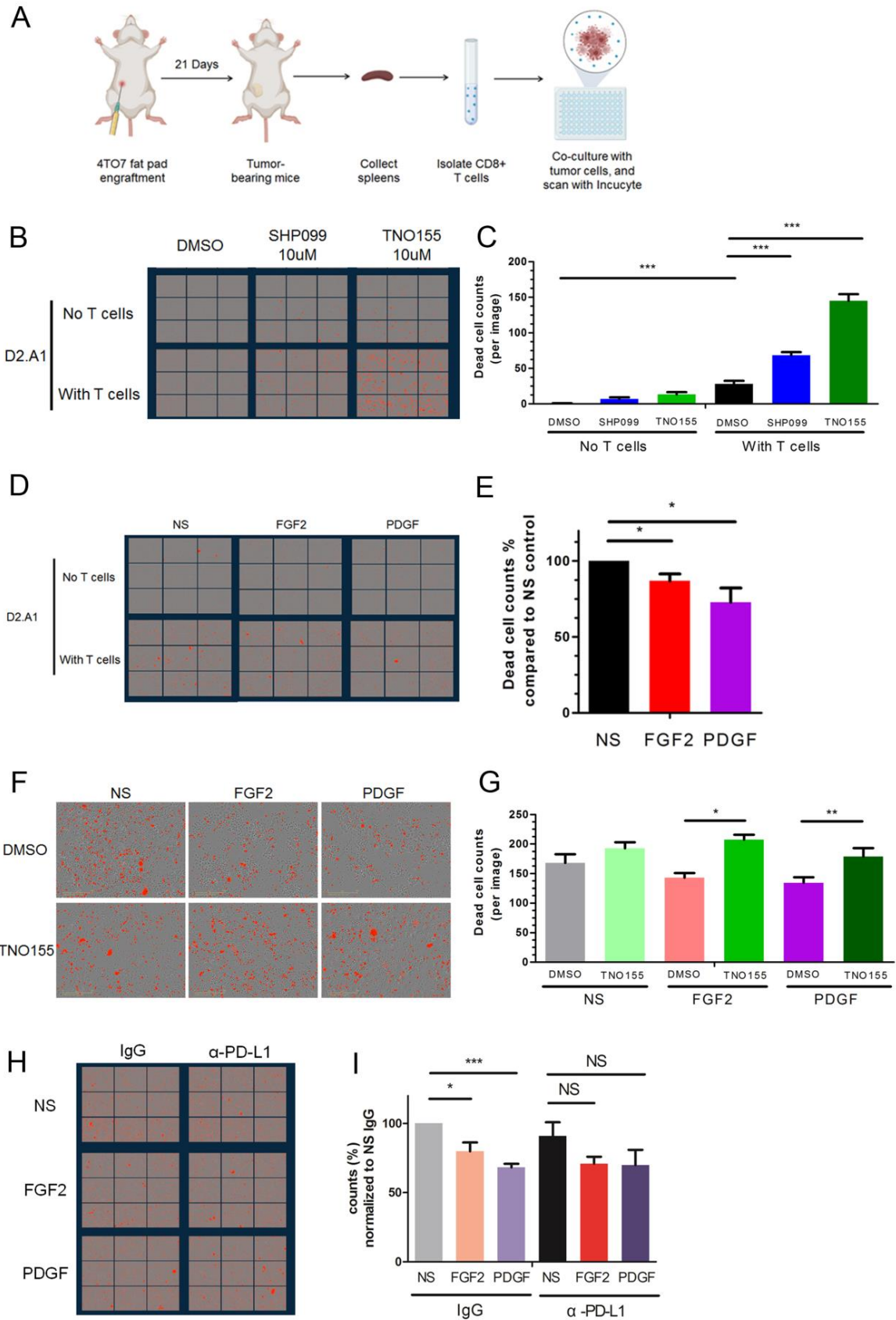


Figure 4.5. Depletion of tumor-cell autonomous SHP2 adjusts tumor associated macrophages composition. A, B, Representative dot plots and quantification of CD11b⁺ population as a frequency of CD45⁺ cells (A) and F4/80⁺ population as a frequency of CD45⁺CD11b⁺ cells (B) in isolated lung tissues of each group. C, Representative dot plots and quantification of CD86⁺ and CD206⁺ population as a frequency of CD45⁺CD11b⁺F4/80⁺ cells in isolated lung tissues of each group. D, Plots comparing the ratio of the frequency of CD86⁺ and CD206⁺. In all panels, *p<0.05, n = 4 for shScramble and shPTPN11 146, n = 5 for shPTPN11 369.

4.4.5 Tumor-cell autonomous SHP2 facilitates growth factors to reduce T cell cytotoxicity

With the depletion of tumor-cell autonomous SHP2 in the 4T1 mice model, we confirmed that SHP2 in tumor cells facilitated the growth of MBC cells *in vivo* via supporting an immunosuppressive TME. The induction of T-cell exhaustion marker on the surface of T cells was one of the mechanisms. To investigate how tumor-cell autonomous SHP2 led to T cell exhaustion, we utilized the Incucyte-based T cell killing assay.

Figure 4.6. SHP2 blockade in MBC cells rescues T-cell cytotoxicity reduced by growth factors. A, Schematic of the Incucyte-based T cell cytotoxicity assays. CD8⁺ T cells are isolated from the spleens of 4T07 tumor-bearing mice. The MBC cells are treated with growth factors and inhibitors, and co-cultured with CD8⁺ T cells. The dead cells are monitored with Incucyte. B, Representative images of the D2.A1 cells at 1 hour following co-culturing with T cells and treated with SHP099 or TNO155. The D2.A1 cells without T cells served as background. C, Bar graph comparing the dead cell counts per image with different treatments, *** $p < 0.001$, $n = 9$. D, Representative images of the MBC cells treated with FGF2 and PDGF at 1 hour following co-culturing with T cells. The MBC cells without T cells served as the background. E, Bar graph comparing the percentage of dead cell counts of FGF2 and PDGF groups to No Stem (NS) group. * $p < 0.05$, $n = 4$ individual repeats. F, Representative images of the MBC cells treated with FGF2 / PDGF and TNO155 at 1 hour following co-culturing with T cells. G, Bar graph comparing the dead cell counts per image with different treatments. * $p < 0.05$, ** $p < 0.01$, $n = 9$. H, Representative images of the D2.A1 cells treated with FGF2 / PDGF and IgG / α -PD-L1 at 1 hour following co-culturing with T cells. I, Bar graph comparing the percentage of dead cell counts with different treatments normalized to the control group. NS: not significant, * $p < 0.05$, *** $p < 0.001$, $n = 4$ individual repeats.



In this assay, CD8⁺ T cells were isolated from the spleens of tumor-bearing mice and co-cultured with MBC cells, and the dead cells stained with red fluorescence were counted by Incucyte live imaging (Figure 4.6A). We first tried to treat the co-culture system with systemic SHP2 inhibitors as a proof of concept. After co-cultured with T cells, the dead cell counts from D2.A1 cells were significantly increased, which was enhanced by additional treatments of SHP099 and TNO155 (Figure 4.6B, 4.6C). These data indicated that systemic SHP2 inhibition enhanced the T-cell cytotoxicity. Next, as we previously demonstrated in chapter 3 that RTK signaling is one of the signaling inputs of SHP2, we focused on the growth factors induction of T-cell exhaustion. We treated the D2.A1 cells with FGF2 and PDGF before co-culturing with T cells, and the dead cell counts were significantly reduced, indicating reduced T cell cytotoxicity (Figure 4.6D, 4.6E). To find whether tumor-cell autonomous SHP2 was involved, the D2.A1 cells were treated with these two growth factors and TNO155, and the reduced T-cell cytotoxicity was significantly rescued (Figure 4.6F, 4.6G). As we also found CD274 was among the DEGs correlated with differential levels of SHP2 phosphorylation, we decided to check whether PD-L1 was involved in the process. As expected, the reduced T-cell cytotoxicity by growth factors was significantly rescued by α -PD-L1 antibody (Figure 4.6H, 4.6I).

These data suggested that SHP2 in tumor cells facilitated growth factors to reduce T-cell cytotoxicity, which induced an immunosuppressive TME. Moreover, PD-L1 might also be involved in the process to reduce T-cell cytotoxicity, which inspired us to investigate whether it could be one of the signaling outputs of SHP2.

4.5 Conclusions

In this section, we establish phosphorylation of SHP2 at Y542 as a promising marker to predict immune profiling in MBC patients. We found that depletion of tumor-cell autonomous SHP2 reduces pulmonary metastasis via adjusting T-cell composition, adjusting TAMs composition, and reliving T-cell exhaustion.

CHAPTER 5. SIGNALING OUTPUTS OF SHP2 REGULATING TUMOR GROWTH AND IMMUNOSUPPRESSION

5.1 Disclaimer

Some parts of the material in this chapter had been prepared as a manuscript for submission to a peer-reviewed scientific journal for publication.

Some parts of the material in this chapter were published in a peer-reviewed journal *Oncogene* in 2020. The citation information for the article is listed below. The article is open access and licensed under a Creative Commons Attribution 4.0 International License.

Chen, H., Libring, S., Ruddraraju, K.V. et al. SHP2 is a multifunctional therapeutic target in drug resistant metastatic breast cancer. *Oncogene* 39, 7166–7180 (2020).

5.2 Introduction

We have proved that inhibition of SHP2 can relieve the T-cell cytotoxicity reduced by the growth factors. This effect can also be confirmed with the α -PD-L1 antibody. In fact, PD-L1 can be regulated transcriptionally and post-transcriptionally under the regulation of growth factors [145]. Besides PD-L1, MHC I is also important to regulate T cell activity. Thus, we focused on the mechanisms of how SHP2 is involved in the regulation of PD-L1 and MHC I in response to multiple growth factors. In this chapter, we demonstrate that PD-L1 and MHC class I are downstream of SHP2-mediated RTK and ECM signaling in MBC cells under differential regulating mechanisms.

5.3 Materials and Methods

5.3.1 Cell lines, culture conditions, drugs and reagents

The sources and culture conditions for 4T1, D2.A1 and BT549 cells were previously described in chapter 2. The D2.A1 cells with doxycycline inducible shRNAs targeting PTPN11 were constructed as previously described in chapter 2. The detailed information for cell lines and culture conditions can also be found in APPENDIX A Table A.1.

The sources and preparation methods for 11a-1, SHP099, TNO155, FIIN4, PP2, PF271 and luciferin were previously described in chapter 2 and chapter 3. The sources and preparation methods for FGF2 and PDGF were previously described in chapter 3. The mouse interferon- γ was purchased from R&D systems, and reconstituted according to the manufacturer's instructions. The master stock of interferon- γ was diluted working stocks at 2 μ g/ml, aliquoted and stored at -20 °C. The working stocks were considered single-use to avoid any freeze-thaw cycle that reduced the efficacy. The detailed information for these drugs and reagents can also be found in APPENDIX A Table A.3.

5.3.2 Immunoblotting assays

In the growth factor-induced signaling assays, the D2.A1 cells were seeded as a single layer in 12-well flat-bottom plates overnight. The cells were washed twice with 1ml/well serum-free media to remove any residual serum. The drugs were prepared with serum-free media (SHP099 and TNO155 at 10 μ M, FIIN4 at 200nM) and added to the cell. Vehicle at the same volume was used as a control in this step. After 24 hours, the cells were then stimulated with FGF2 (20 ng/ml), PDGF (100 ng/ml) and hGF (50 ng/ml) for 5 minutes. The cells were harvested for lysis immediately after stimulation. The immunoblotting to detect the expression levels of p-FRS2, p-FGFR, FGFR1, p-AKT, AKT, p-ERK, ERK, p-SHP2, SHP2, Tubulin and GAPDH was performed according to the protocol described in chapter 2.

To detect downstream signaling in the MBC cells cultured on fibronectin-coated scaffolds, the 4T1 and D2.A1 cells were seeded on the scaffolds, and the cells under 2D culture conditions were used as controls. The cells were allowed to grow for 8 days before being treated with TNO155 at 5 μ M or DMSO for 24 hours. The cells were harvested and moved to the standard immunoblotting protocol to detect p-AKT, p-ERK, ERK and Tubulin in chapter 2.

To identify the balance between STAT1 and MAPK signaling regulated by SHP2, the D2.A1 cells were seeded overnight in 12-well flat-bottom plate. The cells were washed twice with 1ml/well serum-free media to remove any residual serum. FGF2 at 20ng/ml, PDGF at 100ng/ml and TNO155 at 5 μ M were prepared with serum-free media and added to the cell. Vehicle at the same volume was used as a control in this step. After 24 hours, the cells were then stimulated with interferon- γ at 200ng/ml for 5 minutes. The cells were harvested for lysis immediately after stimulation. The immunoblotting to detect the expression levels of p-STAT1,

STAT1, p-ERK, ERK and Tubulin was performed according to the protocol described in chapter 2. The levels of p-STAT1 and p-ERK were quantified with ImageJ 1.52a (NIH), and normalized to Tubulin.

The information on these antibodies in this section was described above and APPENDIX A Table A.6.

5.3.3 Flow cytometry for MBC cells in vitro

The D2.A1 and BT549 cells were treated with desired growth factors and inhibitors for 24 hours. The cells were harvested and stained with primary antibodies at 1:200 per antibody for 45 min at 4 °C in the dark. The primary antibodies were purchased from BioLegend. These antibodies were PE anti-mouse CD274 (B7-H1, PD-L1) Antibody, FITC anti-mouse H-2 Antibody, PerCP/Cyanine5.5 anti-human CD274 (B7-H1, PD-L1) Antibody and PE anti-human HLA-A,B,C Antibody. The stained cells were washed with PBS once and fixed with 10% formaldehyde. Flow cytometry was performed using Guava EasyCyte System (Millipore). The results were analyzed with Flowjo (7.6.1) software. The information on the antibodies, growth factors and inhibitors in this section was described above and APPENDIX A Table A.4.

5.3.4 RNA isolation and Quantitative real-time PCR analysis

Total RNA from treated tumor cells was isolated with EZNA total RNA kit (Omega BioTek). Then, the cDNA was synthesized with Verso cDNA synthesis kit (Thermo Scientific) following the manufacturer's instructions. Quantitative real-time PCR systems were prepared with SYBR Green Master Mix (Thermo Scientific) and amplified with CFX Connect real-time PCR detection system (Bio-Rad). The primer set (Forward 5'-CTCGCCTGCAGATAGTTCCC-3', Reverse 5'-GGGAATCTGCACTCCATCGT-3') was used to detect mouse PD-L1. The primer set (Forward 5'-CAACTTTGGCATTGTGGAAGGGCTC-3', Reverse 5'-GCAGGGATGATGTTCTGGGCAGC-3') was used to detect mouse GAPDH. The mRNA levels of PD-L1 were normalized to GAPDH.

5.3.5 Statistical analysis

A student's t-test was used for comparing differences between two groups of measurements in *in vitro* assays and flow cytometry results with GraphPad Prism 5.0 software. Error bars show the standard error of the mean. The immunoblotting was quantified with ImageJ 1.52a (NIH).

5.4 Results

5.4.1 Phosphorylation of ERK1/2 and ATK are the signaling output of SHP2 in MBC cells

In chapter 2, we demonstrated that the signaling recovery of ERK1/2 and AKT phosphorylation led to the resistance to ErbB-targeted therapies in HME2 cells, which could be blocked by SHP2 inhibitors. In Chapter 3, we also found that RTKs signaling, induced by multiple growth factors including FGF2, was one of the signaling inputs of SHP2. SHP2 inhibitors were also capable of reducing the spheroid growth of HME2-LAPR cells induced by FGF2. The 3D culture environment with ECM signaling was also one of the signaling inputs of SHP2. Hence, we thought that phosphorylation of ERK1/2 and AKT might be the signaling output downstream of both the signaling inputs listed above in MBC cells.

To illustrate the downstream signaling events facilitated by SHP2, we performed signaling assays in D2.A1 cells with the induction of multiple growth factors and SHP099 under serum-free conditions. FGFR inhibitor, FIIN4 was used as a positive control for blocking FGFR signaling. We found that phosphorylation of ERK1/2 and ATK was induced by the addition of FGF2, which was abolished by SHP099 and FIIN4 (Figure 5.1A). Similar results were observed when the cells were induced by PDGF and hGF in the presence of SHP099 (Figure 5.1B). We also confirmed the reduction of ERK1/2 and AKT phosphorylation induced by FGF2, PDGF and hGF in the presence of TNO155, which was more robust than SHP099 (Figure 5.1C). Meanwhile, it was worthwhile to point out that the phosphorylation of FRS2 at Y436 induced by FGF2 was also reduced by SHP099 (Figure 5.1A). It is also unexpected for us to observe that FIIN4 also reduced the phosphorylation of SHP2 induced by FGF2, and the reduction was more significant than SHP099 (Figure 5.1A). These data not only suggested phosphorylation of ERK 1/2 and AKT as signaling output downstream of multiple RTKs signaling but also inspired us with the

possible combination of FIIN4 with SHP2 inhibitors to achieve better signaling inhibition outcomes.

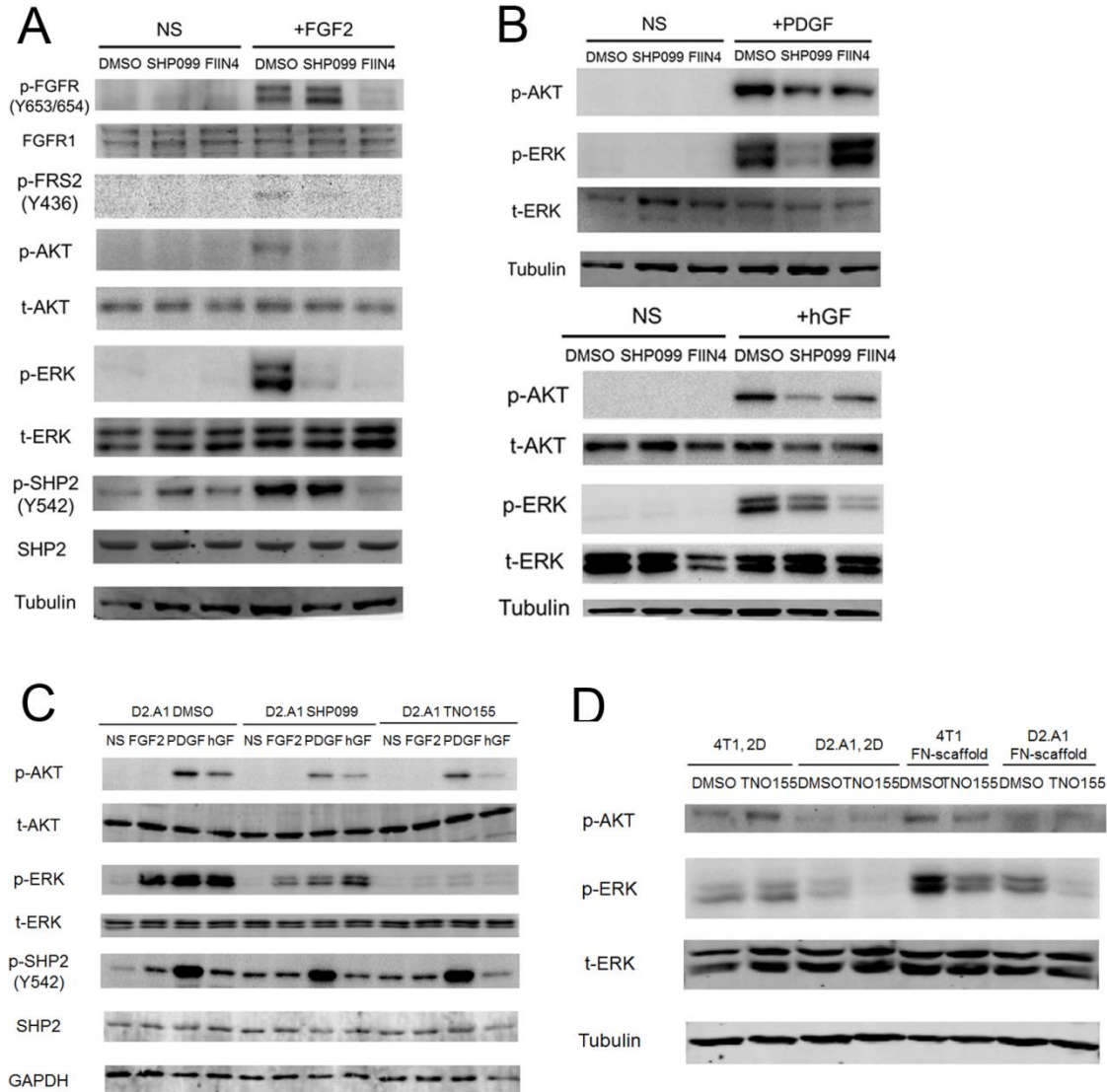


Figure 5.1. Phosphorylation of AKT and ERK1/2 are the signaling outputs of SHP2. A, B, D2.A1 cells were pre-treated with SHP099 or FIIN4 for 24 h in serum-free media and cells were subsequently induced for 5 min with FGF2 (A), PDGF (B, top), or hGF (B, bottom) as indicated. Immunoblotting was used to detect phosphorylation of FGFR, FRS2, ERK1/2, AKT, and SHP2. C, Immunoblotting showing phosphorylation of ERK1/2, AKT and SHP2 in D2.A1 cells induced with FGF2, PDGF and hGF for 5 minutes in the presence of TNO155 at 5 μ M. D, Immunoblotting showing phosphorylation of ERK1/2 and AKT in 4T1 and D2.A1 cells cultured on fibronectin-coated scaffolds for 8 days and treated with TNO155 at 5 μ M for the last 24 hours.

Next, to identify whether 3D culture environment could also induce phosphorylation of ERK1/2 and AKT as signaling output via SHP2, we returned to the 4T1 and D2.A1 cells cultured on fibronectin-coated scaffolds in the presence of TNO155. We found that the phosphorylation of ERK1/2 and AKT was elevated when the cells were cultured on fibronectin-coated scaffolds compared to 2D culture conditions, and the elevated phosphorylation of ERK1/2 and AKT could be reduced by TNO155 (Figure 5.1D). These data indicated that phosphorylation of ERK 1/2 and AKT was also signaling output downstream of 3D culture environment with ECM signaling.

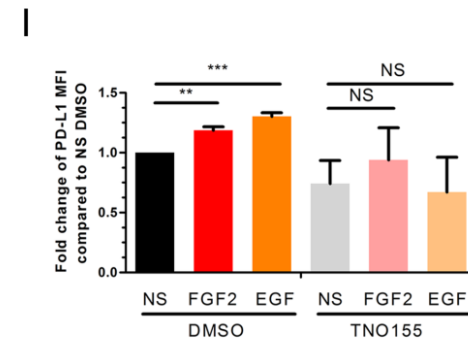
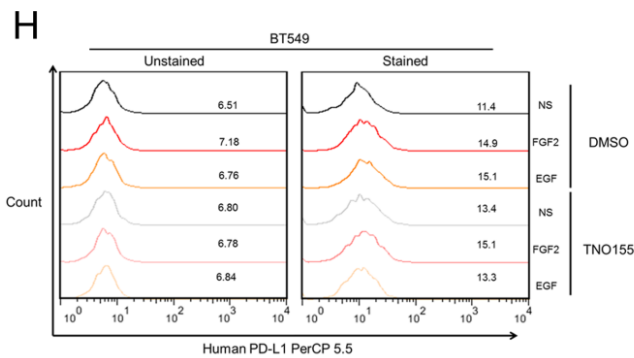
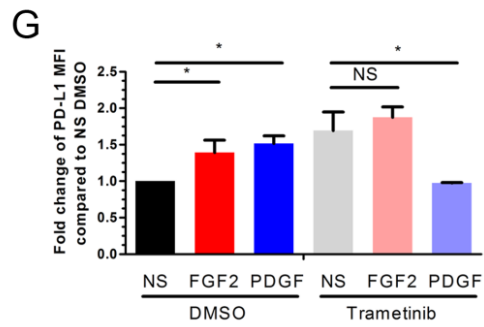
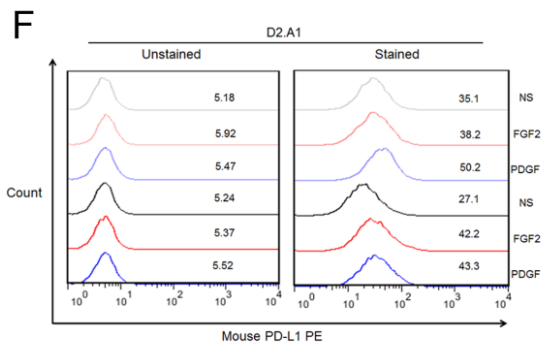
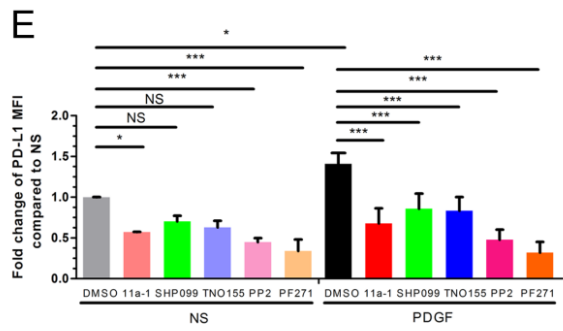
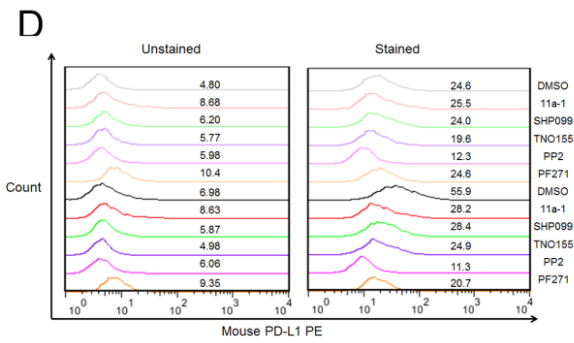
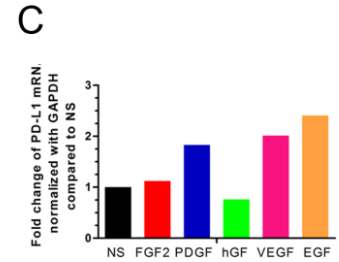
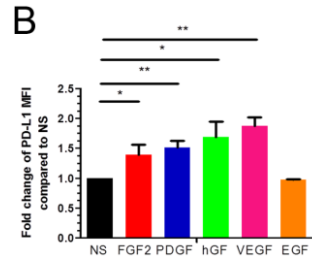
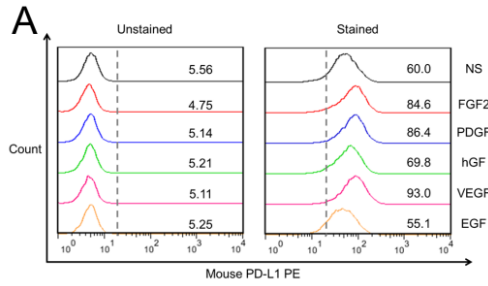
In summary, we identified phosphorylation of ERK1/2 and AKT as one of the signaling outputs of SHP2 under two major signaling inputs we previously described to promote the growth and survival of MBC cells.

5.4.2 SHP2 regulates PD-L1 as a signaling output under multiple RTKs signaling

In chapter 4, we found that tumor-cell autonomous SHP2 facilitated RTKs signaling to reduce T cell cytotoxicity, and created an immunosuppressive TME. However, the mechanisms of how SHP2 in tumor cells reduced T cell cytotoxicity were still uncovered. Inspired by the facts that CD274 changed significantly with differential levels of SHP2 phosphorylation (Figure 4.1D) and the T cell cytotoxicity reduced by growth factors was significantly rescued α -PD-L1 antibody (Figure 4.6H, 4.6I), we thought that PD-L1 might be one of the signaling outputs downstream of SHP2 to facilitate immune evasion of MBC cells.

We first utilized flow cytometry to analyze PD-L1 levels on the surface of D2.A1 cells in the presence of multiple growth factors. The histograms and quantification of Mean Fluorescence Intensity (MFI) revealed that FGF2 and PDGF significantly induced PD-L1 levels in D2.A1 cells (Figure 5.2A, 5.2B). To test whether the induction was due to transcriptional activation, we did quantitative PCR and the results demonstrated that the induction of PD-L1 by growth factors was regulated transcriptionally (Figure 5.2C). Next, to identify the involvement of SHP2 in the regulation of PD-L1 by these growth factors, we treated the D2.A1 cells in the presence of SHP2 inhibitors together with PDGF induction. Treatments of 11a-1, SHP099 and TNO155 significantly abolished the induction of PD-L1 by PDGF, and similar results could be achieved by PP2 (Figure 5.2D, 5.2E). As we found phosphorylation of ERK1/2 was one of the signaling outputs of SHP2, we hypothesized that ERK1/2 was also involved. We treated the cells with a MEK inhibitor, Trametinib with the induction of FGF2 and PDGF.

Figure 5.2. SHP2 blockade reduces PD-L1 induced by growth factors in MBC cells. A, Cell surface analysis of PD-L1 in D2.A1 cells induced by different growth factors at desired concentrations for 24 hours using flow cytometer. B, Bar graph comparing fold change of PD-L1 Mean Fluorescence Intensity (MFI) induced by different growth factors relative to no stem (NS). * $p < 0.05$, ** $p < 0.01$, $n = 3$ as determined by a student's t-test. C, Bar graph comparing fold change of PD-L1 mRNA relative to GAPDH induced by different growth factors compared to no stem (NS). D, E, Cell surface analysis of PD-L1 using flow cytometer and bar graph comparing fold change of PD-L1 Mean MFI in D2.A1 cells induced by PDGF and treated with 11a-1, SHP099, TNO155, PP2 and PF271. * $p < 0.05$, ** $p < 0.01$, *** $p < 0.001$, $n = 3$ as determined by a student's t-test. F, G, Cell surface analysis of PD-L1 using flow cytometer and bar graph comparing fold change of PD-L1 Mean MFI in D2.A1 cells induced by FGF2 or PDGF and treated with Trametinib. NS: not significant, * $p < 0.05$, $n = 3$ as determined by a student's t-test. H, I, Cell surface analysis of PD-L1 using flow cytometer and bar graph comparing fold change of PD-L1 Mean MFI in BT549 cells induced by FGF2 or EGF and treated with TNO155. NS: not significant, ** $p < 0.01$, *** $p < 0.001$, $n = 3$ as determined by a student's t-test.



The results indicated that Trametinib also significantly abolished the induction of PD-L1 by FGF2 and PDGF in D2.A1 cells (Figure 5.2F, 5.2G). Finally, as the results were all achieved in D2.A1 cells, we introduced another MBC cell line, BT549. Not the same as what we observed in D2.A1 cells, FGF2 and EGF significantly induced PD-L1 in BT549 cells, which could be reduced by TNO155 (Figure 5.2H, 5.2I).

In summary, these results in this section suggested that PD-L1 was one of the signaling outputs of SHP2, downstream of multiple RTKs signaling. ERK1/2 was also involved in the regulation of PD-L1 by SHP2 under growth factor stimulations.

5.4.3 SHP2 regulates PD-L1 as a signaling output under 3D culture environments

In chapter 3, we found that 3D culture environment with ECM signaling is another signaling input of SHP2 besides the multiple RTKs signaling. Inspired by the finding that PD-L1 was one of the signaling outputs of SHP2 under multiple RTKs signaling, we thought that PD-L1 might also be regulated under 3D culture environments with ECM signaling.

To test our hypothesis, we continued to use the fibronectin-coated and laminin-coated tessellated scaffolds to get rid of the gel disruption in flow cytometry. The 4T1 and D2.A1 cells cultured on these scaffolds were collected, stained for PD-L1 and analyzed by flow cytometry. We demonstrated that PD-L1 in D2.A1 cells was significantly elevated when cultured on fibronectin-coated and laminin-coated scaffolds compared to 2D culture; while in 4T1 cells, PD-L1 was significantly elevated only when cultured on laminin-coated scaffolds (Figure 5.3A, 5.3B). Hence, we decided to use D2.A1 cultured on fibronectin-coated scaffolds in our next-step study. To identify the involvement of SHP2 in the regulation, we treated these cells with TNO155 and PF271. The results demonstrated that the elevation of PD-L1 with fibronectin-coated scaffolds in D2.A1 cells could be significantly abolished by TNO155 and PF271 (Figure 5.3C, 5.3D). Quantities PCR revealed that both the elevation of PD-L1 and reduction in the presence of these inhibitors were regulated transcriptionally (Figure 5.3E). To confirm whether the results achieved by TNO155 were on-target, we then implemented the D2.A1 cells with doxycycline inducible depletion of SHP2 described in Chapter 2. The results showed that depletion of SHP2 reduced the elevated PD-L1 on scaffolds more than the scramble control (Figure 5.3F). As we previously found that the SHP2-ERK1/2 axis was involved in PD-L1 regulation by growth factors, we thought that it might happen in PD-L1 regulation under

3D culture environment as well. However, Trametinib failed to reduce the elevated PD-L1 on scaffolds in D2.A1 cells (Figure 5.3G). These results indicated some other pathways, other than ERK1/2, might be involved in the PD-L1 regulation under 3D culture environment.

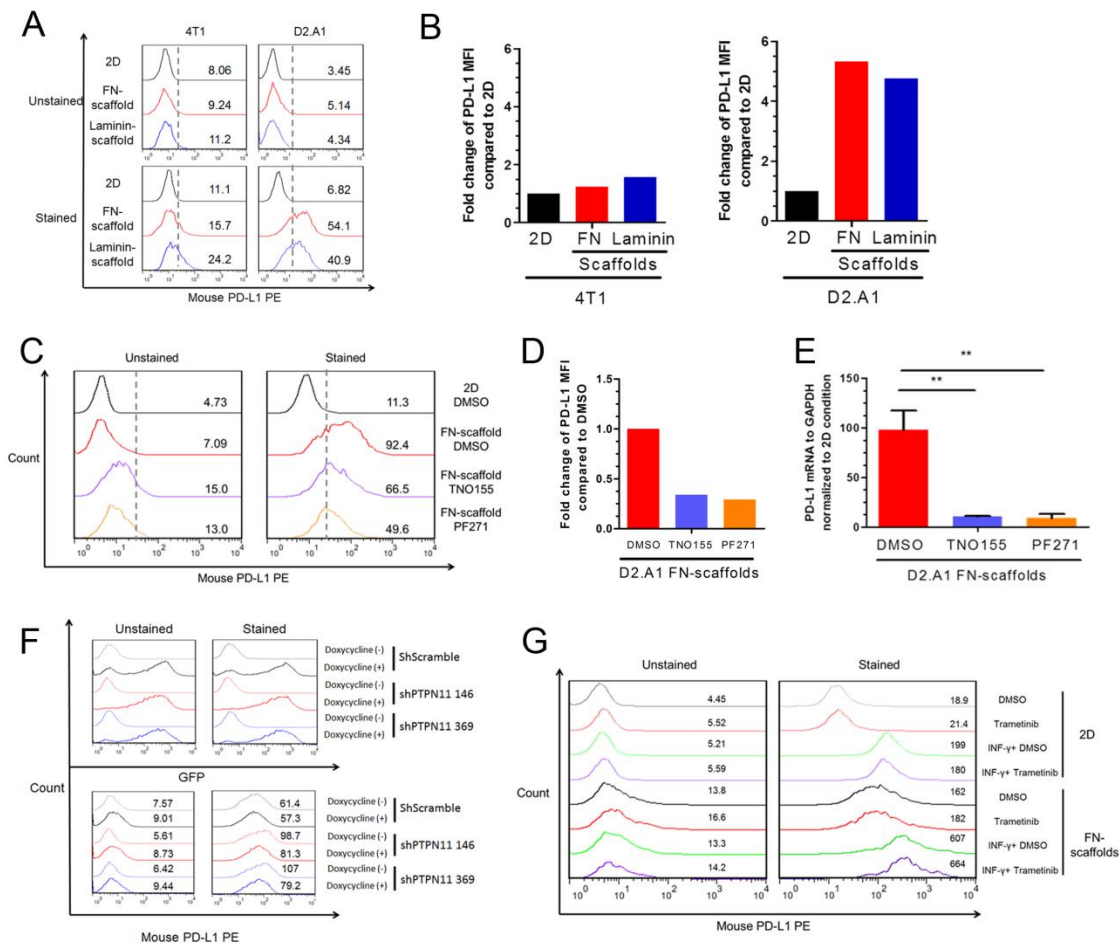


Figure 5.3. SHP2 blockade reduces PD-L1 induced by 3D culture environments in MBC cells. A, B, Cell surface analysis of PD-L1 using flow cytometer and bar graph comparing fold change of PD-L1 Mean MFI in 4T1 and D2.A1 cells cultured on fibronectin-coated or laminin-coated scaffolds compared to 2D. C, D, Cell surface analysis of PD-L1 using flow cytometer and bar graph comparing fold change of PD-L1 Mean MFI in D2.A1 cells induced by FN-scaffold 3D culture environment and treated with TNO155 and PF271. E, Bar graph comparing fold change of PD-L1 mRNA relative to GAPDH compared to 2D. ** $p < 0.01$, $n = 3$ as determined by a student's t-test. F, Cell surface analysis of eGFP and PD-L1 using flow cytometer showing the influence of cell surface PD-L1 by doxycycline inducible depletion of SHP2 in D2.A1 cells. G, Cell surface analysis of PD-L1 using flow cytometer comparing D2.A1 cells cultured on fibronectin-coated scaffolds treated with Trametinib and interferon- γ to 2D culture.

The results in this section suggested that PD-L1 was one of the signaling outputs of SHP2, downstream of 3D culture environment with ECM signaling. Unlike under the growth factor induction, ERK1/2 was not involved in the regulation of PD-L1 by SHP2 under 3D culture environment.

5.4.4 Expression of MHC class I depends on the balance between MAPK and STAT1 signaling regulated by SHP2 in MBC cells

Besides the Activated T-cell Proliferation, we found that Antigen Processing & Presentation was significantly more enriched in patients with lower levels of phosphorylation of SHP2 (Figure 4.1H). Hence, we focused on MHC class I regulated by interferon- γ , which is critical for antigen presentation.

Like the fact that the multiple RTKs were one of the signaling inputs of SHP2, we decided to treat the D2.A1 cells with growth factors in the presence of SHP2 inhibitors. Flow cytometry showed that FGF2 and PDGF significantly reduced the interferon- γ induced MHC class I, which could be rescued by TNO155 in D2.A1 cells (Figure 5.4A, 5.4B).

Similar results were observed in the BT549 cells with FGF2, EGF and TNO155 (Figure 5.4C, 5.4D).

Then, we focused on the mechanisms of how interferon- γ induced MHC class I was regulated via SHP2 under growth factors. Inspired by our previous model about the balance between MAPK and STAT1 signaling under EGF stimulation to control survival & apoptosis in MBC cells, we hypothesized that MHC class I might be regulated in a similar manner [132]. Immunoblotting showed that TNO155 reversed the induced phosphorylation of ERK1/2 and reduced phosphorylation of STAT1 at Y701 with FGF2 and PDGF in presence of interferon- γ in D2.A1 cells (Figure 5.4E). Moreover, Trametinib, but not Alpelisib (PI3K inhibitor) fully rescued interferon- γ induced MHC class I reduced by FGF2 and PDGF (Figure 5.4F).

These data suggested that SHP2 as a key node allowed the signaling from growth factors to flow through MAPK signaling, instead of STAT1 signaling, which reduced MHC class I.

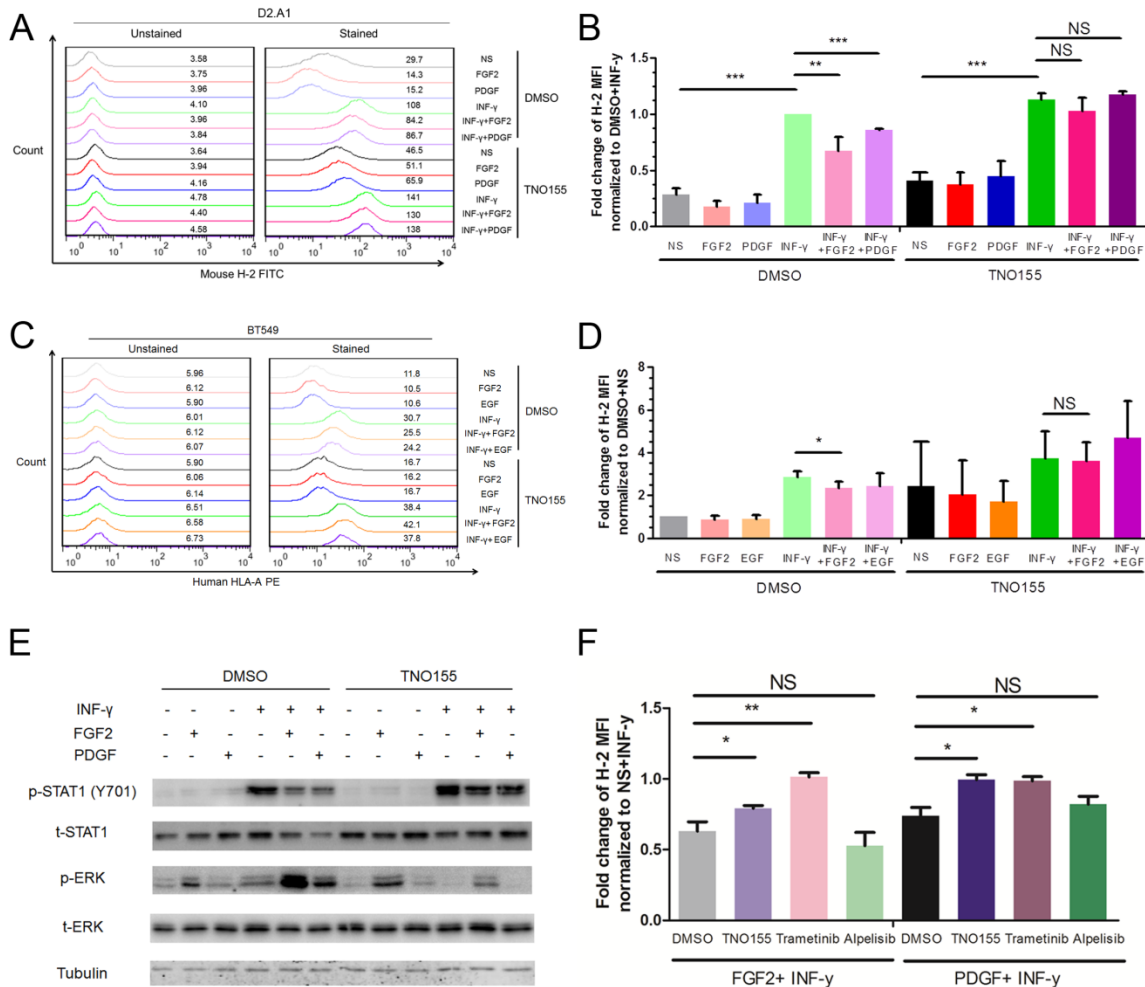


Figure 5.4. SHP2 regulates MHC class I expression via the balance between MAPK and STAT1 signaling. A, Cell surface analysis of H-2 in D2.A1 cells treated with different growth factors, interferon- γ and TNO155 using flow cytometer. B, Bar graph comparing fold change of H-2 MFI induced by different growth factors, interferon- γ and TNO155 compared to DMSO+ interferon- γ . NS: not significant, ** $p < 0.01$, *** $p < 0.001$, $n = 3$ as determined by a student's t-test. C, Cell surface analysis of HLA-A, B, C in BT549 cells treated with different growth factors, interferon- γ and TNO155 using flow cytometer. D, Bar graph comparing fold change of HLA-A, B, C MFI induced by different growth factors, interferon- γ and TNO155 compared to DMSO + no stem group. NS: not significant, * $p < 0.05$, $n = 3$ as determined by a student's t-test. E, Immunoblotting showing differential p-STAT1 and p-ERK in D2.A1 cells treated with different growth factors, interferon- γ and TNO155. F, Bar graph comparing fold change of H-2 MFI induced by different growth factors, interferon- γ and inhibitors compared to ns+ interferon- γ . NS: not significant, ** $p < 0.01$, *** $p < 0.001$, $n = 3$ as determined by a student's t-test.

5.5 Conclusions

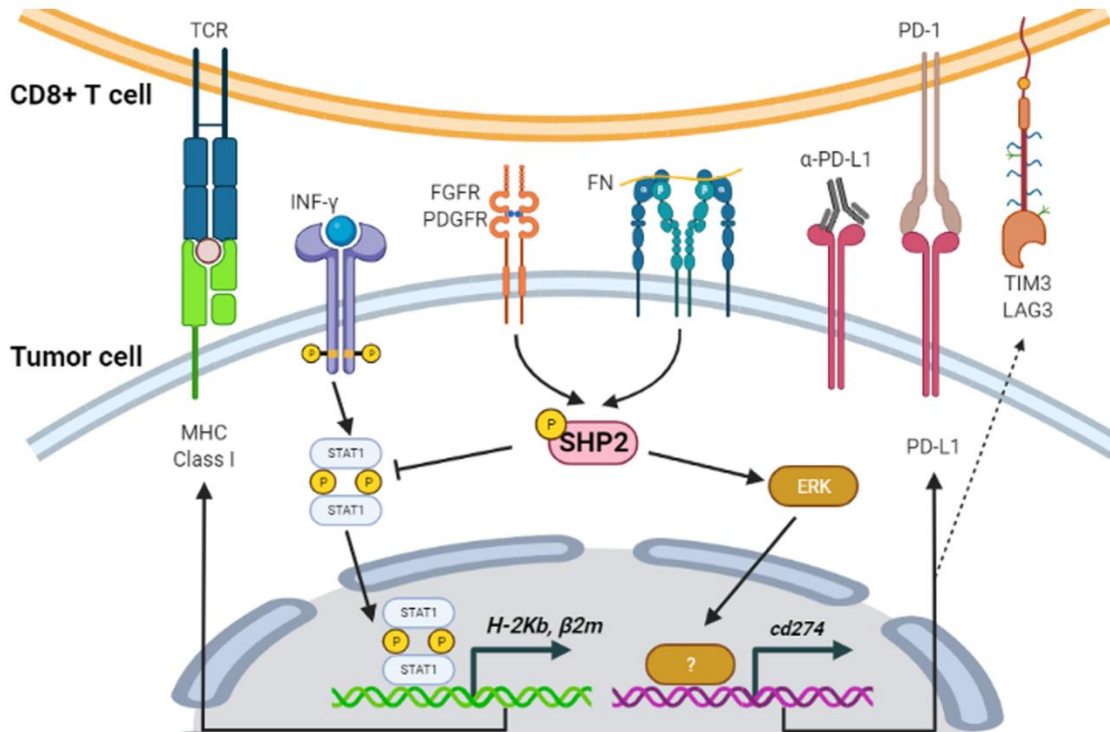


Figure 5.5. Tumor-cell autonomous SHP2 is a key signaling node in response to dynamic TME to induce immune suppression. SHP2 contributes to various downstream signaling pathways including PD-L1 and MHC class I to facilitate immune suppression in response to a varieties of additional signaling inputs in TME, such as growth factor receptor signaling. Figure was created using BioRender.

In this section, we first confirmed that MAPK and PI3K signaling pathways are the signaling outputs for SHP2. These signaling pathways contribute to the growth and survival of MBC cells. Moreover, we found that PD-L1 and HMC class I are the downstream signaling outputs in response to RTKs and ECM signaling. These signaling pathways contribute to the immune evasion of MBC cells. The SHP2-mediated transcriptional regulation of PD-L1 depends on the MAPK signaling under growth factors induction but not under the 3D culture conditions. The SHP2-mediated regulation of MHC I is based on the balance between MAPK and STAT1 signaling. In summary, we showed that tumor-cell autonomous SHP2 is a key signaling node in MBC cells to induce immune suppression with verities of signaling inputs within TME and tumor-cell intrinsic signaling outputs (Fig. 5.5).

CHAPTER 6. COMBINATION STRATEGIES WITH SHP2 INHIBITION TO TREAT METASTATIC BREAST CANCER

6.1 Disclaimer

Some parts of the material in this chapter had been prepared as a manuscript for submission to a peer-reviewed scientific journal for publication.

Some parts of material in this chapter were published in a peer-reviewed journal *Oncogene* in 2020. The citation information for the article is listed below. The article is open access and licensed under a Creative Commons Attribution 4.0 International License.

Chen, H., Libring, S., Ruddraraju, K.V. et al. SHP2 is a multifunctional therapeutic target in drug resistant metastatic breast cancer. *Oncogene* 39, 7166–7180 (2020).

6.2 Introduction

Although ICB is a promising therapeutic to treat MBC, the response rates of MBC patients to ICB are still limited. To enhance the response rates to ICBs, combination strategies were then introduced. Actually, the α -PD-L1 antibody, pembrolizumab has been recently approved combining with chemotherapies in triple-negative breast cancer [146, 147]. As tumor-cell autonomous SHP2 is the shared signaling node promoting MBC growth, survival and immune evasion, it is reasonable to combine SHP2 inhibitors with ICB to enhance the response rates in MBC patients.

In this chapter, we demonstrated the combination of SHP2 inhibitors with FGFR inhibitor or α -PD-L1 antibody inhibits the growth of MBC cells *in vivo*. The combination of SHP2 inhibitors with FGFR inhibitor is synergistic. The combination of SHP2 inhibitor with α -PD-L1 antibody relieves the T-cell exhaustion and adjusts the T-cell and TAMs composition.

6.3 Materials and Methods

6.3.1 Cell lines, culture conditions, drugs and reagents

The sources and culture conditions 4T1, D2.A1, HME2-LAPR, BT474, UACC812 and SK-BR-3 were previously described in chapter 2. The 4T1 cells with doxycycline inducible

shRNAs targeting PTPN11 were constructed as previously described in chapter 2. The sources and preparation methods for 11a-1, SHP099, TNO155, FIIN4 and luciferin were previously described in chapter 2 and chapter 3. The detailed information can also be found in APPENDIX A.

6.3.2 Cell viability assays and drug combination study

The cell viability assays under 2D and 3D culture conditions were described in chapter 2. The tumor sphere assays under 3D culture conditions were described in chapter 3. The combination treatments to MBC cells *in vitro* were prepared in full growth media by adding two drugs directly together. Vehicle at the same volume was added as control. The *in vitro* drug combination study to determine the simulation of synergism and antagonism was designed as described in the user guide of Compusyn 1.0 (ComboSyn Inc.; [148]). The small molecules combination pairs, FIIN4 plus SHP099 and FIIN4 plus 11a-1, were combined at a constant ratio. The Combination Index (CI) was calculated automatically with the software Compusyn 1.0. The CI from 0 to 1 was considered as synergism.

6.3.3 Animal care and combination experiments in vivo

All *in vivo* studies were conducted in 4–6 week old, female BALB/cJ mice purchased from Jackson Laboratories. In the combination studies with the 4T1 model, FIIN4 and SHP099 were administered via oral gavage at the indicated concentrations and frequencies. In the combination studies with the D2.A1 model, SHP099 was administered via oral gavage, and the α -PD-L1 antibodies were administered via intraperitoneal injection at the indicated concentrations and frequencies. Metastasis in both models was monitored using bioluminescent imaging after intraperitoneal injection of luciferin (GoldBio) using an AMI HT (Spectral Instruments). In the 4T1 model, the survival of the mice was monitored; while in the D2.A1 model, the mice were sacrificed at the end of the study to harvest the lungs and spleens for flow cytometry.

6.3.4 Pulmonary tumor and spleen isolation/digestion and flow cytometry

The standard protocol for isolation of single cells, staining and flow cytometry analysis was described in chapter 4. As no GFP was expressed in D2.A1 cells, FITC labeled primary

antibodies could be included in the panels of antibodies. The primary antibodies were all purchased from BioLegend. The panels of lymphoid antibodies included PerCP anti-mouse CD45 Antibody, FITC anti-mouse CD8a Antibody, Brilliant Violet 785™ anti-mouse CD4 Antibody, APC anti-mouse CD366 (Tim-3) Antibody, PE/Dazzle™ 594 anti-mouse CD279 (PD-1) Antibody and PE/Cyanine7 anti-mouse CD223 (LAG-3) Antibody. The panels of myeloid antibodies included PerCP anti-mouse CD45 Antibody, PE/Cyanine7 anti-mouse/human CD11b Antibody, Brilliant Violet 605™ anti-mouse F4/80 Antibody, PE anti-mouse CD274 (B7-H1, PD-L1) Antibody, Brilliant Violet 711™ anti-mouse CD206 (MMR) Antibody, PE/Dazzle™ 594 anti-mouse CD86 Antibody, APC/Cyanine7 anti-mouse Ly-6G Antibody and FITC anti-mouse Ly-6C Antibody. The detailed information for these antibodies can also be found in APPENDIX A Table A.5.

6.3.5 Statistical analysis

A student's t-test was used for comparing differences between two groups of measurements in *in vitro* assays and flow cytometry analysis. Error bars show the standard error of the mean. Group measurements of the *in vivo* assays were compared with a Mann-Whitney non-parametric test. Survival analysis was performed with GraphPad Prism 5.0 software, and the distributions of survival were compared by a log-rank test. No exclusion criteria were used in these studies, all statistical tests were appropriate as the groups being compared met the assumptions of the test and had similar variance.

6.4 Results

6.4.1 Combination of SHP2 inhibitors with FIIN4 blocks the growth of MBC cells under 2D culture conditions

In chapter 5, we found that the phosphorylation of FRS2 at Y436 induced by FGF2 was reduced by SHP099, and FIIN4 reduced the phosphorylation of SHP2 induced by FGF2 (Figure 5.1A). These data suggested that inhibition of SHP2 and FGFR might have compensation with each other to block the signaling events in MBC cells. Hence, we thought that the combination of SHP2 inhibitors with the FGFR inhibitor, FIIN4, might achieve enhanced inhibitory effects in the MBC cells.

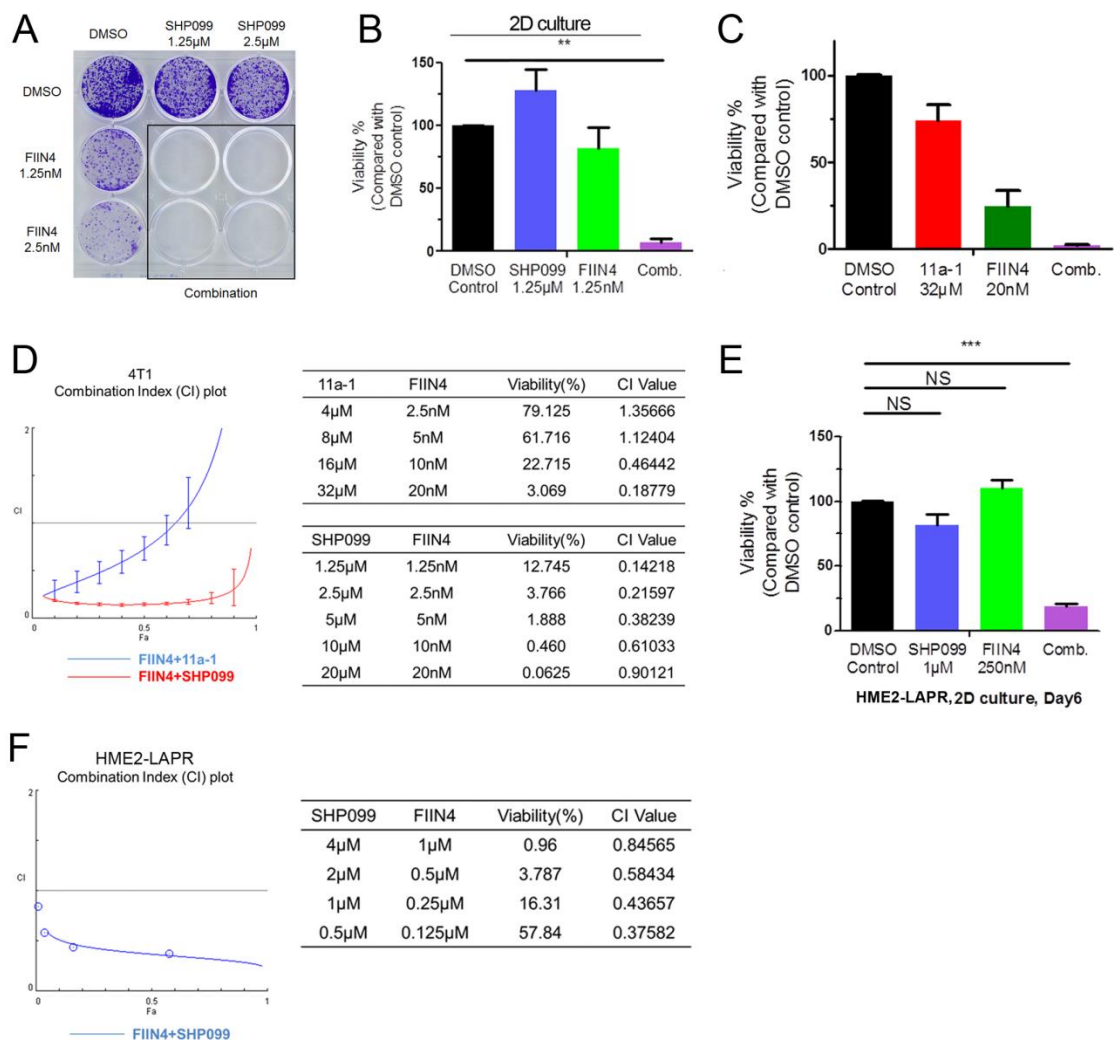


Figure 6.1. SHP2 inhibitors synergize with FIIN4 to inhibit the growth of 4T1 cells under 2D culture conditions. A, crystal violet visualization of the viable 4T1 cells treated with SHP099 and FIIN4 at indicated concentrations. B, C, 4T1 cells were seeded in 2D culture, and treated with the indicated concentrations of SHP099 (B) or 11a-1 (C), FIIN4 alone, or both compounds for 6 days. Data are the mean \pm s.e.m. $**p < 0.01$ as determined by a two-tail Student's t-test. D, Combination Index (CI) plots and charts of 4T1 cells treated with SHP2 inhibitors and FIIN4 generated by Compusyn 1.0. E, HME2-LAPR cells were seeded in 2D culture, and treated with SHP099, FIIN4 or a combination of the two compounds for 6 days. Data are the mean \pm s.e.m. NS: no Significance or $***p < 0.001$ as determined by a two-tail Student's t-test. F, CI plots and charts of SHP2 inhibitors and FIIN4 generated by Compusyn 1.0 in HME2-LAPR cells according to the 2D growth data.

To test our hypothesis, we first treated the 4T1 cells in the presence of SHP099 and FIIN4 under 2D culture conditions. With the crystal violet staining of the viable cells, it was clear that the combination of SHP099 and FIIN4 enhanced the growth inhibitory effects compared to single treatment alone (Figure 6.1A). Using concentrations of both compounds determined here to be below effective dosages against the 4T1 cells, we found that the combination of SHP099 and FIIN4 at these concentrations resulted in significant and complete blockade of 4T1 growth under 2D culture conditions (Figure 6.1B). Similar results were confirmed with another SHP2 inhibitor, 11a-1 (Figure 6.1C).

These data suggested that SHP2 inhibitors could combine with FIIN4 to enhance the growth inhibitory effects in MBC cells under 2D culture conditions.

6.4.2 SHP2 inhibitors synergize with FIIN4 in vitro

The next step was to determine whether SHP2 inhibitors and FIIN4 synergize with each other in the combination. Hence, we combined SHP2 inhibitors with FIIN4 at a constant ratio of concentrations, and determined the viabilities of the 4T1 cells with combinations at different concentrations. Using the COMPUSYN 1.0 software, we established a combination index (CI) plot for the 4T1 cells showing combination indexes at different cell viabilities (Figure 6.1D). The combination index ranging from 0 to 1 indicated synergism between the two drugs. As the tables are shown in the right panel of Figure 6.1D, 11a-1 at 32 μ M and FIIN4 at 20nM led to a CI at 0.18779, and SHP099 at 1.25 μ M and FIIN4 at 1.25nM led to a CI at 0.14218. Both of them suggested synergistic effects when combining SHP2 inhibitors with FIIN4. The results were also consistent with the enhanced inhibitory effects of combination under 2D culture conditions (Figure 6.1B, 6.1C). Similar results were next observed in HME2-LAPR cells. SHP099 at 1 μ M and FIIN4 at 250nM led to a CI at 0.43657 and enhanced significant growth inhibition (Figure 6.1E, 6.1F).

We also confirmed the synergistic effects of SHP2 inhibitors and FIIN4 in other human MBC cells. In BT474 cells, 11a-1 at 0.625 μ M and FIIN4 at 62.5nM led to a CI at 0.44720, and SHP099 at 20 μ M and FIIN4 at 2 μ M led to a CI at 0.98449 (Figure 6.2A). In UACC812 cells, 11a-1 at 0.625 μ M and FIIN4 at 31.25nM led to a CI at 0.51103, and SHP099 at 20 μ M and FIIN4 at 1 μ M led to a CI at 0.31261 (Figure 6.2B). In SK-BR-3 cells, SHP099 at 20 μ M and FIIN4 at 1 μ M led to a CI at 0.52509 (Figure 6.2C).

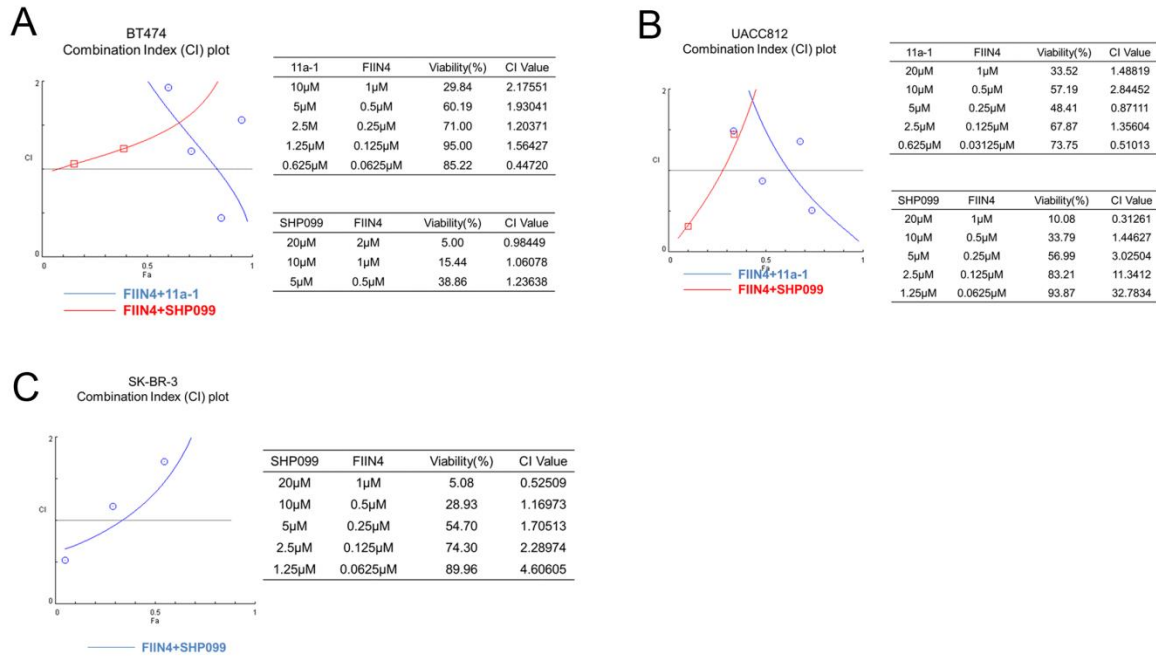


Figure 6.2. Inhibition of SHP2 synergizes with FGFR inhibition in other MBC cells under 2D culture conditions. CI plots and charts of SHP2 inhibitors and FIIN4 generated by Compusyn 1.0 in BT474 (A), SK-BR-3 (B) and UACC812 (C) cells according to the corresponding 2D growth data in these cells.

These data suggested that SHP2 inhibitors synergized with FIIN4 to block the growth of MBC cells under 2D culture conditions.

6.4.3 Combination of SHP2 inhibitors with FIIN4 blocks the growth of MBC cells under 3D culture conditions

In chapter 2, we found that the growth inhibitory effects of SHP2 inhibitors were enhanced under 3D culture conditions compared to 2D. We thought that the combination might achieve another enhancement under 3D culture conditions.

To test our hypothesis, we implemented the 3D culture and 3D tumor sphere assays introduced in chapters 2 and 3. We found that the combination of SHP099 at 1µM and FIIN4 at 4nM completely blocks the growth of 4T1 cells under 3D culture conditions (Figure 6.3A, 6.3B). The combination of 11a-1 at 2µM and FIIN4 at 4nM also significantly reduced the growth of 4T1 cells under 3D conditions (Figure 6.3C, 6.3D). In the D2.A1 cells, we also confirmed the

combination effects of SHP099 plus FIIN4 (Figure 6.3E, 6.3F) and 11a-1 plus FIIN4 (Figure 6.3G, 6.3H) under 3D culture conditions. We next shift the gear to 3D tumor sphere assays in D2.A1 cells. We found that the combination of 11a-1 at 10 μ M and FIIN4 at 200nM significantly reduced the spheroid growth in D2.A1 cells (Figure 6.4A, 6.4B).

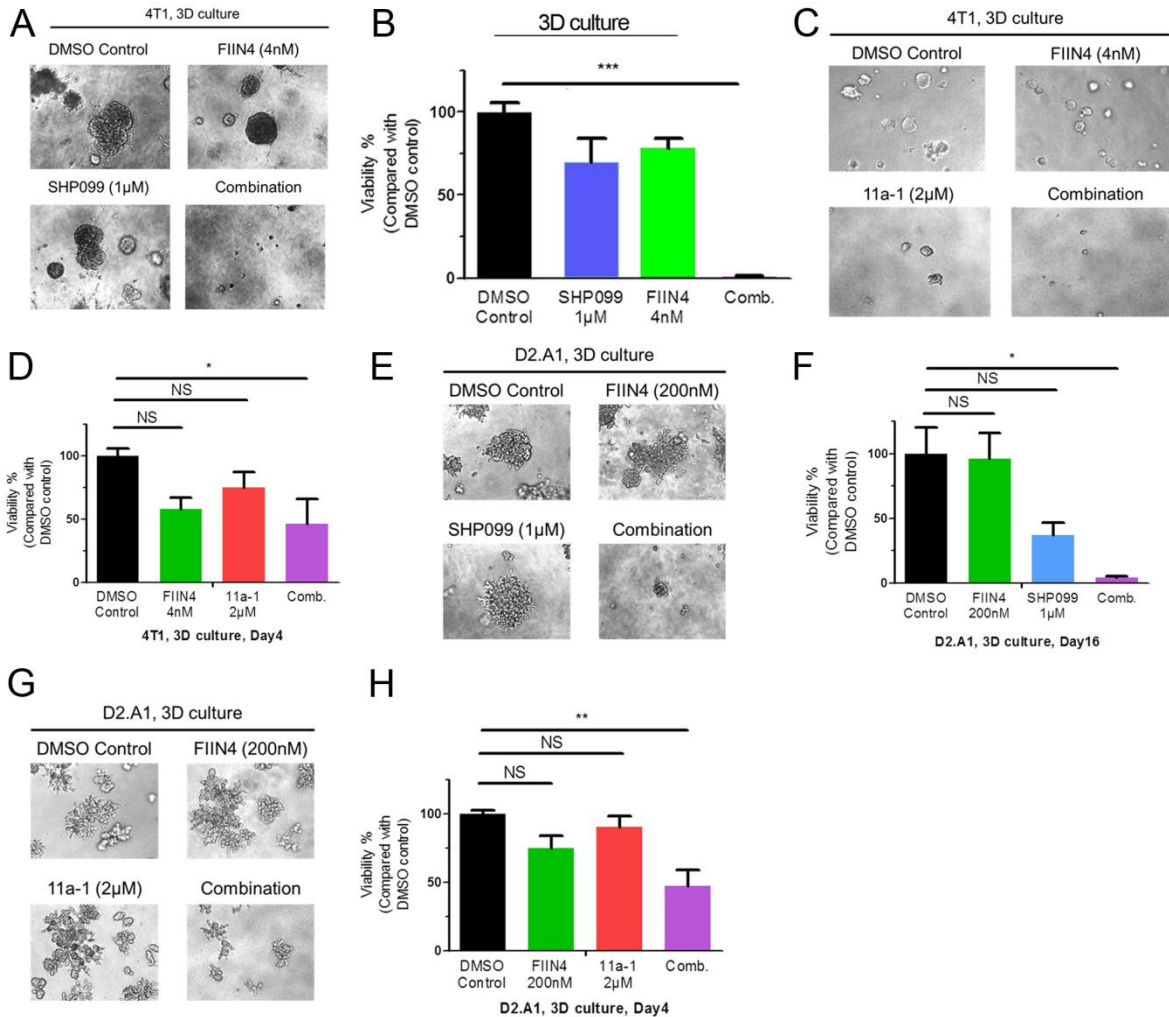


Figure 6.3. SHP2 inhibitors enhance the effects of FIIN4 to inhibit the growth of MBC cells under 3D culture conditions. Single-cell suspensions of 4T1 cells (A-D) and D2.A1 cells (E-H) were plated under 3D culture conditions and treated with the indicated compounds alone or in combination. Media containing DMSO was used as a vehicle control. Data are the mean \pm s.e.m. of at least three independent experiments where NS: no significance, * p <0.05, ** p <0.01, *** p <0.001 as determined by a two-tail Student's t-test.

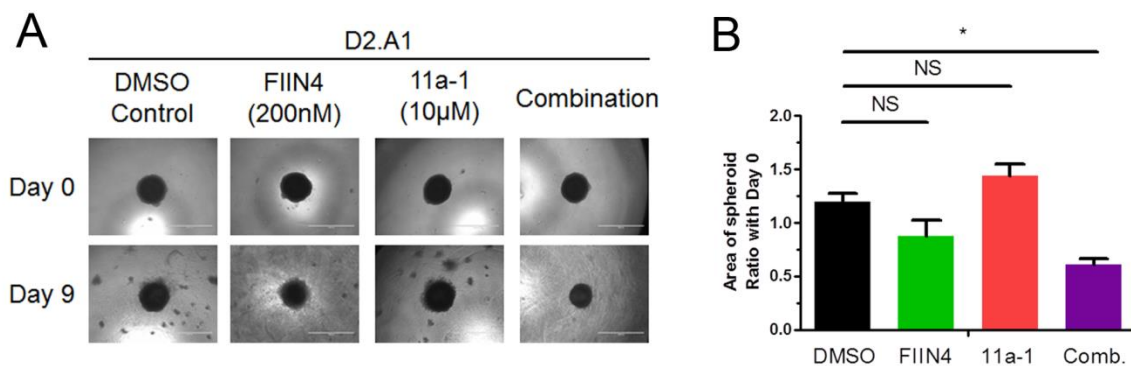


Figure 6.4. SHP2 inhibitors enhance the effects of FIIN4 to inhibit the tumor spheres growth of MBC cells. D2.A1 spheres were treated with FIIN4 or 11a-1 at indicated concentrations alone, or combination. The area of the sphere 9 days after placement on the ECM was measured from the photos (A), and these values were normalized to the initial sphere size at Day 0 (B). In all panels, data are the mean \pm s.e.m. (n = 3), NS as no significance, *p < 0.05 as determined by a student's t-test.

These data enhanced our conclusion that SHP2 inhibitors synergized with FIIN4 to enhance the growth inhibitory effects in MBC cells.

6.4.4 Pharmacological SHP2 inhibition synergizes with FIIN4 in vivo

As we identified the possible synergistic combination of SHP2 inhibitors and FIIN4 to block the growth of MBC cells *in vitro*, we next extended this combined therapeutic approach *in vivo* by treating late-stage 4T1 metastases with SHP099:FIIN4 combination therapy. As opposed to our approach in Chapter 2, the mice were left untreated for 5 additional days following primary tumor removal to allow metastatic outgrowth to progress.

Using this approach, we found that only the combination of SHP099 and FIIN4 was able to significantly delay late-stage metastatic progression and reduce the pulmonary metastasis, determined by luminescence live image (Figure 6.5A, 6.5B). The combination therapy also significantly extended animal survival as compared to control (Figure 6.5C).

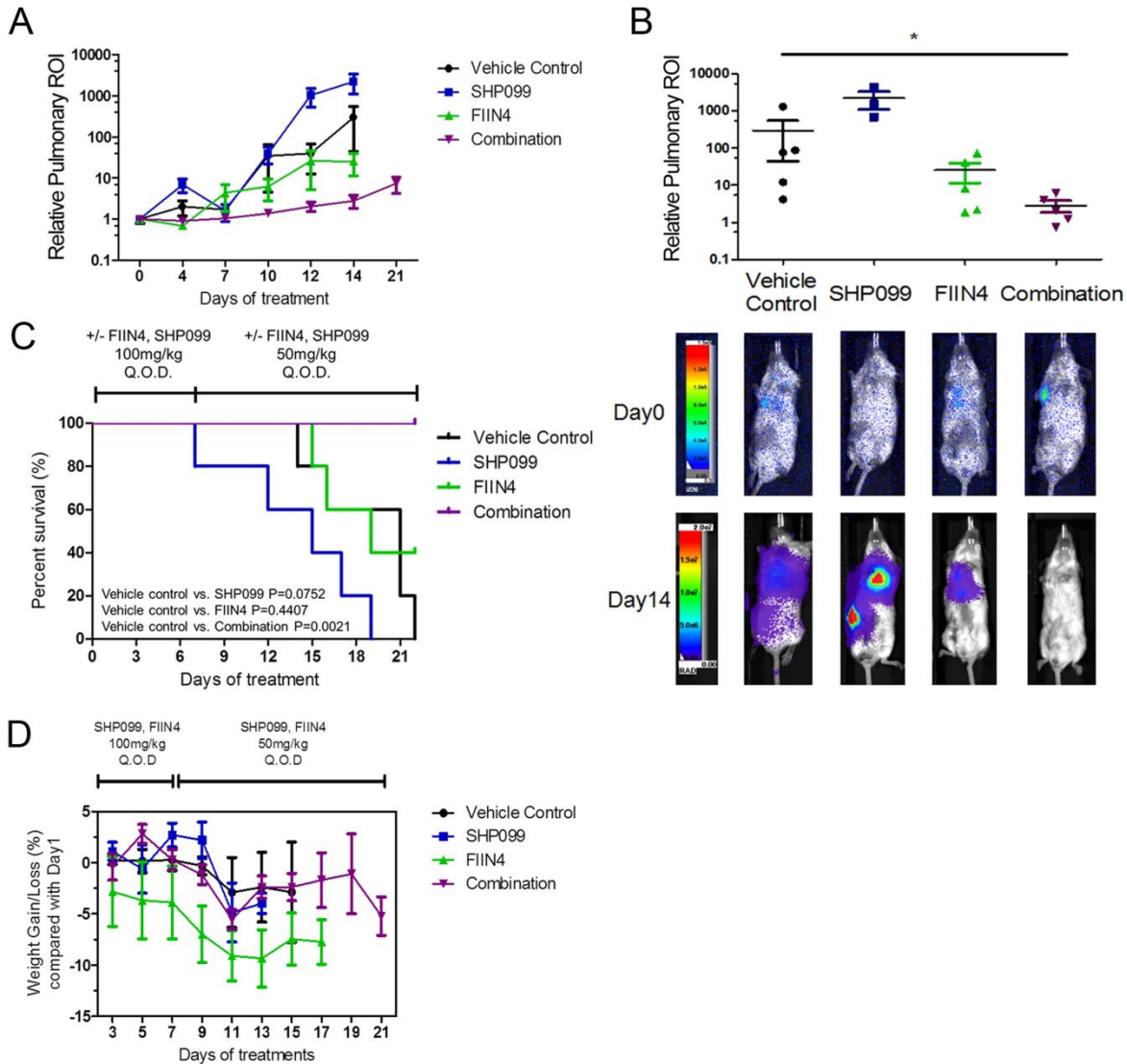


Figure 6.5. Inhibition of SHP2 synergizes with FIIN4 *in vivo*. A, Bioluminescence values for regions of interest (ROI) in the lungs from mice bearing 4T1 metastases relative to values at the initiation of treatment. Data are the mean \pm s.e.m. of 5 mice per treatment group. B, Representative bioluminescent images of metastasis (bottom) and quantified pulmonary ROI values from mice bearing 4T1 metastases 14 days after treatment initiation (top). Data are the mean \pm s.e.m. of 5 mice per group resulting in $*p < 0.05$ as determined by a two-tailed Mann Whitney test. C, Differential survival analyses of tumor bearing mice in each treatment group, resulting in the indicated p-values as determined by a log-rank test. D, Mice bearing 4T1 metastases were treated with SHP099 and FIIN4 alone or in combination as indicated. Data are the mean \pm s.d., body weights (n=5) normalized to day 1 of treatment.

Moreover, no significant weight loss was observed in the combination group, suggesting that the therapeutic protocol did not result in unacceptable toxicity (Figure 6.5D).

These data demonstrated the efficacy and enhanced the feasibility of combining SHP2 inhibitory compounds with FGFR-targeted kinase inhibitors for the treatment of MBC.

6.4.5 Pharmacological SHP2 inhibition sensitizes MBC cells in lungs to α -PD-L1 *in vivo*

In chapters 4 and 5, we found that tumor-cell autonomous SHP2 supported an immunosuppressive TME by regulating PD-L1 and MHC class I. Hence, we hypothesized that inhibition of SHP2 might enhance the effect of immune checkpoint blockade (ICB) by relieving the immunosuppressive TME.

To test the hypothesis, we first utilized a tail vein injection to inoculate the mice with D2.A1 cells as we did in chapter 2.

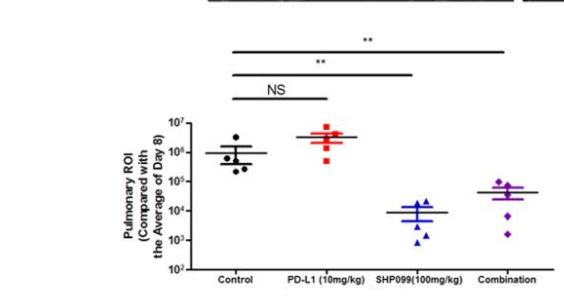
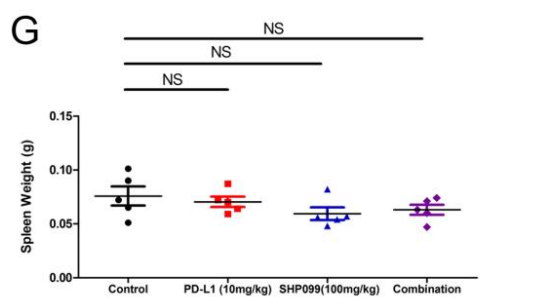
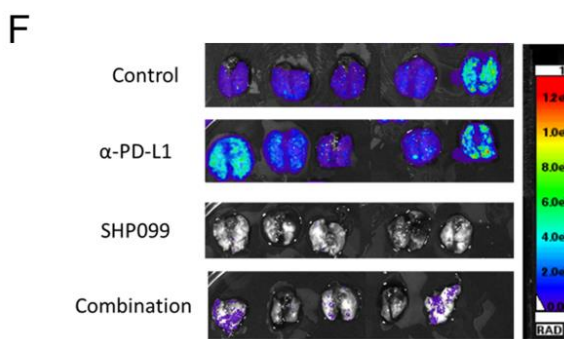
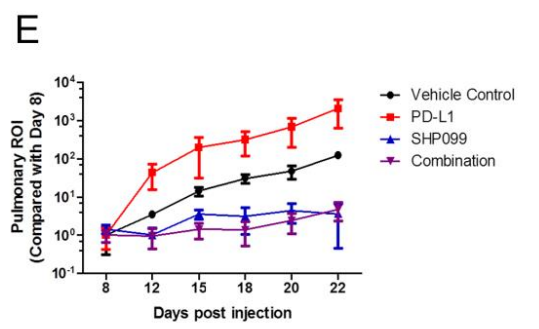
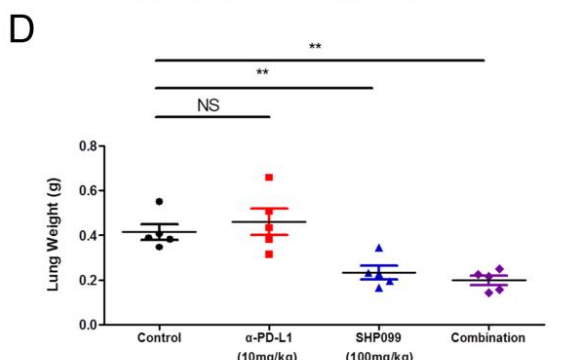
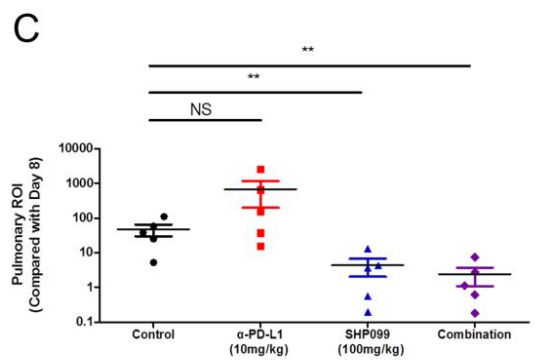
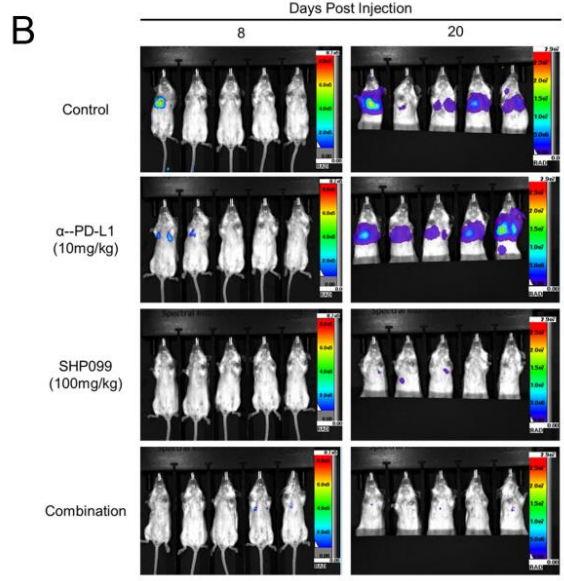
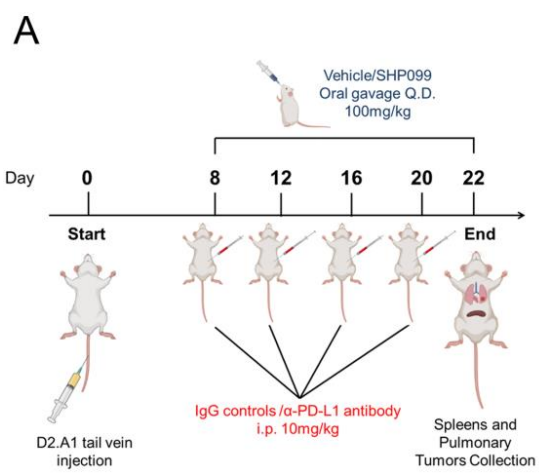
To evaluate the combination efficacy of SHP2 inhibitors and ICB, the mice were treated with SHP099 and α -PD-L1 antibodies according to the treatment plan one week after the tail vein injection (Figure 6.6A).

As determined by luminescence live imaging, the 12-day treatment course of α -PD-L1 antibody did not significantly inhibit the pulmonary growth of D2.A1 cells; while the progression of D2.A1 cells in lungs was significantly reduced and delayed when combining α -PD-L1 antibody with SHP099 (Figure 6.6B, 6.6C, 6.6E). The wet lung weights and corresponding luminescence live imaging also confirmed the reduction of the metastatic burden in the lungs with the combination therapies (Figure 6.6D, 6.6F).

Moreover, we did not observe a significant change in spleen weight with the combination therapy (Figure 6.6G).

These data suggested that D2.A1 was an ideal MBC model in syngeneic hosts to mimic resistance to ICB, which can be sensitized to ICB via systemic SHP2 inhibition.

Figure 6.6. Systemic inhibition of SHP2 sensitizes D2.A1 cells to α -PD-L1 antibody *in vivo* A, Schematic of the study combining SHP099 with α -PD-L1 antibody to inhibit pulmonary tumor growth in D2.A1 model. BALB/c mice (n = 5 / group) were injected with 1 million/mouse D2.A1 cells via tail veins. Cells were allowed to seed for 1 week, and the mice were treated with the doses and frequency described on the schematic. B, Representative bioluminescent images of pulmonary D2.A1 growth on Day 8 and Day 20 post injection. C, Bioluminescent values from pulmonary ROI quantified as the ratio of day 20 to day 8 post injection $**p < 0.01$, n = 5 mice per group as determined by a Mann Whitney test. D, Plots comparing the wet lung weights of the mice on day 22 post injection, $**p < 0.01$, n = 5 mice per group as determined by a Mann Whitney test. E, Bioluminescence values for pulmonary ROI from mice with D2.A1 cell growth in lungs normalized to Day 8 post injection. Data are the mean \pm s.e.m. of 5 mice per treatment group. F, Representative bioluminescent images of the lungs at Day 22 post injection (top) and quantified ROI values of the lungs relative to the average ROI values of Day 8 post injection (bottom). Data are the individual plots and mean \pm s.e.m. of 5 mice per group, NS: not significant, $**p < 0.01$ determined by a Mann Whitney test. G, Dot plot showing the spleen weights of the mice at Day 22 post injection. Data are the individual plots and mean \pm s.e.m. of 5 mice per group, NS: not significant determined by a Mann Whitney test.



6.4.6 Pharmacological SHP2 inhibition relieves T-cell exhaustion induced by α -PD-L1

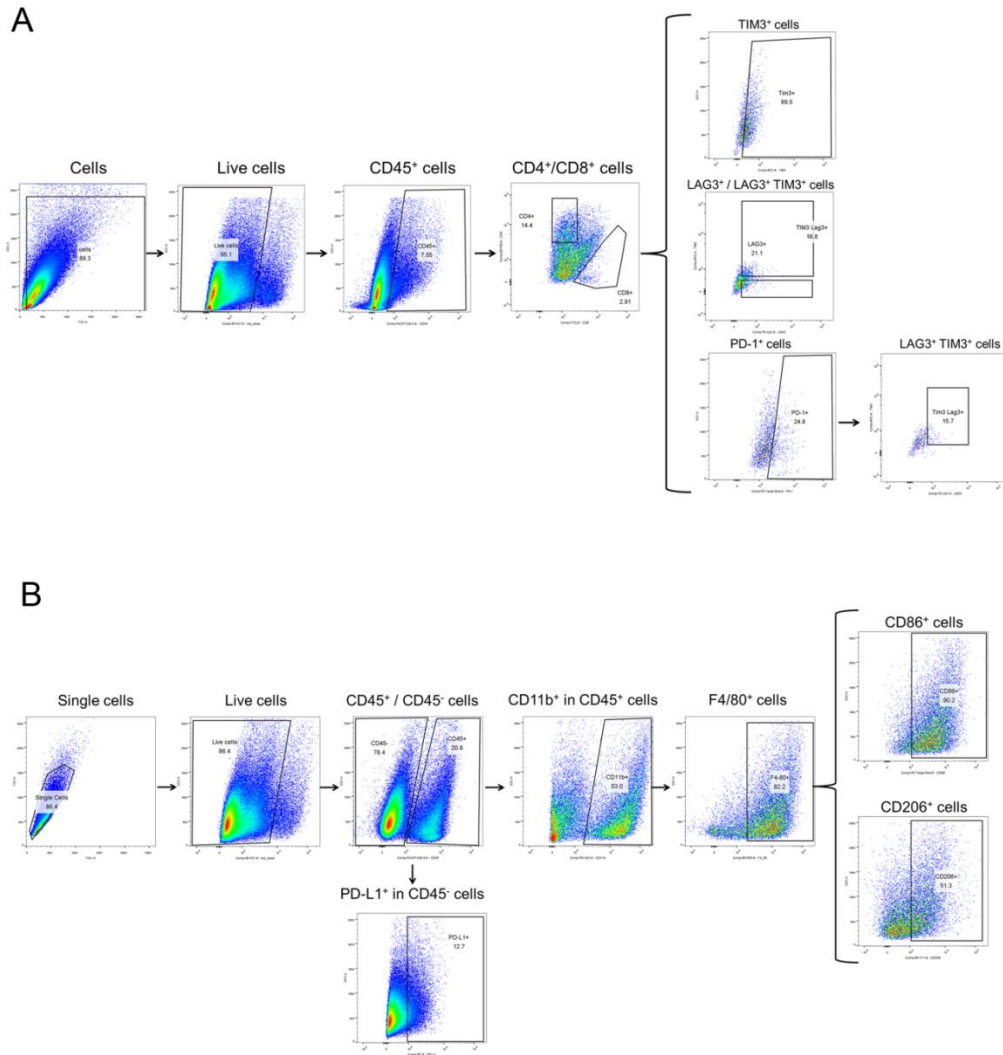


Figure 6.7. The gating ancestry for the populations in the study of D2.A1 model. A, Splens and tumors from lung tissues were isolated and digested into single cell suspensions, and stained with lymphoid antibody panel as described in the materials and methods. These cells were sequentially gated as shown to identify a population of cells, live cells, CD45⁺ and CD4⁺/CD8⁺ cells prior to analysis of TIM3⁺, LAG3⁺, LAG3⁺TIM3⁺ and PD-1⁺. The LAG3⁺TIM3⁺ cells were also gated under PD-1⁺ population. B, Tumors from lung tissues were isolated and digested into single cell suspensions, and stained with myeloid antibody panel as described in the materials and methods. These cells were sequentially gated as shown to identify a population of single cells, live cells, CD45⁺/CD45⁻, CD11b⁺ and F4/80⁺ cells prior to analysis of CD86⁺ and CD206⁺. The PD-L1⁺ cells were also gated under CD45⁻ population.

In chapter 4, we demonstrated that tumor-cell autonomous SHP2 could adjust the T cell composition and induce T-cell exhaustion to support an immunosuppressive TME. Hence, we focused on the T cell composition and T-cell exhaustion markers again to investigate the influence of SHP099: α -PD-L1 combination therapy on immune profiles.

To identify how the TME and peripheral immune composition were reprogrammed by systemic SHP2 inhibition following the combination treatments, we collected the pulmonary tumors and spleens of the mice after 14-day treatments. The single cells were stained with different panels of antibodies, and analyzed by flow cytometry with desired gating strategies to identify desired immune populations (Figure 6.7A, 6.7B).

Flow cytometry revealed that the percentage of CD4⁺ in CD45⁺ cells in spleens significantly decreased with a combination of SHP099 and α -PD-L1 antibody; while the percentage of CD8⁺ in CD45⁺ cells in spleens significantly increased (Figure 6.8A). Similar results in the percentage of CD4⁺ population were observed in the tumor-Infiltrating lymphocytes from pulmonary tumors, but there was no difference in the percentage of CD8⁺ population (Figure 6.8C). These data indicated that the combination of SHP099 and α -PD-L1 antibody adjusted the peripheral and tumor-infiltrated lymphocytes composition.

To further investigate the activities of these T cells, we focused on LAG3 and TIM3 as we did in chapter 4. In spleens, the percentage of LAG3⁺ and TIM3⁺ in CD4⁺ cells was significantly reduced with the combination of SHP099 and α -PD-L1 antibody (Figure 6.8B). In pulmonary tumors, the percentage of TIM3⁺ and LAG3⁺TIM3⁺ in CD4⁺ cells was induced by α -PD-L1 antibody, which was significantly abolished in combining with SHP099 (Figure 6.8D). Meanwhile, the percentage of LAG3⁺, TIM3⁺ and LAG3⁺TIM3⁺ in CD8⁺ cells and the percentage of LAG3⁺TIM3⁺ in PD1⁺CD8⁺ cells were also enhanced by α -PD-L1 antibody, which was significantly attenuated with SHP099 (Figure 6.8E). These data suggested that SHP099 relieved the T-cell exhaustion induced by α -PD-L1 antibody.

In chapter 5, we also identified that PD-L1 was regulated by tumor-cell autonomous SHP2. Hence, we also analyzed the percentage of PD-L1 in CD45⁻ cells from the pulmonary tumors. The percentage of PD-L1⁺ in CD45⁻ cells was significantly reduced by all the treatments, and the reduction was mostly enhanced with the combination therapy (Figure 6.8F). These data not only enhanced the connection of SHP2 inhibition with PD-L1, but also confirmed that the α -PD-L1 antibody was on target in the study.

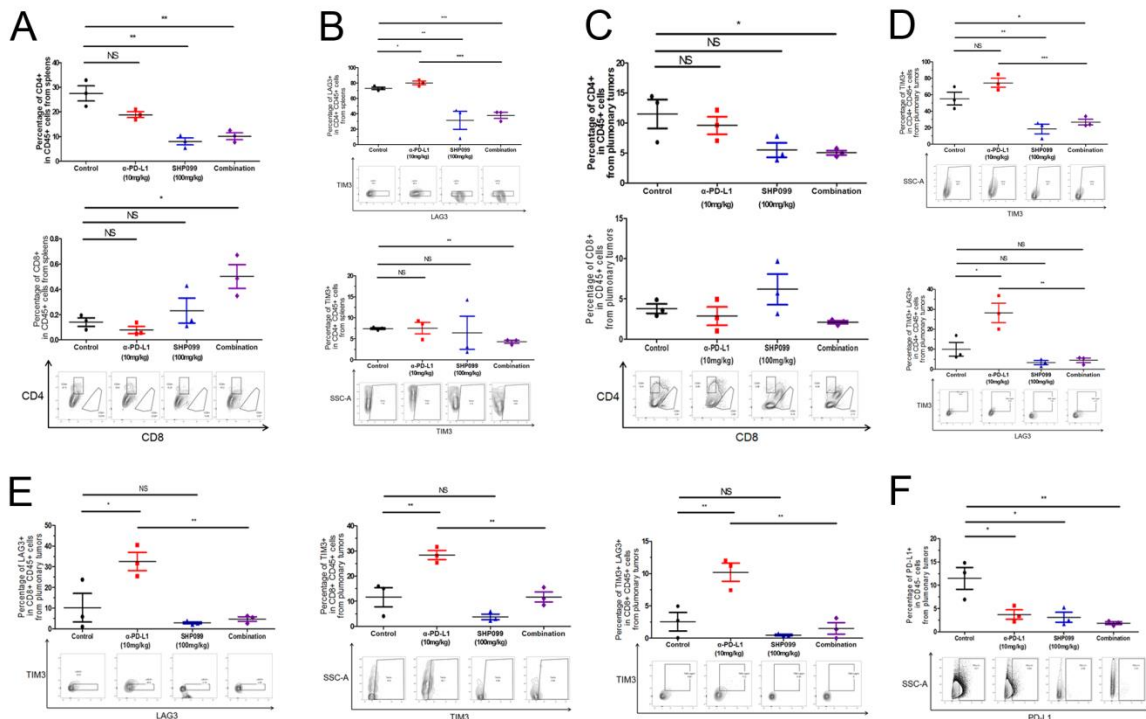


Figure 6.8. Combination of SHP099 and α -PD-L1 relieves T-cell exhaustion. A, C Representative dot plots and quantification of CD4⁺ and CD8⁺ population as a frequency of CD45⁺ cells in isolated spleens (A) and lung tissues (C) of each group. B, Representative dot plots and quantification of LAG3⁺ and TIM3⁺ population as a frequency of CD45⁺CD4⁺ cells in isolated spleens of each group. D, E, Representative dot plots and quantification of LAG3⁺, TIM3⁺ and LAG3⁺TIM3⁺ population as a frequency of CD45⁺CD4⁺ cells (D) and CD45⁺CD8⁺ cells (E) in isolated lung tissues of each group. F, Representative dot plots and quantification of PD-L1⁺ population as a frequency of CD45⁺ cells in isolated lung tissues of each group. In all panels, *p<0.05, **p<0.01, ***p<0.001, n=3 as determined by a student's t-test.

6.4.7 Combination of SHP099 and α -PD-L1 adjusted TAMs composition

In chapter 4, we found that depletion of tumor-cell autonomous SHP2 adjusted the TAMs composition by increasing the ratio of M1/M2. He thought that the SHP099: α -PD-L1 combination therapy might also be capable of adjusting the TAMs composition similarly.

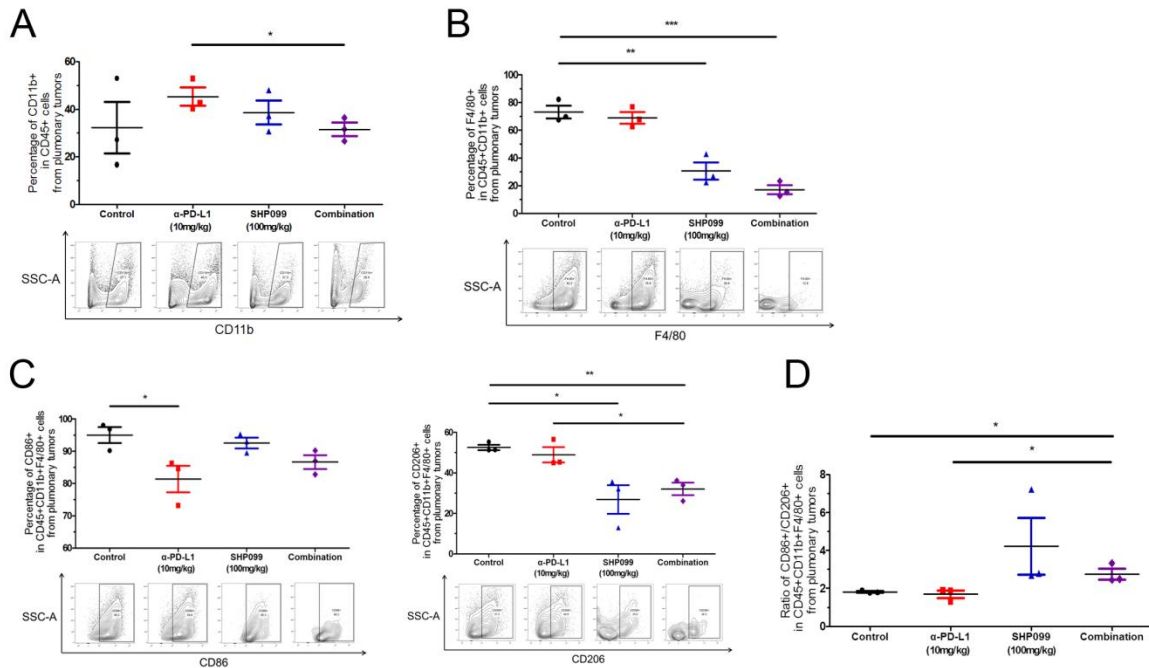


Figure 6.9. Combination of SHP099 and α -PD-L1 adjusts the composition of tumor associated macrophages. A, Representative dot plots and quantification of CD11b⁺ population as a frequency of CD45⁺ cells in isolated lung tissues of each group. B, Representative dot plots and quantification of F4/80⁺ population as a frequency of CD45⁺CD11b⁺ cells in isolated lung tissues of each group. C, Representative dot plots and quantification of CD86⁺ and CD206⁺ population as a frequency of CD45⁺CD11b⁺F4/80⁺ cells in isolated lung tissues of each group. D, Plots comparing the ratio of CD86⁺ and CD206⁺. In all panels, *p<0.05, **p<0.01, ***p<0.001, n=3 as determined by a student's t-test.

To test our hypothesis, we analyzed the single cells from the pulmonary tumors with flow cytometry. The flow cytometry revealed that the SHP099: α -PD-L1 combination therapy significantly reduced the percentage of CD11b⁺ monocytes in CD45⁺ cells compared to the α -PD-L1 group (Figure 6.9A). The percentage of TAMs (F4/80⁺ in CD11b⁺CD45⁺ cells) was significantly reduced with SHP099 and SHP099: α -PD-L1 combination therapy (Figure 6.9B). This result was not consistent with the one in chapter 4, in which there was no significant change in the TAMs composition with depletion of tumor-cell autonomous SHP2 (Figure 4.5B). The result here suggested that systemic SHP2 inhibition might influence the other cells except tumor cells to adjust the percentage of TAMs. We next focused on the M1/M2 ratio in the TAMs. The percentage of M1 macrophages (CD86⁺ in F4/80⁺CD11b⁺CD45⁺ cells) was significantly reduced

by the α -PD-L1 antibody, which was rescued by SHP099; while the percentage of M2 macrophages (CD206⁺ in F4/80⁺CD11b⁺CD45⁺ cells) was significantly reduced by SHP099 and SHP099: α -PD-L1 combination therapy (Figure 6.9C). Hence, the ratio of M1/M2 macrophages increased with SHP099 and SHP099: α -PD-L1 combination therapy (Figure 6.9D).

These data demonstrated that systemic SHP2 inhibition and SHP099: α -PD-L1 combination therapy reduced TAMs and adjusted their composition via increasing the M1/M2 ratio. The changes of TAMs compositions by SHP099 and SHP099: α -PD-L1 combination therapies enhanced the anti-tumor immunity to reduce the MBC progression.

6.5 Conclusions

In this section, we found that SHP099 synergizes with a FGFR inhibitor, FIIN4, to inhibit the growth of MBC cells *in vitro* and *in vivo*. SHP099 also sensitizes MBC cells in the lungs to α -PD-L1 antibody *in vivo*. SHP099 relieves T-cell exhaustion induced by α -PD-L1 antibody and adjusts T-cell composition and TAMs composition.

CHAPTER 7. DISCUSSION AND FUTURE DIRECTIONS

7.1 Disclaimer

Some parts of the material in this chapter had been prepared as a manuscript for submission to a peer-reviewed scientific journal for publication.

Some parts of material in this chapter were published in a peer-reviewed journal *Oncogene* in 2020. The citation information for the article is listed below. The article is open access and licensed under a Creative Commons Attribution 4.0 International License.

Chen, H., Libring, S., Ruddraraju, K.V. et al. SHP2 is a multifunctional therapeutic target in drug resistant metastatic breast cancer. *Oncogene* 39, 7166–7180 (2020).

7.2 SHP2 is dynamic in response to varies signaling inputs

Acquired drug resistance and limited response to ICB when treating MBC remain challenges in clinics, which need the development of novel therapies. Metastatic progression and drug resistance are usually driven by signaling networks inside the tumor cells, such as RTKs and ECM signaling pathways. The complexity of the signaling network emphasizes the importance of finding shared nodes as multifunctional therapeutic targets to treat MBC.

We found that SHP2 facilitated multiple RTKs signaling to promote downstream signaling cascades, including PI3K and MAPK pathways. Our observation that SHP2 is involved in RTKs signaling is also consistent with the other studies demonstrating that SHP2 is one of the signaling adapters for RTKs to drive signaling cascades in response to multiple growth factors, which interacts with Growth factor receptor-bound protein 2 (Grb2), Gab1 and FRS2 [98, 149-152]. This event is critical for maintaining drug resistance in ERK1/2-dependent cancer cells [153].

We observed that the phosphorylation of SHP2 at Y542 is elevated with multiple growth factors induction in a dynamic manner. It is worthwhile to highlight that the induction of SHP2 phosphorylation by multiple growth factors is transient (time-dependent), context-dependent (varies by cell lines) and independent of RTKs expression levels in MBC cells. The result here is consistent with the previous reports that not all growth factors can induce phosphorylation of SHP2 [93, 154]. It is interesting to further investigate why the phosphorylation of SHP2 is transient with the induction of multiple growth factors. There are at least two potential

hypotheses we can provide here. One hypothesis is that the phosphorylation of SHP2 decreases together with the activation of RTKs. In this case, immunoblotting to identify the phosphorylation levels of RTKs is a good start. This hypothesis is supported by the report indicating that tyrosine-phosphorylated RTKs, such as PDGFR β , are sufficient to induce SHP2 activation [155]. Another hypothesis is that some other phosphatases remove the phosphorylation of SHP2 or RTKs, which keeps a balance between the activation of RTKs. This hypothesis is supported by a recent report suggesting that SHP2 can dephosphorylate itself, which is inhibited by a SHP2 inhibitor [156]. To test this hypothesis, we can treat the MBC cells with SHP2 inhibitors to observe whether the induction of SHP2 phosphorylation at Y542 is prolonged.

Besides the time-dependent transient induction, previous reports also demonstrate that growth factors but not all of them contribute to phosphorylation of SHP2, and our results suggest that it varies by different RTKs expressed by the cells [93]. Current models suggest that FRS2 is upstream of SHP2 in driving FGFR signaling and MAPK signaling is the major pathway affected. While our results indicate that SHP2 is also required for FRS2 activation, and the PI3K pathway is regulated by the signaling complex as well. It is interesting to investigate the real substrates of activated SHP2 in the signaling complex in the future. In fact, a recent report with time-resolved phosphoproteomics and a study with SHP2 transforming mutant T507K have revealed several new substrate of SHP2, including occludin, phosphoinositide phospholipase C γ 2 (PLC γ 2) and sprouty1 [157, 158]. As occludin is a key enzyme to regulate cell-cell junctions, it is reasonable to hypothesize that SHP2 is involved in the regulation of EMT in response to TGF- β , which has been proved by several studies [159, 160]. Moreover, recent study shows the role of SHP2, together with FGFR signaling, in regulating protein in phosphoinositide phospholipase C family [161].

In addition to the substrates of SHP2, a recent report also focuses on the phosphatase-activity-independent functions of SHP2 [162]. It is worthwhile for us to introduce SHP2 catalytic site dead mutant C459S and constitutive active SHP2 mutant E76A into our model to investigate whether SHP2 catalytic activation is required for the RTKs signaling in MBC cells [163].

Our results demonstrate that phosphorylation of SHP2 at Y542 is elevated under 3D culture conditions with ECM signaling activation. This result explains our observation that growth inhibitory effects of SHP2 inhibitors are enhanced under 3D culture conditions compared

to 2D. This is an unusual observation for small molecules because 3D culture conditions typically contribute to a drug resistant phenotype. These results may suggest SHP2 inhibition could synergize with several therapeutics via this inhibition of ECM-mediated cell survival. In fact, we have observed that SHP2 inhibitors enhance the growth inhibitory effects of neratinib. We also demonstrate the differential activation mechanisms of SHP2 phosphorylation at Y542 via Src and FAK in response to RTKs and ECM signaling. Our results here match with the previous reports to show the correlation of SHP2 with Src kinase [99, 164, 165]. These reports suggest that SHP2 regulates the Src activity and corresponding FAK activity as a substrate of Src, while our observations indicate that SHP2 activation also depends on Src and FAK activities in 3D environments. Thus, our model suggests that there is a paralleled crosstalk among Src, FAK and SHP2.

7.3 SHP2 contributes immunosuppression and multiple signaling outputs

Our results demonstrate the PI3K and MAPK signaling pathways are the signaling outputs in the tumor cells to promote the MBC growth and survival. As SHP2 is universally expressed in the tumor cells and immune cells, it is worthwhile for us to further investigate how tumor-autonomous SHP2 contributes to the immune escape of MBC. The rationale here was supported by previous reports with population-specific SHP2 manipulation suggesting SHP2 in T cells is dispensable for their exhaustion and the tumor-facilitating role of SHP2 in both myeloid cells and tumor associated endothelial cells [105, 106, 166]. With the doxycycline inducible system we established previously, we demonstrate that depletion of SHP2 specifically in MBC cells reduces pulmonary metastasis *in vivo*, which is consistent with our previous observation *in vitro* and other reports [131, 167, 168]. With the depletion of SHP2 in tumor cells, reduction of CD4⁺ and induction of CD8⁺ T cells were observed from CD45⁺ cells in both pulmonary tumors and spleens, and the T cell exhaustion markers LAG3 and TIM3 were also reduced, which matches the effects of systemic SHP2 inhibition. It is interesting to further investigate how LAG3 and TIM3 are reduced with SHP2 depletion in tumor cells. One potential explanation may be the paracrine signal of the tumor cells to T cells. On the other hand, the TAMs population was not significantly reduced by tumor-cell autonomous SHP2 depletion. The phenomenon here can be explained by the study indicating myeloid-specific SHP2 disruption is sufficient to influence macrophage activation [169]. But the M1/M2 ratio in the TAMs still significantly increased,

which suggests that adjusting the TAMs composition but not reducing total TAMs is one of the mechanisms behind immunosuppression by tumor-cell autonomous SHP2. Overall, with the doxycycline inducible depletion of SHP2 in MBC cells, it is the first time for us to extend the knowledge from systemic SHP2 inhibition to tumor-cell autonomous SHP2 in inducing MBC immune evasion.

Besides correlating phosphorylation of SHP2 at Y542 with the survival rates of breast cancer patients, we pinpointed phosphorylation of SHP2 at Y542 as a promising marker to predict immune profiles in MBC patients. The clinical significance of phosphorylation of SHP2 has been supported by multiple studies, including ours [167, 170, 171]. The correlation of PD-L1 with SHP2 is consistent with recent studies [108, 172]. Our findings on immune scores and pathway enrichment have solidified the clinical impacts of SHP2 phosphorylation.

Mechanistically, we demonstrated that tumor-cell autonomous SHP2 regulates CD8⁺ T cell cytotoxicity downstream of multiple growth factors via PD-L1 and MHC class I as the signaling outputs. The fact that SHP2 is involved in CD8⁺ T cell activity is supported by multiple studies [107, 173, 174]. Consistent with several studies, PD-L1 and MHC class I are the tumor-cell intrinsic regulator of immune evasion downstream of SHP2, and interferon- γ induced MHC class I is downstream of EGFR signaling via the SHP2/STAT1 axis [175-177]. It is the first time to claim that PD-L1 and MHC class I are the direct signaling outputs of SHP2 in response to RTK and ECM signaling. It is interesting to further investigate the detailed components of ECM signaling to promote PD-L1 via SHP2. What's more, our model expands our previous EGF paradox to multiple growth factors regulating interferon- γ induced MHC class I and establishes SHP2 as a key node in balancing STAT1 and MAPK signaling [132].

In summary, we show that tumor-cell autonomous SHP2 is a key signaling node in MBC cells to induce immune suppression with verities of signaling inputs within TME and tumor-cell intrinsic signaling outputs.

7.4 Optimization for combination strategies with SHP2 inhibition

We reported that SHP2 inhibitors could delay metastatic progression in the lung *in vivo* and target drug resistant MBC cells. We also confirm the effective dosing of SHP099 as 50mg/kg q.d. but not 50mg/kg q.o.d. in the 4T1 model, which paves the way for the combination strategies with SHP099. We also find the effective dosing as 100mg/kg q.d. in the D2.A1 model. Our

results are consistent with the previous reports about the oncogenic functions of SHP2 and the anti-tumor effects of SHP2 inhibitors [110, 112, 178]. Recent reports also suggest that SHP2 promotes oncogene expression, tumorigenesis and metastasis in HER2⁺ breast cancer [130, 131]. Furthermore, SHP099 can prevent resistance to MEK inhibitors in triple negative breast cancer [179]. Our observations support the same idea that SHP2 is a promising therapeutic target in MBC, while it is striking that our model also fits the drug resistant HER2 positive breast cancer. It is worthwhile to pinpoint that we have shown the therapeutic effects of SHP2 inhibitor in two immune-competent mice models, indicating the emergency needs for further understanding of the role of SHP2 blockades in anti-cancer immunity, which are inspired by recent reports [101, 180].

Based on the therapeutic effects of SHP2 inhibitors and findings of dosing trials in the 4T1 model, we demonstrated that SHP2 inhibitor could synergize with FGFR inhibitor to target metastasis *in vivo*. It is reasonable to implement our model to explain the synergistic combination, as SHP2 and FGFR signaling are overlapping, but not totally crossover. There is a recent paper coming out to suggest that SHP2 and RTKs inhibitors have intrinsic efficacy towards KRAS mutant cancers, and SHP2 activity may depend on RTK activity [181]. It is a further step that we have shown the synergistic effects of SHP2 and RTKs inhibitors *in vitro* and *in vivo*, which can be mechanistically supported by our model that SHP2 facilitates multiple RTK signaling. Meanwhile, we observed less weight loss in the combination group, suggesting potential protective mechanisms which are meant to uncover in the future.

Therapeutic benefits of ICBs are limited for metastatic breast cancer, emerging novel targeted therapies to combine with ICBs to enhance the efficacy. Beyond tumor cells, TME is a dynamic community composed of immune cells with diverse functions in response to different signaling pathways. In the presence of ICBs, these complicated signaling pathways are engaged both in the tumor cells and immune cells to adjust the balance between immunogenicity and immunosuppression in the TME, which emphasizes the significance of validating multifunctional targets to face the challenge of signaling heterogeneity in TME. Although recent findings have started to illustrate the potential beneficial combination of SHP2 inhibitors with multiple ICBs, the mechanisms by which targeting SHP2 enhances the effects of ICBs, especially in the tumor-autonomous manner, were still waiting to be uncovered [115, 180, 182]. Herein, we demonstrate that tumor-autonomous SHP2 facilitates MBC pulmonary metastasis and

resistance to ICBs via supporting an immunosuppression TME under multiple signaling inputs. Our working model is supported by several recent studies that illustrate systemic targeting SHP2 is sufficient to promote anti-tumor immunity with mechanisms beyond immune cells [107, 141, 175, 183].

Using the D2.A1 administrated on syngeneic mice to observe MBC pulmonary growth, we demonstrate that the α -PD-L1 antibody is capable of inducing immunosuppression via exhausting T-cells, which is abolished by SHP099. The fact that the α -PD-L1 antibody induces immunosuppression via restraining T cell cytotoxicity is clearly supported by multiple studies [184-186]. More studies further pinpointed that LAG3 and TIM3 are among the key T-cell exhaustion markers, which augment resistance to α -PD-L1 antibody and can be rescued by therapeutic antibodies [134, 187-189]. Consistent with these reports, α -PD-L1 antibody treatments did not significantly reduce the pulmonary growth of D2.A1 cells *in vivo*, which indicates resistance to α -PD-L1 antibody existed in this model. The dose of SHP099 we utilize here is the effective one in D2.A1 with our previous dosing trials. Although as expected, SHP099 alone with current treatment plan significantly reduced the pulmonary growth at the end of study, which might require further dosage optimization, we did observe the combination group achieved faster regression in pulmonary tumor burden, which could be a benefit from combination therapy. This benefit in our MBC model was also supported by previous reports about combination of systemic SHP2 inhibition with ICBs in colon cancer and non-small cell lung cancer [141, 180, 182]. Besides the pulmonary tumor growth, the pattern of T-cell exhaustion in the TME with α -PD-L1 antibody treatments was also supported by these reports. Both LAG3 and TIM3 in CD8⁺ T cells from pulmonary tumors were significantly upregulated with α -PD-L1 antibody treatments. Meanwhile, this induction was also observed in CD4⁺ and PD1⁺CD8⁺ T cells from pulmonary tumors. However, the α -PD-L1-induced exhaustion markers did not elevate in CD4⁺ T cells from spleens, suggesting that reprogramming tumor-infiltrating lymphocytes (TILs) is the key to improving therapeutic outcomes. The occurrence of reprogrammed TILs by SHP2 inhibition was proven by these α -PD-L1-induced exhaustion markers in both CD4⁺ and CD8⁺ T cells from pulmonary tumors attenuated with SHP099.

In summary, our model suggests the potential combination strategies of SHP2 inhibition with ICBs via relieving the T cell exhaustion, which provides the rationale for a recent clinical trial (NCT04000529). Further dosing optimization is necessary to show the real synergistic

effects of SHP2 inhibitors and ICB.

APPENDIX A. SUPPLEMENTARY TABLES

Table A.1. Cell lines and culture conditions in this study

Name of cell line	Culture condition
4T1 (ATCC [®] CRL-2539 [™])	DMEM with 10% Fetal Bovine Serum (FBS)
D2.A1	DMEM with 10% Fetal Bovine Serum (FBS)
4TO7	DMEM with 10% Fetal Bovine Serum (FBS)
HME2 parental	DMEM with 10% Fetal Bovine Serum (FBS) and 0.1% Human Insulin solution
HME2 LAPR	DMEM with 10% Fetal Bovine Serum (FBS) and 0.1% Human Insulin solution
BT-474 (ATCC [®] HTB-20 [™])	DMEM with 10% Fetal Bovine Serum (FBS)
HEK-293 (ATCC [®] CRL-1573 [™])	DMEM with 10% Fetal Bovine Serum (FBS)
MDA-MB-435S (ATCC [®] HTB-129 [™])	DMEM with 10% Fetal Bovine Serum (FBS)
SK-BR-3 (ATCC [®] HTB-30 [™])	DMEM with 10% Fetal Bovine Serum (FBS)
UACC-812 (ATCC [®] CRL-1897 [™])	DMEM with 10% Fetal Bovine Serum (FBS) and 32ng/ml EGF
ZR-75-1 (ATCC [®] CRL-1500 [™])	RPMI-1640 with 10% Fetal Bovine Serum (FBS)
BT-549 (ATCC [®] HTB-122 [™])	RPMI-1640 with 10% Fetal Bovine Serum (FBS) and 0.1% Human Insulin solution

Table A.2. Targeting sequences of doxycycline inducible shRNA vectors

Simplified ID	Source Clone ID	Target	Vector	Targeting Sequence
146	V3IMMM CG_14469 146	Ptpn11 3'-UTR	piSMART mCMV/TurboGFP	AGACTAGACGAGCGTTCCC
369	V3IMMM CG_11150 369	Ptpn11 CDS	piSMART mCMV/TurboGFP	ACAGAAGCACAGTACCGGT
404	V3IMMM CG_15981 404	Ptpn11 CDS	piSMART mCMV/TurboGFP	ATCGCGGAGATGGTTTCAC

Table A.3. Drugs and reagents in this study

Drug / Reagent	Source	Identifier / formulation
SHP099 dihydrochloride (<i>in vitro</i> study)	Selleck	Catalog No: S8278
SHP099 dihydrochloride (<i>in vivo</i> grade)	Chemietek	Catalog No: CT-SHP099 Formulation: 0.5% Hydroxypropyl Methylcellulose
TNO155	Chemietek	Catalog No: CT-TNO155
FIIN4	Achemtek	Catalog No: 0107-000063 Formulation: 0.5% Carboxymethylcellulose
Neratinib (HKI-272)	Selleck	Catalog No: S2150
PP2	Selleck	Catalog No: S7008
PF-562,271 (PF271)	Pfizer	Under agreement from Pfizer Inc.
Trametinib	Selleck	Catalog No: S2673
Alpelisib	Selleck	Catalog No: S2814
InVivoMAb anti-mouse PD-L1 (B7-H1)	Bio X Cell	BE0101, Clone 10F.9G2
InVivoMAb rat IgG2b isotype control, anti-keyhole limpet hemocyanin	Bio X Cell	BE0090, Clone LTF-2
Basic FGF (FGF2), Human	GoldBio	Catalog No: 1140-02-10
Recombinant Human PDGF-BB Protein, CF	R&D systems	Catalog No: 220-BB-010
Recombinant Mouse HGF Protein, CF	R&D systems	Catalog No: 2207-HG/CF
Recombinant Mouse VEGF 164 Protein, CF	R&D systems	Catalog No: 493-MV-005/CF
EGF, Human	GoldBio	Catalog No: 1150-04-100
Human interferon- γ	Peprtech	Catalog No: 300-02
Mouse interferon- γ	Peprtech	Catalog No: 315-05
Cultrex® RGF BME PathClear®	Sigma	Catalog No: 3433-005-01 Concentration: 17.05 mg/ml
Doxycycline Hydrochloride	RPI from Fisher	Catalog No: 50-213-285 Formulation: 2mg/ml in drinking water
D-Luciferin, Potassium Salt	GoldBio	Catalog No: LUCK-100

Table A.4. Antibodies used in flow cytometry for MBC cells

Antibody	Source	Catalog No.
PE anti-mouse CD274 (B7-H1, PD-L1) Antibody	Biolegend	124307
FITC anti-mouse H-2 Antibody	Biolegend	125508
PerCP/Cyanine5.5 anti-human CD274 (B7-H1, PD-L1) Antibody	Biolegend	329737
PE anti-human HLA-A,B,C Antibody	Biolegend	311405

Table A.5. Antibodies used in flow cytometry for *in vivo* studies

Antibodies for combination of SHP099 and α -PD-L1 in D2.A1 model			
Name	Source	Catalog	Panel
TruStain FcX™ PLUS (anti-mouse CD16/32) Antibody	Biolegend	101320	Lymphoid & myeloid
Zombie Violet™ Fixable Viability Kit	Biolegend	423114	Lymphoid & myeloid
PerCP anti-mouse CD45 Antibody	Biolegend	103129	Lymphoid & myeloid
FITC anti-mouse CD8a Antibody	Biolegend	100705	lymphoid
Brilliant Violet 785™ anti-mouse CD4 Antibody	Biolegend	100453	lymphoid
APC anti-mouse CD366 (Tim-3) Antibody	Biolegend	134007	lymphoid
PE/Dazzle™ 594 anti-mouse CD279 (PD-1) Antibody	Biolegend	135227	lymphoid
PE/Cyanine7 anti-mouse CD223 (LAG-3) Antibody	Biolegend	125225	lymphoid
PE/Cyanine7 anti-mouse/human CD11b Antibody	Biolegend	101215	myeloid
Brilliant Violet 605™ anti-mouse F4/80 Antibody	Biolegend	123133	myeloid
PE anti-mouse CD274 (B7-H1, PD-L1) Antibody	Biolegend	124307	myeloid
Brilliant Violet 711™ anti-mouse CD206 (MMR) Antibody	Biolegend	141727	myeloid
PE/Dazzle™ 594 anti-mouse CD86 Antibody	Biolegend	105041	myeloid
APC/Cyanine7 anti-mouse Ly-6G Antibody	Biolegend	127623	myeloid
FITC anti-mouse Ly-6C Antibody	Biolegend	128005	myeloid
Antibodies for doxycycline inducible depletion of SHP2 in 4T1 model			
Name	Source	Catalog	Panel
TruStain FcX™ PLUS (anti-mouse CD16/32) Antibody	Biolegend	101320	Lymphoid & myeloid
Zombie Violet™ Fixable Viability Kit	Biolegend	423114	Lymphoid & myeloid
PerCP anti-mouse CD45 Antibody	Biolegend	103129	Lymphoid & myeloid
Pacific Blue™ anti-mouse CD8a Antibody	Biolegend	100728	lymphoid
Brilliant Violet 711™ anti-mouse CD4 Antibody	Biolegend	100447	lymphoid
APC anti-mouse CD366 (Tim-3) Antibody	Biolegend	134007	lymphoid
PE/Dazzle™ 594 anti-mouse CD279 (PD-1) Antibody	Biolegend	135227	lymphoid
PE/Cyanine7 anti-mouse CD223 (LAG-3) Antibody	Biolegend	125225	lymphoid
PE/Cyanine7 anti-mouse/human CD11b Antibody	Biolegend	101215	myeloid
Brilliant Violet 605™ anti-mouse F4/80 Antibody	Biolegend	123133	myeloid
PE anti-mouse CD274 (B7-H1, PD-L1) Antibody	Biolegend	124307	myeloid
Brilliant Violet 711™ anti-mouse CD206 (MMR) Antibody	Biolegend	141727	myeloid
PE/Dazzle™ 594 anti-mouse CD86 Antibody	Biolegend	105041	myeloid
APC/Cyanine7 anti-mouse Ly-6G Antibody	Biolegend	127623	myeloid
APC anti-mouse Ly-6C Antibody	Biolegend	128015	myeloid

Table A.6. Primary antibodies used in this study

Antibody	Source	Identifier	Host
Anti-SHP2 (phospho Y542) antibody [EP508(2)Y]	Abcam	Catalog No: ab62322	Rabbit
SH-PTP2 Antibody (B-1)	Santa Cruz Biotechnology	Catalog No: sc-7384	Mouse
Phospho-FRS2- α (Tyr436) Antibody	Cell Signaling Technology	Catalog No: #3861	Rabbit
Phospho-FAK (Tyr925) Antibody	Cell Signaling Technology	Catalog No: #3284	Rabbit
FAK Recombinant Rabbit Monoclonal Antibody (5H18L19)	Invitrogen	Catalog No: 701094	Rabbit
Phospho-Src Family (Tyr416) Antibody	Cell Signaling Technology	Catalog No: #2101	Rabbit
Phospho-Src (Tyr527) Antibody	Cell Signaling Technology	Catalog No: #2105	Rabbit
Src Antibody	Cell Signaling Technology	Catalog No: #2108	Rabbit
Phospho-Akt (Ser473) Antibody	Cell Signaling Technology	Catalog No: #9271	Rabbit
Akt Antibody	Cell Signaling Technology	Catalog No: #9272	Rabbit
Phospho-p44/42 MAPK (Erk1/2) (Thr202/Tyr204) Antibody	Cell Signaling Technology	Catalog No: #9101	Rabbit
p44/42 MAPK (Erk1/2) Antibody	Cell Signaling Technology	Catalog No: #9102	Rabbit
FGF Receptor 1 (D8E4) XP [®] Rabbit mAb	Cell Signaling Technology	Catalog No: #9740	Rabbit
Phospho-HER2/ErbB2 (Tyr1196) (D66B7) Rabbit mAb	Cell Signaling Technology	Catalog No: #6942	Rabbit
HER2/ErbB2 Antibody	Cell Signaling Technology	Catalog No: #2242	Rabbit
Phospho-FGF Receptor (Tyr653/654) Antibody	Cell Signaling Technology	Catalog No: #3471	Rabbit
PDGF Receptor α (D1E1E) XP [®] Rabbit mAb	Cell Signaling Technology	Catalog No: #3174	Rabbit
PDGF Receptor β (28E1) Rabbit mAb	Cell Signaling Technology	Catalog No: #3169	Rabbit
Met Antibody	Cell Signaling Technology	Catalog No: #4560	Rabbit
Phospho-Stat1 (Tyr701) (58D6) Rabbit mAb	Cell Signaling Technology	Catalog No: #9167	Rabbit
Stat1 Antibody	Cell Signaling Technology	Catalog No: #9172	Rabbit
Tubulin, beta	Developmental Studies Hybridoma Bank (DSHB)	Catalog No: E7	Mouse
GAPDH (2D4A7)	Santa Cruz Biotechnology	Catalog No: sc-59541	Mouse

Table A.7. Secondary antibodies used in this study

Antibody	Source	Identifier	Host
Goat anti-Mouse IgG (H+L) Secondary Antibody, HRP	ThermoFisher	Catalog No: 62-6520	Goat
Goat anti-Rabbit IgG (H+L) Secondary Antibody, HRP	ThermoFisher	Catalog No: 65-6120	Goat
IRDye® 680RD Goat anti-Mouse IgG Secondary Antibody	LI-COR, Inc.	P/N No: 926-68070	Goat
IRDye® 800CW Goat anti-Rabbit IgG Secondary Antibody	LI-COR, Inc.	P/N No: 926-32211	Goat

APPENDIX B. SUPPLEMENTARY INFORMATION

Step-by-step methods for correlation plot

1. Open <http://firebrowse.org/> with browser, select 'Breast invasive carcinoma (BRCA)' cohort.
2. Click 'Reverse Phase Protein Array' tab, and click 'RPPA_AnnotateWithGene (MD5)' to download data package.
3. Open 'BRCA.rppa.txt' in the downloaded data package, and select all the information in the file.
4. Copy and paste the information in the 'BRCA.rppa.txt' to Microsoft EXCEL, and save as csv document type.
5. Search in Microsoft EXCEL for the interested gene names: 'PTPN11|SHP-2_pY542', 'SRC|Src', 'SRC|Src_pY416', 'SRC|Src_pY527', 'STAT3|STAT3_pY705', 'EGFR|EGFR', 'EGFR|EGFR_pY1068', 'EGFR|EGFR_pY1173', 'ERBB2|HER2' 'ERBB2|HER2_pY1248', 'MET|c-Met', 'MET|c-Met_pY1235', and copy these rows and paste as Transpose to a new Microsoft EXCEL file, and save as rppa.csv.
6. Run the R scripts for correlation plots in R studio, and choose rppa.csv as the input.
7. The correlation plot will be generated, and save the plot.

R scripts for correlation plots

```
rm(list = ls())  
x<-read.csv(file.choose()) #Choose rppa.csv here.  
library(corrplot)  
M <- cor(x)  
library(RColorBrewer)  
corrplot(M, method = "circle", type="upper",  
         col = brewer.pal(n=10,name = "RdBu"))
```

Step-by-step methods for survival plot with RPPA data

1. Open <http://firebrowse.org/> with browser, select 'Breast invasive carcinoma (BRCA)' cohort.
2. Click 'Reverse Phase Protein Array' tab, and click 'RPPA_AnnotateWithGene (MD5)' to download data package.

3. Open 'BRCA.rppa.txt' in the downloaded data package, and select all the information in the file.
4. Copy and paste the information in the 'BRCA.rppa.txt' to Microsoft EXCEL, and save as raw_rppa.csv.
5. Click 'Clinical' tab, and click 'Merge_Clinical (MD5)' to download data package.
6. Open 'BRCA.clin.merged.txt' in the downloaded data package, and select all the information in the file.
7. Copy and paste the information in the 'BRCA.clin.merged.txt' to Microsoft EXCEL.
8. Search in the Microsoft EXCEL for the key word 'patient.samples.sample.portions.shipment_portion.shipment_portion_bcr_aliquot_barcode', rename the cell as 'Composite.Element.REF'.
9. Cut this row and paste as the first row of the table, and save the file as clinic.csv.
10. Run the R scripts for merging clinic data with RPPA data in R studio, and choose raw_rppa.csv and clinic.csv as the input.
11. Open the output c.csv in Microsoft EXCEL, and search for the rows named 'PTPN11|SHP-2_pY542' and 'patient.days_to_death'.
12. Copy these rows and paste as Transpose to a new Microsoft EXCEL file, sort the data according the 'PTPN11|SHP-2_pY542', delete all the rows with non-numeric values.
13. Determine the median of 'PTPN11|SHP-2_pY542', and separate the data as two groups.
14. Plot under the threshold of survival with GraphPad Prism 5.0.

R scripts for merging clinic data with RPPA data

```
rm(list = ls())
clinic<-read.csv(choose.files()) #Choose clinic.csv here.
RPPA<-read.csv(choose.files()) #Choose raw_rppa.csv here.
library("dplyr")
a<-merge(clinic,RPPA,all=TRUE)
b<-merge(RPPA,clinic,all=TRUE)
c<-union(a,b)
write.csv(c,"D:/c.csv")
```

Step-by-step methods for survival plot with mRNA data

1. Open <http://firebrowse.org/> with browser, select 'Breast invasive carcinoma (BRCA)' cohort.
2. Click 'mRNA' tab, and click 'mRNA_Preprocess_Median (MD5)' to download data package.
3. Open 'BRCA.medianexp.txt' in the downloaded data package, and select all the information in the file.
4. Copy and paste the information in the 'BRCA.medianexp.txt' to Microsoft EXCEL, and save as raw_mrna.csv.
5. Click 'Clinical' tab, and click 'Merge_Clinical (MD5)' to download data package.
6. Open 'BRCA.clin.merged.txt' in the downloaded data package, and select all the information in the file.
7. Copy and paste the information in the 'BRCA.clin.merged.txt' to Microsoft EXCEL.
8. Search in the Microsoft EXCEL for the key word 'patient.samples.sample.portions.portion.analytes.analyte-2.aliquots.aliquot-2.bcr_aliquot_barcode', rename the cell as 'Hybridization REF'.
9. Cut this row and paste as the first row of the table, and save the file as clinic2.csv.
10. Run the R scripts for merging clinic data with RPPA data in R studio, and choose raw_mrna.csv and clinic2.csv as the input.
11. Open the output d.csv in Microsoft EXCEL, and search for the rows named 'PTPN11' and 'patient.days_to_death'.
12. Copy these rows and paste as Transpose to a new Microsoft EXCEL file, sort the data according the 'PTPN11', delete all the rows with non-numeric values.
13. Determine the median of 'PTPN11', and separate the data as two groups.
14. Plot under the threshold of survival with GraphPad Prism 5.0.

R scripts for merging clinic data with mRNA data

```
rm(list=ls())  
Clinic<-read.csv(choose.files()) #Choose clinic2.csv here.  
mRNA<-read.csv(choose.files()) #Choose raw_mrna.csv here.  
library("dplyr")  
a<-merge(Clinic,mRNA,all=TRUE)
```

```
b<-merge(mRNA,Clinic,all=TRUE)
d<-union(a,b)
write.csv(c,"D:/d.csv")
```

Description for the analysis to predict immune profiles with TCGA datasets

The codes are available at https://github.com/benchlover/SHP2_immunology.

Figure 4.1A and 4.1B demonstrating the differential immune scores and stroma scores in patients grouped by phosphorylation levels of SHP2 at Y542 or expression levels of SHP2 were generated with Python Code 1.

Figure 4.1C demonstrating differential phosphorylation levels of SHP2 at Y542 and expression levels of SHP2 in patients grouped by CD4⁺ T-cell infiltration levels was generated with Python Code 2 and R code 1.

Figure 4.1D and 4.1E demonstrating differential gene expression in patients grouped by phosphorylation levels of SHP2 at Y542 or expression levels of SHP2 were generated with Python Code 3.

Figure 4.1F demonstrating ssGSEA analysis was generated with Python code 4 and corresponding R code 2.

Figure 4.1G and 4.1H demonstrating GSEA analyses were generated with GSEA 4.1.0. The pathway files were downloaded from GSEA websites (<http://www.gsea-msigdb.org/gsea/index.jsp>).

REFERENCES

- [1] Siegel RL, Miller KD, Fuchs HE, Jemal A. Cancer statistics, 2022. *CA: a cancer journal for clinicians* 2022.
- [2] DeSantis CE, Bray F, Ferlay J et al. International variation in female breast cancer incidence and mortality rates. *Cancer Epidemiology and Prevention Biomarkers* 2015; 24: 1495-1506.
- [3] Azamjah N, Soltan-Zadeh Y, Zayeri F. Global trend of breast cancer mortality rate: a 25-year study. *Asian Pacific journal of cancer prevention: APJCP* 2019; 20: 2015.
- [4] Whitman S, Ansell D, Orsi J, Francois T. The racial disparity in breast cancer mortality. *Journal of community health* 2011; 36: 588-596.
- [5] Miles RC, Gullerud RE, Lohse CM et al. Local recurrence after breast-conserving surgery: multivariable analysis of risk factors and the impact of young age. *Annals of surgical oncology* 2012; 19: 1153-1159.
- [6] Shoemaker ML, White MC, Wu M et al. Differences in breast cancer incidence among young women aged 20–49 years by stage and tumor characteristics, age, race, and ethnicity, 2004–2013. *Breast cancer research and treatment* 2018; 169: 595-606.
- [7] Hammond MEH, Hayes DF, Dowsett M et al. American Society of Clinical Oncology/College of American Pathologists guideline recommendations for immunohistochemical testing of estrogen and progesterone receptors in breast cancer (unabridged version). *Archives of pathology & laboratory medicine* 2010; 134: e48-e72.
- [8] Wolff AC, Hammond MEH, Schwartz JN et al. American Society of Clinical Oncology/College of American Pathologists guideline recommendations for human epidermal growth factor receptor 2 testing in breast cancer. *Archives of pathology & laboratory medicine* 2007; 131: 18-43.
- [9] Parise CA, Bauer KR, Brown MM, Caggiano V. Breast cancer subtypes as defined by the estrogen receptor (ER), progesterone receptor (PR), and the human epidermal growth factor receptor 2 (HER2) among women with invasive breast cancer in California, 1999–2004. *The breast journal* 2009; 15: 593-602.

- [10] Wan Z-B, Gao H-Y, Wei L et al. Expression of estrogen receptor, progesterone receptor, human epidermal growth factor receptor 2, and Ki-67 in ductal carcinoma in situ (DCIS) and DCIS with microinvasion. *Medicine* 2018; 97.
- [11] Perou CM, Sørlie T, Eisen MB et al. Molecular portraits of human breast tumours. *nature* 2000; 406: 747-752.
- [12] Sørlie T, Perou CM, Tibshirani R et al. Gene expression patterns of breast carcinomas distinguish tumor subclasses with clinical implications. *Proceedings of the National Academy of Sciences* 2001; 98: 10869-10874.
- [13] Parker JS, Mullins M, Cheang MC et al. Supervised risk predictor of breast cancer based on intrinsic subtypes. *Journal of clinical oncology* 2009; 27: 1160.
- [14] Onitilo AA, Engel JM, Greenlee RT, Mukesh BN. Breast cancer subtypes based on ER/PR and Her2 expression: comparison of clinicopathologic features and survival. *Clinical medicine & research* 2009; 7: 4-13.
- [15] Caan BJ, Sweeney C, Habel LA et al. Intrinsic subtypes from the PAM50 gene expression assay in a population-based breast cancer survivor cohort: prognostication of short-and long-term outcomes. *Cancer Epidemiology and Prevention Biomarkers* 2014; 23: 725-734.
- [16] Lumachi F, Brunello A, Maruzzo M et al. Treatment of estrogen receptor-positive breast cancer. *Current medicinal chemistry* 2013; 20: 596-604.
- [17] Arteaga CL, Sliwkowski MX, Osborne CK et al. Treatment of HER2-positive breast cancer: current status and future perspectives. *Nature reviews Clinical oncology* 2012; 9: 16-32.
- [18] Loibl S, Gianni L. HER2-positive breast cancer. *The Lancet* 2017; 389: 2415-2429.
- [19] Yagata H, Kajiura Y, Yamauchi H. Current strategy for triple-negative breast cancer: appropriate combination of surgery, radiation, and chemotherapy. *Breast Cancer* 2011; 18: 165-173.
- [20] Prat A, Lluch A, Albanell J et al. Predicting response and survival in chemotherapy-treated triple-negative breast cancer. *British journal of cancer* 2014; 111: 1532-1541.
- [21] Cejalvo JM, De Dueñas EM, Galvan P et al. Intrinsic subtypes and gene expression profiles in primary and metastatic breast cancer. *Cancer research* 2017; 77: 2213-2221.

- [22] Lindstrom LS, Karlsson E, Wilking UM et al. Clinically used breast cancer markers such as estrogen receptor, progesterone receptor, and human epidermal growth factor receptor 2 are unstable throughout tumor progression. *J Clin Oncol* 2012; 30: 2601-2608.
- [23] Brierley JD, Gospodarowicz MK, Wittekind C. TNM classification of malignant tumours. John Wiley & Sons 2017.
- [24] Frederick L, Page DL, Fleming ID et al. AJCC cancer staging manual. Springer Science & Business Media 2002.
- [25] Polyak K. On the birth of breast cancer. *Biochimica et Biophysica Acta (BBA)-Reviews on Cancer* 2001; 1552: 1-13.
- [26] Pagani O, Senkus E, Wood W et al. International guidelines for management of metastatic breast cancer: can metastatic breast cancer be cured? *Journal of the National Cancer Institute* 2010; 102: 456-463.
- [27] Hanahan D, Weinberg RA. The hallmarks of cancer. *cell* 2000; 100: 57-70.
- [28] Giordano SH, Buzdar AU, Smith TL et al. Is breast cancer survival improving? Trends in survival for patients with recurrent breast cancer diagnosed from 1974 through 2000. *Cancer: Interdisciplinary International Journal of the American Cancer Society* 2004; 100: 44-52.
- [29] Chia SK, Speers CH, D'yachkova Y et al. The impact of new chemotherapeutic and hormone agents on survival in a population-based cohort of women with metastatic breast cancer. *Cancer* 2007; 110: 973-979.
- [30] Martínez-Sález O, Prat A. Current and future management of HER2-positive metastatic breast cancer. *JCO oncology practice* 2021; 17: 594-604.
- [31] Sundquist M, Brudin L, Tejler G. Improved survival in metastatic breast cancer 1985–2016. *The Breast* 2017; 31: 46-50.
- [32] Mariotto AB, Etzioni R, Hurlbert M et al. Estimation of the number of women living with metastatic breast cancer in the United States. *Cancer Epidemiology and Prevention Biomarkers* 2017; 26: 809-815.
- [33] Peart O. Metastatic breast cancer. *Radiologic technology* 2017; 88: 519M-539M.
- [34] Pruessmann J, Pursche T, Hammersen F et al. Conditional Disease-Free and Overall Survival of 1,858 Young Women with Non-Metastatic Breast Cancer and with

- Participation in a Post-Therapeutic Rehab Programme according to Clinical Subtypes. *Breast Care* 2021; 16: 163-172.
- [35] Greenberg P, Hortobagyi GN, Smith TL et al. Long-term follow-up of patients with complete remission following combination chemotherapy for metastatic breast cancer. *Journal of clinical oncology* 1996; 14: 2197-2205.
- [36] Gogate A, Wheeler SB, Reeder-Hayes KE et al. Projecting the prevalence and costs of metastatic breast cancer from 2015 through 2030. *JNCI Cancer Spectrum* 2021; 5: pkab063.
- [37] Blumen H, Fitch K, Polkus V. Comparison of treatment costs for breast cancer, by tumor stage and type of service. *American health & drug benefits* 2016; 9: 23.
- [38] Hudis CA. Trastuzumab—mechanism of action and use in clinical practice. *New England journal of medicine* 2007; 357: 39-51.
- [39] Scheuer W, Friess T, Burtscher H et al. Strongly enhanced antitumor activity of trastuzumab and pertuzumab combination treatment on HER2-positive human xenograft tumor models. *Cancer research* 2009; 69: 9330-9336.
- [40] Gradishar WJ, Anderson BO, Abraham J et al. Breast cancer, version 3.2020, NCCN clinical practice guidelines in oncology. *Journal of the National Comprehensive Cancer Network* 2020; 18: 452-478.
- [41] Akhand SS, Chen H, Purdy SC et al. Fibroblast growth factor receptor facilitates recurrence of minimal residual disease following trastuzumab emtansine therapy. *NPJ breast cancer* 2021; 7: 1-11.
- [42] Konecny GE, Pegram MD, Venkatesan N et al. Activity of the dual kinase inhibitor lapatinib (GW572016) against HER-2-overexpressing and trastuzumab-treated breast cancer cells. *Cancer research* 2006; 66: 1630-1639.
- [43] Burstein HJ, Sun Y, Dirix LY et al. Neratinib, an irreversible ErbB receptor tyrosine kinase inhibitor, in patients with advanced ErbB2-positive breast cancer. *J Clin Oncol* 2010; 28: 1301-1307.
- [44] Martin M, Holmes FA, Ejlertsen B et al. Neratinib after trastuzumab-based adjuvant therapy in HER2-positive breast cancer (ExteNET): 5-year analysis of a randomised, double-blind, placebo-controlled, phase 3 trial. *The lancet oncology* 2017; 18: 1688-1700.

- [45] Hanker AB, Brewer MR, Sheehan JH et al. An acquired HER2 T798I gatekeeper mutation induces resistance to Neratinib in a patient with HER2 mutant–driven breast cancer. *Cancer discovery* 2017; 7: 575-585.
- [46] He X, Xu C. Immune checkpoint signaling and cancer immunotherapy. *Cell research* 2020; 30: 660-669.
- [47] Hanahan D, Weinberg RA. Hallmarks of cancer: the next generation. *cell* 2011; 144: 646-674.
- [48] Ribas A, Wolchok JD. Cancer immunotherapy using checkpoint blockade. *Science* 2018; 359: 1350-1355.
- [49] Esteva FJ, Hubbard-Lucey VM, Tang J, Pusztai L. Immunotherapy and targeted therapy combinations in metastatic breast cancer. *The Lancet Oncology* 2019; 20: e175-e186.
- [50] Tang J, Pearce L, O'Donnell-Tormey J, Hubbard-Lucey VM. Trends in the global immuno-oncology landscape. *Nat. Rev. Drug Discov* 2018; 130: 112.
- [51] Adams S, Loi S, Toppmeyer D et al. Pembrolizumab monotherapy for previously untreated, PD-L1-positive, metastatic triple-negative breast cancer: cohort B of the phase II KEYNOTE-086 study. *Annals of Oncology* 2019; 30: 405-411.
- [52] Adams S, Loi S, Toppmeyer D et al. Phase 2 study of pembrolizumab as first-line therapy for PD-L1–positive metastatic triple-negative breast cancer (mTNBC): preliminary data from KEYNOTE-086 cohort B. In *Edition American Society of Clinical Oncology* 2017.
- [53] Podsypanina K, Du Y-CN, Jechlinger M et al. Seeding and propagation of untransformed mouse mammary cells in the lung. *Science* 2008; 321: 1841-1844.
- [54] Hüsemann Y, Geigl JB, Schubert F et al. Systemic spread is an early step in breast cancer. *Cancer cell* 2008; 13: 58-68.
- [55] Klevesath M, Pantel K, Agbaje O et al. Patterns of metastatic spread in early breast cancer. *The Breast* 2013; 22: 449-454.
- [56] Zavyalova M, Denisov E, Tashireva L et al. Intravasation as a key step in cancer metastasis. *Biochemistry (Moscow)* 2019; 84: 762-772.
- [57] Mego M, Mani SA, Cristofanilli M. Molecular mechanisms of metastasis in breast cancer—clinical applications. *Nature reviews Clinical oncology* 2010; 7: 693-701.
- [58] Peinado H, Zhang H, Matei IR et al. Pre-metastatic niches: organ-specific homes for metastases. *Nature Reviews Cancer* 2017; 17: 302-317.

- [59] Shinde A, Wilmanski T, Chen H et al. Pyruvate carboxylase supports the pulmonary tropism of metastatic breast cancer. *Breast cancer research* 2018; 20: 1-12.
- [60] Bell ES, Shah P, Zuela-Sopilniak N et al. Low lamin A levels enhance confined cell migration and metastatic capacity in breast cancer. *bioRxiv* 2021.
- [61] Denais CM, Gilbert RM, Isermann P et al. Nuclear envelope rupture and repair during cancer cell migration. *Science* 2016; 352: 353-358.
- [62] Wang Y, Zhou BP. Epithelial-mesenchymal transition—a hallmark of breast cancer metastasis. *Cancer hallmarks* 2013; 1: 38-49.
- [63] Zhao H, Achreja A, Iessi E et al. The key role of extracellular vesicles in the metastatic process. *Biochimica et Biophysica Acta (BBA)-Reviews on Cancer* 2018; 1869: 64-77.
- [64] Solé C, Lawrie CH. MicroRNAs in metastasis and the tumour microenvironment. *International Journal of Molecular Sciences* 2021; 22: 4859.
- [65] Quail DF, Joyce JA. Microenvironmental regulation of tumor progression and metastasis. *Nature medicine* 2013; 19: 1423-1437.
- [66] Angus L, Smid M, Wilting SM et al. The genomic landscape of metastatic breast cancer highlights changes in mutation and signature frequencies. *Nature genetics* 2019; 51: 1450-1458.
- [67] Robinson DR, Wu Y-M, Lin S-F. The protein tyrosine kinase family of the human genome. *Oncogene* 2000; 19: 5548-5557.
- [68] Hubbard SR. Structural analysis of receptor tyrosine kinases. *Progress in biophysics and molecular biology* 1999; 71: 343-358.
- [69] Ritter CA, Perez-Torres M, Rinehart C et al. Human breast cancer cells selected for resistance to trastuzumab in vivo overexpress epidermal growth factor receptor and ErbB ligands and remain dependent on the ErbB receptor network. *Clinical Cancer Research* 2007; 13: 4909-4919.
- [70] Stuhlmiller TJ, Miller SM, Zawistowski JS et al. Inhibition of lapatinib-induced kinome reprogramming in ERBB2-positive breast cancer by targeting BET family bromodomains. *Cell reports* 2015; 11: 390-404.
- [71] Shattuck DL, Miller JK, Carraway KL, Sweeney C. Met receptor contributes to trastuzumab resistance of Her2-overexpressing breast cancer cells. *Cancer research* 2008; 68: 1471-1477.

- [72] Brown WS, Akhand SS, Wendt MK. FGFR signaling maintains a drug persistent cell population following epithelial-mesenchymal transition. *Oncotarget* 2016; 7: 83424.
- [73] Helsten T, Elkin S, Arthur E et al. The FGFR landscape in cancer: analysis of 4,853 tumors by next-generation sequencing. *Clinical Cancer Research* 2016; 22: 259-267.
- [74] Brown WS, Tan L, Smith A et al. Covalent targeting of fibroblast growth factor receptor inhibits metastatic breast cancer. *Molecular cancer therapeutics* 2016; 15: 2096-2106.
- [75] Minuti G, Cappuzzo F, Duchnowska R et al. Increased MET and HGF gene copy numbers are associated with trastuzumab failure in HER2-positive metastatic breast cancer. *British journal of cancer* 2012; 107: 793.
- [76] Alexander PB, Chen R, Gong C et al. Distinct receptor tyrosine kinase subsets mediate anti-HER2 drug resistance in breast cancer. *Journal of Biological Chemistry* 2017; 292: 748-759.
- [77] Jechlinger M, Sommer A, Moriggl R et al. Autocrine PDGFR signaling promotes mammary cancer metastasis. *The Journal of clinical investigation* 2006; 116: 1561-1570.
- [78] Yue B. Biology of the extracellular matrix: an overview. *Journal of glaucoma* 2014; S20.
- [79] Winkler J, Abisoye-Ogunniyan A, Metcalf KJ, Werb Z. Concepts of extracellular matrix remodelling in tumour progression and metastasis. *Nature communications* 2020; 11: 1-19.
- [80] Mitra A, Sawada K, Tiwari P et al. Ligand-independent activation of c-Met by fibronectin and $\alpha 5 \beta 1$ -integrin regulates ovarian cancer invasion and metastasis. *Oncogene* 2011; 30: 1566-1576.
- [81] Salmerón-Sánchez M, Dalby MJ. Synergistic growth factor microenvironments. *Chemical Communications* 2016; 52: 13327-13336.
- [82] Li D-M, Feng Y-M. Signaling mechanism of cell adhesion molecules in breast cancer metastasis: potential therapeutic targets. *Breast cancer research and treatment* 2011; 128: 7.
- [83] Turner N, Grose R. Fibroblast growth factor signalling: from development to cancer. *Nature Reviews Cancer* 2010; 10: 116.
- [84] Dhatchinamoorthy K, Colbert JD, Rock KL. Cancer immune evasion through loss of MHC class I antigen presentation. *Frontiers in immunology* 2021; 12: 469.

- [85] Lei X, Lei Y, Li J-K et al. Immune cells within the tumor microenvironment: Biological functions and roles in cancer immunotherapy. *Cancer letters* 2020; 470: 126-133.
- [86] Cordeiro MH, Smith RJ, Saurin AT. A fine balancing act: a delicate kinase-phosphatase equilibrium that protects against chromosomal instability and cancer. *The international journal of biochemistry & cell biology* 2018; 96: 148-156.
- [87] LaPorte D, Koshland DE. A protein with kinase and phosphatase activities involved in regulation of tricarboxylic acid cycle. *nature* 1982; 300: 458-460.
- [88] Kerk D, Templeton G, Moorhead GB. Evolutionary radiation pattern of novel protein phosphatases revealed by analysis of protein data from the completely sequenced genomes of humans, green algae, and higher plants. *Plant physiology* 2008; 146: 351.
- [89] Paul S, Lombroso P. Receptor and nonreceptor protein tyrosine phosphatases in the nervous system. *Cellular and Molecular Life Sciences CMLS* 2003; 60: 2465-2482.
- [90] Hof P, Pluskey S, Dhe-Paganon S et al. Crystal structure of the tyrosine phosphatase SHP-2. *cell* 1998; 92: 441-450.
- [91] Mohi MG, Neel BG. The role of Shp2 (PTPN11) in cancer. *Current opinion in genetics & development* 2007; 17: 23-30.
- [92] Frankson R, Yu Z-H, Bai Y et al. Therapeutic targeting of oncogenic tyrosine phosphatases. *Cancer research* 2017; 77: 5701-5705.
- [93] Araki T, Nawa H, Neel BG. Tyrosyl phosphorylation of Shp2 is required for normal ERK activation in response to some, but not all, growth factors. *Journal of Biological Chemistry* 2003; 278: 41677-41684.
- [94] Bunda S, Burrell K, Heir P et al. Inhibition of SHP2-mediated dephosphorylation of Ras suppresses oncogenesis. *Nature communications* 2015; 6: 8859.
- [95] Zhang SQ, Tsiaras WG, Araki T et al. Receptor-specific regulation of phosphatidylinositol 3'-kinase activation by the protein tyrosine phosphatase Shp2. *Molecular and cellular biology* 2002; 22: 4062-4072.
- [96] Zehender A, Huang J, Györfi A-H et al. The tyrosine phosphatase SHP2 controls TGF β -induced STAT3 signaling to regulate fibroblast activation and fibrosis. *Nature communications* 2018; 9: 3259.
- [97] Wöhrle FU, Daly RJ, Brummer T. Function, regulation and pathological roles of the Gab/DOS docking proteins. *Cell Communication and Signaling* 2009; 7: 22.

- [98] Hadari Y, Kouhara H, Lax I, Schlessinger J. Binding of Shp2 tyrosine phosphatase to FRS2 is essential for fibroblast growth factor-induced PC12 cell differentiation. *Molecular and cellular biology* 1998; 18: 3966-3973.
- [99] Zhang SQ, Yang W, Kontaridis MI et al. Shp2 regulates SRC family kinase activity and Ras/Erk activation by controlling Csk recruitment. *Molecular cell* 2004; 13: 341-355.
- [100] Hartman ZR, Schaller MD, Agazie YM. The tyrosine phosphatase SHP2 regulates focal adhesion kinase to promote EGF-induced lamellipodia persistence and cell migration. *Molecular cancer research* 2013; 11: 651-664.
- [101] Yokosuka T, Takamatsu M, Kobayashi-Imanishi W et al. Programmed cell death 1 forms negative costimulatory microclusters that directly inhibit T cell receptor signaling by recruiting phosphatase SHP2. *Journal of Experimental Medicine* 2012; 209: 1201-1217.
- [102] Marasco M, Berteotti A, Weyershaeuser J et al. Molecular mechanism of SHP2 activation by PD-1 stimulation. *Science advances* 2020; 6: eaay4458.
- [103] Patsoukis N, Duke-Cohan JS, Chaudhri A et al. Interaction of SHP-2 SH2 domains with PD-1 ITSM induces PD-1 dimerization and SHP-2 activation. *Communications biology* 2020; 3: 1-13.
- [104] Hui E, Cheung J, Zhu J et al. T cell costimulatory receptor CD28 is a primary target for PD-1-mediated inhibition. *Science* 2017; 355: 1428-1433.
- [105] Rota G, Niogret C, Dang AT et al. Shp-2 is dispensable for establishing T cell exhaustion and for PD-1 signaling in vivo. *Cell reports* 2018; 23: 39-49.
- [106] Xiao P, Guo Y, Zhang H et al. Myeloid-restricted ablation of Shp2 restrains melanoma growth by amplifying the reciprocal promotion of CXCL9 and IFN- γ production in tumor microenvironment. *Oncogene* 2018; 37: 5088-5100.
- [107] Fedele C, Li S, Teng KW et al. SHP2 inhibition diminishes KRASG12C cycling and promotes tumor microenvironment remodeling. *Journal of Experimental Medicine* 2021; 218.
- [108] Feng HB, Chen Y, Xie Z et al. High SHP2 expression determines the efficacy of PD-1/PD-L1 inhibitors in advanced KRAS mutant non-small cell lung cancer. *Thoracic cancer* 2021; 12: 2564-2573.
- [109] Fodor M, Price E, Wang P et al. Dual allosteric inhibition of SHP2 phosphatase. *ACS chemical biology* 2018; 13: 647-656.

- [110] Garcia Fortanet J, Chen CH-T, Chen Y-NP et al. Allosteric inhibition of SHP2: identification of a potent, selective, and orally efficacious phosphatase inhibitor. *Journal of medicinal chemistry* 2016; 59: 7773-7782.
- [111] LaMarche MJ, Acker M, Argintaru A et al. Identification of TNO155, an Allosteric SHP2 Inhibitor for the Treatment of Cancer. *Journal of medicinal chemistry* 2020; 63: 13578-13594.
- [112] Zeng L-F, Zhang R-Y, Yu Z-H et al. Therapeutic potential of targeting the oncogenic SHP2 phosphatase. *Journal of medicinal chemistry* 2014; 57: 6594-6609.
- [113] Zhang R-Y, Yu Z-H, Zeng L et al. SHP2 phosphatase as a novel therapeutic target for melanoma treatment. *Oncotarget* 2016; 7: 73817.
- [114] Chen Y-NP, LaMarche MJ, Chan HM et al. Allosteric inhibition of SHP2 phosphatase inhibits cancers driven by receptor tyrosine kinases. *Nature* 2016; 535: 148-152.
- [115] Liu C, Lu H, Wang H et al. Combinations with allosteric SHP2 inhibitor TNO155 to block receptor tyrosine kinase signaling. *Clinical Cancer Research* 2021; 27: 342-354.
- [116] Brana I, Shapiro G, Johnson ML et al. Initial results from a dose finding study of TNO155, a SHP2 inhibitor, in adults with advanced solid tumors. In *Edition Journal of Clinical Oncology: Wolters Kluwer Health* 2021; 3005.
- [117] Paget S. The distribution of secondary growths in cancer of the breast. *The Lancet* 1889; 133: 571-573.
- [118] Wirtz D, Konstantopoulos K, Searson PC. The physics of cancer: the role of physical interactions and mechanical forces in metastasis. *Nature Reviews Cancer* 2011; 11: 512-522.
- [119] Chen M-T, Sun H-F, Zhao Y et al. Comparison of patterns and prognosis among distant metastatic breast cancer patients by age groups: a SEER population-based analysis. *Scientific reports* 2017; 7: 1-8.
- [120] Brown WS, Wendt MK. Integrin-mediated resistance to epidermal growth factor receptor-targeted therapy: an inflammatory situation. *Breast cancer research* 2014; 16: 1-3.
- [121] Jun BH, Guo T, Libring S et al. Fibronectin-expressing mesenchymal tumor cells promote breast cancer metastasis. *Cancers* 2020; 12: 2553.

- [122] Gava F, Rigal L, Mondesert O et al. Gap junctions contribute to anchorage-independent clustering of breast cancer cells. *Bmc Cancer* 2018; 18: 1-9.
- [123] Fujita-Sato S, Galeas J, Truitt M et al. Enhanced MET translation and signaling sustains K-Ras-driven proliferation under anchorage-independent growth conditions. *Cancer research* 2015; 75: 2851-2862.
- [124] Pulaski BA, Ostrand-Rosenberg S. Mouse 4T1 breast tumor model. *Current protocols in immunology* 2000; 39: 20.22. 21-20.22. 16.
- [125] Jungwirth U, van Weverwijk A, Melake MJ et al. Generation and characterisation of two D2A1 mammary cancer sublines to model spontaneous and experimental metastasis in a syngeneic BALB/c host. *Disease models & mechanisms* 2018; 11: dmm031740.
- [126] Wendt MK, Taylor MA, Schiemann BJ et al. Fibroblast growth factor receptor splice variants are stable markers of oncogenic transforming growth factor β 1 signaling in metastatic breast cancers. *Breast cancer research* 2014; 16: 1-15.
- [127] Wendt MK, Schiemann WP. Therapeutic targeting of the focal adhesion complex prevents oncogenic TGF- β signaling and metastasis. *Breast cancer research* 2009; 11: 1-16.
- [128] Tan L, Wang J, Tanizaki J et al. Development of covalent inhibitors that can overcome resistance to first-generation FGFR kinase inhibitors. *Proceedings of the National Academy of Sciences* 2014; 111: E4869-E4877.
- [129] Shinde A, Libring S, Alpsy A et al. Autocrine fibronectin inhibits breast cancer metastasis. *Molecular Cancer Research* 2018; 16: 1579-1589.
- [130] Zhao H, Martin E, Matalkah F et al. Conditional knockout of SHP2 in ErbB2 transgenic mice or inhibition in HER2-amplified breast cancer cell lines blocks oncogene expression and tumorigenesis. *Oncogene* 2019; 38: 2275-2290.
- [131] Aceto N, Sausgruber N, Brinkhaus H et al. Tyrosine phosphatase SHP2 promotes breast cancer progression and maintains tumor-initiating cells via activation of key transcription factors and a positive feedback signaling loop. *Nature medicine* 2012; 18: 529-537.
- [132] Ali R, Brown W, Purdy SC et al. Biased signaling downstream of epidermal growth factor receptor regulates proliferative versus apoptotic response to ligand. *Cell death & disease* 2018; 9: 1-12.
- [133] Lu L, Bai Y, Wang Z. Elevated T cell activation score is associated with improved survival of breast cancer. *Breast cancer research and treatment* 2017; 164: 689-696.

- [134] Saleh R, Toor SM, Khalaf S, Elkord E. Breast cancer cells and PD-1/PD-L1 blockade upregulate the expression of PD-1, CTLA-4, TIM-3 and LAG-3 immune checkpoints in CD4+ T cells. *Vaccines* 2019; 7: 149.
- [135] Terranova-Barberio M, Pawlowska N, Dhawan M et al. Exhausted T cell signature predicts immunotherapy response in ER-positive breast cancer. *Nature communications* 2020; 11: 1-10.
- [136] Wang K, Shen T, Siegal GP, Wei S. The CD4/CD8 ratio of tumor-infiltrating lymphocytes at the tumor-host interface has prognostic value in triple-negative breast cancer. *Human pathology* 2017; 69: 110-117.
- [137] Jin YW, Hu P. Tumor-infiltrating CD8 T cells predict clinical breast cancer outcomes in young women. *Cancers* 2020; 12: 1076.
- [138] Huang Y, Ma C, Zhang Q et al. CD4+ and CD8+ T cells have opposing roles in breast cancer progression and outcome. *Oncotarget* 2015; 6: 17462.
- [139] Guillot A, Tacke F. Liver macrophages: old dogmas and new insights. *Hepatology communications* 2019; 3: 730-743.
- [140] Xiang X, Wang J, Lu D, Xu X. Targeting tumor-associated macrophages to synergize tumor immunotherapy. *Signal transduction and targeted therapy* 2021; 6: 1-12.
- [141] Quintana E, Schulze CJ, Myers DR et al. Allosteric inhibition of SHP2 stimulates antitumor immunity by transforming the immunosuppressive environment. *Cancer research* 2020; 80: 2889-2902.
- [142] Yoshihara K, Shahmoradgoli M, Martínez E et al. Inferring tumour purity and stromal and immune cell admixture from expression data. *Nature communications* 2013; 4: 1-11.
- [143] Subramanian A, Tamayo P, Mootha VK et al. Gene set enrichment analysis: a knowledge-based approach for interpreting genome-wide expression profiles. *Proceedings of the National Academy of Sciences* 2005; 102: 15545-15550.
- [144] Mootha VK, Lindgren CM, Eriksson K-F et al. PGC-1 α -responsive genes involved in oxidative phosphorylation are coordinately downregulated in human diabetes. *Nature genetics* 2003; 34: 267-273.
- [145] Li C-W, Lim S-O, Xia W et al. Glycosylation and stabilization of programmed death ligand-1 suppresses T-cell activity. *Nature communications* 2016; 7: 1-11.

- [146] Schmid P, Cortes J, Puzstai L et al. Pembrolizumab for early triple-negative breast cancer. *New England Journal of Medicine* 2020; 382: 810-821.
- [147] Hernando-Calvo A, Cescon DW, Bedard PL. Novel classes of immunotherapy for breast cancer. *Breast Cancer Research and Treatment* 2021; 1-15.
- [148] Chou T-C. Drug combination studies and their synergy quantification using the Chou-Talalay method. *Cancer research* 2010; 70: 440-446.
- [149] Montagner A, Yart A, Dance M et al. A novel role for Gab1 and SHP2 in epidermal growth factor-induced Ras activation. *Journal of Biological Chemistry* 2005; 280: 5350-5360.
- [150] Koyama T, Nakaoka Y, Fujio Y et al. Interaction of scaffolding adaptor protein Gab1 with tyrosine phosphatase SHP2 negatively regulates IGF-I-dependent myogenic differentiation via the ERK1/2 signaling pathway. *Journal of Biological Chemistry* 2008; 283: 24234-24244.
- [151] Gotoh N, Ito M, Yamamoto S et al. Tyrosine phosphorylation sites on FRS2 α responsible for Shp2 recruitment are critical for induction of lens and retina. *Proceedings of the National Academy of Sciences* 2004; 101: 17144-17149.
- [152] Cunnick JM, Dorsey JF, Munoz-Antonia T et al. Requirement of SHP2 binding to Grb2-associated binder-1 for mitogen-activated protein kinase activation in response to lysophosphatidic acid and epidermal growth factor. *Journal of Biological Chemistry* 2000; 275: 13842-13848.
- [153] Ahmed TA, Adamopoulos C, Karoulia Z et al. SHP2 Drives Adaptive Resistance to ERK Signaling Inhibition in Molecularly Defined Subsets of ERK-Dependent Tumors. *Cell reports* 2019; 26: 65-78. e65.
- [154] Agazie YM, Hayman MJ. Molecular mechanism for a role of SHP2 in epidermal growth factor receptor signaling. *Molecular and cellular biology* 2003; 23: 7875-7886.
- [155] Bennett AM, Tang TL, Sugimoto S et al. Protein-tyrosine-phosphatase SHPTP2 couples platelet-derived growth factor receptor beta to Ras. *Proceedings of the National Academy of Sciences* 1994; 91: 7335-7339.
- [156] Hartman Z, Geldenhuys WJ, Agazie YM. Novel small-molecule inhibitor for the oncogenic tyrosine phosphatase SHP2 with anti-breast cancer cell effects. *Acs Omega* 2020; 5: 25113-25124.

- [157] Vemulapalli V, Chylek LA, Erickson A et al. Time-resolved phosphoproteomics reveals scaffolding and catalysis-responsive patterns of SHP2-dependent signaling. *Elife* 2021; 10: e64251.
- [158] Zhang R-Y, Yu Z-H, Chen L et al. Mechanistic insights explain the transforming potential of the T507K substitution in the protein-tyrosine phosphatase SHP2. *Journal of Biological Chemistry* 2020; 295: 6187-6201.
- [159] Buonato JM, Lan IS, Lazzara MJ. EGF augments TGF β -induced epithelial–mesenchymal transition by promoting SHP2 binding to GAB1. *Journal of cell science* 2015; 128: 3898-3909.
- [160] Sun X, Zhang J, Wang Z et al. Shp2 plays a critical role in IL-6-induced EMT in breast cancer cells. *International Journal of Molecular Sciences* 2017; 18: 395.
- [161] Lin C-C, Suen KM, Jeffrey P-A et al. Receptor tyrosine kinases regulate signal transduction through a liquid-liquid phase separated state. *Molecular Cell* 2022.
- [162] Guo W, Xu Q. Phosphatase-independent functions of SHP2 and its regulation by small molecule compounds. *Journal of Pharmacological Sciences* 2020; 144: 139-146.
- [163] Lu W, Shen K, Cole PA. Chemical dissection of the effects of tyrosine phosphorylation of SHP-2. *Biochemistry* 2003; 42: 5461-5468.
- [164] Bertotti A, Comoglio PM, Trusolino L. β 4 integrin activates a Shp2–Src signaling pathway that sustains HGF-induced anchorage-independent growth. *J Cell Biol* 2006; 175: 993-1003.
- [165] Sausgruber N, Coissieux M, Britschgi A et al. Tyrosine phosphatase SHP2 increases cell motility in triple-negative breast cancer through the activation of SRC-family kinases. *Oncogene* 2015; 34: 2272.
- [166] Xu Z, Guo C, Ye Q et al. Endothelial deletion of SHP2 suppresses tumor angiogenesis and promotes vascular normalization. *Nature communications* 2021; 12: 1-15.
- [167] Chen H, Libring S, Ruddraraju KV et al. SHP2 is a multifunctional therapeutic target in drug resistant metastatic breast cancer. *Oncogene* 2020; 39: 7166-7180.
- [168] Mainardi S, Mulero-Sánchez A, Prahallad A et al. SHP2 is required for growth of KRAS-mutant non-small-cell lung cancer in vivo. *Nature medicine* 2018; 24: 961-967.

- [169] Tao B, Jin W, Xu J et al. Myeloid-specific disruption of tyrosine phosphatase Shp2 promotes alternative activation of macrophages and predisposes mice to pulmonary fibrosis. *The Journal of Immunology* 2014; 193: 2801-2811.
- [170] Prahallad A, Heynen GJ, Germano G et al. PTPN11 is a central node in intrinsic and acquired resistance to targeted cancer drugs. *Cell reports* 2015; 12: 1978-1985.
- [171] Nagamura Y, Miyazaki M, Nagano Y et al. SHP2 as a Potential Therapeutic Target in Diffuse-Type Gastric Carcinoma Addicted to Receptor Tyrosine Kinase Signaling. *Cancers* 2021; 13: 4309.
- [172] Toral KJ, Wuenschel MA, Black EP. Genomic data from NSCLC tumors reveals correlation between SHP-2 activity and PD-L1 expression and suggests synergy in combining SHP-2 and PD-1/PD-L1 inhibitors. *Plos one* 2021; 16: e0256416.
- [173] Li J, Sui Y, Berzofsky JA. Fine tuning CD8+ T cell functional avidity by the PD-1/SHP2 axis. In *Edition Am Assoc Immunol* 2020.
- [174] Liu W, Guo W, Shen L et al. T lymphocyte SHP2-deficiency triggers anti-tumor immunity to inhibit colitis-associated cancer in mice. *Oncotarget* 2017; 8: 7586.
- [175] Wang Y, Mohseni M, Grauel A et al. SHP2 blockade enhances anti-tumor immunity via tumor cell intrinsic and extrinsic mechanisms. *Scientific reports* 2021; 11: 1-23.
- [176] Concha-Benavente F, Srivastava RM, Ferrone S, Ferris RL. EGFR-mediated tumor immunoescape: the imbalance between phosphorylated STAT1 and phosphorylated STAT3. *Oncoimmunology* 2013; 2: e27215.
- [177] Srivastava RM, Trivedi S, Concha-Benavente F et al. STAT1-induced HLA class I upregulation enhances immunogenicity and clinical response to anti-EGFR mAb cetuximab therapy in HNC patients. *Cancer immunology research* 2015; 3: 936-945.
- [178] Chen Y-NP, LaMarche MJ, Chan HM et al. Allosteric inhibition of SHP2 phosphatase inhibits cancers driven by receptor tyrosine kinases. *Nature* 2016; 535: 148.
- [179] Fedele C, Ran H, Diskin B et al. SHP2 inhibition prevents adaptive resistance to MEK inhibitors in multiple cancer models. *Cancer discovery* 2018; 8: 1237-1249.
- [180] Zhao M, Guo W, Wu Y et al. SHP2 inhibition triggers anti-tumor immunity and synergizes with PD-1 blockade. *Acta Pharmaceutica Sinica B* 2019; 9: 304-315.
- [181] Hao H-X, Wang H, Liu C et al. Tumor intrinsic efficacy by SHP2 and RTK inhibitors in KRAS mutant cancers. *Molecular cancer therapeutics* 2019; molcanther. 0170.2019.

- [182] Chen D, Barsoumian HB, Yang L et al. SHP-2 and PD-L1 inhibition combined with radiotherapy enhances systemic antitumor effects in an anti-PD-1-resistant model of non-small-cell lung cancer. *Cancer immunology research* 2020.
- [183] Gao J, Wu Z, Zhao M et al. Allosteric inhibition reveals SHP2-mediated tumor immunosuppression in colon cancer by single-cell transcriptomics. *Acta Pharmaceutica Sinica B* 2021.
- [184] Dammeijer F, van Gulijk M, Mulder EE et al. The PD-1/PD-L1-checkpoint restrains T cell immunity in tumor-draining lymph nodes. *Cancer Cell* 2020; 38: 685-700. e688.
- [185] Sheng J, Wang H, Liu X et al. Deep Sequencing of T-Cell Receptors for Monitoring Peripheral CD8+ T Cells in Chinese Advanced Non-Small-Cell Lung Cancer Patients Treated With the Anti-PD-L1 Antibody. *Frontiers in Molecular Biosciences* 2021; 8.
- [186] Blackburn SD, Shin H, Freeman GJ, Wherry EJ. Selective expansion of a subset of exhausted CD8 T cells by α PD-L1 blockade. *Proceedings of the National Academy of Sciences* 2008; 105: 15016-15021.
- [187] Kraman M, Faroudi M, Allen NL et al. FS118, a bispecific antibody targeting LAG-3 and PD-L1, enhances T-cell activation resulting in potent antitumor activity. *Clinical Cancer Research* 2020; 26: 3333-3344.
- [188] Oweida A, Hararah MK, Phan A et al. Resistance to radiotherapy and PD-L1 blockade is mediated by TIM-3 upregulation and regulatory T-cell infiltration. *Clinical Cancer Research* 2018; 24: 5368-5380.
- [189] Harding JJ, Moreno V, Bang Y-J et al. Blocking TIM-3 in treatment-refractory advanced solid tumors: a Phase Ia/b study of LY3321367 with or without an anti-PD-L1 antibody. *Clinical Cancer Research* 2021; 27: 2168-2178.

VITA

Hao Chen was born and raised in Jiading, Shanghai. He received his bachelor's in science from the School of Pharmacy, Shanghai Jiao Tong University in July 2013. His bachelor thesis about the combination therapies of novel antibody with tamoxifen to inhibit cancer cell growth was awarded as Top 1% Excellent. He continued his study at Shanghai Jiao Tong University in a novel expression platform for therapeutic humanized antibodies. He received his master's in medicine in March 2016 and was awarded the national scholarship for a master's and excellent graduate of Shanghai. Then, he enrolled in the Purdue University Interdisciplinary Life Sciences (PULSe) Program in August of 2016. After rotation, he decided to join Dr. Michael K. Wendt's lab in May 2017 to work on research about metastatic breast cancer. During his doctoral research, Hao received several fellowships including SIRG Graduate Research Assistantship, Lilly Endowment Research Award, and the Bilsland Dissertation Fellowship. After his graduation, he decided to work as a postdoctoral fellow to continue the exploration of novel cancer therapeutics.

PUBLICATIONS

- Akhand S S, **Chen H**, Purdy S, et al. Fibroblast growth factor receptor facilitates recurrence of minimal residual disease following trastuzumab emtansine therapy. *npj Breast Cancer* (2021). 7, 5
- Chen H**, Libring S, Ruddraraju K, et al. SHP2 is a multifunctional therapeutic target in drug resistant metastatic breast cancer. *Oncogene* 39.49 (2020) 7166-7180
<https://doi.org/10.1038/s41388-020-01488-5>
- Kim D, Sun Y, Xie D, Denton K E, **Chen H**, Lin H, et al. Application of a Substrate-Mediated Selection with c-Src Tyrosine Kinase to a DNA-Encoded Chemical Library. *Molecules*, 24.15 (2019): 2764
- Krabill AD, **Chen H**, Hussain S, et al. Optimization and Anti-Cancer Properties of Fluoromethylketones as Covalent Inhibitors for Ubiquitin C-Terminal Hydrolase L1. *Molecules* (2021) 26(5):1227.
- Krabill A D, **Chen H**, Hussain S, et al. Biochemical and cellular characterization of a cyanopyrrolidine covalent Ubiquitin C - terminal hydrolase L1 inhibitor. *ChemBioChem* (2019).
- Shinde A, Wilmanski T, **Chen H**, et al. Pyruvate carboxylase supports the pulmonary tropism of metastatic breast cancer. *Breast Cancer Research*. 20.1 (2018): 76.